Scalability of Electric Axles for System-Level Design in the Early Development Phases of Electric Vehicles

prepared by Ayoub Aroua

Dissertation submitted to obtain the academic degrees of:

- Docteur en Génie électrique from the University of Lille, France
- Doctor of Electromechanical Engineering from Ghent University, Belgium

Publically defended on December 19, 2023, in Lille, France

Supervisors:

Dr. HDR. Walter Lhomme	University of Lille promotor
Prof. Kurt Stockman	Ghent University promotor
Prof. Alain Bouscayrol	University of Lille co-promotor
Prof. Peter Sergeant	Ghent University co-promotor

Members of the joint examination board:

Prof. Theo Hofman	Eindhoven University of Technology, The Netherlands	Referee
Dr. HDR. Emmanuel Vinot	University Gustave Eiffel, France	Referee
Prof. Lieven Vandevelde	Ghent University, Belgium	Referee
Prof. Florence Ossart	Sorbonne University, France	Chair
Prof. Elena Lomonova	Eindhoven University of Technology, The Netherlands	Examiner
Prof. Hennie De Schepper	Ghent University, Belgium	Co-chair
Dr. HDR. Walter Lhomme	University of Lille, France	Promotor
Prof. Kurt Stockman	Ghent University, Belgium	Promotor

Mise à l'échelle des entraînements électromécaniques pour la conception au niveau système dans les premières phases de développement des véhicules électriques

préparée par Ayoub Aroua

Thèse présentée en vue de l'obtention des grades académiques de:

- Docteur en Génie électrique de l'Université de Lille, France
- Doctor in de ingenieurswetenschappen: werktuigkunde-elektrotechniek de l'Université de Gand, Belgique

Soutenue publiquement le 19 décembre 2023 à Lille, France

Encadrants:

Dr. HDR. Walter Lhomme	Directeur de thèse, Université de Lille
Pr. Kurt Stockman	Directeur de thèse, Université de Gand
Pr. Alain Bouscayrol	Encadrant, Université de Lille
Pr. Peter Sergeant	Encadrant, Université de Gand

Composition du jury:

Pr. Theo Hofman	Université de technologie d'Eindhoven, Pays-Bas	Rapporteur
Dr. HDR. Emmanuel Vinot	Université Gustave Eiffel, France	Rapporteur
Pr. Lieven Vandevelde	Université de Gand, Belgique	Rapporteur
Pr. Florence Ossart	Sorbonne Université, France	Présidente
Pr. Elena Lomonova	Université de technologie d'Eindhoven, Pays-Bas	Examinatrice
Pr. Hennie De Schepper	Université de Gand, Belgique	Co- présidente
Dr. HDR. Walter Lhomme	Université de Lille, France	Directeur de thèse
Pr. Kurt Stockman	Université de Gand, Belgique	Directeur de thèse

Schaalbare elektromechanische aandrijvingen voor ontwerp op systeemniveau in de vroege stadia van de ontwikkeling van elektrische voertuigen

opgesteld door Ayoub Aroua

Proefschrift ingediend tot het behalen van de graad van:

- Docteur en Génie électrique van de Universiteit Rijsel, Frankrijk
- Doctor in de ingenieurswetenschappen: werktuigkunde-elektrotechniek van de Universiteit Gent, België

Publiekelijk verdedigd op 19 december 2023 in Rijsel, Frankrijk

Promotoren:

Dr. HDR. Walter Lhomme	Promotor, Universiteit Rijsel
Prof. Kurt Stockman	Promotor, Universiteit Gent
Prof. Alain Bouscayrol	Co-promotor, Universiteit Rijsel
Prof. Peter Sergeant	Co-promotor, Universiteit Gent

Leden van de gezamenlijke examencommissie:

Prof. Theo Hofman	Technische Universiteit Eindhoven, Nederland	Beoordelaar
Dr. HDR. Emmanuel Vinot	Universiteit Gustave Eiffel, Frankrijk	Beoordelaar
Prof. Lieven Vandevelde	Universiteit Gent, België	Beoordelaar
Prof. Florence Ossart	Universiteit Sorbonne, Frankrijk	Voorzitter
Prof. Elena Lomonova	Technische Universiteit Eindhoven, Nederland	Examinator
Prof. Hennie De Schepper	Universiteit Gent, België	Co-voorzitter
Dr. HDR. Walter Lhomme	Universiteit Rijsel, Frankrijk	Promotor
Prof. Kurt Stockman	Universiteit Gent, België	Promotor

Acknowledgment

Preface

This Ph.D. thesis has been an invaluable learning experience for me, both scientifically and personally. I would not describe the journey as consistently smooth and straightforward; however, the encountered challenges have been crucial in shaping me into the researcher I am today.

I wish to express my appreciation to the members of the examination board to whom I had the opportunity to present and discuss my research work. I want to acknowledge the time and efforts invested by Theo Hofman, Emmanuel Vinot, and Lieven Vandevelde in reviewing my dissertation as well as the discussion in which we engaged during the Q&A session. I want to extend my thanks to Florence Ossart for presiding over the defense, Hennie De Schepper for co-chairing the session, and Elena Lomonova for accepting to be an examiner of my thesis.

This work would have never seen the light without the support and guidance that I received over the past three years from my supervisors to whom I owe some words.

I would like to express my deepest gratitude to my promotor Walter Lhomme at the University of Lille. Walter, I am indebted to you as you played a significant role in convincing me to embark on the journey of pursuing a Ph.D. and diving into the world of research. This possibility, which I had not considered three years ago, is now a transformational path in my career. I appreciate all the diverse discussions that we had together, the confidence in my abilities that you demonstrated to me, as well as the freedom and autonomy you granted me in conducting this research. Beyond the scientific discussions, it is the human qualities that you embody that I appreciate even more. It has been an enriching experience for both my research and personal development under your mentorship over these years.

My sincere gratitude goes to my promotor Kurt Stockman at Ghent University for his invaluable support and guidance. Undertaking a Ph.D. thesis with an emphasis on both theoretical and experimental aspects concerning power loss in mechanical transmissions was a big challenge, especially for a Ph.D. student with a purely electrical background. Nevertheless, walking through this challenge has been essential in my personal and professional growth. Kurt, I am grateful for the valuable discussions and insights, constructive feedback, and guidance that played a vital role in completing the investigation on the power loss scaling of mechanical transmissions and the experimental testing.

I wish to convey my appreciation to my co-promotor at the University of Lille Alain Bouscayrol for his valuable input regarding the system-level investigation. Alain, the

Contents

Abstract

The automotive industry is required to accelerate the development and deployment of electrified vehicles at a faster pace than ever, to align the transportation sector with the climate goals. Reducing the development time of electric vehicles becomes an urgent priority. On the other hand, the industry is challenged by the increasing complexity and large design space of the emerging electrified powertrains. The existing approaches to address component design, such as numerical methods exemplified by finite element method, computational fluid dynamic, etc., are based on a detailed design process. This leads to a long computational burden when trying to incorporate them at system-level. Speeding up the early development phases of electrified vehicles necessitates new methodologies and tools, supporting the exploration of the system-level design space. These methodologies should allow for assessing different sizing choices of electrified powertrains in the early development phases, both efficiently in terms of computational time and with reliable results in terms of energy consumption at system-level. To address this challenge, this Ph.D. thesis aims to develop a scaling methodology for electric axles, allowing system-level investigation of different power-rated electric vehicles. The electric axle considered in this thesis comprises a voltage source inverter, an electric machine, a gearbox, and a control unit. The scaling procedure is aimed at predicting the data of a newly defined design of a given component with different specifications based on a reference design, without redoing time and effort-consuming steps. For this purpose, different derivations of scaling laws of the electric axle components are thoroughly discussed and compared at component-level in terms of power loss scaling. A particular emphasis is placed on examining the linear losses-to-power scaling method, which is widely employed in system-level studies. This is because, this method presents questionable assumptions, and has not been the subject of a comprehensive examination. A key contribution of the presented work is the derivation of power loss scaling laws of gearboxes, which has been identified as a gap in the current literature. This is achieved through an intensive experimental campaign using commercial gearboxes. To incorporate the scaling laws at system-level and study the interaction between the scaled components, the energetic macroscopic representation formalism is employed. The novelty of the proposed method lies in structuring a scalable model and control for a reference electric axle to be used in system-level simulation. The novel organization consists of a reference model and control complemented by two power adaptation elements at the electrical and mechanical sides. These latter elements consider the scaling effects, including the power losses. The methodology is applied for different case studies of battery electric vehicles, ranging from light to heavy-duty vehicles. Particular attention is paid to assessing the impact of the linear

power-to-losses scaling method on energy consumption considering different power scaling factors and driving cycles, as compared to high-fidelity scaling methods.

Keywords: early development phases, efficiency, electric vehicles, energetic macroscopic representation, energetic study, experimental campaign, modularity, scalable modeling and control, scaling laws, system-level design

Résumé

L'industrie automobile est contrainte d'accélérer le développement et le déploiement des véhicules électrifiés à un rythme sans précédent, afin d'aligner le secteur du transport avec les objectifs climatiques. La réduction du temps de développement des véhicules électriques devient une priorité urgente. D'autre part, l'industrie est confrontée à une complexité accrue et à l'ampleur de l'espace de conception des chaînes de traction électrifiées émergentes. Les approches existantes pour aborder la conception des composants, notamment les méthodes numériques telles que la méthode des éléments finis, la mécanique des fluides numérique, etc., reposent sur un processus de conception détaillé. Cela entraîne une longue charge de calcul lorsqu'on essaie de les intégrer au niveau système. L'accélération des premières phases de développement des véhicules électrifiés nécessite de nouvelles méthodologies et de nouveaux outils, permettant d'explorer l'espace de conception au niveau système. Ces méthodologies devraient permettre d'évaluer les différents choix de pré-dimensionnement des chaînes de traction électrifiées dans les phases de pré-étude. Cette évaluation devrait se faire de manière efficace en termes de temps de calcul, tout en garantissant des résultats fiables en ce qui concerne la consommation énergétique au niveau système. Pour relever ce défi, cette thèse de doctorat vise à développer une méthodologie de mise à l'échelle pour les systèmes d'entraînement électromécaniques, permettant l'étude au niveau système de différents véhicules électriques. Un système d'entraînement électromécanique se compose d'un ensemble comprenant un onduleur, une machine électrique, un réducteur mécanique et une unité de contrôle. La procédure de mise à l'échelle vise à prédire les données d'une conception nouvellement définie d'un composant donné avec des spécifications différentes sur la base d'une conception de référence, sans avoir à refaire des étapes qui demandent beaucoup de temps et d'efforts. À cette fin, différentes formulations de lois de mise à l'échelle des composants du système d'entraînement électromécanique sont examinées en détail et comparées au niveau composant en termes de mise à l'échelle de la perte de puissance. Un accent particulier est mis sur l'examen de la méthode de mise à l'échelle linéaire des pertes par une homothétie, qui est largement employée dans les études au niveau système. En effet, cette méthode présente des hypothèses discutables et n'a pas fait l'objet d'une étude approfondie. En outre, l'une des principales contributions de ce travail est la formulation des lois de mise à l'échelle des pertes de puissance des réducteurs mécaniques, qui ont été identifiées comme une lacune dans la littérature actuelle. Pour ce faire, une campagne expérimentale intensive a été menée sur des réducteurs mécaniques commerciaux. Pour intégrer les lois d'échelle au niveau système et étudier l'interaction entre les composants mis à l'échelle, le formalisme de la représentation macroscopique énergétique est utilisé. La nouveauté de la méthode proposée réside dans la structuration d'un modèle et d'une commande évolutifs du système d'entraînement électromécanique de référence à utiliser dans

la simulation au niveau système. La nouvelle organisation consiste en un modèle et une commande de référence complétés par deux éléments d'adaptation de puissance du côté électrique et mécanique. Ces derniers éléments prennent en compte les effets d'échelle, y compris les pertes de puissance. La méthodologie est appliquée à différents cas d'étude de véhicules électriques à batterie, allant des véhicules légers aux véhicules lourds. Une attention particulière est accordée à l'évaluation de l'impact de la méthode de la mise à l'échelle linéaire sur la consommation d'énergie, en tenant compte de différents facteurs de mise à l'échelle de la puissance et des cycles de conduite, par rapport à d'autres méthodes de mise à l'échelle avec une haute-fidélité.

Mots clefs : phases de développement préliminaire, cartographie de rendement, véhicules électriques, représentation macroscopique énergétique, étude énergétique, campagne expérimentale, modularité, modélisation et contrôle évolutifs, lois d'échelle, conception système.

Samenvatting

De auto-industrie moet de ontwikkeling en introductie van elektrische voertuigen sneller dan ooit realiseren om de transportsector op één lijn te brengen met de klimaatdoelstellingen. Het reduceren van de ontwikkelingstijd van elektrische voertuigen wordt een dringende prioriteit. De auto-industrie wordt hierbij uitgedaagd door de toenemende complexiteit en de grote ontwerpruimte van de opkomende geëlektrificeerde aandrijflijnen. De bestaande benaderingen om het ontwerp van componenten aan te pakken, zoals numerieke methoden en eindige-elementenmethodes, computational fluid dynamic, enzovoort, zijn gebaseerd op een gedetailleerd ontwerpproces. Dit leidt tot een grote rekenlast wanneer geprobeerd wordt om ze op systeemniveau toe te passen. Om de vroege ontwikkelingsfasen van elektrische voertuigen te versnellen, zijn nieuwe methodologieën en hulpmiddelen nodig die de verkenning van de ontwerpruimte op systeemniveau ondersteunen. Deze methodologieën moeten het mogelijk maken om verschillende dimensioneringskeuzes van geëlektrificeerde aandrijflijnen te beoordelen, waarbij hun efficiëntie in termen van rekentijd en betrouwbare in termen van energieverbruik op systeemniveau belangrijk zijn. Om deze uitdaging aan te gaan, is dit proefschrift gericht op het ontwikkelen van een schaleringsmethode voor elektromechanische aandrijfsystemen, waardoor onderzoek op systeemniveau van verschillende elektrische voertuigen met verschillende vermogens mogelijk wordt. Het elektromechanisch aandrijfsysteem dat in dit proefschrift wordt bestudeerd bestaat uit een spanningsbronomvormer, een elektrische machine, een tandwielkast en een besturingseenheid. De schalingsmethodiek is gericht op het voorspellen van de gegevens van een nieuw gedefinieerd ontwerp van een component met verschillende specificaties op basis van een referentieontwerp, zonder tijd- en inspanningrovende stappen opnieuw uit te voeren. Voor dit doel worden verschillende schalingswetten van de componenten van het elektromechanische aandrijfsysteem grondig besproken en vergeleken op componentniveau in termen van vermogensverlies. Er wordt speciale nadruk gelegd op het onderzoeken van de lineaire methode voor het schalen van verliezen aangezien deze veel wordt gebruikt in studies op systeemniveau. De reden hiervoor is dat deze methode dubieuze aannames bevat en niet uitgebreid is onderzocht. Een belangrijke bijdrage van het gepresenteerde werk is de afleiding van de wetten voor de schaling van vermogensverliezen van tandwielkasten, wat een hiaat is in de huidige literatuur. Dit wordt bereikt door een intensieve experimentele campagne met commerciële tandwielkasten. Om de schalingswetten op systeemniveau op te nemen en de interactie tussen de geschaalde componenten te bestuderen, wordt het formalisme van de energetische macroscopische representatie gebruikt. De nieuwigheid van de voorgestelde methode ligt in het structureren van een schaalbaar model en de regeling ervan voor een referentie elektromechanisch aandrijfsysteem voor gebruik in simulatie op systeemniveau. De

nieuwe organisatie bestaat uit een referentiemodel en -regeling aangevuld met twee vermogensaanpassingselementen aan de elektrische en mechanische kant. Deze laatste elementen houden rekening met de schaaleffecten, inclusief de vermogensverliezen. De methodologie wordt toegepast op verschillende studiegevallen van batterij-elektrische voertuigen, variërend van lichte tot zware voertuigen. Er wordt bijzondere aandacht besteed aan de beoordeling van de impact van de lineaire schalingsmethode op het energieverbruik, rekening houdend met verschillende vermogensschalingsfactoren en rijcycli, in vergelijking met high-fidelity schalingsmethoden.

Trefwoorden: vroege ontwikkelingsfasen, efficiëntie, elektrische voertuigen, energetische macroscopische weergave, energetische studie, experimentele campagne, modulariteit, schaalbare modellering en regeling, schaalwetten, ontwerp op systeemniveau

Extended summary

The automotive industry is required to accelerate the development and deployment of electrified vehicles at a faster pace than ever, to align the transportation sector with the climate goals. Reducing the development time of electric vehicles becomes an urgent priority. On the other hand, the industry is challenged by the increasing complexity and large design space of the emerging electrified powertrains. The existing approaches to address component design, such as numerical methods exemplified by finite element method, computational fluid dynamic, etc., are based on a detailed design process. This leads to a long computational burden when trying to incorporate them at system-level. Speeding up the early development phases of electrified vehicles necessitates new methodologies and tools, supporting the exploration of the system-level design space. These methodologies should allow for assessing different sizing choices of electrified powertrains in the early development phases, both efficiently in terms of computational time and with reliable results in terms of energy consumption at system-level. To address this challenge, this Ph.D. thesis aims to develop a scaling methodology for electric axles, allowing system-level investigation of different power-rated electric vehicles. The electric axle considered in this thesis comprises a voltage source inverter, an electric machine, a gearbox, and a control unit. Given the abundance of technology for electric axle components, the scope of the study is confined to permanent magnet synchronous machines, IGBT-based inverters, and planetary gearboxes due to their relevance in the automotive industry. The scaling procedure is aimed at predicting the data of a newly defined design of a given component with different specifications based on a reference design, without redoing time and effort-consuming steps. For this purpose, different derivations of scaling laws of the electric axle components are thoroughly examined and compared at component-level in terms of power loss scaling and at system-level with regards to energy consumption.

Regarding the scaling of permanent magnet synchronous machines and IGBT-based inverters, collectively referred to as an electric drive system, the literature demonstrates a plethora of scaling laws with different derivations. The literature, essentially addressing system-level investigation, reveals an extensive utilization of the linear losses-to-power scaling method. The method has gained widespread popularity due to its ease of use, simplicity, and the scarcity of component data with different sizes available to powertrain designers in the early development phases of electric vehicles. The linear scaling method does not require in-depth expertise in electric drive system design. Instead, the method assumes that the total losses of a reference design can be linearly scaled according to the desired new power rating regardless of the geometry scaling. The last aforementioned assumption lacks clearly defined explanations in literature, making the reliability of the linear scaling method questionable. Consequently, a focal concern in this dissertation is to assess whether the linear scaling method

can yield satisfactory results in terms of efficiency scaling and the computation of energy consumption. Furthermore, the conditions, e.g. geometry scaling, power scaling factor, driving patterns of the vehicle, etc., under which the method is deemed reliable are thoroughly investigated.

To tackle this challenge, the outcomes of the linear scaling method are compared to more sophisticated scaling laws validated through the finite element method, ensuring their high fidelity. These scaling laws delve into the component design theory and provide clear relationships for the scaled parameters as a function of the geometry change. Regarding permanent synchronous machines, linear scaling has been compared to geometric scaling laws based on three scaling choices that consist of preserving the magnetic field density, the temperature rise in the windings, and a hybrid choice that combines the aforementioned choices. The comparison between linear scaling and geometric scaling laws reveals that the difference in terms of efficiency scaling depends on the operating regions within the torque-speed plane. The efficiency discrepancy is greater in high-torque and low-speed regions, where copper losses prevail. This efficiency disparity is more pronounced in downscaling cases, particularly when comparing linear scaling and geometric scaling that preserves the magnetic field density. In the last aforementioned region, the difference in terms of efficiency is less significant when comparing linear scaling with geometric scaling based on the preservation of the temperature rise. At high-speed regions of the machines, the efficiency difference between linear and geometric scaling laws decreases, where the iron and mechanical losses dominate. This holds for upscaling and downscaling cases and the different scaling choices.

A methodology is presented to incorporate a geometrical information layer into the linear losses-to-power scaling method using the energetic macroscopic representation. The linear scaling method of permanent magnet synchronous machines is demonstrated as a particular case of the geometric scaling laws. There exists at least one combination of axial and radial geometric scaling factors that yield a particular case of linear scaling of losses. Nonetheless, the last statement is true for solely upscaling cases. It has been demonstrated for such scaling cases that no geometric combinations resulted in linear scaling cases.

Regarding IGBT-based inverters, linear scaling is compared against an efficiency benchmarking of three commercialized inverters of the same family. The analysis encompasses other scaling choices available in literature, such as data-driven power loss scaling, and scaling laws based on preserving power density and temperature rise between the scaled and the reference inverters. The efficiency map scaling comparison between the linear losses-to-power scaling method and efficiency benchmarking of commercialized inverters demonstrates comparable results. This is attributed to the linear scaling of conduction losses and the non-significant impact of nonlinearities in the switching losses throughout the scaling process. The last statement is true for upscaling and downscaling cases.

Regarding the scaling of mechanical transmissions, the literature shows comparatively less research work as compared to electric drive systems. Most studies are confined to studying the effect of the transmission geometry on relevant parameters, such as the maximal output torque and inertia. Nonetheless, scaling laws for mechanical transmissions taking into account

the losses are still lacking in literature due to the complexity of such scaling process. The derivation of power loss of mechanical transmission becomes particularly challenging at high-speed regions due to the limited data on the losses in the previously mentioned regions. The requirements for high-speed transmissions stem from the upward trend toward high-speed electric machines to improve power density. To address this challenge, an extensive experimental campaign is conducted to investigate the power losses of five commercial planetary reducers, featuring different speed and torque ratings and gear ratios. Both load-dependent and load-independent losses have been experimentally characterized at speed values up to 14,000 rpm. However, the maximal torque rating differs from the requirements typically encountered in automotive gearboxes due to the low-rated power rating of the tested specimens. The testing results allow for defining a data-driven model, containing physics-based terms, i.e. speed, torque, and gear ratio parameters. Scaling laws are then derived based on maximal input speed, output torque, and gear ratio requirement using a training set, containing the data of 3 gearboxes. A second dataset, containing data from two other gearboxes has been used as a validation case for the scaling process. A methodology based on the scaling laws is subsequently proposed to create a power loss map or efficiency map of a scaled gearbox using solely the data of a reference gearbox. The results of this investigation show that scaling the torque and speed of a reference gearbox while preserving the same gear ratio leads to outstanding results. However, the scaling exercise becomes more challenging when the gear ratio is incorporated because of the nonlinearity of losses at high-speed values. On top of that, linear scaling has been investigated to assess its reliability for mechanical transmissions. The analysis demonstrates that while the linear scaling method can guarantee good results within low-speed regions, it is not suitable for high-speed regions.

Regarding the investigation at system-level, a new methodology based on energetic macroscopic formalism is proposed to facilitate the incorporation of the scaling laws at system-level. The proposed methodology is intended to provide a unified simulation environment to assess the energetic performance of different design candidates of electric axles for electric vehicles with various classes. To achieve this aim, the model of each scaled component of the electric axle is reorganized by keeping the reference model fixed but complimented with two power adaptation elements on the input and output sides of the reference model. The scaling effect according to each adopted method is included in the power adaptation element. The methodology is first applied to each component separately at component-level, then extended to the system-level to investigate the interaction between the scaled components. This permits the derivation of a scalable model and control of the reference electric axle, complemented by solely two power adaptation elements at the electrical and mechanical sides. The presented methodology is intended to reuse the model and control of the reference electric axle, aimed at contributing to speeding up the simulation process of a wide range of electric vehicles.

Furthermore, the impact of the linear scaling method on energy consumption is extensively investigated by considering 4 scaling cases for different transport applications. The study cases encompass a range of power scaling, spanning from 0.58 to 1.96. The investigation has been performed considering different standardized and on-road driving cycles featuring different patterns, e.g. urban, rural, and highway. The outcomes of the linear scaling method in terms of energy consumption are compared with scaled design candidates of electric

machines with distinct geometry resulting from geometric scaling laws, combined with efficiency benchmarking of inverters. Concerning upscaling cases, the sensitivity analysis shows that linear scaling for the electric drive system yields comparative results as compared to the second scaling method, with differences spanning from 0% to 3.2% in absolute terms. Regarding the downscaling cases, it is found that linear scaling consistently underestimates energy consumption. A discrepancy ranging from 3% to 8% is found when applying linear scaling to the electric drive when investigating the urban driving cycle as compared to the geometric scaling laws of the electric machine. Consequently, caution is recommended when dealing with downscaling cases for such specific case scenarios. For highway driving cycles, the differences in terms of energy consumption are found negligible for both upscaling and downscaling cases.

Uitgebreide samenvatting

De auto-industrie moet de ontwikkeling en introductie van elektrische voertuigen sneller dan ooit realiseren om de transportsector op één lijn te brengen met de klimaatdoelstellingen. Het verkorten van de ontwikkelingstijd van elektrische voertuigen wordt een dringende prioriteit. Aan de andere kant wordt de industrie uitgedaagd door de toenemende complexiteit en de grote ontwerpruimte van de opkomende geëlektrificeerde aandrijflijnen. De bestaande benaderingen om het ontwerp van componenten aan te pakken met numerieke methoden zoals de eindige-elementenmethode, computational fluid dynamic, enzovoort, zijn gebaseerd op een gedetailleerd ontwerpproces. Dit leidt tot een grote rekenlast wanneer geprobeerd wordt om ze op systeemniveau toe te passen. Om de vroege ontwikkelingsfasen van elektrische voertuigen te versnellen, zijn nieuwe methodologieën en hulpmiddelen nodig die de verkenning van de ontwerpruimte op systeemniveau ondersteunen. Deze methodologieën moeten het mogelijk maken om verschillende dimensioneringskeuzes van geëlektrificeerde aandrijflijnen te beoordelen in de vroege ontwikkelingsfasen, zowel efficiënt in termen van rekentijd als met betrouwbare resultaten in termen van energieverbruik op systeemniveau. Om deze uitdaging aan te gaan, is dit proefschrift gericht op het ontwikkelen van een schalingsmethodologie voor elektromechanische aandrijfsystemen, waardoor onderzoek op systeemniveau van verschillende elektrische voertuigen met verschillende vermogens mogelijk wordt. Het elektromechanische aandrijfsysteem in dit proefschrift bestaat uit een spanningsbronomvormer, een elektrische machine, een versnellingsbak en een besturingseenheid. Gezien de overvloed aan technologie voor elektromechanische aandrijfcomponenten, is de reikwijdte van het onderzoek beperkt tot synchrone machines met permanente magneten, op IGBT gebaseerde omvormers en planetaire tandwielkasten vanwege hun relevantie in de auto-industrie. De schaalprocedure is gericht op het voorspellen van de gegevens van een nieuw gedefinieerd ontwerp van een bepaalde component met verschillende specificaties op basis van een referentieontwerp, zonder tijd- en inspanningsrovende stappen opnieuw uit te voeren. Hiervoor worden verschillende afleidingen van de schalingswetten van de elektromechanische aandrijfcomponenten grondig onderzocht en vergeleken op componentniveau wat betreft de schaling van het vermogensverlies en op systeemniveau wat betreft het energieverbruik.

Met betrekking tot de schaling van synchrone machines met permanente magneten en op IGBT-gebaseerde omvormers, waarnaar collectief wordt verwezen als een elektrisch aandrijfsysteem, onthult de literatuur een overvloed aan schalingswetten met verschillende afleidingen. De literatuur, die zich voornamelijk richt op onderzoek op systeemniveau, onthult een uitgebreid gebruik van de lineaire verlies/vermogen-schalingsmethode. De methode

heeft veel aan populariteit gewonnen vanwege het gebruiksgemak, de eenvoud en de schaarste aan componentgegevens met verschillende afmetingen die beschikbaar zijn voor ontwerpers van aandrijflijnen in de vroege ontwikkelingsfasen van elektrische voertuigen. De lineaire schalingsmethode vereist geen diepgaande expertise in het ontwerp van elektrische aandrijfsystemen. In plaats daarvan gaat de methode ervan uit dat de totale verliezen van een referentieontwerp lineair kunnen worden geschaald volgens het gewenste nieuwe vermogen, ongeacht de geometrieschaling. Deze laatste aanname wordt niet duidelijk uitgelegd in de literatuur, waardoor de betrouwbaarheid van de lineaire schaalmethode twijfelachtig is. Daarom richt dit proefschrift zich op de vraag of de lineaire schalingsmethode bevredigende resultaten kan geven in termen van efficiëntie schaling en berekening van het energieverbruik. Verder wordt grondig onderzocht onder welke voorwaarden, bijv. geometrieschaling, vermogensschalingsfactor, rijpatronen van voertuigen, etc., de methode betrouwbaar wordt geacht.

Om deze uitdaging aan te gaan, worden de resultaten van de lineaire schalingsmethode vergeleken met meer verfijnde schalingswetten die gevalideerd zijn met de eindige-elementenmethode. Deze verschalingswetten gaan dieper in op de ontwerptheorie van componenten en geven duidelijke relaties voor de verschaalde parameters als functie van de verandering van de geometrie. Voor synchrone machines met permanente magneten is de lineaire schaling vergeleken met geometrische schalingswetten op basis van drie schalingskeuzes die bestaan uit het behoud van de magnetische velddichtheid, behoud van de temperatuurstijging in de wikkelingen en een hybride keuze die de bovengenoemde keuzes combineert. De vergelijking tussen lineaire schaling en geometrische schalingswetten onthult dat het verschil in efficiëntie afhangt van de werkingsgebieden binnen het koppel-snelheidsvlak. Het rendementsverschil is groter in gebieden met een hoog koppel en lage snelheid, waar koperverliezen de overhand hebben. Dit rendementsverschil is meer uitgesproken bij het terugschalen, vooral bij het vergelijken van lineaire schaling en geometrische schaling waarbij de magnetische velddichtheid behouden blijft. In de laatstgenoemde regio is het verschil in efficiëntie minder groot wanneer lineaire schaalvergroting wordt vergeleken met geometrische schaalvergroting op basis van het behoud van de temperatuurstijging. Bij hogesnelheidsregio's van de machines neemt het verschil in efficiëntie tussen lineaire en geometrische schalingswetten af, waar de ijzer- en mechanische verliezen domineren. Dit geldt voor op- en afschalen en de verschillende schaalkeuzes.

Er wordt een methodologie gepresenteerd om een geometrische informatielaag op te nemen in de lineaire schalingsmethode van verliezen naar vermogen met behulp van de energetische macroscopische voorstelling. De lineaire schalingsmethode van synchrone machines met permanente magneten wordt gedemonstreerd als een bijzonder geval van de geometrische schalingswetten. Er bestaat ten minste één combinatie van axiale en radiale geometrische schalingsfactoren die een bijzonder geval van lineaire schaling van verliezen oplevert. De laatste bewering geldt echter alleen voor opschaling. Voor dergelijke opschalingis aangetoond dat geen enkele geometrische combinatie resulteerde in lineaire opschaling.

Voor op IGBT-gebaseerde omvormers wordt lineaire schaling vergeleken met een efficiëntiebenchmarking van drie gecommercialiseerde omvormers van dezelfde familie. De analyse omvat andere schalingskeuzes die in de literatuur beschikbaar zijn, zoals gegevensgestuurde schaling van vermogensverliezen en schalingswetten op basis van behoud van vermogensdichtheid en temperatuurstijging tussen de geschaalde en de referentieomvormers. De vergelijking van de schaling van de efficiëntiekaart tussen de schaling van verliezen naar vermogen en de efficiëntiebenchmarking van gecommercialiseerde omvormers toont vergelijkbare resultaten. Dit wordt toegeschreven aan de lineaire schaling van geleidingsverliezen en de niet-significante invloed van niet-lineariteiten in de schakelverliezen tijdens het schalingsproces. De laatste verklaring geldt voor opschalen en terugschalen.

Wat betreft de schaalbaarheid van mechanische transmissies is er in de literatuur relatief minder onderzoek gedaan dan bij elektrische aandrijfsystemen. De meeste studies beperken zich tot het bestuderen van het effect van de geometrie van de transmissie op relevante parameters, zoals het maximale uitgaande koppel en de massatraagheid. Desalniettemin ontbreken in de literatuur nog steeds schalingswetten voor mechanische transmissies die rekening houden met de verliezen, vanwege de complexiteit van een dergelijk schalingsproces. Het afleiden van vermogensverliezen van mechanische transmissies wordt vooral een uitdaging bij hoge snelheden vanwege de beperkte gegevens over de verliezen in de eerder genoemde gebieden. De vereisten voor hogesnelheidstransmissies komen voort uit de stijgende trend naar hogesnelheidselektrische machines om de vermogensdichtheid te verbeteren. Om deze uitdaging aan te gaan, is een uitgebreid experimenteel onderzoek uitgevoerd naar de vermogensverliezen van vijf commerciële planetaire reductoren, met verschillende snelheids- en koppelwaarden en overbrengingsverhoudingen. Zowel belastingsafhankelijke als belastingsonafhankelijke verliezen zijn experimenteel gekarakteriseerd bij toerentallen tot 14.000 tpm. De maximale koppelwaarde wijkt echter af van de vereisten die gewoonlijk worden aangetroffen in versnellingsbakken voor auto's vanwege het lage nominale vermogen van de geteste exemplaren. De uitgevoerde testresultaten maken het mogelijk om een gegevensgestuurd model te definiëren dat op fysica gebaseerde termen bevat, d.w.z. parameters voor snelheid, koppel en overbrengingsverhouding. Vervolgens worden schaalwetten afgeleid op basis van de maximale ingangssnelheid, het maximale uitgangskoppel en de maximale overbrengingsverhouding die vereist zijn.

Voor het onderzoek op systeemniveau wordt een nieuwe methodologie voorgesteld die gebaseerd is op een energetisch macroscopisch formalisme om de integratie van de schalingswetten op systeemniveau te vergemakkelijken. De voorgestelde methodologie is bedoeld om een uniforme simulatieomgeving te bieden om de energetische prestaties van verschillende ontwerpkandidaten van elektromechanische aandrijfsystemen voor elektrische voertuigen van verschillende klassen te beoordelen. Om dit doel te bereiken, wordt het model van elke geschaalde component van het elektromechanische aandrijfsysteem gereorganiseerd door het referentiemodel vast te houden, maar aangevuld met twee vermogensaanpassingselementen aan de ingangs- en uitgangszijde van het referentiemodel. Het schaaleffect volgens elke toegepaste methode is opgenomen in het

vermogensaanpassingselement. De methodologie wordt eerst toegepast op elke component afzonderlijk op componentniveau en vervolgens uitgebreid naar het systeemniveau om de interactie tussen de geschaalde componenten te onderzoeken. Dit maakt de afleiding mogelijk van een schaalbaar model en regeling van het elektromechanische aandrijfsysteem, aangevuld met slechts twee vermogensaanpassingselementen aan de elektrische en mechanische kant. De gepresenteerde methodologie is bedoeld om het model en de regeling van het elektromechanische referentiesysteem te hergebruiken, met als doel het simulatieproces van een groot aantal elektrische voertuigen te versnellen.

Verder wordt de impact van de lineaire schaalmethode op het energieverbruik uitgebreid onderzocht door vier schaalscenario's voor verschillende transporttoepassingen te bestuderen. De studiegevallen omvatten een schaalbereik van 0,58 tot 1,96. Het onderzoek is uitgevoerd op basis van verschillende gestandaardiseerde rijcycli met verschillende patronen, bijvoorbeeld in de stad, op het platteland en op de snelweg. De resultaten van de lineaire schaalmethode in termen van energieverbruik worden vergeleken met geschaalde ontwerpkandidaten van elektrische machines met een verschillende geometrie die het resultaat zijn van geometrische schaalwetten, in combinatie met efficiëntiebenchmarking van omvormers. Wat betreft de gevallen van opschaling toont de gevoeligheidsanalyse aan dat lineaire schaling voor het elektrische aandrijfsysteem vergelijkbare resultaten oplevert in vergelijking met de tweede schalingsmethode, met verschillen van 0% tot 3,2% in absolute termen. Wat betreft het terugschalen, blijkt dat lineaire schaling het energieverbruik consequent onderschat. Een verschil variërend van 3% tot 8% wordt gevonden bij het toepassen van lineaire schaling op de elektrische aandrijving bij het onderzoeken van de rijcyclus in de stad in vergelijking met de geometrische schalingswetten van de elektrische machine. Daarom is voorzichtigheid geboden bij het omgaan met downscaling voor dergelijke specifieke scenario's. Voor rijcycli op de snelweg zijn de verschillen in energieverbruik verwaarloosbaar klein voor zowel opschalen als terugschalen.

Notations

To distinguish the parameters of the scaled components from those of the reference components, the following notations are employed throughout the remainder of this manuscript. The parameters of the reference components are denoted with a superscript (0), whereas an apostrophe (') is employed to refer to those of the scaled components. For instance, the torque of the reference machine is denoted as T^0, while the scaled torque is referred to as T'.

A superscript (*) is utilized to refer to the parameters defined by the control level. For example, the torque setpoint of the reference machine is expressed as T^{*0}, while $T^{*'}$ is the torque setpoint of the scaled machine.

A superscript (~) is used to refer to fictitious variables resulting from mathematical manipulation of the models, e.g. permutation manipulation.

A subscript using an underscore symbol (-) is employed to refer to a vector of parameters. For example, $\underline{v}_{s,dq}$ refers to a vector containing the voltages in the *dq* axis of the Park Transform, $\underline{v}_{s,dq} = \begin{bmatrix} v_{s,d} \\ v_{s,q} \end{bmatrix}$.

The notation (~1) is utilized to indicate the preservation of a specific parameter during the scaling process. For instance, the choice $B{\sim}1$ refers to the preservation of the magnetic field density during the scaling process.

List of abbreviations

Numbers

1D	One dimension
2D	Two dimensions
3in1	Three components combined into one single entity

A

ADVISOR	ADvanced VehIcle SimulatOR
AGMA	American Gear Manufacturers Association
AWD	All-Wheel Drive

B

BEV	Battery Electric Vehicles

C

CAFC	Corporate Average Fuel Consumption
CAFE	Corporate Average Fuel Economy
CFD	Computational Fluid Dynamics
CO$_2$	Carbon Dioxide
COP28	The 28th Conference Of the Parties
CUMIN	Campus of University with Mobility based on Innovation and Carbon Neutrality

D

DT4V	Digital Twins for Validation of dynamic performance and reliability of drive systems
DTC	Direct-Torque Control
DySC	Dynamical Systems and Control research group

E

e-axle	electric axle system
EDS	Electric Drive System
EM	Electric Machine
EMR	Energetic Macroscopic Representation
EPA	Environmental Protection Agency
EU	European Union
EVOLUTION	EffectiVeness Of Lorries and bUses

F

FCEV	Fuel Cell Electric Vehicles
FEM	Finite Element Method
FOC	Field-Oriented Control
FW	Field Weakening
FWD	Front Wheel Drive

G

GaN	Gallium Nitride
GB	Gearbox

H

HDV	Heavy-Duty Vehicles
HEV	Hybrid Electric Vehicles
HiL	Hardware-in-the-loop testing

I

ICCT	International Council on Clean Transportation
IEA	International Energy Agency
IGBT	Insulated Gate Bipolar Transistors
IM	Induction Machines
ISO	International Organization for Standardization

L

L2EP	Laboratory of Electrical Engineering and Power Electronics
LDV	Light-Duty Vehicles

M

MCM	Modular Cascaded Machine
MOSFET	Metal Oxide Semiconductor Field Effect Transistors
MPC	Model Predictive Control
MTPA	Maximum Torque Per Ampere

N

NEDC	New European Driving Cycle
NHTSA	National Highway Traffic Safety Administration

O

OEM	Original Equipment Manufacturers
OP	Operating point

P

PA	Power adaptation
PMaSynRM	Permanent Magnet-assisted Synchronous Reluctance Machine
PMSM	Permanent Magnet Synchronous Machines
PWM	Pulse Width Modulation

Q

QSS	Quasi-Static Simulation toolbox

R

RWD	Rear Wheel Drive

S

SAFE	Safer Affordable Fuel-Efficient
SiC	Silicon Carbide
SPWM	Sinusoidal Pulse Width Modulation
SRM	Switched Reluctance Machine
STeVE	Scalability of powerTrain for electrified Vehicles of an Eco-campus
SVPWM	Space Vector Pulse Width Modulation

T

THI   Third Harmonic Injection

U

UNFCCC   United Nations Framework Convention on Climate Change
USA   United States of America

V

VSI   Voltage Source Inverter

W

WLTP   Worldwide Harmonised Light Vehicles Test Procedure
WRSM   Wound Rotor Synchronous Machine

X

xEV   Electrified Vehicles

General introduction

Being one of the largest emission emitters over the years, the transportation sector is confronted with pressing and paramount requirements to steer its course in accordance with the goals delineated in the Paris Agreement [1], [2]. The duty of the transportation sector is to move forward in routes, that contributes to limiting global warming to 1.5 °C above pre-industrial levels. In pursuit of this goal, several major economies worldwide, with leadership from the European Union, the United States of America, and China, have vowed to mitigate transport emissions. This commitment is demonstrated through putting forth progressive emission and fuel economy standards, that mandate annual or multi-year timeframe reduction targets [3], [4]. These environmental policies have played an important role in reshaping the automotive industry by supporting the development of low and zero-emissions vehicles [5]. This is exemplified by the exponential growth in the electrified vehicles market, with sales exceeding 10 million vehicles in 2022 as compared to hardly 120,000 a decade ago [6].

The efforts to reduce emissions from the transportation sector are decent, however, they are still not sufficient. This is evidenced by the continuous growth in emissions in the year 2023, eight years after the historic Paris Agreement [7]. This upward trend is attributed to the growth in population, economic activity, and transport demand, all of which are expected to continue rising in the coming years. Consequently, the time window before reaching the 1.5°C goal is rapidly narrowing. As postulated in [8], it might not be feasible to keep this goal within reach unless there is tremendous carbon dioxide mitigation on an unprecedented scale by the year 2030. The end of the year 2023 will be critical as the world heads into the next round of climate negotiations at the 28th Conference Of the Parties (COP28) of the United Nations Framework Convention on Climate Change (UNFCCC) in November 2023 [9]. This is an unmissable opportunity to increase the pace of the global transition towards low and zero-emissions mobility and strengthen climate change actions and policies worldwide. As a result, the entire automotive industry is at a tipping point. All involved parties, e.g. carmakers, stakeholders, and original equipment manufacturers etc., are fully cognizant that the upcoming years will require a surge in electrification to successfully meet the climate goals.

The massive introduction of new electrified models to the market will inevitably bring forth a multitude of challenges. Beyond adhering to stringent emission standards and tight timelines, the automotive industry is confronted with new challenges arising principally from the technological disruption and escalating system complexity of the emerging electrified powertrains [10], [11]. In this regard, the design space of electrified powertrains is significantly large and flexible, providing an extensive diversity of technical solutions, as compared to their conventional counterparts. The design space of an electrified powertrain encompasses

different layers, namely powertrain topology, technology selection, components design, and sizing, as well as control design [12], [13]. During the early development phases of an automotive project, a thorough examination of the aforementioned design layers is required. The analysis should adopt a systemic approach [14], taking into account the interaction between all these layers, to ensure solutions that align with the project specifications and constraints. Consequently, the complexity of the development process increases, particularly when it comes to electrifying a wide range of vehicle classes within the automotive fleet. This is due to distinct specifications and requirements associated with each transport application, resulting in different potential technical solutions. This factor intensifies the pressure on the automotive industry, which is requested to deliver efficient electrified vehicle designs at a faster pace than ever before. Reducing the time-to-market of the next generation of vehicles is thereby becoming a top priority. To achieve this goal, new and flexible methodologies to support and effectively address the early development challenges are needed [15] .

The early development phases of electrified vehicles heavily rely on virtual development [10]. The assessment of the performance of the potential solutions is usually done through system-level simulations, employing high-level models based on component data [16]. This data is typically established using high-fidelity numerical methods such as finite element methods [17], computational fluid dynamics [18], etc. Although these methods are recognized for their high accuracy, they are time and effort-consuming. Hence, the task of studying the impact of design changes is cumbersome, making their incorporation of the previously mentioned method at system-level challenging. As part of the endeavors to speed up the design and sizing process of electrified powertrain components, scalability has attracted widespread attention in system-level investigation in recent literature [19]–[22]. The main idea behind scalability is to leverage existing design solutions of a given component and reuse them to quickly derive a virtual scaled component with different specifications. This makes it unnecessary to redo cumbersome design steps.

In effect, scalability is not an emerging research area, but rather a deeply rooted topic in literature addressing the sizing problem of components. This is evidenced by research papers discussing the scalability of electric machines dating back to the 1970s [23], [24]. Scaling attracted widespread attention due to the constrained computational efficiency available at the time. Due to the notable advancements in computer computation, the subject has witnessed a diminishing level of interest over time. Notwithstanding, scalability has reignited a renewed and strong interest in a recent body of literature centered on the system-level design of electrified powertrains [19]–[22]. This is attributed to the computational efficiency and the ease of implementation provided by scalability in addressing complex, multi-objective, and coupled optimization problems of electrified powertrains [12], [13].

Different approaches to implement scalability are adopted in system-level studies. Such approaches include different derivations of scaling laws. Indeed, scaling laws enable studying the effect of varying representative parameters of a reference component design, e.g. geometry, power, etc., to deduce the scaled parameters of a new design. Regarding electric drive systems, i.e. electric machines and power electronic converters, there is an abundance of scaling laws in literature which can be classified into two main categories. The first one utilizes a

simplified version of scaling laws, known as linear losses-to-power scaling or simply linear scaling [16], [25], [26]. The aforementioned scaling method assumes that the overall power loss scale follows the new desired power rating. Due to its simplicity and computational efficiency, the linear scaling method has found widespread application in system-level studies to assess the energy consumption of electrified vehicles of different power ratings. Nonetheless, the assumptions behind the latter method are doubtful and have been not subjected to a thorough examination. In this regard, reference [27] states that the accuracy of the linear scaling method is uncertain and recommends approaching the scaling process with caution using the aforementioned method, without providing further insight. The second category employs more advanced scaling laws that delve into the component design and geometry [28]–[30]. These latter are primarily applied at component-level to assess design changes of components. Despite significant efforts to derive scaling laws in earlier studies, no comprehensive understanding of the impact of these scaling laws on the efficiency scaling and energy consumption computation of electrified vehicles is available. Furthermore, the literature shows comparatively less research work on the scaling of mechanical transmissions as compared to electric drive systems. Most studies are confined to studying the effect of the transmission geometry on relevant parameters, such as the maximal output torque and inertia [31], [32]. Nonetheless, scaling laws for mechanical transmissions taking into account the losses are still lacking in literature due to the complexity of such scaling process. On top of that, no clear structuration is employed for the scalable models in simulation environments. The scaling laws are used as a set of equations combined with the reference model of the components. This originates from the fact that the theory of scaling laws is established at component-level. Consequently, the interactions between the scaled components when analyzing the system are inherently not considered. Accordingly, a comprehensive examination of the impact of component scalability at system-level becomes a challenging task. For this reason, it becomes desirable to establish a new organization of scalable models, following a systemic approach.

In this context, the research motivation of this Ph.D. thesis is to contribute to a reduction of the time-to-market of electrified vehicles by accelerating the design process in the early development phases of the electric axle components employing a scaling methodology. An electric axle consists of a power electronic converter, an electric machine, a mechanical transmission, and a control unit. The objective of this research work is to develop a scaling method for the electric axle components, allowing the investigation of the energetic performance of different classes of vehicles at system-level. The Energetic Macroscopic Representation (EMR) formalism [33] is employed to provide an innovative organization of the scaling laws at system-level. This is intended to offer a unified simulation framework of various power ranges and allows for investigation of the interaction between the scaled components. Furthermore, an intensive experimental campaign on different commercialized mechanical transmissions is conducted to address the literature gap on power loss scaling laws.

This dissertation is structured as follows. Chapter I is dedicated to presenting the context and the framework of this research work, and delves into the challenges of system-level design of electrified vehicles. The specification of the work is introduced to define the scope of this Ph.D. In Chapter II, a comparative analysis is performed between several scaling laws of electric drive systems. The chapter is intended to increase the understanding of the adopted

scaling laws on efficiency scaling over the operating range. A particular emphasis is placed on examining the assumptions and outcomes of the linear scaling method. A novel organization of the model of the scaled electric machines and power electronic converters is proposed. Chapter III addresses the derivation of the scaling laws of mechanical transmissions through an intensive experimental campaign. In Chapter IV, the interaction between the scaled components is investigated at system-level. A new organization based on EMR is presented, allowing the use of a unique system-level model and control of the electric axle to simulate the performance of multiple vehicle classes. This methodology incorporates different choices of scaling law for each individual component in a unified way. This permits conducting an in-depth comparative analysis of the impact of the scaling choices on the energy consumption of different electric vehicles. Considerable emphasis is paid to evaluating how the linear scaling method impacts energy consumption based on different power scaling factors and driving patterns. Several appendices are provided to complement some of the sections presented in each chapter at the end of this dissertation.

Chapter I

Need for new methodologies to expedite the development and deployment of electrified vehicles

1 Introduction

Emissions mitigation of the transportation sector is nowadays an urgent global environmental challenge that is a top priority for many governments. The vision towards zero-emission transport is increasingly becoming universal. Over the past few years, much effort on the part of policymakers has been devoted to emission performance standards in the transportation sector because of its share of total emissions and its continuous growth [7]. These new emission standards create a perfect storm to put the transport sector on the right pathway toward green mobility. However, this comes with a myriad of challenges that lie ahead for the automotive industry, especially when it comes to electrifying a wide range of vehicle classes within a short timeframe. The increasing electrification trend can only be achieved with a high degree of scalability in terms of requirements (e.g. power rating, dimensions, etc.) of the electric axle system (e-axle), i.e. the association of power electronics converter, electric machine, and gearbox. The design of a new e-axle involves multiple layers, namely the selection of the topology, the technology of the components, sizing, and control. Consequently, this yields a large design space that needs to be thoroughly explored and assessed. Notwithstanding, the existing approaches are based on detailed design, which leads to a long computational time. Consequently, there is a need to develop new methodologies, offering the possibility of synthesizing, assessing, and comparing different preliminary virtual design candidates of an e-axle for different vehicle classes in the initial stages of system development. This helps to make decisions before the initiation of detailed component design. In this context, this chapter addresses the research question in the present work by stressing the urgent need to find new methodologies that support the fast development of electrified vehicles.

This chapter is organized as follows. Section 2 presents an overview of the environmental policies promoting a strong electrification trend. Section 3 provides an overview of the main phases of the development of an automotive project. Section 4 discusses the state of the art of

the methods employed in the design of the e-axle. Section 5 is dedicated to discussing the research motivations and questions. The research goal, framework, and organization of this Ph.D. thesis are reported in Section 6.

2   Strong electrification trend to cope with new environmental policies

2.1   Tracking CO_2 emissions in the transportation sector

Undeniably, the transportation sector is one of the largest emitters of carbon dioxide (CO_2) emissions in different countries worldwide, as depicted in Fig. 1.
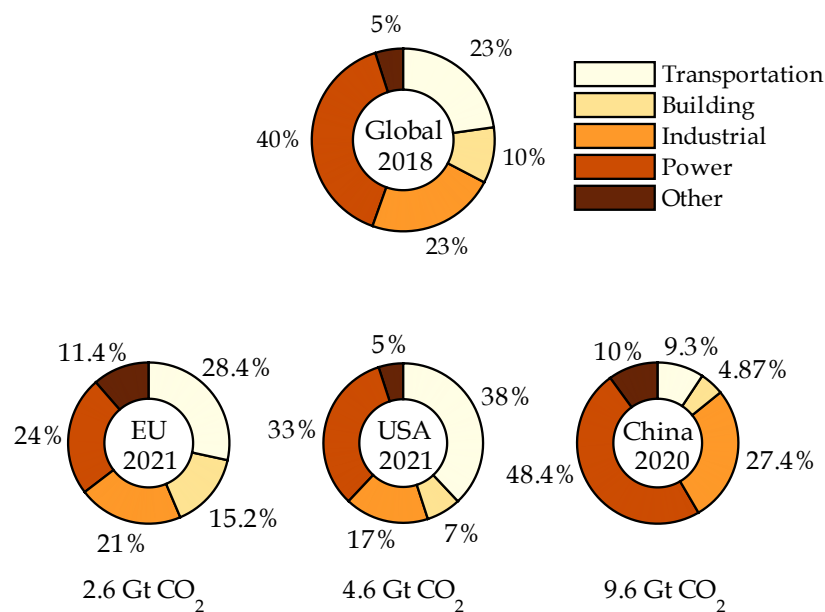
Fig. 1: Breakdown of energy-related emissions of carbon dioxide CO_2 from fuel combustion, by economic sector, data sourced from [34]–[37]. The number mentioned in Gt CO_2 refers to the total CO_2 emissions emitted by the concerned nations, including all economic sectors.

At a global scale, transportation stands as the second-largest contributor of CO_2 emissions, accounting for approximately 23% of emissions in 2018 according to the International Energy Agency (IEA) database [34]. The shares of CO_2 emissions across sectors depend on the energetic mix and environmental policy of each country. Hence, the distribution of CO_2 emissions per sector differs from one country to another. A more in-depth analysis of the breakdown of emissions by sector in the world's most prominent markets, particularly the European Union (EU), and the United States of America (USA), reveals that the transportation sector is the largest emitter of CO_2. In the EU, the transport sector accounts for 28.4% of total CO_2 emissions [35]. The Environmental Protection Agency (EPA) showed that after substantial declines in emissions from the electric power sector following 2017, the transportation sector became the leading source of CO_2 with 38% of total emissions in the USA in 2021 [36]. However, in China, the transportation sector is not the main contributor to CO_2 emissions, accounting for approximately 9% of the overall emissions in 2020 relative to 48% for the power sector [37]. This is

6

because of the reliance of the power sector on coal. For instance, CO_2 emissions from the steel and cement sectors, two uppermost components of the power sector in China, alone surpass the overall CO_2 emissions of the EU [38].

Historically, the transportation sector has exhibited a consistent growth pattern over time, as illustrated in Fig. 2, except for two notable disruptions: the financial crisis in 2008, and the COVID-19 pandemic in 2020 [39]. The sector experienced a minor reduction of about 2.2% in 2009 relative to the 2008 level. However, this decrease was followed by an emission-increasing trend until 2020. Thereafter, the pandemic resulted in an unprecedented reduction in CO_2 emissions due to transport restrictions, but this was short-lived as emissions rebounded by 8% in 2021. Preliminary data suggest that emissions are heading toward their peak of early 2020, returning to the historical upward trend of emissions [1]. Compared to other sectors, Fig. 3. reveals that the transportation sector stands out as the sole sector with no significant downward trend in the past three decades, despite the efforts made to establish emissions regulation standards (cf. Appendix I). All other sectors experienced noteworthy declines in their CO_2 emissions. For instance, the power sector in the EU and the USA have seen a decrease of about 36% and 16%, respectively in CO_2 emissions relative to the 1990 baseline. Emissions from the transportation sector increased by approximately 24% in the same nations, over the same period. This is mainly due to an increase in demand for travel and road freight activities. In the coming decades, transport demand is expected to increase worldwide due to population growth, urban sprawl, and economic growth. IEA forecasts that global transport (passenger per kilometer) will double from 2019 to 2070, and car ownership rates are expected to increase by 60% [40].
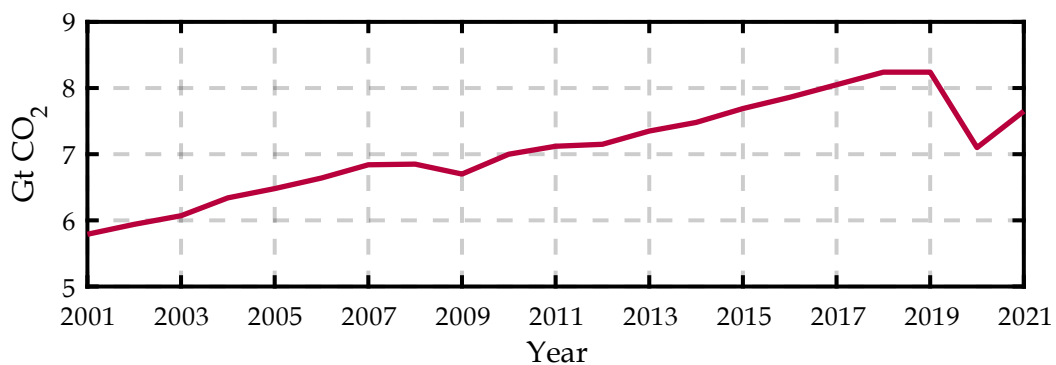
Fig. 2: Global CO_2 emissions evolution of the transportation sector, data extracted from [39].

2.2 Intensified policy framework for decarbonizing road transportation

Over the past two decades, efforts have been made worldwide to set CO_2 regulations standards, aiming to mitigate emissions from the transportation sector. These standards, which vary by country, have established different CO_2 reduction targets and deadlines based on specific transportation segments. To gain a good understanding of CO_2 emissions regulations, the primary contributors of emissions in the transportation sector are first discussed. For this aim, Fig. 4 provides a breakdown of the CO_2 emissions contributed by various transport applications. From this figure, it is evidenced that road transport, which encompasses both passenger and freight transport, is the leading contributor to global transportation-related

emissions, totaling about 75% [41]. In the EU in 2022, this proportion is approximately 72% [42], whereas, in the USA, it is as high as 83% in 2019 [36]. Of all the on-road vehicles, Light-Duty Vehicles (LDV), e.g. passenger cars and light commercial vehicles, have globally the greatest share of emissions, followed by Heavy-Duty Vehicles (HDV), such as trucks and buses. For instance, passenger cars were responsible for 60.6% of the total emissions emitted in 2022 in the EU, as compared to 11% for light commercial vehicles. Heavy-duty trucks and buses together accounted for 27.1% of road transport emissions during the same year in the EU. Similar observations can be made when examining the breakdown of contributors to transport emissions in the USA.
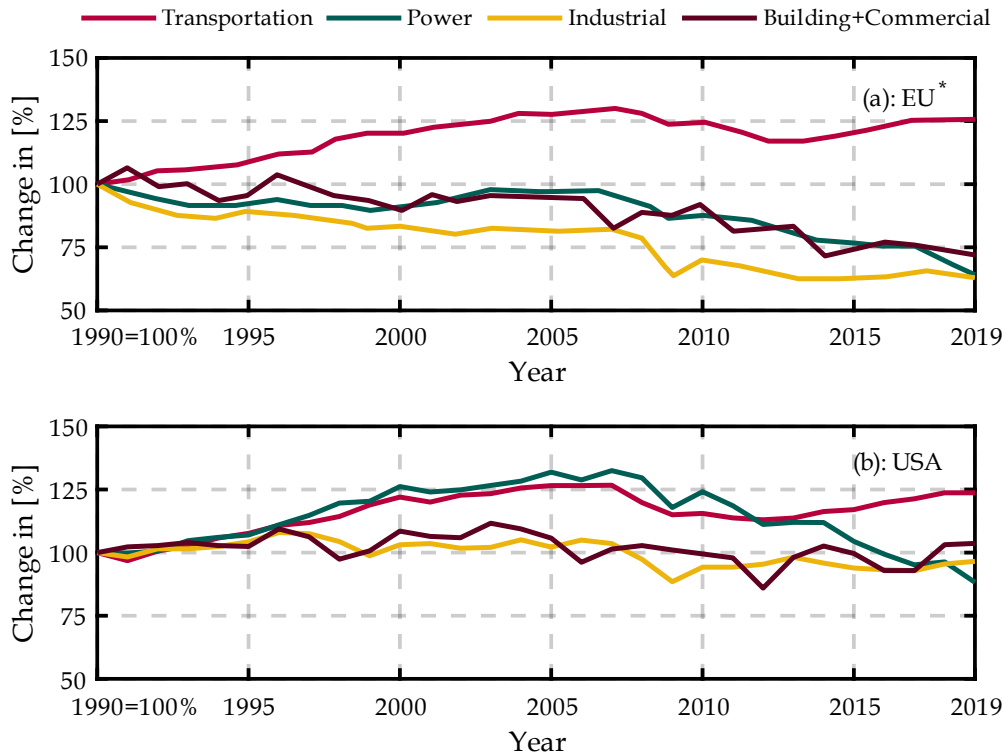
Fig. 3: Evolution of CO_2 emissions in the European Union (*data excluding the United Kingdom) and the United States of America by economic sector, data extracted from [36], [43].
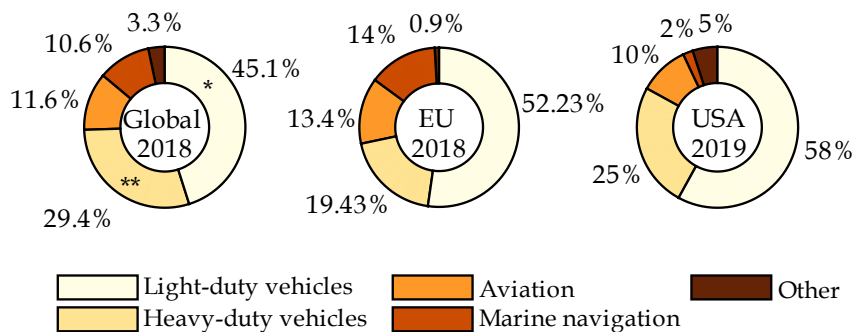
Fig. 4: Shares of CO_2 emissions by transportation sub-sector, data extracted from [36], [41], [42]. * indicates that emissions from buses were included in the mentioned part, ** refers to road freight transport.

To mitigate the likely increase in the road transportation sector, major markets have been intensifying their efforts to set short- and long-term vehicle emissions regulations, targeting

LDV and HDV. An overview of the history of CO_2 emissions regulations in the major automotive markets, exemplified by the EU, USA, and China cases, is presented in Appendix I. This section specifically highlights the CO_2 reduction targets for the period from 2025 to 2035. In this context, the EU is demonstrating leadership in climate policy, by setting bold policies that are propelling the transition towards zero-emissions transport as part of the European Green Deal strategy [44]. In March 2023, the EU made significant steps by amending its 2019 regulations and setting more ambitious objectives [45]. Compared to the 2019 regulation, the EU has strengthened the 2030 reduction target for newly registered passenger cars from 37.5% to 55% relative to the 2021 baseline (95 g CO_2/km based on the New European Driving Cycle, NEDC, procedure). Additionally, the 2030 reduction target for vans was strengthened from 31% to - 50%, compared to the 2021 baseline (about 180 g CO_2/km) as well. Most importantly, the EU introduced a groundbreaking target for 2035, aiming for a 100% cut in CO_2 emissions (0 g CO_2/km) for both passenger cars and vans. The amended regulation maintains the 2025 reduction target of 15% without any further changes. In the same year 2023, the European Commission released a proposal to amend the CO_2 standard for HDV, aiming to accelerate the deployment of zero-emissions vehicles[1] in this sector. If approved, the amendment would require a 90% reduction for trucks by 2040, while city buses would be required to achieve a 100% reduction by 2030 [46].

The USA, by its turn, has set a goal of net-zero emissions by 2050 [47]. In 2023, EPA revealed a new more ambitious standard proposal to further reduce CO_2 emissions from the entire LDV fleet for the timeframe 2027-2032 [48]. This standard aims to achieve an average target of 82 g CO_2/mi of CO_2 in 2032 (about 41 g CO2/km normalized to NEDC test procedures[2]) for the LDV fleet. Regarding HDV, the regulation adopted in 2016 for the timeframe 2018-2027, targets a reduction from 15-27% depending on the vehicle type, relative to the 2017 baseline. In 2023, the EPA proposed a revision of the existing standards for HDV aiming at further reduction of emissions in 2027 [50].

China has committed to achieving carbon neutrality before 2060 [38]. For this aim, China adopted a fuel economy standard for passenger cars in 2021, setting an average fuel consumption target of 4 L/100 km (about 93 g CO_2/km) by 2025 and 3.2 L/100 km (75 g CO_2/km) by 2030 [51]. As far as HDV are concerned, a proposal was issued in 2022, suggesting increasing the stringency by 15% relative to the regulation of 2019 [52].

2.3 Decent efforts, yet insufficient

Notwithstanding the efforts dedicated to the development of standards and the increased stringency in CO_2 reduction targets, certain analyses suggest that the currently adopted standards fall short of achieving the decarbonization of road transportation within the set timeframe. In the case of the EU, the International Council on Clean Transportation (ICCT)

---

[1] The terminology zero-emission vehicles is commonly used in the current literature and emission regulations standards to describe vehicles with zero tailpipe emissions. However, from a precise point of view, the terminology is not completely accurate as any type of vehicles still emit some local emissions such as particulates during braking phases.

[2] It is worth noting that the American emissions testing procedure differs from the European one. This conversion has been performed using the conversion tool provided by the International Council on Clean Transportation, converting from the Corporate Average Fuel Economy (CAFE) procedure to the New European Driving Cycle (NEDC) procedure [49].

recommends increasing the stringency of the 2025 objective as much as possible, to guarantee the attainment of zero-emissions vehicles by 2035 [53]. Furthermore, the recommended level of stringency for the LDV fleet-average CO_2 targets in 2030 should be at least a 70% reduction relative to the 2021 baseline, surpassing the newly adopted target of 55%. Alternatively, it was suggested to bring forward the 2030 CO_2 target to a date earlier than 2027. Concerning the USA case, the ICCT suggests that the CO_2 standard needs to be as much lower as 57 g CO_2/mi by 2030 [54]. This would represent a 69% reduction in comparison to the 2026 target. The analysis conducted by the ICCT for the Chinese case recommends imposing stringent targets for new passenger car CO_2 emissions, aiming for 30 g CO_2/km by 2030 [55]. This represents a substantial 60% reduction compared to the existing target. Additionally, it was advisable to establish a target of achieving zero-emissions passenger cars by 2035, to ensure steady progress toward the Chinese carbon neutrality target set for 2060.

2.4   How to comply with emissions standards in the transportation sector?

The continuous tightening of the CO_2 and fuel economy standards results in a strong transformation pressure on the automotive industry. This latter is at a tipping point, where rapid adaptation and technological changes are urgently needed. Although the adopted standards dictate clear emission reduction targets, they leave an open policy to choose suitable solutions enabling a shift towards low- and zero-emission mobility. The central question remains: how will manufacturers and stakeholders react to achieve the new regulation objectives in a short timeframe, while transport demands are increasing?

In effect, manufacturers can make use of a variety of measures and technological solutions, that could help to achieve CO_2 mitigation and can be summarized as follows [5]:

➤ **Usage optimization:** shared mobility and connectivity of roads using intelligent transport networks and automated driving systems exhibit the potential to reduce fuel consumption, such as intelligent eco-driving guidance and vehicle platooning.

➤ **Efficiency improvement**: one option for manufacturers is to improve the effectiveness of their internal combustion engines. New engine management systems, improved injection systems, and recovering heat waste can contribute to reducing fuel consumption. An efficiency increase can be also made possible by improving the aerodynamic performances, lowering the rolling resistance tires, and lightweighting the body of the vehicles using other types of materials.

➤ **Adaptation of alternative fuels:** liquefied natural gas and liquefied biogas are low-emission fuel alternatives for reducing the road transport sector emissions in the short term. Due to its chemical composition, gas-based technologies lead to lower CO_2 emissions compared to diesel vehicles and can be used with no major adjustments to conventional engines.

> **Electrification:** emerging electrified powertrains[3] introduce novel components, technologies, and functionality. The degree of electrification varies from low-emissions vehicles encompassing several solution forms of Hybrid Electric Vehicles (HEV), to zero-emissions vehicles, such as Battery Electric Vehicles (BEV), and Fuel Cell Electric Vehicles (FCEV).

The three first solutions could provide some relief to achieve the short-term reduction targets. Nevertheless, a crucial question arises: to what extent is there room for improvement in conventional powertrains or making use of alternative fuels? To comply with the strengthened objectives of the 2025-2035 timeframe, manufacturers must dedicate their resources and research toward implementing extensive electrification [56]. Electrified Vehicles (xEV[4]) hold the potential to succeed in meeting low and zero-emission mobility objectives.

Accordingly, the market share of xEV is projected to grow massively over the next decade. At a global scale, the stated policies scenario of the IEA projects that the global share of xEV sales, given current policies and established objectives worldwide, will reach 35% by 2030 [6]. Focussing on the three major markets, namely the EU, USA, and China, Fig. 5 illustrates the historical development and future targets of xEV share.
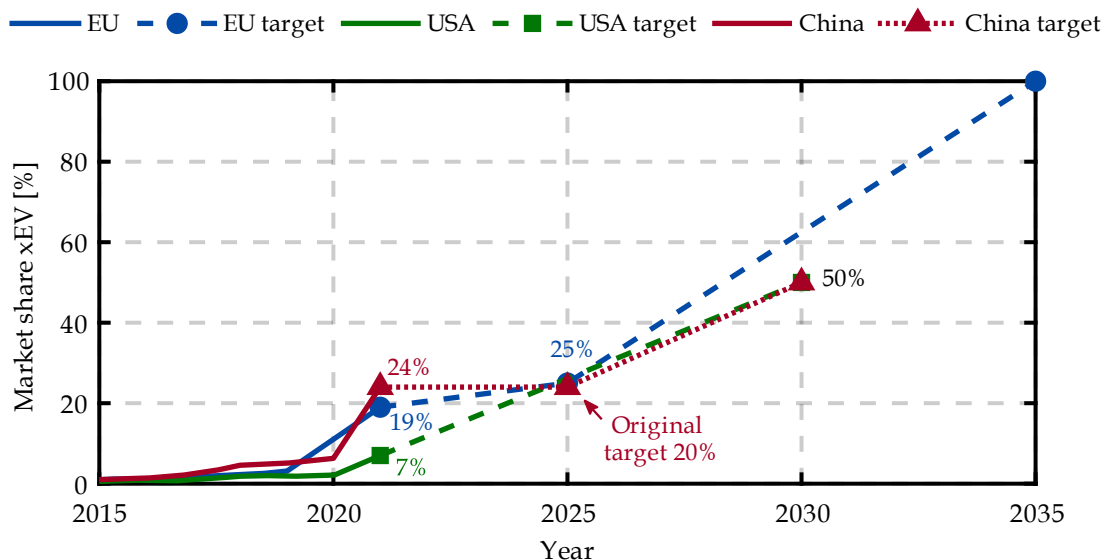
Fig. 5: Historical development and future targets of battery electric and plug-in hybrid vehicles among all new light-duty vehicle registrations, for EU, USA, and China. Data for China and Europe only includes passenger cars, whereas data for the USA includes light commercial vehicles. Data sourced from [57] and updated based on the 2023 amendment of EU regulation for LDV and [58] for the Chinese case.

The EU announced the end of the era of engine-powered vehicles with a full transition to 100% zero-emissions passenger car sales by 2035. The mandatory CO_2 emissions regulations in the EU have shown a good impact on the uptake of xEV, as evidenced by a substantial rise in the market penetration of passenger cars from around 3% in 2019 to 11% in 2020, and further to 19% in 2021 [57]. Assuming the EU upholds its current pace of market transition, it is projected to surpass a 90% market share of electric passenger car sales by 2030 and achieve 100%

---

[3] A powertrain system is responsible for the propulsion of the vehicle and encompasses an assembly of elements from the energy storage or generation systems to the wheels.

[4] The letter x in xEV stands for the energy storage or generation system in the vehicle: Battery (B), Hybrid (H), and Fuel Cell (FC)

electrification by 2032 (three years ahead of its original target set for 2035). In the USA, the American Administration, under President Biden, pledged to achieve a 50% share of electric vehicle sales among all new vehicle registrations by 2030. The market share in the USA still has a long way to go as the current market share of xEV remains relatively low, standing at about 7% in 2022. As far as China is concerned, the market share of xEV climbed to 25% by mid-2022. Looking ahead, China has set an ambitious goal of deploying new xEV from 40% to 50% of new passenger vehicle sales by 2030 [58]. Regarding HDV, the Dutch government and Drive to Zero program launched an initiative called Global MoU on Zero-Emission Medium- and Heavy-Duty Vehicles [59]. By 2040, the signatories countries, numbering 27 worldwide, aim for 100% of xEV bus and truck sales, with an interim goal of 30% by 2030.

Following the new market requirements, automotive manufacturers have announced plans and strategic measures to cope with this rapid, and aggressive electrification wave [60]. Fig. 6 provides an overview of the xEV sales targets for LDV, established by major manufacturers across six major markets: EU, USA, China, India, Japan, and Korea. These latter represent about 80% of total annual global LDV sales, and the mentioned manufacturers encompass about 95% of those sales. If manufacturers successfully achieve the described objectives in the figure, this would result in 31% of xEV sales by 2030 and 55% by 2035 within the six major vehicle markets. Nonetheless, it is expected that manufacturer announcements will evolve in response to the future amendment of emissions policies in regions other than Europe.
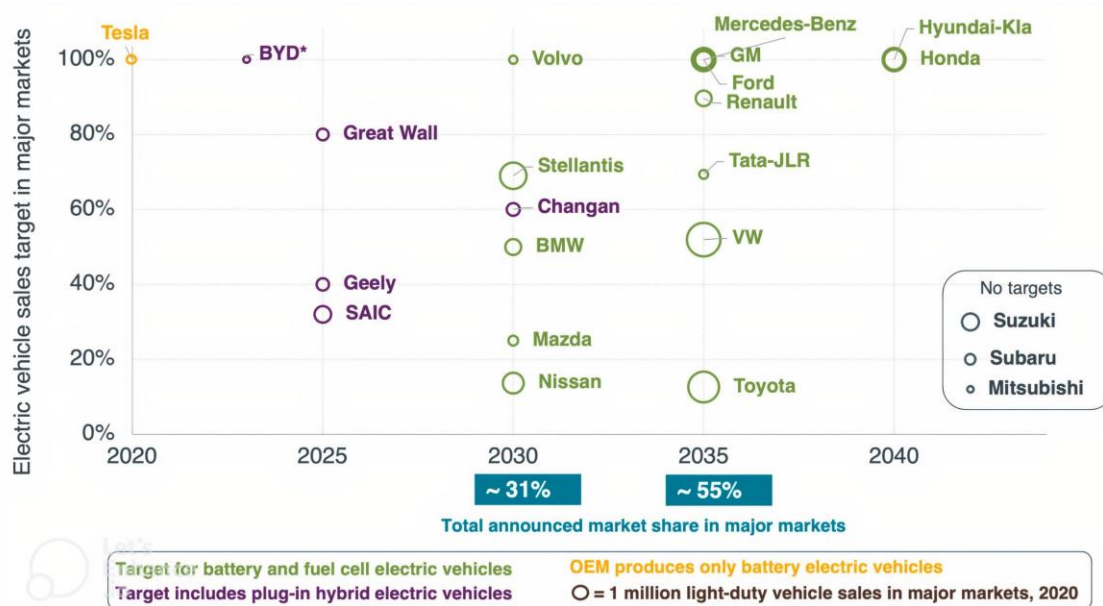
Fig. 6: Manufacturer targets[5] for the future share of electric passenger cars and light commercial vehicles in six major markets, as of October 2022 [60]. The size of the bubbles in the figure corresponds to the number of sales in the major market in 2020, according to the scale illustrated in the legend.

In light of this, the automotive industry is approaching a critical juncture, starting in 2025, when an expeditious and substantial transition is required to effectively develop and deploy

---

[5] Note that some manufacturers have announced different EV targets for each region worldwide, the regional targets were therefore normalized based on the sales within each respective region. For example, Stellantis has set a 100% xEV by 2030 target in Europe for passenger cars, while aiming for a 50% xEV penetration by 2030 target in the United States for the entire LDV fleet. These two regional targets, when combined, lead to an aggregated 69% global xEV target by 2030.

significantly more xEV within a relatively short timeframe. The electrification wave should encompass a wide range of models and segments, addressing the diverse needs and preferences of users. This is expected to disrupt the development process activities significantly, necessitating drastic changes to align with the requirements set forth by the 2025-2035 timeframe.

3 Automotive projects development process

3.1 Main phases of the development process

The automotive industry relies on a development process to effectively develop a vehicle. The core principle of a development process lies in establishing a fundamental comprehension of the pathway from requirements to a mature solution that is ready for mass production. In essence, the development process provides a guideline, defining what needs to be done at each stage of the system development. The main phases of the vehicle development process are presented in Fig. 7. The depicted phases in the figure solely pertain to the lead time of the vehicle development. The lead time is actually the pure development time of a new vehicle, excluding the pre-business study and the production plan from the time-to-market[6]. The following is a brief overview of the main phases of the development process as referenced in [61].
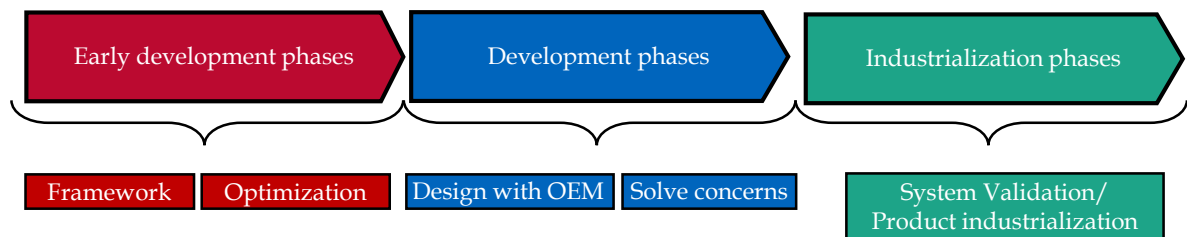
Fig. 7: Lead-time main phases of a vehicle development process [61]

In the early development phases, also referred to as upstream phases, the vehicle concept idea is derived. This development stage can be further divided into two parts, namely the framework and optimization phases. In the framework phase, concurrent studies of different technical solutions are conducted to select the most suitable technical definition of the vehicle and its subsystems. Subsequently, during the optimization phase, the selected technical solution is further examined and optimized. At this stage, the technical definition of the vehicle is finalized. Simulation serves as a primary tool during these early development phases. Initially, the level of available detail for the systems or the entire vehicle is quite limited. However, the level of detail progressively increases according to the technical details investigated during this phase.

The development phase is characterized by the design activities of subsystems and components undertaken in collaboration with Original Equipment Manufacturers (OEM), aligning with the technical definition previously defined in the early development phase. Once the final

---

[6] The time-to-market is a business term that refers to the overall time duration from conception to market availability of a given product.

design is determined, OEM construct prototypes, and real tests are conducted to validate their products. The subsequent actions focus on solving issues that may arise during the integration of the subsystems in the vehicle.

The industrialization phase comprises two phases that are running in parallel, each serving different purposes. The first phase involves a series of tests, ranging from system validation within the vehicle to the entire vehicle validation. These tests enable the acquisition of vehicle homologation, guaranteeing compliance with safety standards. Simultaneously, preparations are made within the manufacturing facility and supply chain with OEM to facilitate the start of production for the new vehicle.

3.2   Procedural models

Procedural models are employed in the automotive industry to organize the development process and its subprocesses [10]. The V-model is a long-standing procedural model in the industry. This latter organizes the early development and development phases (Fig. 7) following a top-down approach (development axis on the left side) and a bottom-up approach (validation axis on the right side), as illustrated in Fig. 8. The development axis is a process of design, continuous assessment, and optimization. The overall goal of these activities is to provide well-defined solutions, that are ready for implementation. The process starts at the top of the left-hand side with system specifications, stemming from customers' requirements and targets (e.g. the range and emission targets, etc.). The following activities focus on product development with increasing levels of detail, from system-level to component-level. System-level consists of high-level development specifications, e.g. defining the vehicle architecture. The next phase consists in decomposing the complex system into several subsystems. This means that the main specifications are broken down into subsystem specifications (for example battery energy, electric machine power, etc.). The last stage of the development axis ends at the component level, where the focus is on detailed component design. During this step, virtual computer-aided design and simulations are typically used to evaluate design choices. Once the components are built, the next activities on the right-hand side of the V-model consist of testing and integrating from component-level to system-level. Firstly, the components are initially tested separately. Next, the components are assembled and tested progressively to form a working prototype. In parallel, verification against the defined specifications is performed. These comparisons ensure that the obtained results are consistent with the defined specifications.

Internal and iterative loops may appear during the development process, in case the obtained performances during the validation and testing phases do not meet the specified requirements. Iterative loops focus on repeating activities on the same level, whereas internal loops consist of a recursive execution of activities over several levels. To adjust the system performance, a combination of iterative and recursive actions is required [62]. The obtained results help to readjust some considerations and refine details that have been incorrectly defined or estimated in previous steps. The development process can be repeated several times until the results converge toward the requirements. Therefore, these loops can have a significant impact on the development time and costs. The later a loop appears in the cycle, the

greater its impact on development time and cost will be. False choices during the first stages of development can have costly consequences in the subsequent stages of the development process.
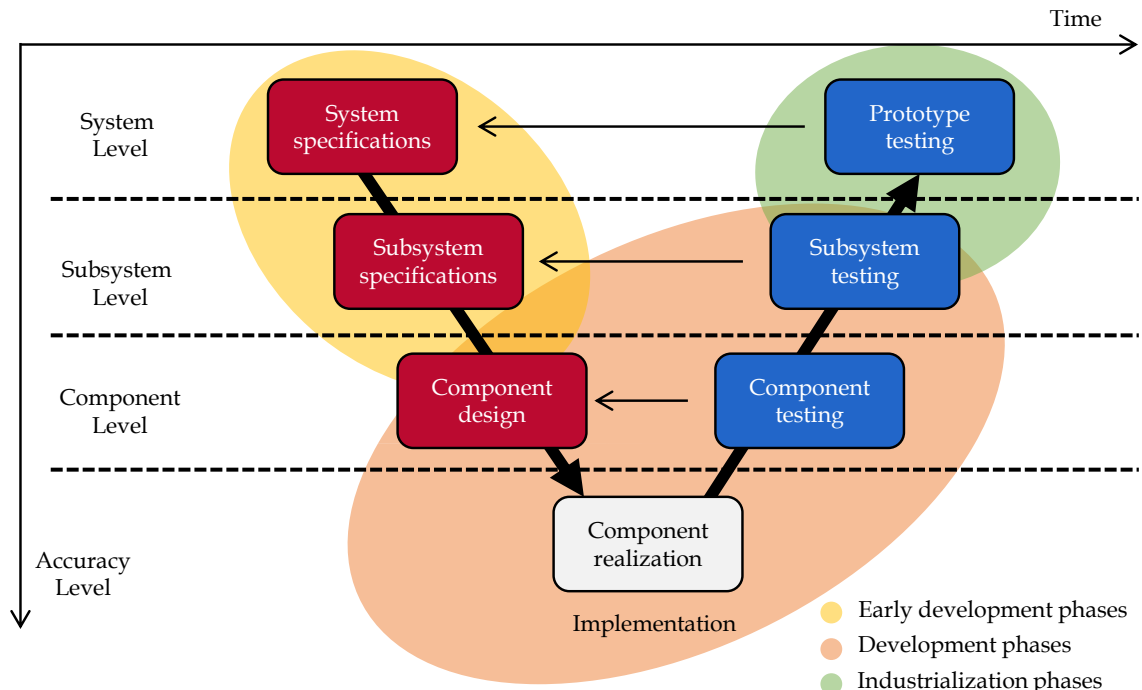
Fig. 8: V-model for industrial product development

The development of xEV differs from conventional vehicles as it encompasses too many areas and aspects that necessitate a close collaboration of several engineering teams with experts from different disciplines [10]. To effectively manage the workflow, the V-model can be further expanded and updated, resulting in a cube model representation with three dimensions, as shown in Fig. 9 [63]. The breadth dimension captures the various disciplines involved in the development of a system, e.g. electric, mechanic, software, etc. The second dimension, called width, describes the involved technical domains in development such as design, development, verification & validation, etc. Lastly, the depth dimension describes the detailed level of the development process, reflecting the system hierarchy, ranging from global to specified development processes. Another type of representation of the V-model is the W-model, as depicted in Fig. 10 [64]. By incorporating a virtual validation axis, the W-model adapts the workflow to address the specific challenges associated with xEV test and validation. Despite the variety of procedural models, the V-model remains the most adopted model in today's automotive industry. This is because of the inherent work methodologies that have been adopted for the development of thermal vehicles.

Following the adopted procedural models, the process of introducing new xEV models to the market can range from 3 to 7 years [10], [64]. This duration varies from one manufacturer to another and even among different vehicle models. For instance, reference [61] reports that the lead time of an entirely new model of an electric vehicle totals 180 weeks (about 4 years). The specific time durations of each phase of the lead time, illustrated in Fig. 7, have been

quantified as follows: 70 weeks for the early development phases, 50 weeks for the development phases, and 60 weeks for the industrialization phases.
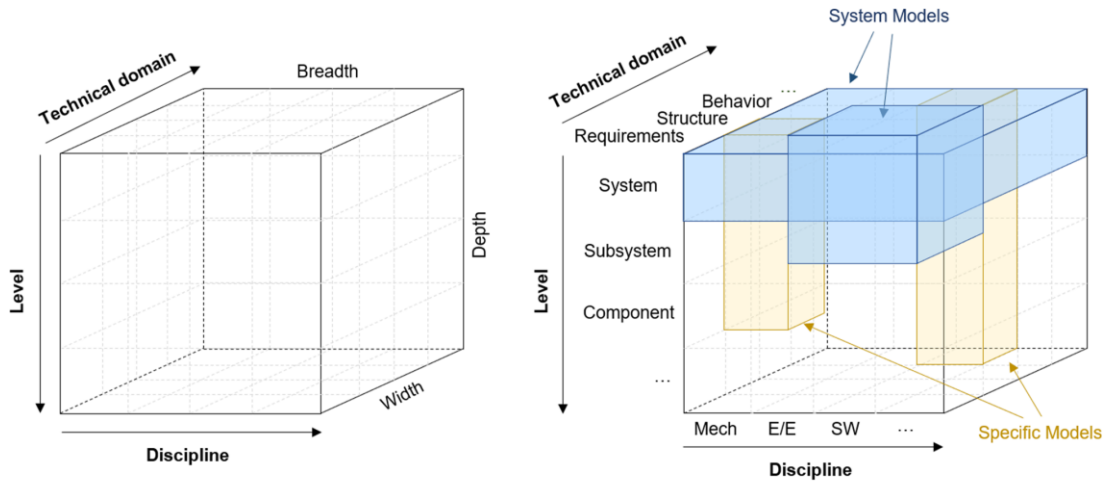
Fig. 9: Cube-model representation of the development process [63]
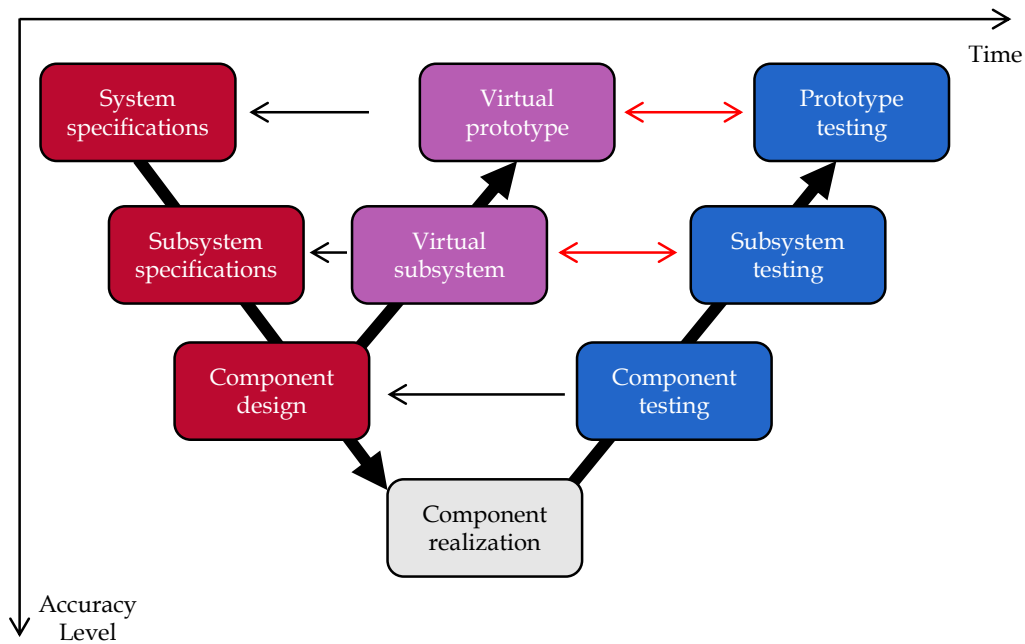
Fig. 10: W-model

4 Electric axle design of electrified vehicles

As mentioned in the previous section, the development of xEV is fundamentally different from conventional vehicles. Essentially, the primary challenge brought by electrification lies in the extensive diversity of technical solutions that can be adopted. One illustrative example of this diversity is the variety of available powertrain systems, as shown in Fig. 11. All these electrified powertrains have an e-axle in common, comprising a Voltage Source Inverter (VSI), an Electric Machine (EM), and a gearbox (GB). Hence, it is necessary to analyze a broad and flexible design space that provides a multitude of solutions. From this perspective, the scope

of this thesis is exclusively centered on the system-level design of the e-axle, without delving into an in-depth discussion on the design of the remaining powertrain components. In the sequel, the design process of the e-axle for xEV is thoroughly discussed.
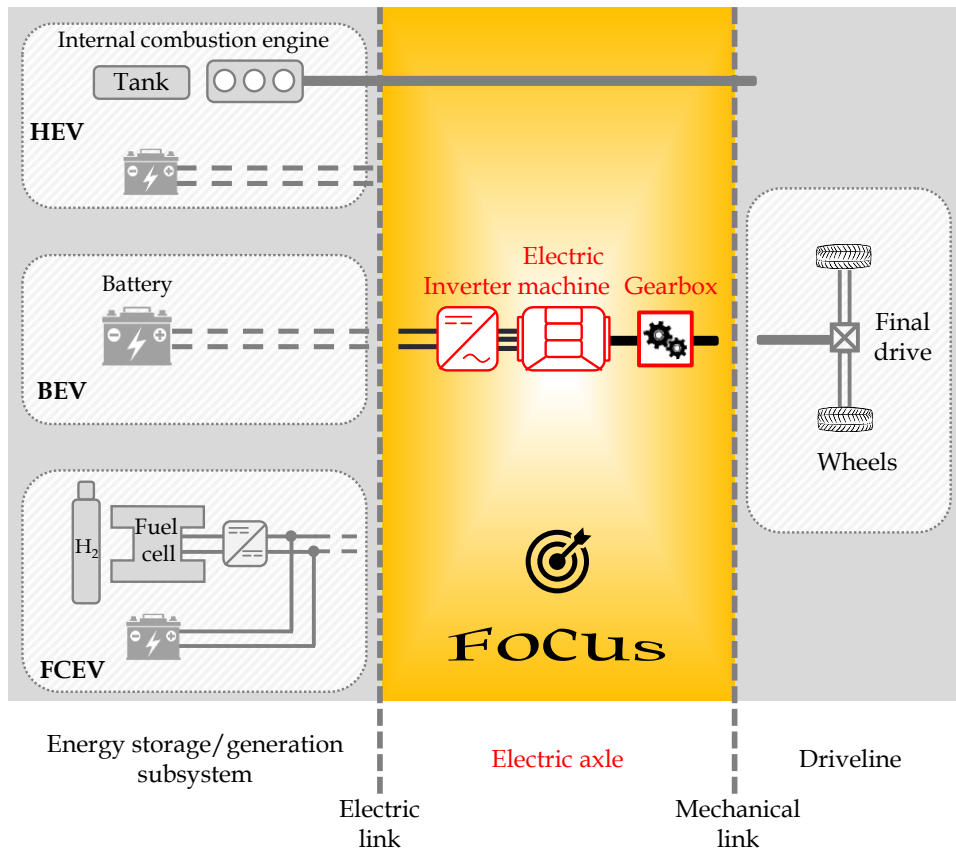
Fig. 11: Electrified vehicles powertrain schematics

4.1 Vehicle performance requirements

The specification of the e-axle can be derived from the general requirements of the vehicle, the most important of which are outlined as follows:

- **Acceleration performance:** this requirement in most cases is expressed as the minimal time to accelerate from a standstill to 100 km/h. Other requirements for passing maneuvers may be specified, such as the acceleration time needed from 60-100 km/h or 80-120 km/h.
- **Top speed:** a vehicle should meet a maximal speed, which highly depends on the vehicle segment.
- **Gradeability:** this requirement is described as the maximal slope that a vehicle can climb while sustaining a specified speed. For instance, the American technical specifications of xEV specify that vehicles should be able to ascend a grade of 25% (about 14°), maintain a speed of 88.5 km/h on a 3% grade, and sustain 72.4 km/h on a 6% grade [65].
- **Driving range**: this requirement refers to the distance that the vehicle can drive, which mainly depends on the battery size.

- **Driving comfort**: encompasses factors such as drivability in specific maneuvers (e.g., take off, gear shifting, etc.) as well as aspects of noise, vibration, and harshness.
- **Emissions:** defined by regulation rules and can vary from one region to another.
- **Packaging and weight:** this will depend on the technological choices, available space, and cost boundaries.
- **Recyclability and second life:** the ability to recycle materials, as well as explore opportunities for extending the lifespan of some components in other applications is becoming of high interest to promote a circular economy in the automotive industry.

The market of xEV, particularly LDV, shows a wide diversity in requirements aimed at promoting these vehicles. This is evidenced by Fig. 12, in which acceleration time, top speed, maximal traction power, curb weight (i.e. the weight of standard equipment without considering the weight of passengers or any additional cargo), and range data, pertaining to a sample of 60 models of electric LDV models commercialized from 2019 to 2022 are visualized. Appendix II presents further details, along with the vehicle brands and models.
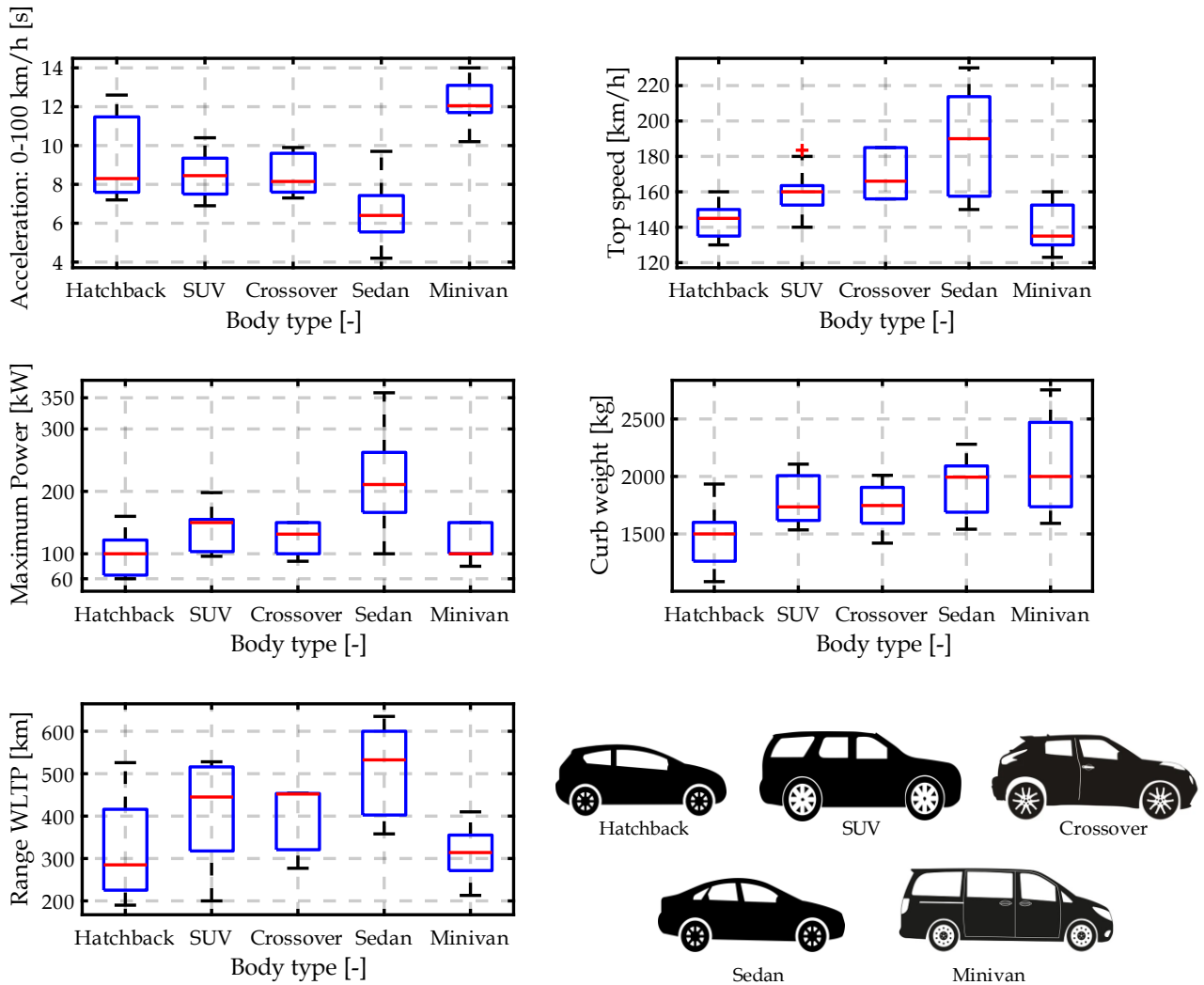
Fig. 12: Overview of the requirements of different commercialized light-duty vehicles

The data is herein classified according to the body type of the vehicle. Analysis of this data reveals a wide range of variation. For example, the acceleration time to reach 100 km/h varies from 4s to 14s. Sedan-shaped vehicles, including sports cars, show the shortest acceleration times, while minivans exhibit the longest time. The high-acceleration time impacts the maximal traction power, which is observed higher in sedan vehicles as compared to minivans. The top speed varies between 110 km/h to 230 km/h to handle highway driving conditions. Sedans demonstrated the highest top speeds. Among all vehicles, hatchback-shaped vehicles have the lightest curb weight, ranging from 1100 kg and 2000 kg, whereas minivans are the heaviest. The range, determined based on the Worldwide Harmonised Light Vehicles Test Procedure (WLTP), shows substantial variation among the selected vehicles, with a maximum range of about 600 km and a minimum range of 190 km.

Fig. 12 serves as a clear indication that each vehicle possesses specific requirements that vary following the preferences and needs of customers. This presents a significant challenge for the automotive industry in designing and delivering adaptable solutions for their electric axles to cover different types of vehicles.

4.2 Electric axle design layers

Fig. 13 outlines the design layers of the e-axle, which entail determining powertrain architectures, selecting technology, sizing components, and designing the control [12], [13], [66]. All of these layers are crucial and require careful consideration during the early development phases (cf. Section 3.1, and Fig. 7). This is of significant importance when addressing the definition of the system and subsystems specifications within the procedural models, i.e. the V, W, and cube models, presented in Section 3.2. In the following sections, each design layer is discussed. It is worth noting that the scope of the subsequent discussion does not encompass the energy storage and generation subsystem.
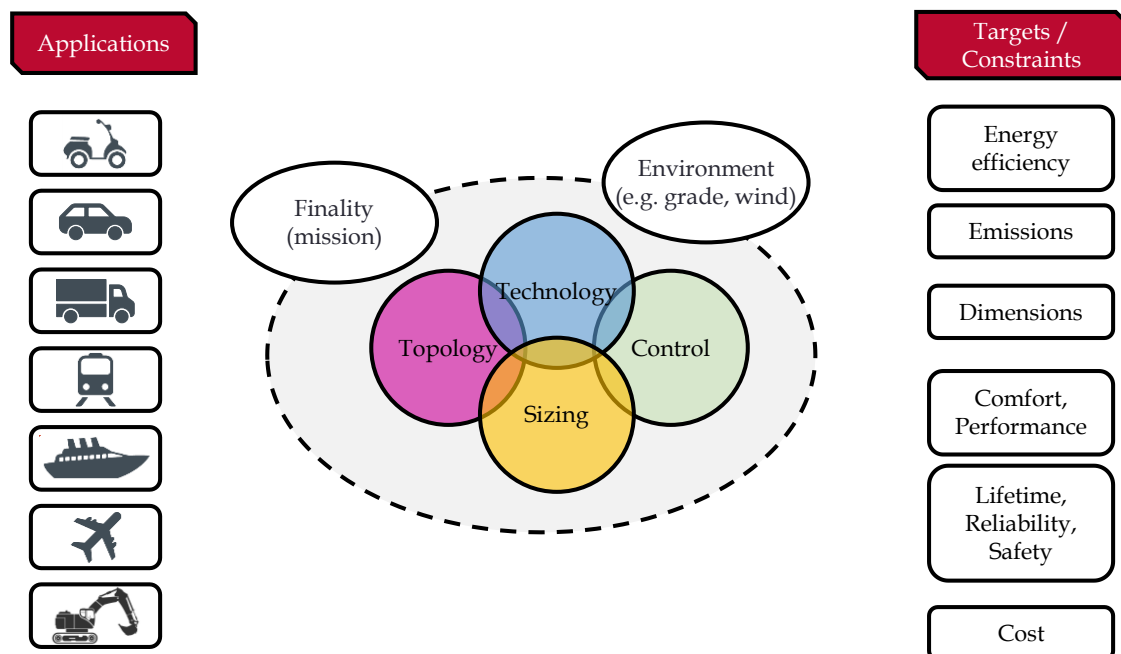
Fig. 13: System-level design of electric vehicles [67]

4.2.1 Topology

From system-level perspective (high-level view of the system), the topology is the arrangement by which the components within the powertrain are connected. According to the V-model, the topology selection belongs to the system specification, occurring during the early development phases (see Fig. 8). An abundance of topologies is reported in market trends and academic research [68]–[70]. Fig. 14 presents a few examples of the topologies used in the context of BEV and FCEV. By varying the number of components and their locations, different powertrain topologies can be derived, including mono or multi-drive systems, as well as distributed and central powertrains. This variety of powertrain topologies leads to front, rear, and all-wheel drive vehicles.
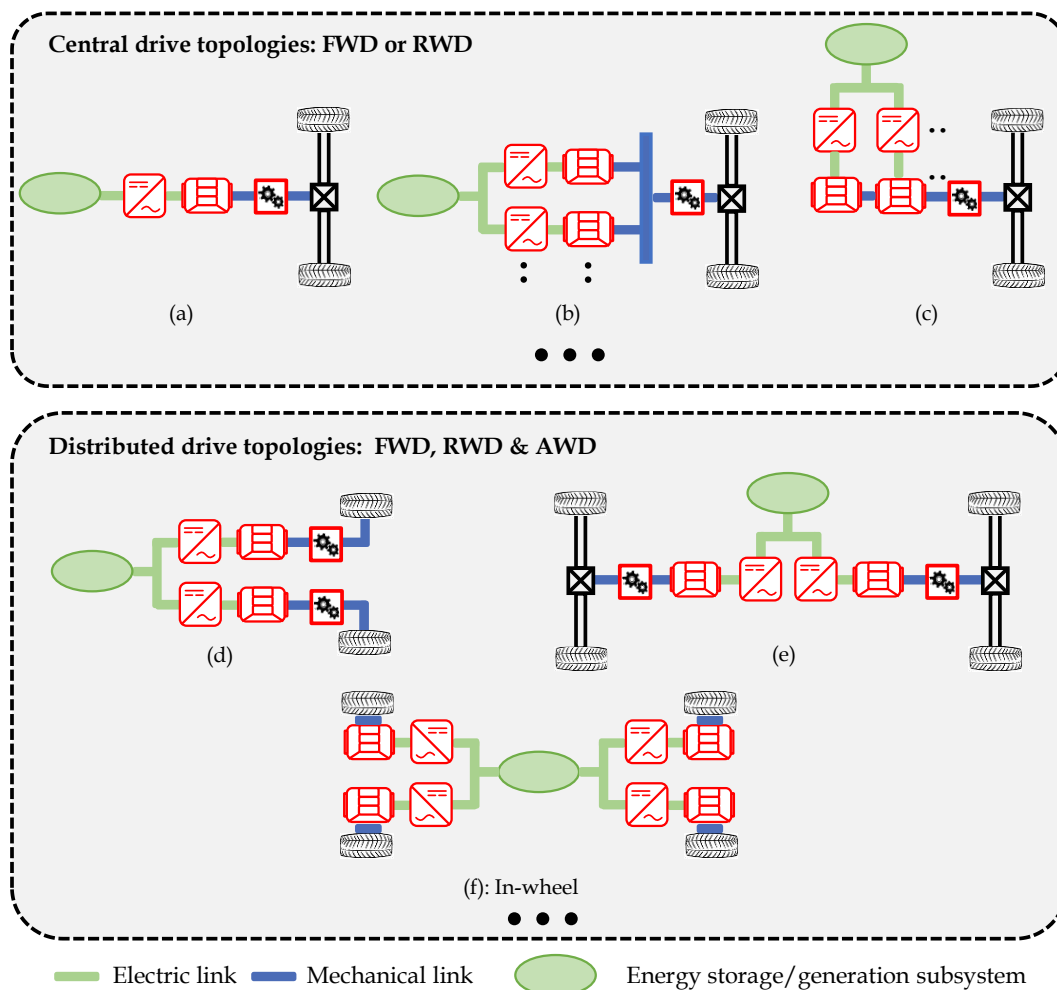
Fig. 14: Examples of topologies used in battery and fuel cell electric vehicles. The acronym FWD in the figure refers to Front-Wheel Drive, RWD denotes Rear-Wheel Drive, and AWD describes All-Wheel Drive.

Central drive powertrain topologies are herein defined as a powertrain that has one mechanical port. The topology depicted in Fig. 14.a is the most used in the automotive industry for BEV and FCEV because of its simplicity. This is because this topology does not need a huge modification to the chassis configuration of conventional engine-powered vehicles. To

increase the system efficiency and redundancy, other central multi-drive-based powertrains are proposed, as shown in Fig. 14. b, and c. In such powertrain configuration, the machines can be mounted on the same shaft or have parallel shafts that can be coupled through a coupling device, such as a planetary gear set or a belt. The inconvenience of this type of topology is the tight arrangement of the mechanical components, making it challenging to accommodate large-capacity energy storage systems.

Distributed drive powertrains have at least two mechanical ports, allowing more flexibility to separately control each wheel (Fig. 14. d), each axle (Fig. 14. e), or both of them (Fig. 14. f). Therefore, vehicle dynamics, steering performance, efficiency (more recovered energy during braking and different torque distribution strategies), and vehicle safety can be improved. Additionally, this kind of topology allows for the elimination of mechanical transmission, e.g. the gearbox, the differential, or both, which can provide weight reduction, volume, and cost savings.

Regarding HEV, a wide range of topologies exists, which vary based on their architecture, i.e. series, parallel, and series-parallel. For further details, readers can refer to [69].

4.2.2 Technology

In the context of the V-model, the technology selection is addressed when dealing with the definition of the subsystem specifications. There is a plethora of electric axle component technologies available [71]. The suitability of each technology depends on the specific context, requirements, and boundaries of a given application. Consequently, it is not straightforward to judge the superiority of one technology over others. Instead, a technological decision should be made following a comprehensive analysis of various factors specific to the application at hand. The following is a brief overview of the technological solution for the electric axle components.

The prevalent tractive EM technology in xEV consists of Permanent Magnet Synchronous Machines (PMSM) and relatively less Induction (IM) Machines [72]–[74]. PMSM, in particular, hold a higher market share because of a higher power/torque density and efficiency as compared to their counterparts. Other technologies such as the Wound Rotor Synchronous Machine (WRSM), Switched Reluctance Machine (SRM), and Permanent Magnet assisted Synchronous Reluctance Machine (PMaSynRM) are employed in a few commercialized models, however, their usage is relatively limited. A qualitative comparison between the different technologies, based on the aforementioned references, is given in Table 1. In this comparison, a point grading system ranging from A to F is employed, with F representing the lowest performance and A indicating the highest performance. Different arrangement configurations are available for each technology of electric machines. For example, in the case of most commercialized PMSM, the rotor can be present with different arrangements of permanent magnets, such as tangential, V-shaped, and delta-shaped, etc. As for IM, the rotor can be either a squirrel cage type or wound type. The pros and cons of each topology are discussed in detail in [72].

Table 1: Evaluations of different electric machines for electrified vehicles

Criteria	PMSM	IM	WRSM	PMaSynRM	SRM
Power density	A	F	D	B	D
Efficiency	A	F	C	B	C
Cost	F	A	B	D	A
Robustness	D	A	C	D	A
Noise	A	A	A	A	F
Recyclability	F	A	A	F	A

As far as inverters are concerned, the choice of the right semiconductor technology depends on the desired voltage level and switching frequency. Since 1996, Silicon-Insulated Gate Bipolar Transistors (IGBT) have dominated the market of tractive voltage source inverters because of high voltage/current ratings, reasonable cost, and decent efficiency [11]. In the last decades, wide band-gap semiconductor devices, namely the Silicon Carbide (SiC) based-Metal Oxide Semiconductor Field Effect Transistors (MOSFET), are beginning to establish themselves as a viable option for traction inverters because of higher efficiency, power density, and switching frequency [75]. SiC-MOSFET exhibit better efficiency at partial load regions and the maximal efficiency of the inverter can be pushed to over 99%, compared to about 96% achieved with Si-IGBT [76]. However, IGBT are still advantageous in terms of cost. Gallium Nitride (GaN) semiconductors are also gaining attention. Nonetheless, it is not yet deemed suitable for use in traction inverters because of voltage rating limitations. The predominant topology used in tractive inverters, for automotive applications, is a two-level voltage source with six switches [77]. This choice is driven by its simplicity, cost-effectiveness, ease of manufacturing, and simple control requirements. Although there are other available topologies, most of them necessitate the incorporation of additional switches and passive elements as compared to the standard topology. Instances of such alternatives include Z-source and multi-level inverters [77].

As far as gearboxes are concerned, single-speed gearboxes[7], generally with two stages, are widely used in LDV, particularly, BEV and FCEV [78], [79]. This is attributed to their simplicity, cost-effectiveness, efficiency, and their ability to satisfy acceleration, and top-speed requirements. These gearboxes use either spur or helical gears, with a preference for helical gears due to better noise behavior [78]. Recent models of commercialized BEV have started to apply planetary gearboxes because of their more compact design and co-axial shaft arrangements [80]. Furthermore, in the context of powertrains involving multi-drive systems, planetary gearboxes have been proposed as an interesting solution for coupling the machines [68], [81]. Additionally, as the xEV market is expanding to cover a broader range of vehicle segments, including HDV, there is a growing adoption of multi-speed gearboxes to meet the load requirements effectively [82]. Alternative gearbox technologies are also available such as continuous variable transmissions, dual-clutch transmissions, automated manual transmissions, magnetic gear transmissions, and automatic transmissions [83]. However, the last-mentioned solutions

---

[7] Single-speed gearboxes are often refered to as speed reducers or simply reducers in some works in literature.

are less used in BEV and FCEV, with greater prevalence in HEV powertrains. The advantages and disadvantages of each type of gearbox are discussed in-depth in [78], [82]

Emerging trends in electric axle technologies for the next generation of xEV involve high-speed powertrains. By increasing the operating speed of EM, it is possible to further enhance power density, thereby reducing the volume and weight of the machines and the use of rare-earth materials in electric machines [84]. This trend arises as a result of the space limitations in vehicles for holding large energy storage systems. Currently, the maximum speed of commercialized machines is within the range of 8000 rpm to 18,000 rpm. Appendix II provides further details, exemplified by commercialized EM. Ongoing efforts are focussing on further expanding the speed range. For instance, a commercially available tractive PMSM that can achieve 30,000 rpm and prototypes capable of reaching 50,000 rpm have been proposed in [85]. Other emerging technological trends include axial flux machines [86], the use of additive manufacturing [87], in-wheel machines [88], high-voltage inverters and machines (upgrading to 800 V as compared to the commonly used 400 V) [89], and highly integrated electric axles components into one package (3in1) [73].

4.2.3 Control design

The control design is part of the system and subsystem specifications activities of the V-model. The following is a cursory overview of the commonly used control laws in the context of xEV. The control design can be tackled from two perspectives: component and system levels. When referring to component-level control, it signifies the control laws used for each individual component of the electric axle. System-level control stands for the control strategy to manage the distribution of the power flows within the system, referred to often as an energy management strategy.

The output voltages produced by the VSI and feeding the EM are generated through Pulse Width Modulation (PWM) wherein the power semiconductors are switched in a predetermined pattern. Four modulation techniques are commonly employed in the context of tractive inverters [77]: Sinusoidal modulation (SPWM) is one of the most classic techniques, Space Vector modulation (SVPWM) is employed to reduce total harmonic distortion and enhance efficiency, Sinusoidal modulation with a Third Harmonic Injection (THI) is used for maximizing the RMS output voltage of the inverter for a given DC input voltage, and Square wave modulation is typically employed in the flux-weakening region to improve the performance of the machine.

The control of electric machines can be divided into three categories: Field-Oriented Control (FOC), Direct-Torque Control (DTC), and Model Predictive Control (MPC) [72], [74]. FOC is extensively applied in xEV due to its ability to ensure accurate torque output. DTC finds typical usage in high-power xEV and for applications where a fast torque response is needed. MPC is gaining increasing attention in xEV due to the possibility of attaining a wide speed range, and fast dynamic response, as well as providing high flexibility to improve different criteria of the electric machine performance (e.g. torque ripples, and efficiency). Emerging

control techniques such as fault-tolerant control and sensorless control are worth mentioning as well.

Single-speed gearboxes do not use a control law, whereas multi-speed gearboxes employ control laws to shift from one speed to another [82]. The basic control law involves upshifting and downshifting based on the speed of the vehicle. However, more complex control laws can be classified into two groups: dynamic shift schedules, which primarily focus on achieving the requested speed and acceleration, and energy-efficient shift schedules, which aim to optimize powertrain efficiency.

At system-level, particularly for multi-drive systems, the use of global control is crucial to managing power distribution [68], [90]. This control can be categorized into three groups: rule-based, optimization-based, and learning-based [12], [13], [66], [91], [92]. Rule-based control relies on engineering experience and proves effective for real-time applications. However, the optimal vehicle performance in various driving scenarios is not guaranteed. Optimization-based control employs optimization algorithms to find the optimal solutions for a given problem and can be further classified into two categories: online (suitable for real-time applications) and offline (not feasible for real-time implementation). Learning-based control, on the other hand, employs data-driven methods, to derive the optimal control laws based on historical and real-time information.

4.2.4 Sizing and component design

A major part of the subsystem specification and component design activities of the V-model comprises the sizing of the e-axle, which aims to define the appropriate specifications of its components that match the driving requirements of the vehicle. This process involves targeting a mono/multi-objective(s) function, wherein achieving high efficiency is one of the major considerations. The sizing problem involves a wide parameter variation that can be classified based on two levels: system and component [93]. The system-level sizing considers high-level (macro) parameters to determine the torque-speed characteristic of the electric axle. On the other hand, the component-level sizing delves into the component design details, aiming to propose a well-defined design solution that fulfills the requirements at system-level. It is important to emphasize that both levels are interconnected as changes in parameters at the system-level lead to corresponding variations in the outcomes of component-level sizing.

Most important high-level parameters have been identified and discussed in pertinent literature [15], [93], [94]. These parameters are visually presented in Fig. 15. The electric machine can serve as a central element of the sizing problem. The torque-speed characteristic of an electric machine is defined according to 4 key parameters, namely the nominal torque, maximal torque, base speed, and maximal speed. When combined with the gear ratio of the gearbox, the overall torque-speed characteristic of the electric axle can be deduced. The nominal torque of the machine is generally defined as the average torque that satisfies the driving requirements of the vehicle. This can be performed by analyzing different load profiles of different driving cycles. The choice of the gear ratio impacts also the definition of the nominal torque of the machine. On the other hand, the maximal torque is established to satisfy short-term

driving needs, such as during acceleration phases. Based on the last parameter, the current rating of the inverter can be defined. The base speed is constrained by the voltage rating of the inverter. The combination of the base speed and nominal torque determines the nominal power of the machine. The maximal speed of the machine and the gear ratio are inherently connected and need to be both defined to ensure the maximal speed of the vehicle. Typically, the maximal speed of the machine is limited by the switching frequency of the inverter.
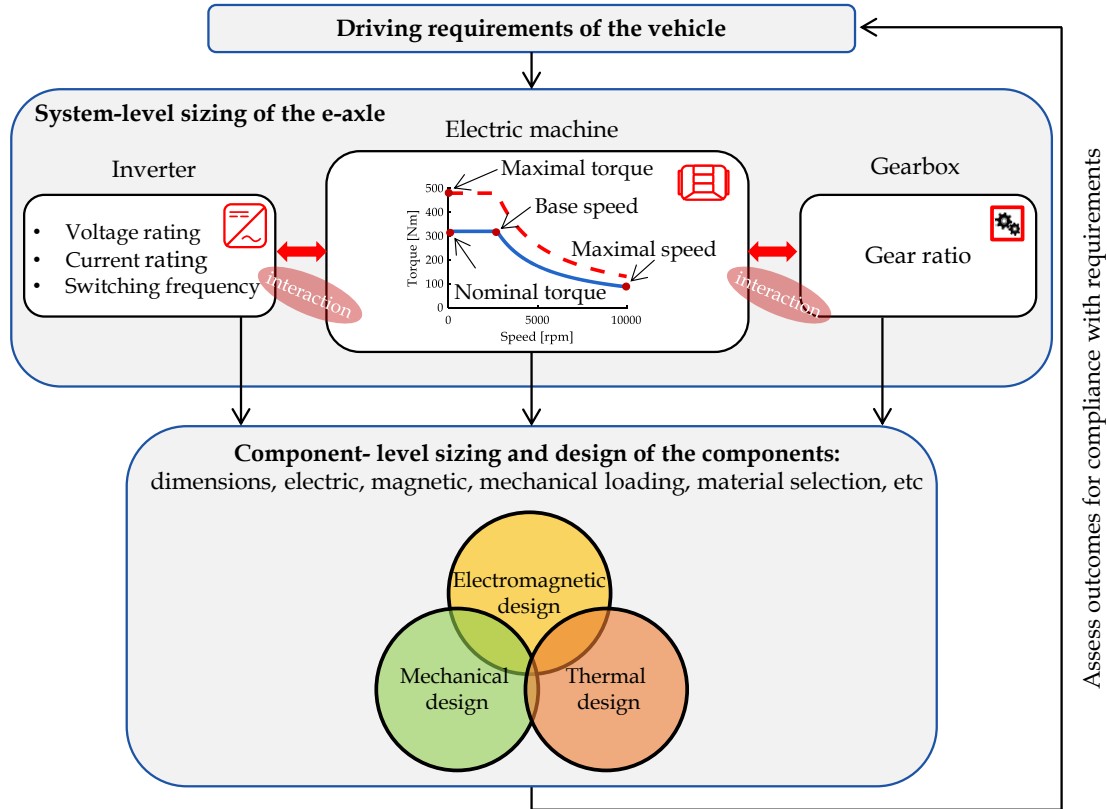
Fig. 15: sizing of the electric axle

Once the high-level sizing parameters have been established, the design of the components commences. This process entails an extensive exploration of numerous design parameters such as geometry parameters, winding parameters as well as electric, magnetic, and mechanical loading, and many others. To assess the performance of the electric axle, various disciplinary-level analyses, such as electromagnetic, mechanical, and thermal analyses, need to be conducted. In this design analysis, the primary concerns are power losses and efficiency. This approach results in more detailed modeling and analysis of the examined component. Acquiring a deep understanding of each individual component is crucial in this process.

At the end of the sizing process, power loss or efficiency maps are generated to assess the energetic performance of different designs. These maps consist of contour plots of efficiency/power loss as a function of each torque-speed operating point. To this end, a control paradigm is needed to establish the efficiency map. For instance, the Maximum Torque Per Ampere (MTPA) control is extensively used to generate the efficiency map of PMSM [95]. The accuracy of the mapping relies on how the data is generated [96]. These data can be obtained using different methods, which will be discussed later in the next section. Finally, it should be

noted that the sizing problem entails an iterative process, with each iteration requiring the generation of an efficiency map.

5 Problem statement

This section aims to elucidate the research problem of the present work. For this aim, the currently employed approaches to solve the design of e-axles are initially reviewed.

5.1 State of the art of e-axle design

In recent literature, several research studies have dedicated their efforts to addressing the system-level design of the electric axles [12], [13], [93]. To identify the best sizing, an optimization routine is commonly employed to vary the parameters, enabling the exploration of a broad range of solutions. These optimization routines are incorporated with a high-level powertrain model to assess the different solutions at system-level, particularly in terms of energy consumption. Notably, optimization-based methods combine the different layers of the electric axle design. Thereby, this leads to a coupled optimization problem, which can be solved following different approaches as shown in Fig. 16, and detailed in the following:
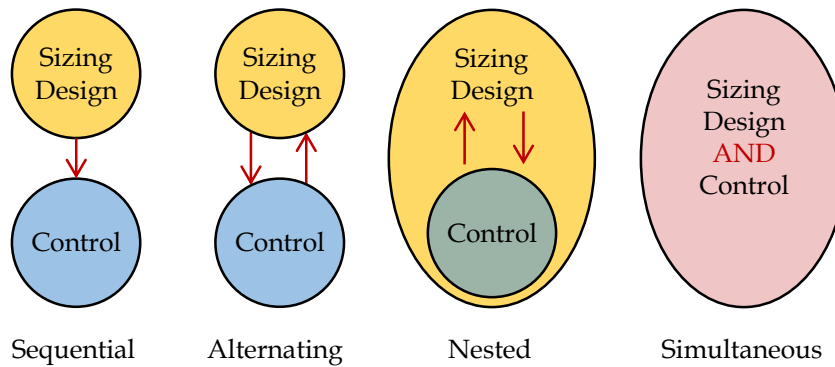
Fig. 16: Optimization framework for system-level design of the electric-axle

➢ **Sequential:** for a given topology and technology, the sizing of the electric axle is initially optimized through individual investigations at component-level for each component. Subsequently, the control design is optimized for the optimal powertrain sizing obtained from the previous step.

➢ **Alternating:** for a given topology and technology, the process of optimizing the sizing and control design occurs in distinct and iterative steps. In this way, this method keeps alternating between the sizing and the control optimization by adding a further iteration until the results converge.

➢ **Nested:** optimization is performed following a top-down approach, where each iteration in one layer involves optimizing all the other layers. For a given topology, the nested approach involves two nested optimization loops. For this reason, this approach is often referred to as a bilevel optimization framework. The component sizing is optimized in an outer loop, while the control optimization is conducted in an inner loop. The nested optimization method requires a higher number of total function evaluations, which rapidly increases as more design parameters are added. Global optimum can be reached following this approach.

➢ **Simultaneous:** as compared to the nested approach, simultaneous optimizations of the different layers are conducted in a single loop. This approach involves formulating a mathematically complex problem with a significant number of variables, all incorporated into a single framework.

To address the sizing problem of the components, models are needed to synthesize, assess, and compare different design candidates (i.e. different dimensions, power ratings, etc.) of components. Particular emphasis is usually placed on energetic performance during the initial stages of development. In this sense, various models with different levels of detail and granularity exist in the literature, as shown in Fig. 17, to address different design problems. The models exhibit variations in accuracy, computational time, and the number of parameters they incorporate. For instance, numerical models rely on computationally intensive numerical techniques that are generally implemented in specific computational tools. A semi-analytical model serves as an intermediate model between purely numerical and analytical models. An analytical model is based on an analytical formulation, primarily derived from linear or non-linear mathematical expressions. Analytical models provide insight into the behavior of the component/system under study and can be classified as either physics-based analytical models or data-driven analytical models. Physics-based analytical models require a solid understanding and knowledge of the physical phenomenon to be modeled. Data-driven models, on the other hand, are mathematical expressions derived from experiments or databases without a direct relationship to the physical phenomenon. All these models enable the creation of maps or mapping-based models, which can be integrated into system-level simulations to evaluate the performance of the generated design in terms for example of energy consumption.
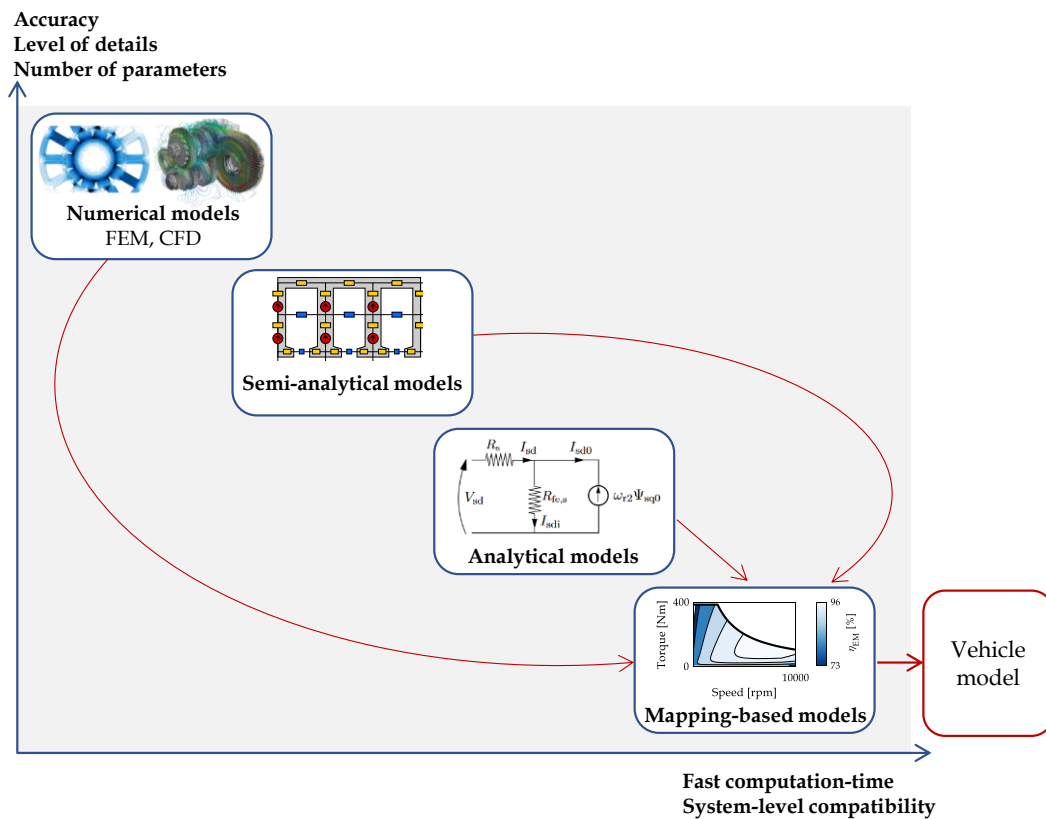
Fig. 17: Different granularity of models for component design

In the subsequent section, an overview of the most commonly utilized models in the context of electric axles is presented.

5.1.1 Voltage source inverter

The design of power electronics converters involves various elements, including the sizing of semiconductor components and passive components, as well as the design of the microcontroller unit, circuitry, and cooling unit. Therefore, numerous design variables are implied and knowledge from various engineering disciplines is required. A comprehensive review of the power electronics converter design steps is presented in [97].

Starting from the system-level specification, the semiconductor components of the inverter need to be selected to meet the desired performance. Typically, this can be accomplished by choosing devices from the manufacturers' catalog. However, this may result in sub-optimal sizing as components are available in discrete sets of values in the catalogs. Hence, determining the minimal size of the semiconductor components that fulfill the requirements becomes a critical task. To optimize the sizing of the semiconductors, losses need to be computed as a function of the operating conditions and chip area, typically employing analytical models [98]. Further steps involve thermal analysis using either a thermal lumped parameter model [99] or numerical methods [100]. For power electronics converters, thermal modeling is crucial because of a low thermal time constant, i.e. fast dynamic. The power loss can be then translated via thermal calculations to a junction temperature for the devices of a given area. Based on the outcomes of the thermal analysis, the area of the semiconductors is adjusted accordingly through an iterative process to respect the maximal allowable temperature. At this point, the size of the semiconductor components is optimized for the studied application, and it becomes feasible to generate an efficiency/loss map for the obtained chip area. Apart from the semiconductor components, the sizing of the DC-link capacitor is of utmost importance for achieving a more compact design of the inverter. This is because the DC-link capacitor is one of the bulkiest components in the converter. For this sizing task, analytical models exist in literature [101]. Furthermore, it is crucial to appropriately size passive components and electromagnetic interference filters based on the chosen switching frequency. This is essential to prevent any potential electromagnetic compatibility issues that may arise.

5.1.2 Electric machine

The electromagnetic design serves as the initial phase in the machine design process. The primary objective is to calculate fundamental electromagnetic parameters by analyzing the magnetic field and its distribution and to assess the efficiency of the proposed design. This analysis is conducted based on geometrical sizing, commonly following well-known design handbooks [102], [103]. The electromagnetic design of tractive EM is addressed following different approaches which are discussed in the following paragraphs.

The Finite Element Method (FEM) is widely used in electric machine design because of its high accuracy. The theoretical foundations of FEM can be found in several books such as [17]. FEM considers the detailed geometry of the component and uses accurate modeling of

the various phenomena occurring in the component. By utilizing FEM, the electromagnetic parameters of the designed machines, such as flux linkage, back electromotive force, inductance, and losses can be calculated. These parameters are then used to assess machine performance, such as output torque, power, and efficiency maps across the different operating points [104]. In earlier studies, optimization approaches were coupled with FEM to maximize the efficiency of electric machines [105], [106]. However, the complexity of FEM introduces a significant computational burden, making it impractical for use in the optimization process of the overall system, particularly when searching for both optimal sizing and control solutions. To address this issue, some studies have proposed reducing the number of geometric parameters and limiting the optimization routine to some representative points of the driving cycle [107], [108].

The magnetic equivalent circuit model, often referred to as the magnetic reluctance network, is a semi-analytical model that can be employed to perform the electromagnetic design of EM. This model employs a magneto-electrical equivalence based on physical geometry and material characteristics. This results in a magnetic circuit where each reluctance depends on the geometrical parameters. By using this model, the performance and loss characteristics of the machine can be determined at any specific operating point. Furthermore, non-linearities can be taken into account using this model. It has been reported in [109] that this modeling technique provides a good trade-off between computational time and accuracy in the design of EM as compared to FEM. Consequently, several studies have incorporated the magnetic reluctance network into multi-objective optimization processes for electric machine sizing, particularly in the context of system-level design [110], [111]. Although the magnetic equivalent circuit model is faster than FEM, the computational effort for a first general assessment of the size of a design remains relatively high.

Analytical models are frequently utilized in various studies as they offer a computationally efficient solution for electromagnetic design problems. This is attributed to their comparatively simpler mathematical formulation. Nevertheless, the achievable accuracy is relatively limited due to some simplifications as compared to FEM or magnetic circuit model [112]. For instance, nonlinear magnetic properties pose a significant challenge when utilizing analytical models, as they result in changes in machine parameters. Several machine design tools based on an analytical model were proposed in the literature [113]–[115] to compute the efficiency maps of different machine designs using a few input parameters. These tools enable the computation of efficiency maps for diverse machine designs using only a small set of input parameters. Another analytical model is proposed to derive efficiency maps of EM in [116]. The model describes the different loss components using a polynomial expression as a function of torque, speed, and other coefficients that need to be identified.

After completing the electromagnetic design, thermal design and mechanical design can be conducted. In thermal design, the focus is on calculating the temperature distribution in the machine based on the power loss obtained from the electromagnetic analysis. Two widely used methods for thermal analysis in electrical machines are the lumped thermal network model and FEM [72]. Some studies employ a combination of the lumped thermal and magnetic reluctance network models to address multidisciplinary design challenges [117]. The

mechanical design addresses the stress, deformation, and vibration of the machine considering both electromagnetic and thermal analyses. This can also be accomplished using FEM [72].

5.1.3 Gearbox

The mechanical design of mechanical transmissions involves various branches of theoretical and applied mechanics such as machine design theory, tribology, material engineering, etc. The challenge when designing a gearbox is to find the right balance between load-carrying capabilities, volume, expected life, noise, and efficiency. This leads to a multi-objective optimization routine, extensively detailed in [118].

The load-carrying capability and geometrical sizing are usually done through analytical models based on stress analysis to avoid material failure, e.g. tooth breakage, pitting, micro pitting, wear, and scuffing during contact behavior. This is well-documented in standards such as the American Gear Manufacturers Association (AGMA) [119] and the International Organization for Standardization (ISO) [120]. To enhance the understanding of the mesh mechanism of gear, there are three widely used modeling methods, namely FEM, lumped parameter model, or a hybrid FEM/lumped model [121]. These latter enable to conduct dynamic analysis, thereby enhancing the understanding of stress distributions and displacements. Consequently, the sizing of the gearbox can be improved as compared to the analytical model, but at the expense of increased complexity and computational time.

Regarding efficiency computation, an abundance of analytical and empirical relations exists to calculate the different power loss components [122], [123]. These models enable decent prediction of losses resulting from friction between gear meshes and bearings due to sliding and rolling actions. However, it is still challenging to accurately calculate the power loss generated by the interaction of the gearbox components with the surrounding medium (oil, air, or a mixture of oil and air). Most of the existing models are derived from extensive experimental testing. Nonetheless, these models are not sufficiently reliable for predicting power losses when there are variations in some proprieties such as geometries, speeds, or lubricant properties, as compared to the experimental test conditions [18]. In other words, the applicability of these models is limited to the conditions for which they have been tuned. To tackle this issue, a methodology based on parameter identification is proposed in [124]. The methodology consists in calibrating the empirical parameters presented in the analytical models based on an experimental power loss map of a tested gearbox. Following that, this methodology is used to gain insights into the power loss distribution of the gearbox at system-level over a driving cycle. The primary objective is to subsequently optimize the gearbox design based on the analysis conducted using the introduced methodology. Nevertheless, one of the shortcomings of this approach is the requirement to identify a large number of empirical parameters, which poses a challenge in terms of generalizing it as a well-founded method for design optimization.

Recognizing the last mentioned limitations, there has been a shift towards using Computational Fluid Dynamics (CFD) to accurately calculate gear power loss and study the impact of design parameters on the losses [18], [125]. CFD is a numerical method primarily utilized to solve fluid flow and heat transfer problems. Its key advantage consists of providing a

comprehensive understanding of the lubricant distribution inside the gearbox, which is not feasible with other methods. Additionally, CFD offers great flexibility for analyzing various gear geometries and gear housing, facilitating the investigation of a broad range of operating conditions and geometric variations. In [126], an illustration of a case study using CFD for analyzing the design and the losses of the gearbox of an electric vehicle is presented. Nonetheless, this approach entails a substantial computational burden.

5.2 Need for methods allowing fast development of electric vehicles

As discussed earlier in the previous section, the design of the e-axle is flexible, and complex, necessitating a deeper level of modeling and a solid knowledge of each specific component. Most importantly, these methods result in a significant computational time, which makes their adaptation at system-level not practical, despite their high accuracy level. Additionally, it becomes hard to study the interaction between the components using such models. These limitations hinder their suitability for system-level design purposes, where the ability to quickly generate and predict the performance of different design solutions is crucial. As a result, these methods are typically confined to the subsystem or component levels, allowing for detailed design and analysis to ensure the readiness of the component for implementation and testing.

The findings from the reviewed literature lend support to the last statement, as demonstrated by the computational times reported in the studies conducted in [127], [128]. For example, the FEM simulation of an optimized efficiency map of a PMSM using 24 cores required approximately 16 hours, considering 10,000 variations for the optimization routine [127]. Similarly, in [128], it was reported that the CFD simulation of one operating point of a gearbox using a workstation equipped with 16 cores took around 20 hours. Therefore, multiplying this computational time by the number of the different design candidates to be evaluated and the number of components results in a cumbersome design process. On the other hand, shortening the development time of e-axles has become now an explicit demand in the automotive industry to meet environmental policies and the electrification trend in time.

Despite efforts to reduce the computational burden by restricting the design optimization to some specific operating points, as mentioned in Section 5.1.2, this approach does not completely solve the system-level design problem. The example of multi-drive systems is a good illustration of this. This is because the operating points of each drive component are predominantly influenced by the high-level control of the vehicle, rather than being directly influenced by the driving cycle. Furthermore, the utilization of semi-analytical or analytical models, which are more computationally efficient as compared to FEM, involves many design parameters and requires a high number of function evaluations in optimization routines.

Accordingly, different assumptions have been undertaken to simplify the system-level design of the e-axle. Examples include the use of a constant efficiency of 87% and 95% for the electric drive system [129], [130], and the gearbox [131], respectively. The impact of this simplification on energy consumption was validated by a comparison between simulation results and on-road testing. These assumptions, even though too simplified, can be accepted to some

extent, particularly when the main objective is to solely investigate the control design, as was done in [132]. Nevertheless, this fails to consider the impact of the power rating or design change on the efficiency of the component. Additionally, the last assumption is valid for a given driving cycle with a specific distribution of the operating point. When the driving cycle changes, this results in different operation points. Therefore, a new average efficiency needs to be defined, to account for these variations.

For all the exposed reasons mentioned above, there is a need for methods allowing powertrain designers to investigate different component designs in a short time without having a deeper knowledge of the component itself. On the other hand, this needs to be done while keeping decent accuracy. Most importantly, these methods need to offer ease of integration of the component models at system-level simulation to conduct holistic sizing and performance optimization. Furthermore, these methods need to be flexible supporting the diversity in the powertrain requirements, and can be applied in the development process of a large spectrum of xEV.

In this context, the research motivation of this thesis is to contribute to a reduction of the lead time of e-axles by accelerating the design process in the early development phases.

6 Research specifications

6.1 Scalability: a promising solution for accelerating early stages of development

To reduce the lead time of new xEV, an approach worth considering is to explore the potential of transferring the design knowledge and solutions of a reference powertrain conceived for a reference application (passenger car as an example) to derive others (e.g. light vehicles, vans, medium-duty trucks, etc). This leads to the notion of the "scaling" approach. The main purpose of scaling is to alter the properties of a reference component/system by adjusting a known solution according to specific rules [32]. In the automotive field, there is a broad understanding of the term "scalability" or "scaling". Scaling, in most literature, is commonly associated with a change in the power rating of a reference powertrain. Therefore, different solutions can be adopted to achieve this scalability in terms of power, namely geometric scaling of the components or scaling the number of the components, as illustrated in Fig. 18.

Originally, the term "scalability" or "scaling" was defined in Euclidean geometry as a geometric change in the size of a reference object to derive adjacent scaled objects. Scaling is then a transformation that increases (scale-up) or shrinks (scale-down) the size of an object, following the similarity theory. This approach is interesting as the power rating of electric and mechanical components is inherently linked with their size [102], [119]. Therefore, applying the concept of scalability for a pre-existing design, called a reference design, will result in a wide product range of scaled components with different power ranges that fit different transport applications. The main challenge lies in predicting the scaled proprieties and performances without redoing a cumbersome detailed design. In this regard, scaling laws can be of use [32]. In effect, scaling laws enable studying the effect of varying representative design parameters,

such as the geometry of the reference design, on the other parameters. Thereby, the performance of the scaled design can be predicted by using data from the reference design. By following this concept, an opportunity arises for the powertrain designer to explore a vast powertrain design space for different automotive applications in a shorter time, before starting detailed component design activities.
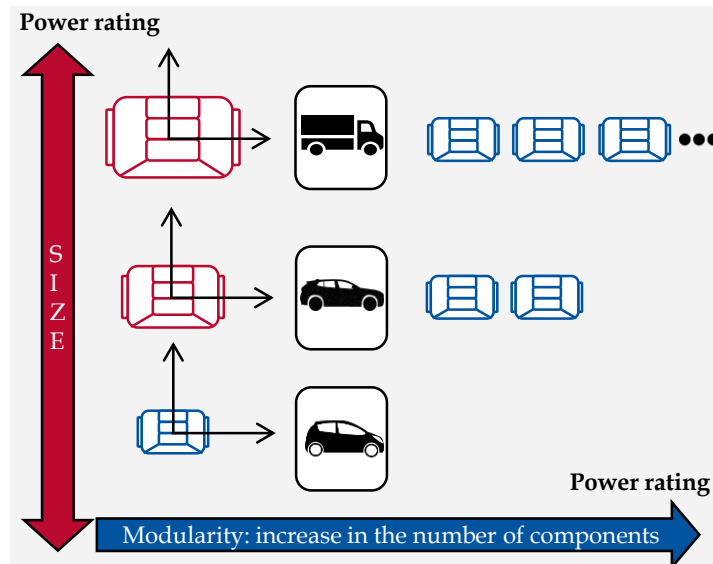
Fig. 18: Scaling possibilities of electric axle components: electric machine as an illustrative case

The second option to scale the power relies on increasing the number of components by cascading or paralleling them. This approach is more often known as a "modular approach" or simply "modularity". Multi-drive systems (Fig. 14) are a good example of a modular system. This approach provides more degrees of freedom for the system-level design of the e-axle, by combining different technologies or sizing options [133]. Additionally, modularity is of high importance when there are high integration constraints for the e-axle or when system redundancy is demanded. However, this approach can be applied in only one power scaling direction, namely for increasing the power. When it comes to downscaling the power, the modular approach cannot be applied. For this reason, geometric scaling is a more practicable option in such cases. Even more, the geometric scaling can be applied to derive a modular drive system using reference components. This means that the scope of geometric scaling is broader as compared to the modular approach. In other words, modularity can be considered a particular case of scalability.

Over the past few years, there has been a growing interest in scalability in the automotive industry. Car manufacturers such as Volkswagen aims to develop scalable powertrain platform to reduce the time-to-market of their vehicles [134]. Early in 2021, Stellantis announced its plans to have four all-electric platforms, facilitating the development of 39 xEV models that would cover all market segments [135]. Each platform is designed to enable the interchangeability of a scalable e-axle system within the range of 70-330 kW. Component suppliers, as well, provide the scalability option for their e-axle system. For example, Bosh proposes an electric drive with a power rating ranging from 50 to 300 kW, making it suitable for different vehicles

[136]. Vitesco in its turn has developed a scalable e-axle capable of providing power from 80 to 230 kW [137].

6.2 Scientific goal, and key challenges

The presented work aims to develop a scaling method for the electric axle system, i.e. the set of voltage source inverter, electric machine, and gearbox, in the early development phases of electrified vehicles, allowing to perform fast system-level investigation.

Taking the system-level design space of xEV as a reference, the scope of this work will primarily focus on the component sizing, with a comparatively lesser emphasis on the control design layer, as depicted in Fig. 19. The method should allow the development of powertrains of various power ratings, ranging from light to heavy-duty vehicles and optimize them within a common framework to reduce their development time. Additionally, the scaling method should enable the investigation of different powertrain topologies.

Regarding the technology choice, the method will be applied to an electric axle consisting of an IGBT-based inverter, a permanent magnet synchronous machine, and a planetary gearbox. This choice is driven by the reasons and market trends exposed in Section 4.2.2.
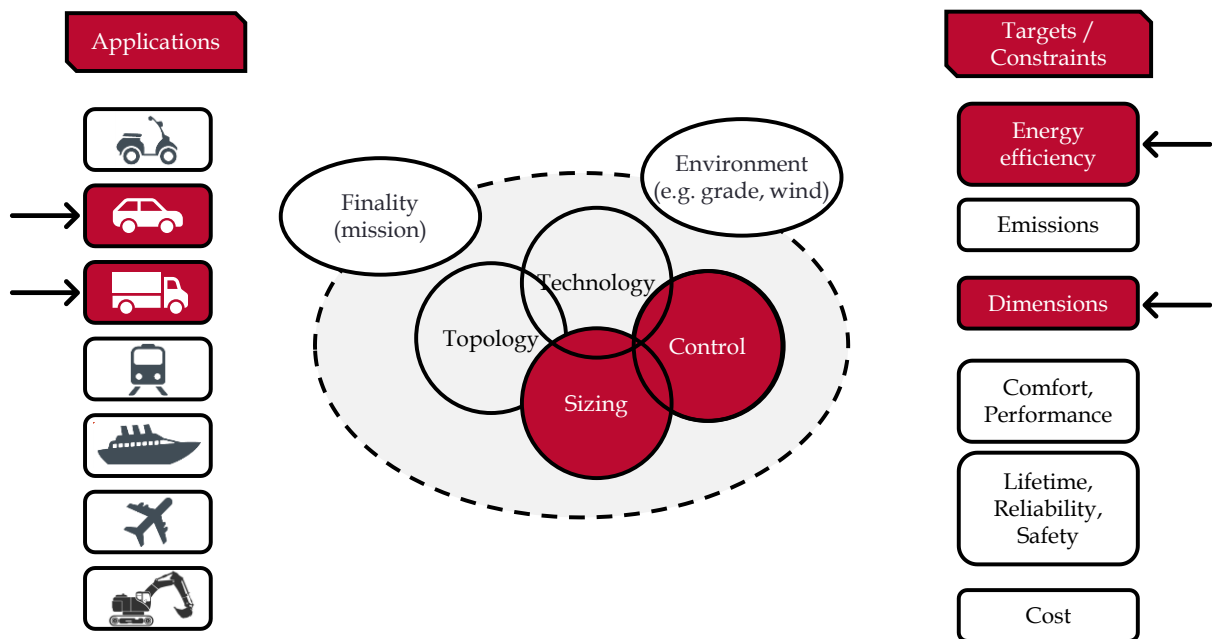
Fig. 19: Scope of the presented work within the system-level design space

Over the past few years, there has been a surge in the number of published papers related to the scalability of xEV [20], [21], [138]. In the same context, many European projects such as OBELICS [22], VISION-xEV [139], and 1000kmPLUS [140] have focussed on developing scalable powertrains to reduce the lead time of xEV. Nevertheless, even if all the aforementioned references are taken into account, 5 key challenges remain to be pointed out:

1. The scaling of electric machines is deeply rooted in literature, as evidenced by recent studies [28], [29] as well as earlier papers dating back to the 1970s [23], [24]. Different

approaches and choices have been undertaken that differ from component and system levels. However, no comprehensive comparison between these approaches is available in the literature to assess their impact on the performance of the scaled machines and the energy consumption of the vehicle at system-level.

2. Contrary to the electric machine, few contributions have been made to the scalability of gearboxes [31], [141]. The last aforementioned references have exclusively focused on geometrical scaling to achieve a new desired torque demand or to have insights into the mass and inertia. Nevertheless, scaling laws for gearboxes taking into account the losses are still lacking. Losses are considered independent of the scaling, without further explanation. This challenge is further intensified by the high input speed values of automotive gearboxes (up to 18,000 rpm) since there is currently limited knowledge of gearbox loss modeling at high-speed regions.

3. At system-level, the holistic sizing of electric axles components using scaling laws is not comprehensively addressed. Typically, the scalability approach is applied to the electric machine in optimization routines [138], [142], [143], while neglecting the scalability and interaction of other components. To address this issue, it is crucial to adopt a comprehensive approach to the scaling process that considers all interconnected components.

4. So far, the scaling laws are just employed as a set of equations combined with the model of the reference component. This is because the theory of scaling laws has been derived at component-level. The incorporation of the scaling laws into system-level simulation lacks a clear organizational and unified framework.

5. In addition to scaling the component model, the control needs to be scaled as well. Until now scalable control has only been applied to electric machines [30]. No scalable control exists for other components.

It is noteworthy that a comprehensive discussion of the state-of-the-art of scaling methods at component and system levels will be provided in the subsequent chapters of this dissertation, to support the last-mentioned statements.

6.3 Framework of the work

The presented work is conducted within the framework of the CUMIN (Campus of University with Mobility based on Innovation and Carbon Neutrality) program [144]. This research program, launched in 2015, aims to develop an eco-campus based on an electromobility to reduce the greenhouse gas emissions of the Cité Scientifique campus of the University of Lille. To achieve this, the solutions proposed by CUMIN involve restricting access to thermal cars on campus, promoting sustainable modes of transportation, and encouraging drivers to transition to low-emission vehicles. A possible future mobility option at the campus Cité Scientifique of the University of Lille is depicted in Fig. 20.

CUMIN is an interdisciplinary program that brings together researchers from national and international academic and industrial environments, encompassing expertise in different fields such as electric engineering, mechanical engineering, urban planning development, economics, and public policy. This results in different projects to promote electromobility as depicted in Fig. 21 [145]. In this context, the presented work is conducted within the STeVE

project (Scalability of powerTrain for electrified Vehicles of an Eco-campus). STeVE involves a joint Franco-Belgian Ph.D. thesis between the L2EP laboratory (Laboratory of Electrical Engineering and Power Electronics) of the University of Lille in France and the Department of Electromechanical, Systems and Metal Engineering of Ghent University in Belgium. The presented work aims to support the STeVE project by proposing a scaling methodology allowing the simulation of different types of electric vehicles with different power ratings and assessing their energy consumption. The outcomes of the project could be beneficial for other projects such as the TESS project to perform techno-economical investigations of electric vehicles.
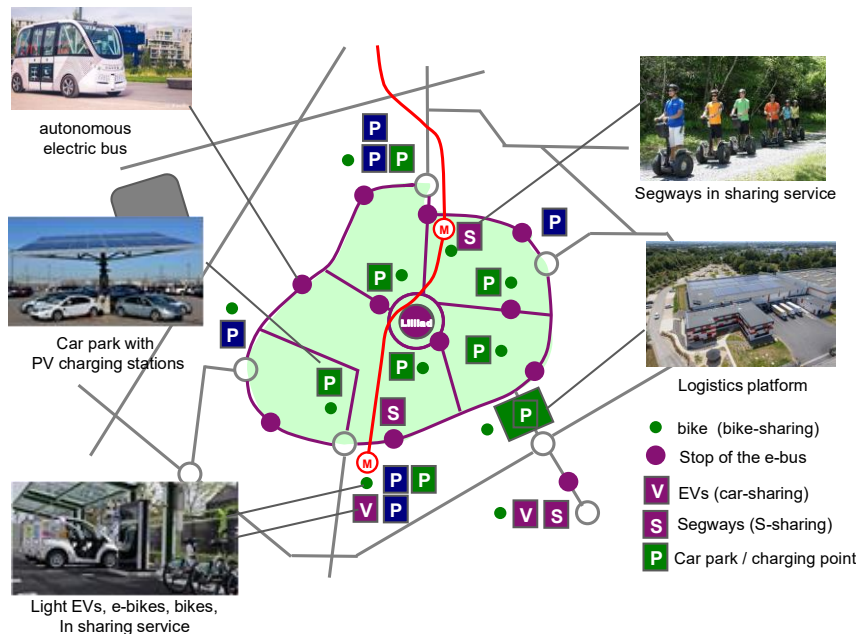
Fig. 20: Possible future composition of the campus Cité Scientifique of the University of Lille [145]
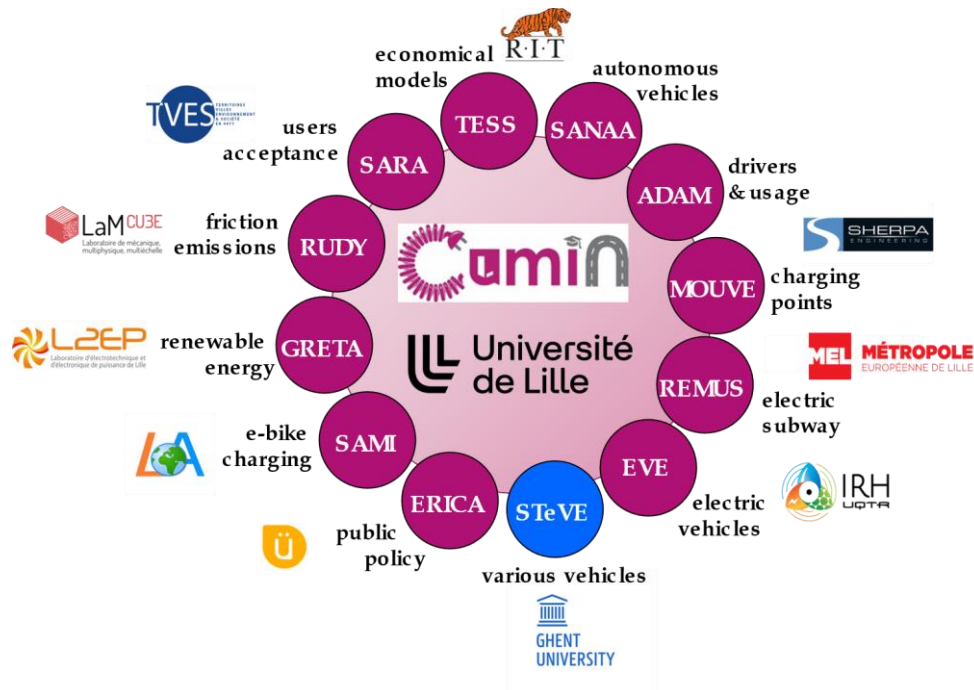
Fig. 21: On-going projects of the CUMIN program [145]

6.4 Positioning of the work

The scientific positioning of the presented work among the previous and current conducted research activities in both universities is depicted in Fig. 22.
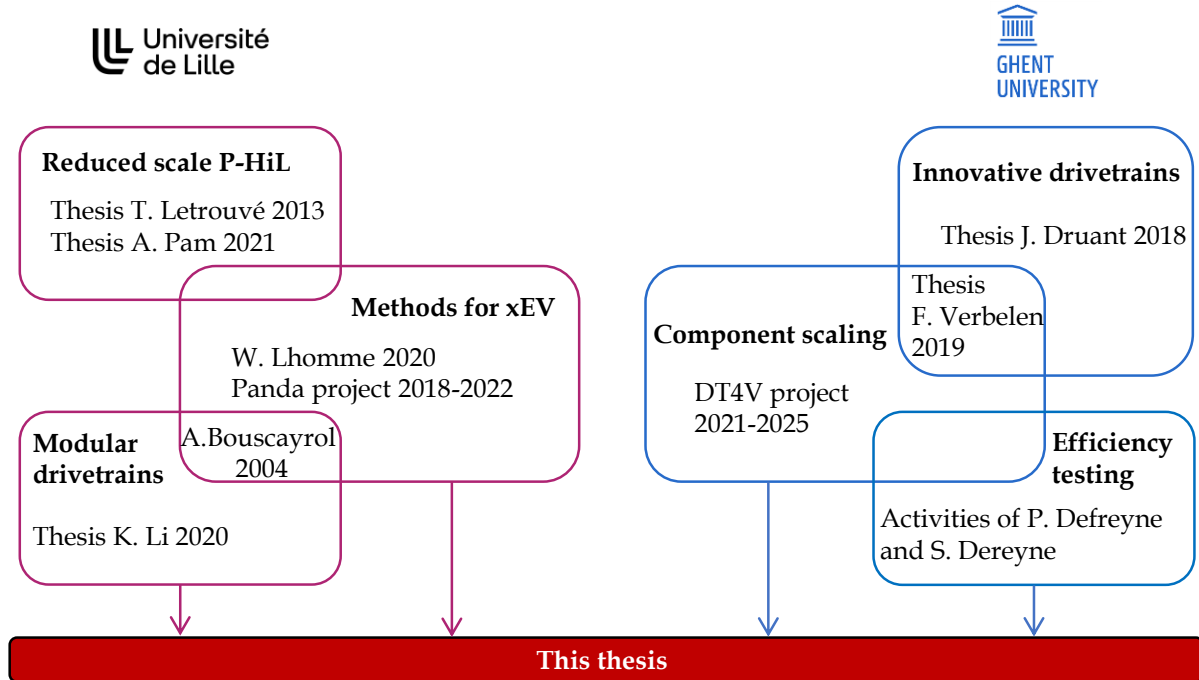
Fig. 22: Scientific positioning within both universities

Regarding the French part, the L2EP laboratory of the University of Lille has strong expertise at system-level. The Control team of L2EP is recognized for its expertise in developing methodologies and graphical organizations of complex systems, namely the Energetic Macroscopic Representation (EMR) [33]. EMR is a graphical formalism used to organize the models of energetic systems based on physical causality. One of the main research areas of L2EP is electromobility, where the EMR formalism is used to deduce global control and energy management strategies of different powertrain topologies of xEV. For instance, W. Lhomme in his thesis for the accreditation to supervise research has presented a common framework using EMR to structure the control of different types of HEV [67]. Additionally, the ambition of this research work is aligned with the PANDA EU project [64], coordinated by the University of Lille, which proposed a new methodology based on EMR to reduce the lead time of xEV. Herein, the EMR will be used to organize and describe the different models and controls of the scaled components. Moreover, modular drivetrain or multi-converter multi-machine systems have been a major research topic since the 2000s, exemplified by the contributions of A. Bouscayrol [146] and recently K. Li [147]. Another significant research axis of the control team of the L2EP laboratory is the reduced-scale Power Hardware-In-the-Loop. EMR has been useful in organizing various power emulators for different automotive applications at a reduced-power scale. The Ph.D. theses of T. Letrouvé [148] and A. Pam [149] have demonstrated the effectiveness of EMR in this field. The expertise gained in scaling for testing and validation provides a good foundation for extending the applied methodologies to the development axis, rather than the test and validation axis.

Regarding the Belgian part, the proficiency of the Dynamical Systems and Control (DySC) team within the electromechanical department at Ghent University lies in the design, modeling, and low-level control of mechatronic systems. The expertise of the department has led to the development of innovative drivetrains to increase the efficiency of a variety of applications (wind turbine, robotics, industrial, automotive, etc.). Notable contributions include the works of J. Druant [150] and F. Verbelen [151] on electrical and mechanical variable transmissions. To support the research activity, the department possesses well-equipped test facilities located at Ghent University Campus Kortrijk [152]. These facilities consist of modular test benches and calorimeter setups, enabling extensive experimental investigations for both academic and industrial purposes. These test facilities have been useful for the experimental activities conducted by S. Dereyne and P. Defreyne to benchmark the efficiency of a series of gearbox products [153]. Scaling is emerging as a new significant research axis within the department. Initial contributions have been proposed by F. Verbelen in his Ph.D. thesis, by developing a scaling methodology for the electric variable transmission (dual rotors electric machine). This Ph.D. thesis, aligned with the work of F. Verbelen, aims to broaden the scaling scope to consider other components. Additionally, this thesis shares interests with a regional project entitled Digital Twins for Validation of dynamic performance and reliability of drive systems (DT4V) [154]. One of the objectives of the DT4V project is to develop a virtual framework to minimize the costs of validating new motion drivetrains for industrial applications with a partially modified functionality and/or rescaled power rating, using the concept of digital twins.

This Ph.D. is not the first collaboration between the two research groups. In 2019, a collaborative project named EVOLUTION (EffectiVeness Of Lorries and bUses using innovative TransmissION) was launched to study the benefits of electrifying heavy-duty vehicles using innovative transmissions. Within the framework of this project, I investigated during my Master Thesis in 2020 the benefits of hybridizing a long-haul truck using an electric variable transmission in terms of energy savings [143]. In the aforementioned work, scaling laws of the electric variable transmissions have been incorporated into system-level optimization routines to minimize fuel consumption. Furthermore, the outcomes of EVOLUTION have yielded two international conference papers, putting forth a new structuration of the scalable model of electric variable transmission (with myself as a co-author) [155], and PMSM [156] using the EMR formalism.

6.5   Research organization and approaches

The present research is organized following three main axes: methods, components, and vehicles as illustrated in Fig. 23. In this section, the adopted approach for each stage of the work is outlined.
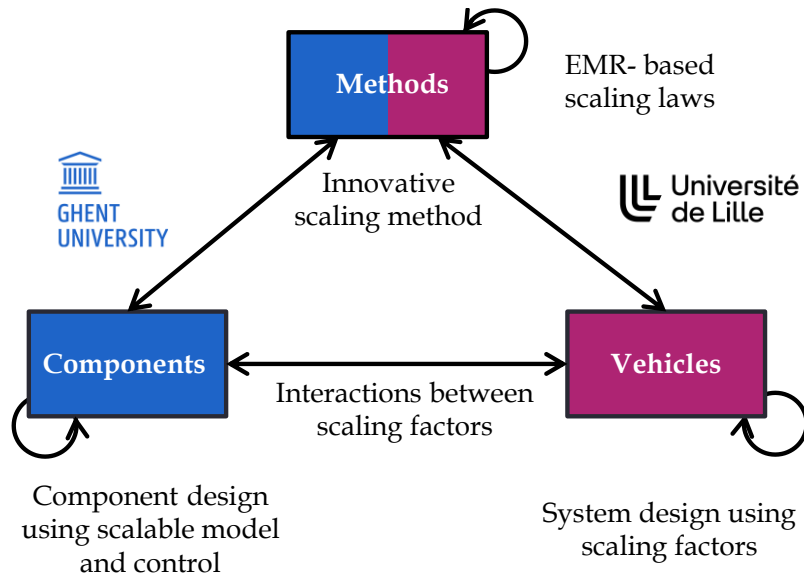
Fig. 23: Ph.D. thesis organization

6.5.1 Method: EMR to organize the scalable model and deduce a scalable control

The scaling laws will be developed for relevant properties (e.g. output torque and losses, etc.), as well as component parameters (e.g. inductance, resistance, inertia, etc.). EMR will be then used to organize the scalable component models including scalable control, in a unified way. The organization consists of keeping the model and the representation of a reference component but complemented with two power adaptation elements as shown in Fig. 24. The new part is to embed the scaling laws in power adaptation elements and scale only the input and output properties of the reference model. The losses due to the scalability of the components should be carefully analyzed and considered in the new model structure. In this way different design candidates, i.e. different dimensions and power ratings of scaled components can be easily assessed and incorporated at system-level simulations. This description is called EMR-based scaling laws in the remainder of this report. It is important to stress that the primary goal of EMR formalism is to systemically deduce the control structure rather than focusing on the design of the components. The work conducted in this research contributes to formalism by incorporating this aspect. In effect, the power adaptation elements of the EMR formalism in earlier works have served two purposes. Initially, power adaption elements have been introduced to scale input control variables of a given system to perform power hardware-in-the-loop testing using a reduced-scale experimental setup [157]. Subsequently, power adaptation elements have been employed to simplify the representation of complex systems such as railway systems with various cars [130]. For more details on the EMR formalism basics and the historical usage of the power adaptation elements, the reader is referred to Appendix III.
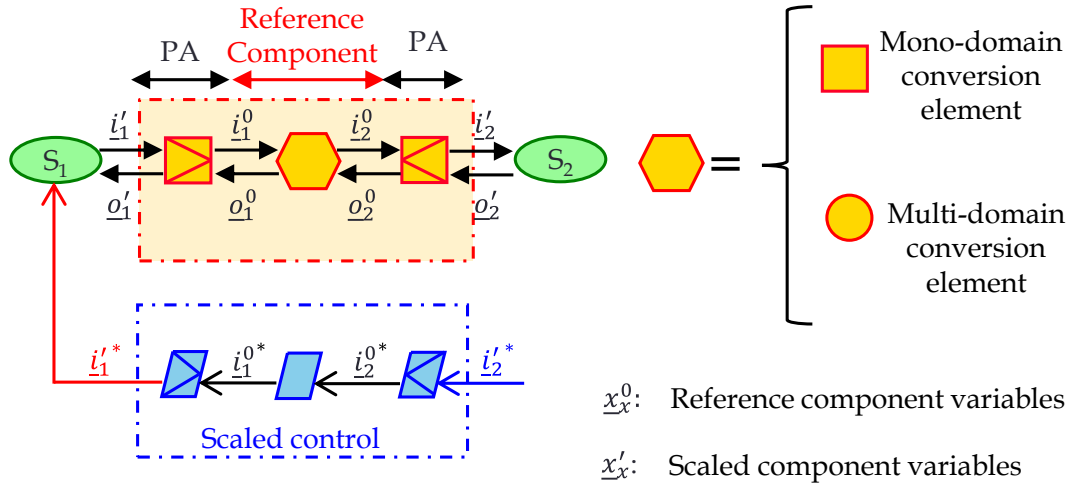
Fig. 24: EMR-based scaling laws of a scaled component, PA stands for Power Adaptation elements [156]

6.5.2 Components: experimental and numerical campaigns to validate scalable models

To establish and validate the scaling laws for components, a combination of numerical and experimental approaches will be employed as illustrated in Fig. 25. The methodology involves starting with a well-known design of a given component and subsequently applying the derived scaling laws. These laws will be derived using either analytical models of component design or data-driven approaches from experimental campaigns. Different scaling choices and assumptions will be studied. The accuracy of the scaling laws will be assessed by comparing them with physical or virtual scaled components. To this end, a dedicated high-speed test bench for gearbox testing is used to investigate the efficiency of various gearboxes with different power ratings and dimensions. The literature body on the scalability of electric machines demonstrates substantial and reliable research foundations. However, there is a notable knowledge gap in the power loss scaling of gearboxes, necessitating in-depth investigations through experimental campaigns. For these reasons, it is decided to allocate all available resources, to exclusively conduct intensive experimental testing on different gearbox specimens. Regarding electric machines, FEM will be used to support the development and validation of scaling laws. As far as voltage source inverters are concerned, data extracted from the datasheets of commercialized inverters will be used to validate the scaling laws.

6.5.3 Vehicles: e-axle sizing based on scalability and systemic approach

Once the different scaled models for components are validated and organized following the EMR methodology, the subsequent steps involve studying the interaction of the scaling model to form the desired scaled e-axle. For this aim, further organization is aimed by keeping only two power adaptations at the input and output of the reference system as shown in Fig. 26. In this way, models and control can be easily reused to simulate a whole range of powertrains with different specifications. Additionally, the impact of the scaling choices made at component-level will be assessed at system-level to investigate their impact on energy consumption.
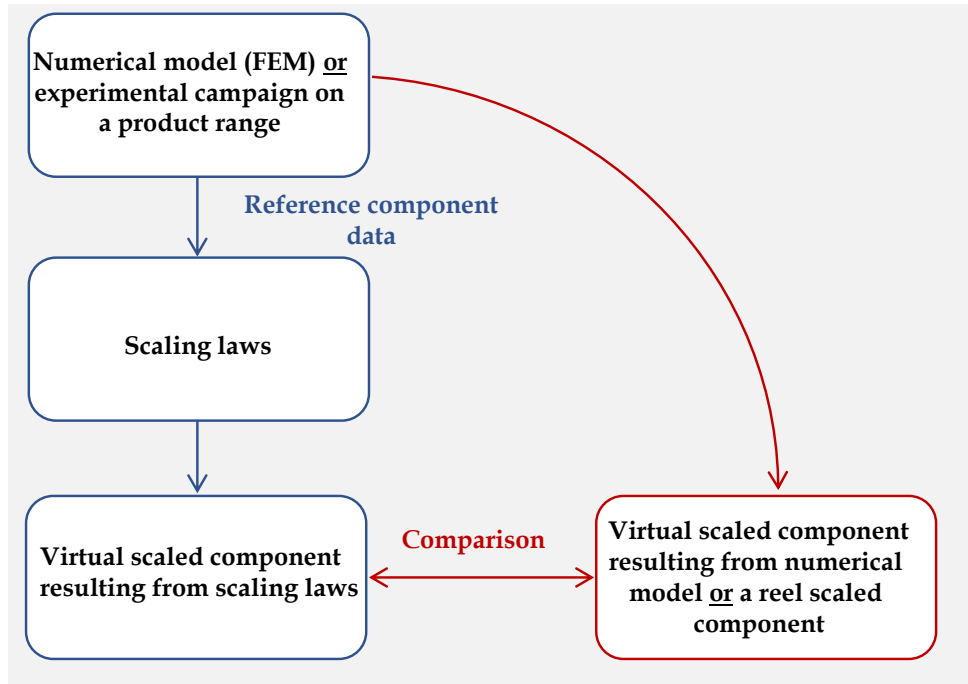
Fig. 25: Scaling approach for components
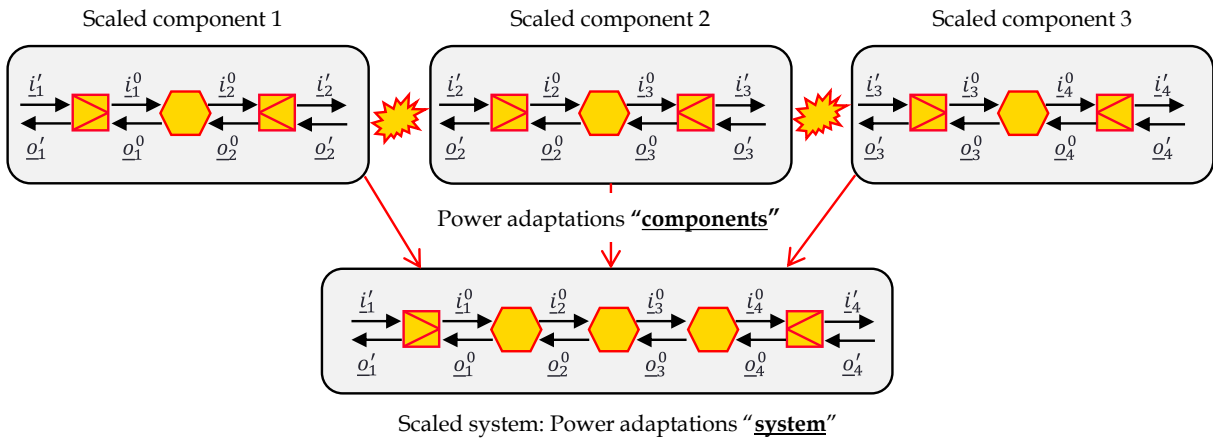
Fig. 26: EMR-based-scaling laws of a scaled system

It is worth noting that the work is organized following a top-down and bottom-up approach. The top-down approach implies employing the EMR-based scaling laws to organize both the component and vehicle axes. On the other hand, the bottom-up approach involves updating and refining the method from the investigation carried out at component and system levels. Following this organization, an overview of the dissertation outline is depicted in Fig. 27. Given that both the inverter and electrical machine are intrinsically connected, the set of which is commonly known as the electric drive system, Chapter II considers a comprehensive approach to address the scaling issue. The scaling of gearboxes is tackled in Chapter III. Chapter IV capitalizes on the scaling laws developed and discussed for the components in the previous chapter to approach the scaling of the e-axle at system-level.
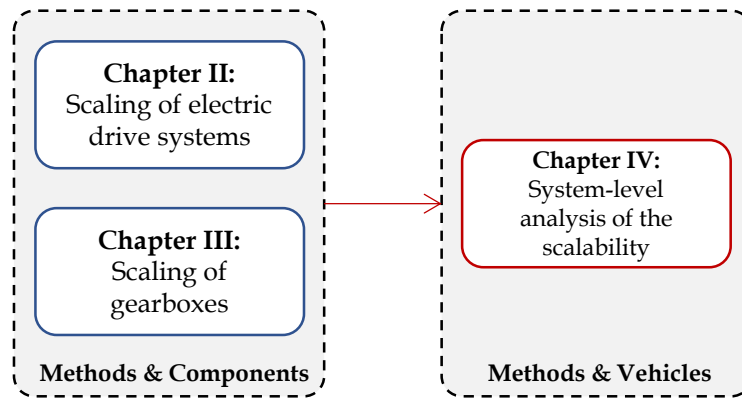
Fig. 27: Outline of the subsequent chapters of this Ph.D. thesis following the research organization

6.6 List of publications

What follows is an overview of the published papers within the time framework of this Ph.D. thesis, spanning from October 1, 2020 to September 30, 2023.

Articles in peer-reviewed international journals:

- **A. Aroua**, W. Lhomme, E. Redondo-Iglesias, and F. Verbelen, "Fuel saving potential of a long haul heavy duty vehicle equipped with an electrical variable transmission," *Applied Energy*, vol. 307, p. 118264, Feb. 2022, doi: 10.1016/j.apenergy.2021.118264. [IF: 11.2]

- **A. Aroua**, P. Defreyne, F. Verbelen, W. Lhomme, A. Bouscayrol, P. Sergeant, and K. Stockman "Power loss scaling laws of high-speed planetary reducers," *Mechanism and Machine Theory*, vol. 189, p. 105428, Nov. 2023, doi: 10.1016/j.mechmachtheory.2023.105428. [IF: 5.2]

- **A. Aroua**, W. Lhomme, F. Verbelen, M. N. Ibrahim, A. Bouscayrol, P. Sergeant, and K. Stockman "Impact of scaling laws of permanent magnet synchronous machines on the accuracy of energy consumption computation of electric vehicles," *eTransportation*, vol. 18, p. 100269, Oct. 2023, doi: 10.1016/j.etran.2023.100269. [IF: 11.9]

- **A. Aroua**, W. Lhomme, F. Verbelen, A. Bouscayrol, P. Sergeant, and K. Stockman, "Reliability of linear losses-to-power scaling method of electric drive systems", *IEEE Transactions on Vehicular Technology,* **accepted paper**

Articles in conference proceedings:

- F. Verbelen, W. Lhomme, **A. Aroua**, A. Bouscayrol, and P. Sergeant, "Scalable Electrical Variable Transmission model for HEV simulations using Energetic Macroscopic Representation," in *2020 IEEE Vehicle Power and Propulsion Conference (VPPC)*, Gijon, Spain: IEEE, Nov. 2020, pp. 1–6. doi: 10.1109/VPPC49601.2020.9330957.

- **A. Aroua**, W. Lhomme, F. Verbelen, A. Bouscayrol, and K. Stockman, "Inversion-based Control of Scaled PMSM for Battery Electric Vehicles," in *2021 IEEE Vehicle Power and Propulsion Conference (VPPC)*, Gijon, Spain: IEEE, Oct. 2021, pp. 1–6. doi: 10.1109/VPPC53923.2021.9699198.

- L. Ramirez, **A. Aroua**, P. Delarue, and W. Lhomme, "Linear Scaling Evaluation of Losses for Automotive Traction Voltage Source Inverters," in *2022 IEEE Vehicle Power and Propulsion Conference (VPPC)*, Merced, CA, USA: IEEE, Nov. 2022, pp. 1–6. doi: 10.1109/VPPC55846.2022.10003330.
- **A. Aroua**, W. Lhomme, F. Verbelen, A. Bouscayrol, P. Sergeant, and K. Stockman "Energetic Macroscopic Representation-based scaling laws of PMSM for electric vehicles simulations", in *2023 Electrical Engineering Symposium (SGE)*, Lille, France, July 2023
- **A. Aroua**, W. Lhomme, F. Verbelen, A. Bouscayrol, P. Sergeant, and K. Stockman, "Comparative Study on the Effect of PMSM Scaling Choices on Electric Vehicle Energy Consumption," **accepted paper** in the *2023 IEEE Vehicle Power and Propulsion Conference (VPPC)*, Milan, Italy: IEEE, Oct. 2023.

7 Conclusion

This chapter presents the motivation for this research work, which essentially revolves around the need to accelerate the lead time of electrified vehicles in response to stringent emission regulations. The current development phases and their associated methods have been thoroughly reviewed, showing a high complexity and particularly a high computational burden. This hinders their incorporation at system-level for investigating different solutions to develop electrified vehicles. Shortening the development time of electric axle systems, i.e. inverters, electric machines, and gearboxes is becoming an unequivocal market necessity. In this context, this research aims to develop a scaling methodology for electric axles for system-level investigations, contributing to a time reduction of the lead time. The major challenges and the organization of the work have been presented as well.

Chapter II

Comparative analysis of the effect of scaling methods on efficiency scaling of electric drive systems

1 Introduction

This chapter focuses on conducting a comparative analysis of the scaling laws of Electric Drive Systems (EDS) at component-level, intending to clarify their influence on the efficiency scaling of a reference EDS. As a reminder, the terminology EDS refers to the set of a voltage source inverter, an electric machine, and a control unit. This allows subsequently elucidating the impact of the scaling laws on energy consumption at system-level in Chapter IV. In this context, the literature review on scaling laws of EDS reveals an abundance of different scaling approaches that can be classified into two categories, based on the level at which the parameters are varied, namely component and system levels.

The literature, primarily focussing on system-level investigation, shows different scaling laws derived for different purposes, e.g. reduced-scale hardware-in-the-loop and the sizing of EDS. In the context of reduced-scale hardware-in-the-loop, the Buckingham π- theorem [158] is employed to derive scaling laws, that preserve dynamic similarity between a reference and scaled systems [159]. Moreover, the π- theorem finds applications in time-accelerated hardware-in-the-loop simulations, considering tests involving long-duration missions [160]. In [157], another scaling approach is proposed for reduced-scaled hardware-in-the-loop testing. The purpose of such a method is to test the real-time execution of control algorithms using a hardware setup. This is achieved by introducing scaling factors, defined as the ratio between the parameters of the reduced-scaled experimental setup and those of the full-scale system.

Another body of literature centered on electrified powertrain sizing employs different scaling methods, principally aimed at scaling the efficiency map of the entire EDS or one of its key components. This is exemplified by the Willans line, which is an affine representation relating the input and output powers of a power converter [16]. This method was initially introduced for internal combustion engines and later extended to electric machines by Rizzoni et

al. [161]. The Willans method is made scalable by normalizing all the torque and speed quantities involved. For electric machines, scalability is achieved by introducing the concept of mean effective pressure to describe the ability to produce mechanical work and tangential speed to describe the operating speed of the machine. Nevertheless, this method is only applied to scale electric machines and does not consider the voltage source inverter. For this reason, another set of literature utilizes linear losses-to-power scaling or simply linear scaling. This method gained widespread popularity in system-level investigations because of its simplicity and applicability to the early design stages due to its minimal input requirements [16]. Linear scaling does not need an extensive understanding of the reference EDS design. Instead, the method assumes that the total losses of a reference design can be linearly scaled according to the desired new power rating. This assumption applies to the power loss scaling of both voltage source inverters and electric machines. Given its ease of utilization and computational efficiency, the linear scaling method has been incorporated into optimization routines to evaluate the performance of EDS of varying power ratings in various transportation applications, ranging from light to heavy-duty vehicles. Examples can be found in literature on hybrid electric vehicles [25], [162], battery electric vehicles [163], [164], and fuel-cell electric vehicles [165], [166]. This method has been applied also in vehicle simulation packages, such as ADVISOR (ADvanced VehIcle SimulatOR) [167] and Quasi-Static Simulation (QSS) toolbox [168].

Notwithstanding the extensive use of linear scaling in literature, the assumptions of the method are highly questionable. This scaling method provides neither the geometrical parameters nor insights into the electromagnetic or electric parameters of the scaled machine and inverter. Most importantly, the assumption that the overall losses of EDS, including both inverter and machine, scale linearly with the new desired power rating is questionable. This raises a lot of concerns regarding the accuracy of the method in forecasting efficiency at component-level, and the trustworthiness of the method on energy consumption results at system-level. To date, there is limited evidence in literature demonstrating the reliability of the linear scaling method in terms of efficiency forecasting and its impact on energy consumption simulation results of vehicles, notwithstanding the extensive use of the method. One of the scarce references in literature [110] suggests that linear scaling might present optimistic results in terms of fuel consumption for hybrid electric vehicles considering scaled Permanent Magnet Synchronous Machines (PMSM) with low power ratings. However, no further explanation is provided to justify the last statement. Therefore, a central concern in this dissertation is whether the linear scaling method can yield satisfactory results for the scaling process at the early stages of the development of EDS, and whether more sophisticated scaling methods that delve into more component design details are required.

As concerns about the reliability of linear scaling of EDS emerged, alternative scaling methods have gained a surge in attention in recent research studies on system-level design. Regarding the scalability of electric machines, research studies are increasingly exhibiting a heightened interest in employing geometric scaling laws. This is demonstrated by recent research on the optimal sizing of electric machines using geometric scaling laws within the context of electric vehicles [20], [21], [138] and hybrid electric vehicles [142], [143]. Contrary to the linear scaling method, geometric scaling laws provide a way to gain insight into how the parameters, most importantly the losses, of the reference machine change by varying the macro-

geometric parameters, mainly the core length and diameters, combined with a rewinding scaling. The geometric scaling method is derived at component-level for design analysis for PMSM [28] and is extended afterward to dual rotors permanent magnet synchronous machines (commonly known as electrical variable transmissions) [30], as well as to induction machines [29]. In [169], the authors showed that geometric scaling laws for PMSM guarantee highly accurate results in terms of efficiency prediction of scaled machines across the possible operating points of the speed-torque plane. These have been validated with numerical campaigns using Finite Element Method (FEM) for upscaling and downscaling cases of a reference PMSM with torque scaling factors of 1.64 and 0.64, respectively. The comparison between the geometric scaling laws and FEM reveals an average percentage discrepancy in terms of efficiency significantly below 1%. It is worth noting that the scaling laws, mentioned in the last aforementioned references, are derived based on a choice that assumes the flux density and saturation levels in the reference and scaled machines are preserved during the scaling process. This scaling choice is denoted as $B \sim 1$ in the remainder. The motivation behind this choice is driven by the ability to reuse the magnetic field solutions of the reference design for the scaled one.

In general terms, a scaling choice, in the context of electric machines, refers to the decision made regarding the consistency of one or multiple parameters during the scaling process. Consequently, the derivation of the scaling laws based on geometric changes is impacted by the scaling choice. A comprehensive review of the literature on electric machine scaling at component-level reveals alternative scaling choices in earlier works. For example, scaling laws based on a choice that maintains the temperature rise in the winding between the reference and scaled machines are derived in [23], [170] for induction machines, as well as for PMSM in [171], [102], [172], [173]. This choice is referred to as $\Theta \sim 1$ in the sequel. The latter references justify the choice $\Theta \sim 1$ by underlying the importance of maintaining a balance between the temperature rise and the maximal temperature of the insulating materials. This criterion is critical for the lifespan of the machine and is not considered while opting for the choice $B \sim 1$. In [174], [175], a hybrid choice, combining the choices $B \sim 1$ and $\Theta \sim 1$, is reported. This choice ensures that the magnetic saturation and temperature limits are not exceeded. Another scaling choice, which consists in conserving the current density is postulated in [103]. However, this choice overlooks the fact that the current density should be adjusted according to the power rating to deal with the cooling challenges. Additionally, keeping the current density constant would violate the flux density constraint, as explained in the case of PMSM [176]. It is worth mentioning that the use of the previously mentioned scaling choices is confined to design analysis at component-level and not extended to system-level, as in the case of the choice $B \sim 1$.

Regarding the scaling of the voltage source inverter, few studies have been published on this research topic. One of the contributions is a data-driven model, which has been derived based on the parameters extracted from datasheets of a group of IGBT inverters [177]. This scalable data-driven model has been incorporated later at system-level simulations [21]. Another data-driven scalable model has been proposed in [178] based on experimental campaigns on Si- and SiC components of traction inverters. The findings of the last study suggest that the switching loss linearly scales with the chip area of the semiconductor components. In contrast, the conduction loss demonstrates a scaling relationship that is inversely proportional to the

chip area. The same outcomes have been reported for IGBT-based power electronic converters in reference [179]. The last statement is comparable, to some extent, with the assumption of linear losses-to-power scaling, where the overall losses are scaled according to the power scaling factor [26]. In another approach, general efficiency scaling laws are derived in [180] for power electronics converters, by adopting a choice of a constant power density and heating of different scaled converters. Other scaling laws have been proposed in [181] for GaN-on-Si HEMT, SiC MOSFET, and Si MOSFET to scale the on-resistance, and the charge-equivalent capacitance as a function of the voltage rating.

The literature review shows a plethora of scaling laws for electric machines and relatively few for inverters. However, a comprehensive comparison between these scaling laws is still lacking, making it challenging to decide which scaling method should be selected when dealing with the system-level design. Of significant importance, each component of the EDS is scaled with a specific scaling method, highlighting the absence of a common scaling method for the entire EDS, except for linear scaling. Another important point is that the input requirements of the scaling process can be limited, in some cases, to one global efficiency map of the reference EDS. This is particularly applicable to experimental efficiency maps of EDS, without separate details on the loss distribution of each component. Consequently, implementing some scaling methods becomes challenging because they necessitate a detailed model of the component such as a FEM model, including the distribution of each loss component. In contrast, the linear scaling method holds an advantage in this point, as it only requires an efficiency or loss map to conduct the scaling process. Hence, a pivotal concern addressed in this chapter revolves around the reliability of linear losses-to-power scaling of EDS.

The objective in this chapter is to make a comprehensive comparison between the different scaling laws proposed in literature, for electric machines and voltage source inverters. Particular emphasis is paid to comparing the outcomes of the linear scaling method with those resulting from alternative scaling laws of inverters and electric machines that delve more profoundly into the component design. Moreover, this chapter proposes a derivation of the conditions that result in a reliable linear losses-to-power scaling case of the EDS. This is achieved by a new organization of the scalable model of EDS following the Energetic Macroscopic Representation (EMR) rules. Through the new model organization using EMR, criteria that result in a linear scaling case of the component are not only highlighted but also the reuse of the reference model of EDS becomes possible. This aspect stands out as one of the novelties put forth in this chapter. Note that the scope of this comparison is confined to PMSM and IGBT-based inverters, for the reasons exposed in Section 6.2 in Chapter I. This is justified by the extensive utilization of the aforementioned technologies in the current automotive industry. Furthermore, it is important to mention that this chapter is not aimed at deriving new scaling laws for the EDS, on the other hand, the focus is placed on the comparison itself at component-level. The contribution of this work is summarized as follows:

1) Assessment of the reliability of linear losses-to-power scaling for PMSM, and IGBT-based inverters, in terms of efficiency scaling.
2) Derivation of EMR-based scaling laws of EDS to enhance the reusability of the reference model of EDS, facilitating the implementation of scalability at system-level

simulation. This is attained by a new model structuration of the scaled EDS following the EMR rules.

3) Derivation of the conditions, e.g. geometric parameters of the machine, scaling of the electric parameters of the inverter, etc., that result in a losses-to-power scaling. This is achieved by the new organization of the scaling laws using EMR.

4) Assessment of the feasibility of the derived conditions of the linear scaling method.

This chapter is organized as follows. Section 2 presents the theoretical background of the linear losses-to-power scaling method of the EDS. A comparison of the scaling laws based on different choices for PMSM and the EMR-based scaling laws of PMSM is presented in Section 3. Section 4 is dedicated to the comparison of the scaling laws of IGBT-based inverters and the presentation of their corresponding EMR-based scaling laws.

2   Linear scaling method of electric drive systems

The input requirement of the linear scaling method is an efficiency or loss map of a reference EDS. The efficiency map of an EDS η_{ED} consists of the product of the efficiency maps of an inverter η_{INV} and an electric machine η_{EM}, as depicted in Fig. 28. This implies that linear scaling is employed for both the inverter and electric machine throughout the scaling process. Note that an efficiency map of an EDS is established for a given control law of each component, and a given temperature. The last two parameters are assumed consistent when applying the linear scaling method.
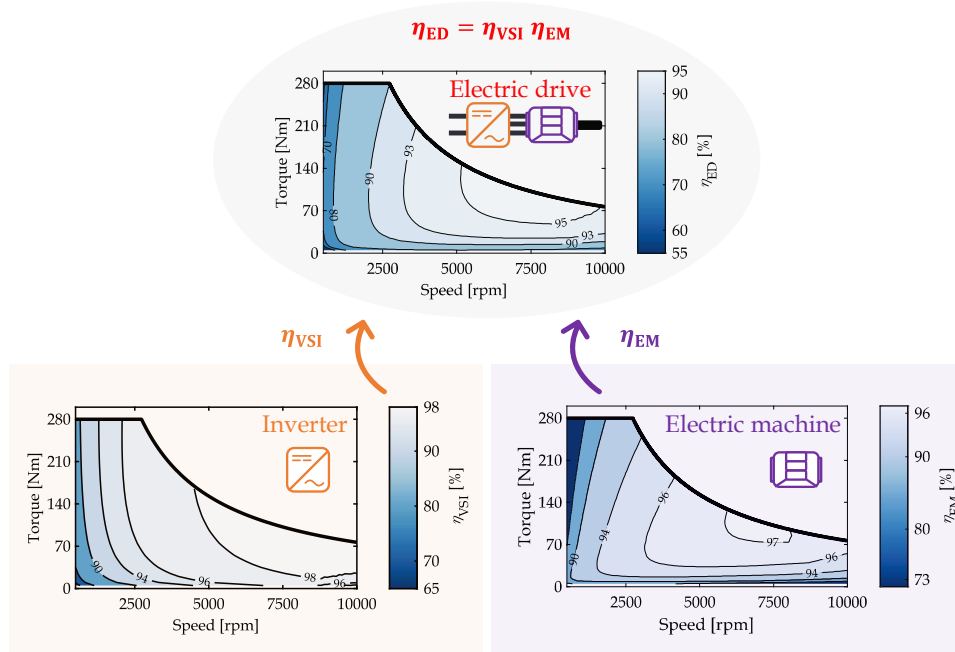
Fig. 28: Illustration of the efficiency map of an electric drive system

The linear scaling of efficiency maps is performed using a power scaling factor K_P that represents the ratio between the peak mechanical power of the scaled EDS $P'_{m,max}$ and the reference one $P^0_{m,max}$ (1). Thereby, the torque axis of a reference efficiency map is stretched or narrowed using a torque scaling factor K_T, while conserving the same base speed Ω_b and

maximal speed Ω_{max} as illustrated in Fig. 29. The torque scaling factor K_{T} is defined as the ratio between the maximum torque of the reference EDS T_{max}^0 and the new desired one T_{max}' (1). Given that the base speed Ω_{b} is maintained, the torque scaling factor K_{T} will be equal to the power scaling factor K_{P}, as indicated in (1).

$$\begin{cases} K_{\mathrm{P}} &= \dfrac{P'_{\mathrm{m,max}}}{P^0_{\mathrm{m,max}}} \\[2mm] K_{\mathrm{T}} &= \dfrac{T'_{\mathrm{max}}}{T^0_{\mathrm{max}}} \\[2mm] K_{\mathrm{T}} &= K_{\mathrm{P}} \qquad \text{with } \Omega'_{\mathrm{b}} = \Omega^0_{\mathrm{b}} \end{cases} \tag{1}$$
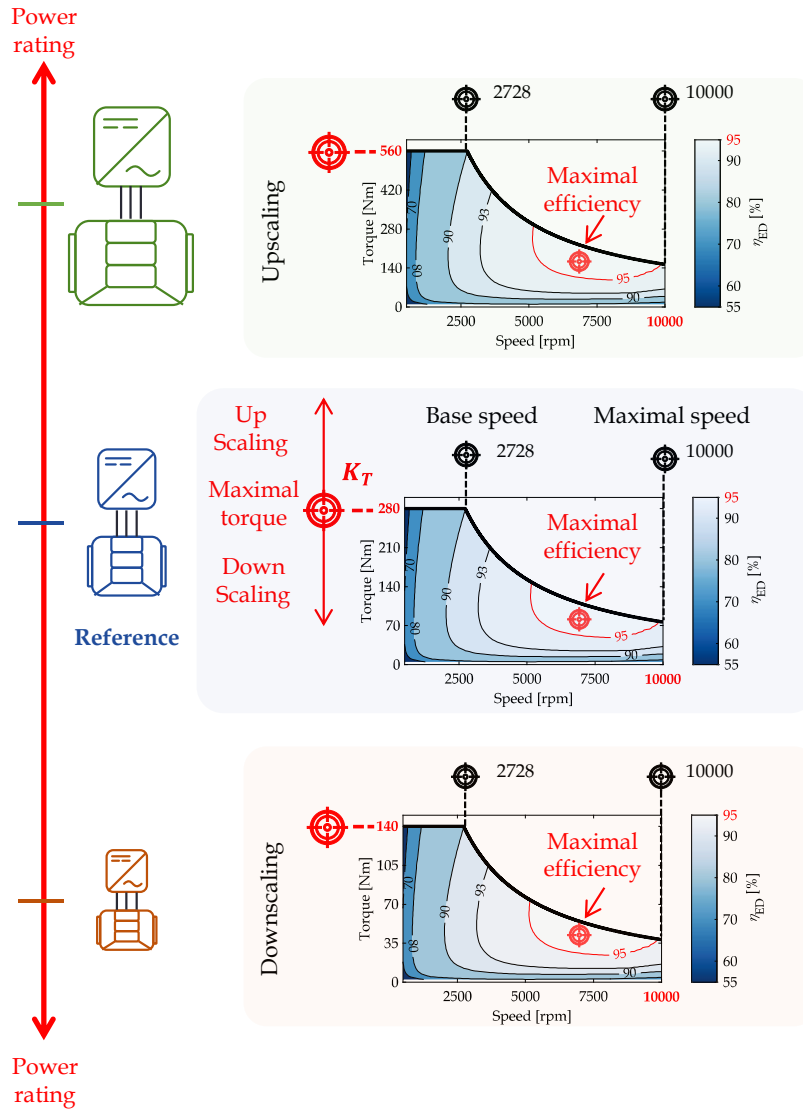
Fig. 29: Linear scaling illustration of electric drive system

It is worth noting that the apostrophe ', in (1), is used to indicate the parameters of the scaled component, whereas the superscript ^{0} is used to denote the parameters of the reference component throughout the rest of this chapter. According to the linear scaling method, the different loss components of the reference PMSM, namely the copper P_{cu}^0, iron P_{fer}^0, permanent magnet P_{PM}^0, and mechanical P_{mech}^0 losses, scale as a function of K_{T} (2). Similarly, the losses of

the reference inverter, i.e. the conduction P_{cond}^0 and switching losses P_{sw}^0, scale following (3), assuming that the switching frequency is unchanged. For this reason, this method is referred as to linear scaling. Note that the superscript LS in the last aforementioned equations, (2), and (3), stands for Linear Scaling.

$$\begin{cases} P_{cu}^{LS} & = & K_T P_{cu}^0 \\ P_{fer}^{LS} & = & K_T \, P_{fer}^0 \\ P_{PM}^{LS} & = & K_T P_{PM}^0 \\ P_{mech}^{LS} & = & K_T P_{mech}^0 \end{cases} \tag{2}$$

$$\begin{cases} P_{cond}^{LS} & = & K_T P_{cond}^0 \\ P_{sw}^{LS} & = & K_T \, P_{sw}^0 \end{cases} \tag{3}$$

Consequently, the efficiency at an operating point (T', Ω) of the scaled EDS corresponds to the efficiency of the reference EDS at the operating point (T^0, Ω). This results in the same maximal efficiency between the reference and scaled EDS (see red marker in Fig. 29). In [110], it is postulated that linear scaling is optimistic for downscaled machines and pessimistic for upscaled machines. To address this issue, correction factors (a_{LS} and b_{LS} in (4)) are proposed in [182] to obtain a more realistic maximal efficiency for scaled machines with different power ratings. These correction factors are derived from manufacturers' catalogs of PMSM by performing a regression law that translates the evolvement of maximal efficiency as a function of the power. The new maximal efficiency of the scaled machine can be calculated by applying a linear variation as indicated in (4). It is important to emphasize that these correction factors are solely applied to the maximal efficiency, and do not cover the other efficiencies present in the torque-speed plane. This limitation is due to the lack of data regarding the efficiency maps in the last aforementioned reference.

$$\eta'_{max} = \eta^0_{max}(a_{LS} + b_{LS} \, K_T) \tag{4}$$

Despite the widespread use of linear scaling, the absence of geometrical information on the scaled machines and details regarding the scaled parameters and the distribution of the different loss components of the EDS is recognized as one of the major weaknesses of the method. Most importantly, all losses are considered to be scaled with the same factor, which is highly questionable due to the non-linearity of losses. To assess the reliability of linear scaling, the subsequent sections delve into the scaling of the electric machine and inverter using scaling methods that provide a greater level of design details for these components. Fig. 30 presents an overview of the scaling laws considered for the comparative analysis. The assessment is conducted separately for each component to identify the individual differences in terms of efficiency scaling. For the electric machine, the linear scaling is compared against the geometric scaling laws, with the latter serving as a reference because of its high fidelity in computing efficiency. Concerning the inverter, linear scaling, data-driven scaling laws, and scaling laws based on the choice that preserves the power density and the temperature rise are compared against an efficiency benchmarking study using the well-known models available in literature to compute the efficiency of power electronic converters.
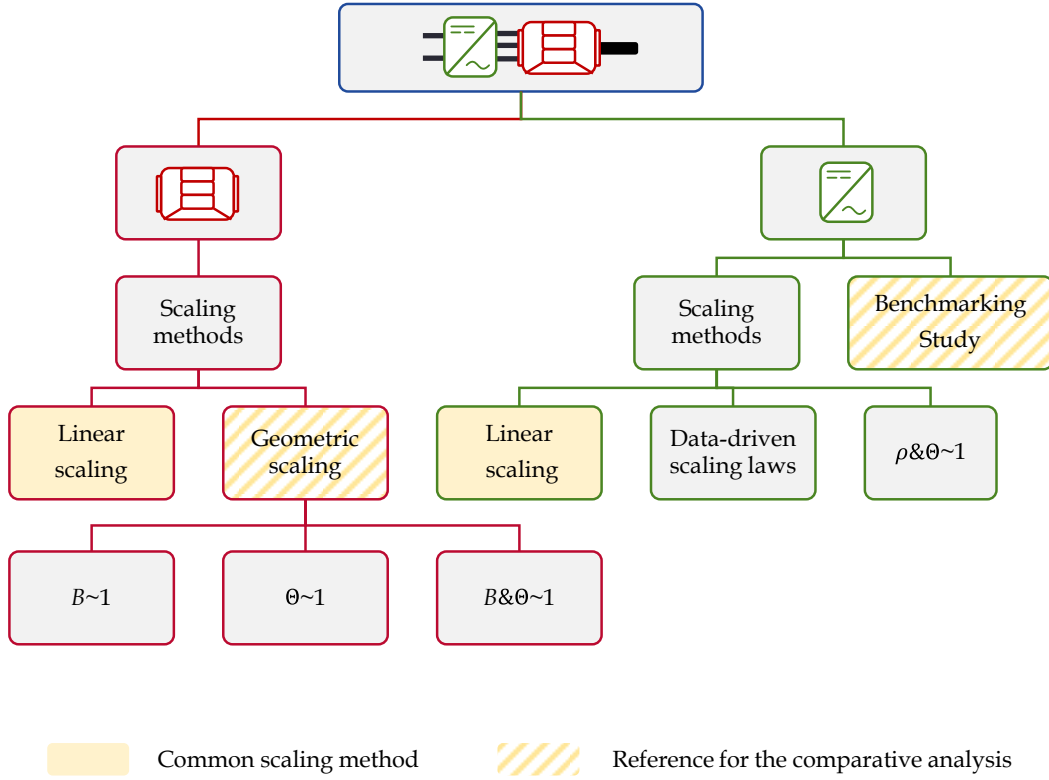
Fig. 30: Overview of the scaling methods considered for the comparison

3   Geometric scaling laws of permanent magnet synchronous machines

This section focuses on a comparison of the impact of the geometric scaling laws based on different scaling choices on efficiency as compared to the linear losses-to-power scaling. As indicated in Fig. 30, three choices are retained, which consist of preserving the magnetic flux density $B\sim1$, the temperature rise in the windings $\Theta\sim1$, and the hybrid choice $B\&\Theta\sim1$. As a reminder, a scaling choice refers to the decision made regarding the consistency of one or multiple parameters during the scaling process. In the following sections, a scaling factor, denoted as K_x for a given parameter x, is defined as the ratio between the parameters in the framework of the scaled x' and reference machines x^0 (5).

$$K_x = \frac{x'}{x^0} \tag{5}$$

3.1   Geometric scaling laws based on different scaling choices

3.1.1   Geometric scaling procedures

For any scaling choice, the geometric scaling procedures involve a proportional change of the dimensions of the reference machine in the axial and radial directions, alongside a third scaling procedure for the winding as illustrated in Fig. 31. The materials and technology

(winding type, slot-fill factor, etc.), and the number of pole pairs N_p remain unchanged during the scaling process.
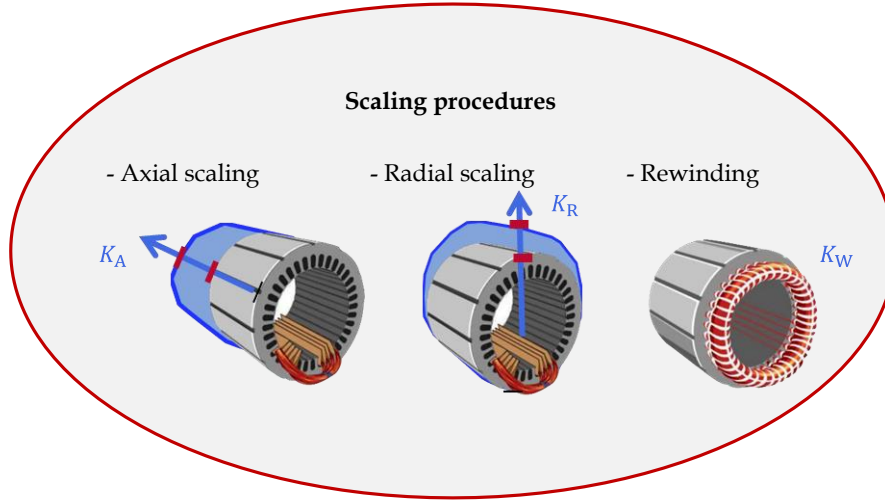
Fig. 31: Scaling procedures of electric machines

The axial scaling procedure consists of altering the core length of the machine l^0 using an axial scaling factor K_A, while preserving the lamination cross-section (6). This procedure supposes adding or removing laminations from the stator and rotor stacks. The lamination thickness is unchanged, which conforms with the manufacturing process.

$$K_A = \frac{l'}{l^0} \tag{6}$$

The radial scaling procedure consists of proportionally altering the geometrical parameters of the cross-section with a radial scaling factor K_R. During this procedure, it is assumed that the angles and aspect ratios are preserved. This scaling factor is therefore equal to the ratio of the outer stator diameters of the scaled D' and reference D^0 machines, respectively (7). Based on the axial and radial scaling procedures, the scaling relationships for the area, volume, and mass can be derived as mentioned in (8).

$$K_R = \frac{D'}{D^0} \tag{7}$$

$$
\begin{aligned}
\text{Area} &\propto K_A K_R \\
\text{Volume} &\propto K_A K_R^2 \\
\text{Mass} &\propto K_A K_R^2
\end{aligned}
\tag{8}
$$

The rewinding scaling procedure consists of adjusting the machine terminal voltage to the predefined DC bus voltage rating through a rewinding scaling factor K_W. This scaling procedure considers a change in the number of turns per coil N_{turns}^0 and the number of parallel paths a_p^0 of the reference machine. As postulated in [28], the current density, the cross-section geometry, and the slot fill factor are assumed unchanged during the rewinding scaling.

$$K_W = \frac{a_p^0}{a_p'} \frac{N_{turns}'}{N_{turns}^0} \tag{9}$$

3.1.2 Conditions of each geometric scaling choice

Table 2 presents an overview of the scaling conditions associated with the different scaling choices examined in this study.

Table 2: Scaling conditions and consequences associated with each geometric scaling choice on the magnetic, electric, and thermal loading

Scaling factors	$B\sim 1$	$\Theta\sim 1$	$B\&\Theta\sim 1$
Magnetic field density K_B [-]	1	$1/\sqrt{K_R}$	1
Temperature rise K_Θ [-]	$1/K_R$	1	≈ 1
Current density K_J [-]	$1/K_R$	$1/\sqrt{K_R}$	$1/\sqrt{K_R}$
Electric load K_{eload} [-]	1	$\sqrt{K_R}$	$\sqrt{K_R}$
Current K_i^{PMSM} [-]	$\dfrac{K_R}{K_W}$	$\dfrac{K_R^{1.5}}{K_W}$	$\dfrac{K_R^{1.5}}{K_W}$
Flux linkage K_ψ [-]	$K_A K_R K_W$	$K_A K_R^{0.5} K_W$	$K_A K_R K_W$

The scaling choice $B\sim 1$ assumes that the magnetic field density B in all active parts is preserved during the scaling process. In other words, the magnetic fields in the scaled machine are the exact images of the magnetic fields present in the reference machine, as described in [28], [183]. To satisfy this choice, the current density J needs to be scaled by a factor inversely proportional to K_R as indicated in Table 2. This condition can be found by examining Poisson's equation, in which the same magnetic permeability μ is kept constant in the corresponding points of the scaled geometry in the space coordinates (x,y,z) to deal with the saturation challenges. Consequently, the electric load A is kept consistent during the scaling process.

The scaling choice $\Theta\sim 1$ assumes that the growth in losses follows the growth of the cooling surface which evolves proportionally with $K_A K_R$ during the scaling process [102], [171], [172]. Thus, this choice ensures the preservation of the temperature rise in the winding Θ. This choice is often referred to as preserving the losses-to-cooling surface of the machine. To comply with this requirement references [102], [172] postulate that the current density J and the magnetic field density B need to be altered inversely proportional to the square root of the radial scaling factor K_R, as shown in Table 2. The conditions for J and B can be found by analyzing the evolution of the predominant losses, namely the copper loss in the core part $P_{cu,co}$, and iron P_{fer} losses, according to the machine size. The last aforementioned loss components should align with the growth of the cooling surface growth, resulting in the relationships of J and B as described in (10), and (11). The contribution of the other loss components is considered marginal as compared to the copper and iron losses in this reasoning. Note that Appendix IV.1.2 provides more details on the derivation of these conditions.

$$P'_{cu,co} = K_A K_R P^0_{cu,co} \Rightarrow J' = \frac{1}{\sqrt{K_R}} J^0 \tag{10}$$

$$P'_{\text{fer}} = K_A K_R P^0_{\text{fer}} \Rightarrow B' = \frac{1}{\sqrt{K_R}} B^0 \tag{11}$$

The hybrid choice B&Θ~1 represents a compromise between the two scaling choices discussed earlier [174], [175]. To achieve this choice, the magnetic field density B is conserved during the scaling process, similar to the choice B~1. To ensures a comparable thermal situation, although not completely identical, between the reference and scaled machines, the current density J scales similarly to the choice Θ~1. Therefore, the electric load A follows the scaling law, as given in Table 2. Note that an identical thermal situation cannot be achieved as the loss scaling for the iron loss, in the case of the hybrid choice does not follow the surface growth. This will be discussed in the next section, focussing on the loss scaling.

As a result of the magnetic and electric loading scaling conditions, the current and flux linkages scale differently depending on the scaling choice, as shown in Table 2.

3.1.3 Discussion on the scaling choices of geometric scaling laws

This section presents a comprehensive discussion of the scaling laws, centered on four criteria: torque, magnetic loading, thermal loading, and loss scaling.

3.1.3.1 Torque scaling

At a constant speed, the electromagnetic torque T_{EM} of a PMSM evolves as a function of the tangential stress σ_{Ftan}, diameter D_r, and the active length l_r of the rotor.

$$T_{\text{EM}} \propto \sigma_{\text{Ftan}} D_r^2 l_r \tag{12}$$

Referring to Table 2, the scaling of the electric A and magnetic loading B dictates the scaling factors of the tangential stress σ_{Ftan}, indicated in Table 3. It can be readily observed from the aforementioned table, that adopting the scaling choices B~1 and Θ~1 ensures the preservation of the same tangential stress. Thereby, this enables maintaining material within the scaled machine series. Knowing the tangential stress scaling, the torque scaling for the previously mentioned choices follows the volume growth $K_A K_R^2$, as shown in Table 3. The hybrid choice B&Θ~1 exhibits a higher torque scaling with $K_A K_R^{2.5}$ as compared to $K_A K_R^2$, for the same volume growth. Therefore, the torque scaling, using the hybrid choice, is increased faster than the volume (8). However, this comes at the expense of increasing the tangential stress σ_{Ftan} with a factor of $K_R^{0.5}$. The values of σ_{Ftan} depend on the chosen material and cooling technique, and are typically constrained by a maximal value. The maximal tangential stress values related to the tractive electric machines for automotive applications are scarce in literature, however, it is possible to find typical values for industrial machines in [102]. Due to the constraint of tangential stress, the torque scaling law using the hybrid choice cannot always be achieved. In [175], it is postulated that the torque scaling law for the hybrid choice can be amended as described in (13). The electric load is capped to a maximal value A_{max} to avoid the risk of magnet demagnetization, particularly when applying a large K_R. The calculation for determining this value is given in (14), following what is reported in [184].

$$\begin{cases} T'_{\text{EM}} &= K_A K_R^{2.5} T_{\text{EM}}^0 & \text{if } A \leq A_{\max} \\ T'_{\text{EM}} &= K_A K_R^2 T_{\text{EM}}^0 & \text{if } A > A_{\max} \end{cases} \tag{13}$$

$$A_{\max} = \sqrt{\frac{\alpha_{\text{th}} \Delta\Theta_{\max}}{k_{ew} \rho_{\text{cond}}}} \sqrt{\frac{V_{\text{cu}}}{S_{\text{th}}}} \tag{14}$$

In (14), α_{th} is the surface heat exchange coefficient, $\Delta\Theta_{\max}$ is the maximal temperature rise, k_{ew} is a coefficient added to consider the impact of the end-winding part, ρ_{cond} is the resistivity of the conductors, V_{cu} is the total copper volume, and S_{th} is the heat exchange surface with the cooling fluid.

Table 3: Torque scaling based on each scaling choice

Scaling factors	$B \sim 1$	$\Theta \sim 1$	$B \& \Theta \sim 1$
Tangential stress K_σ [-]	1	1	$K_R^{0.5}$
Torque scaling factor K_T^{PMSM} [-]	$K_A K_R^2$	$K_A K_R^2$	$K_A K_R^{2.5}$

3.1.3.2 Magnetic loading

The choice $B \sim 1$ and the hybrid choices assume that the field solutions are kept unchanged during the scaling process (Table 2). This is a pragmatic choice because it allows reusing the finite element simulation solutions without any concerns related to magnetic saturation and demagnetizing fields. Consequently, the pre-design process of scaled machines can be expedited. Regarding the choice of $\Theta \sim 1$, the air gap flux density B_g needs to be scaled by a factor inversely proportional to the root square of K_R (Table 2). This becomes critical when considering small radial scaling factors K_R, which results in high values of B_g. The last statement holds until saturation in the iron becomes significant, and therefore B_g can no longer be increased. Additionally, the scaling of B_g is bounded by the magnet residual flux density B_r. On the other hand, a very large K_R will lead to inefficient iron material use. Therefore, a more thorough analysis to set boundaries for the radial scaling procedure is required when employing the choice $\Theta \sim 1$.

The sizing boundary should keep the maximal flux density below a well-defined maximum value to avoid saturation problems. However, this will be highly dependent on the reference design, in which different electrical sheets can be used. For example, FeSe and CoFe materials exhibit typical maximum values of flux density of 1.7 T and 2.2 T, respectively [185]. Fig. 32.a depicts a brute force search to study the sensitivity of the magnetic field density B scaling. The scaled values of the field density are described as a function of different combinations of the radial scaling factor K_R and the peak value of B in the reference machine, irrespective of the area where the maximum value is obtained. Next, a constraint for B is added, consisting of a tolerance interval from 1.2 T to 2.2 T. Fig. 32.b shows that based on the maximal value of the magnetic flux density in the reference machine, a feasible range for K_R falls between 0.6 and 1.75.
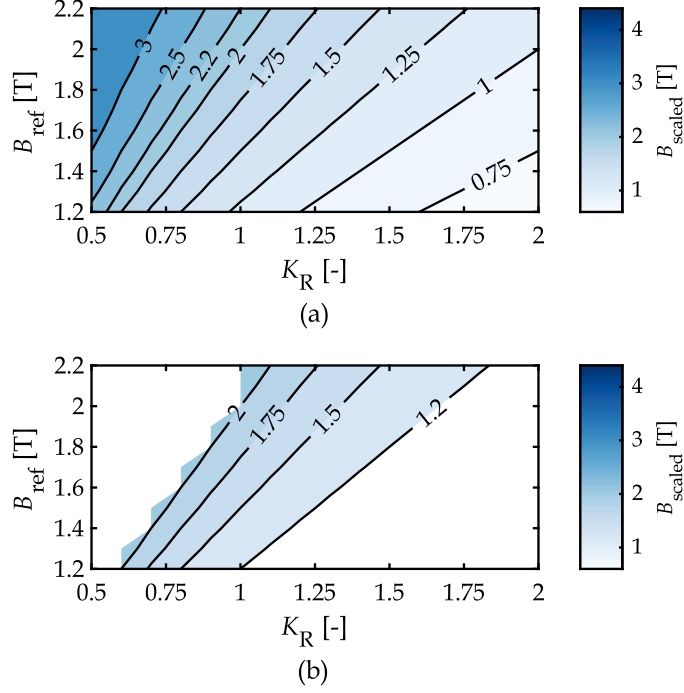
Fig. 32: Scaling of the peak value of the magnetic field density B using the scaling choice $\theta \sim 1$ as a function of the radial scaling factor K_R and the original magnetic field density in the reference machine B_{ref}: (a) search space without constraints, (b) search space with imposed constraints.

To derive the condition depicted in Table 2, allowing the scaling of the air gap field density B_g, a simplified magnet equivalent circuit is used. This latter allows the expression of B_g, as shown in (15), in terms of the magnet residual flux density B_r, the magnet relative permeability μ_{rm}, the length of magnets l_m, and the air gap length g. Note that the latter is derived based on 1D reluctance equation, neglecting fringing fluxes at the magnet edges and along the circumference of the machine in the axial direction.

$$B_g \cong \frac{1}{1 + \mu_{rm}\dfrac{g}{l_m}} B_r \tag{15}$$

From (15), it can be readily observed that there are two options to achieve the condition of the scaling of B_g. Both options involve the introduction of an additional scaling factor, either for the air gap g or the radial dimensions of the magnet l_m. In other words, during the radial scaling procedure, all the parameters of the cross-section scale proportionally with K_r, except for either the air gap or the magnet length. One of these two dimensions needs to be scaled with a scaling factor K_g or K_m that can be expressed as follows:

$$\begin{cases} K_g = \dfrac{K_r^{1.5}(l_m + g) - K_r l_m}{g} & \text{if air gap scaling} \\ K_m = \dfrac{K_r g}{l_m(K_r^{0.5} - 1) + K_r^{0.5} g} & \text{if magnet length scaling} \end{cases} \tag{16}$$

Typically, the ratio l_m/g is within the range of 3 to 5 [186]. As the value of B_g approaches B_r, the aforementioned scaling procedures become unfeasible due to convergence. As a result,

either the magnet length or the air gap length tends towards infinity. Additionally, it is worth noting that if the scaling factor K_m is chosen, the scaling of permanent magnet loss requires amendment. Consequently, it is convenient to say that the choice $\Theta \sim 1$ presents more challenges to use in the pre-design phases, because of the magnetic field density scaling.

3.1.3.3 Thermal loading

Regarding the choice $B \sim 1$, consistent use of materials can be achieved as both electrical load A and flux density B remain unchanged during the scaling process. Nevertheless, the growth of the losses is not proportional to the cooling surface, leading to a different thermal situation between the reference and scaled machines. Scaling in the radial direction with a small factor leads to an increase in the temperature rise in the windings with a factor inversely proportional to K_R (Table 2). The thermal scaling of PMSM has been the subject of recent literature, wherein diverse thermal scaling laws have been proposed based on the choice $B \sim 1$ [187]–[190]. These thermal scaling laws describe the temperature changes in different parts of the machine as a function of the scaling procedures employed. Further development has been made in [191], wherein the authors have proposed scaling laws for the water-cooling jacket subsystem. It is worth emphasizing that the thermal scaling falls out of the scope of this thesis. This is because the assessment of the energy consumption is generally conducted using an efficiency map established at a nominal temperature, following the current state of the art on system-level investigations [16]. This assumption stems from the fact that the assessment of the energy consumption is conducted employing standardized driving cycles, characterized by durations shorter than the time required for the temperature of the machine to rise. This is because, under such driving cycles, the electric machine seldom operates at conditions requesting maximal power. Additionally, tractive electric machines are equipped with a cooling system designed to regulate temperature. For a more comprehensive examination of how thermal constraints influence the sizing of electric machines in the context of electrified vehicles, the reader is referred to [192].

Regarding the choice $\Theta \sim 1$, it can guarantee an equivalent thermal situation between the reference and the scaled machine. This is because the scaling of the predominant losses, namely the copper and iron losses, follows the surface growth, as indicated in Table 2. By using the hybrid choice, a similar thermal condition can be achieved, although not identical. This is due to the difference in scaling the iron loss caused by maintaining the magnetic field density unchanged during the scaling process, which is highlighted in the next section.

3.1.3.4 Losses scaling

Table 4 describes the scaling of the individual losses as a function of the geometric scaling laws, alongside the scaling factors for the resistances at the core and end winding parts of the machine. By consulting Table 4, it is apparent that the rewinding scaling factor K_W does not intervene in the scaling laws of the losses. However, the scaling of certain parameters, including resistances, current, and flux linkages, are dependent on this latter scaling factor K_W. A complete derivation of these scaling laws can be found in Appendix IV.1.

Table 4: Overview of the scaling factors for each loss component of PMSM for each scaling choice

Scaling factors	$B\sim 1$	$\Theta\sim 1$	$B\&\Theta\sim 1$
Core resistance K_R^{co} [$-$]	$\dfrac{K_W^2 K_A}{K_R^2}$	$\dfrac{K_W^2 K_A}{K_R^2}$	$\dfrac{K_W^2 K_A}{K_R^2}$
Copper loss (active part) K_{cu}^{co} [-]	K_A	$K_A K_R$	$K_A K_R$
End-winding resistance K_R^{ew} [$-$]	$\dfrac{K_W^2}{K_R}$	$\dfrac{K_W^2}{K_R}$	$\dfrac{K_W^2}{K_R}$
Copper loss (end winding part) K_{cu}^{ew} [-]	K_R	K_R^2	K_R^2
Iron loss K_{fer} [-]	$K_A K_R^2$	$K_A K_R$	$K_A K_R^2$
Permanent magnet loss K_{PM} [-]	$K_A K_R^4$	$K_A K_R^3$	$K_A K_R^4$
Bearing loss K_{br} [-]	$K_A K_R^2$	$K_A K_R^2$	$K_A K_R^2$
Windage loss K_{win} [-]	$K_A K_R^3$	$K_A K_R^3$	$K_A K_R^3$

To compare the loss scaling for each choice, illustrative cases are presented herein focusing on torque upscaling with a factor of 2, and torque downscaling with a factor of 0.5. In this sense, Fig. 33 shows the different loss scaling factors, K_{cu}^{co}, K_{cu}^{ew}, K_{fer}, and K_{PM} which correspond to the scaling of copper loss in the core and end-winding, iron loss, and permanent magnet loss, respectively. These scaling factors are shown as a function of the radial scaling factor K_R. For each value of K_R, the corresponding axial scaling factor K_A is computed based on the desired torque scaling factor K_T, following the scaling law indicated in Table 3. The mechanical losses are not included in this analysis because they scale in the same way using the three geometric scaling choices, as indicated in Table 4 for the scaling of windage and bearing losses. This is because the aforementioned loss components are independent of the magnetic and electric load scaling.

The initial observation derived from Fig. 33 reveals that when K_R is equal to 1, all the scaling choices yield equivalent power loss scaling. By consulting Fig. 33.a and b, it is apparent that maintaining the choice $\Theta\sim 1$ results in lower copper losses compared to the two other choices. Nevertheless, this holds solely for K_R values less than 1. Conversely, when K_R values exceed 1, the choice $B\sim 1$ leads to greater reduction of copper losses. Note that the hybrid choice and $\Theta\sim 1$ yield the same copper loss scaling in the end-winding part of the machine, as they share the same power loss scaling factor $\left(\propto K_R^2\right)$. Concerning the iron loss, the choice $\Theta\sim 1$ results in higher iron loss, when K_R is less than 1, as compared to the other choices. This power loss scaling trend is reversed when K_R exceeds 1, resulting in lower iron loss. The scaling of the latter power loss when opting for the choice $B\sim 1$, remain constant, regardless the scaling factors. This is because the scaling of the iron loss for the last aforementioned choice follows the volume and torque scaling $\left(\propto K_A K_R^2\right)$, as indicated in Table 2. Concerning the permanent magnet power loss, they are higher for the choice $B\sim 1$ as compared to the other choices, when using a radial scaling factor K_R values above 1, and vice versa. Irrespective to the values of K_R, the hybrid choice offers a balanced compromise in terms of power loss scaling as compared to the other two choices. Additionally, it is interesting to note that the power scaling laws remain

the same if an axial procedure is solely performed without any radial scaling procedure, regardless of the scaling choice. To summarize, Table 5 presents the scaling choices that result in a lower loss for each loss component, depending on the chosen value of K_R. The analysis of the losses is further elaborated in Section 3.3, where a comparison of the efficiency is presented for the entire torque speed of the scaled machines.
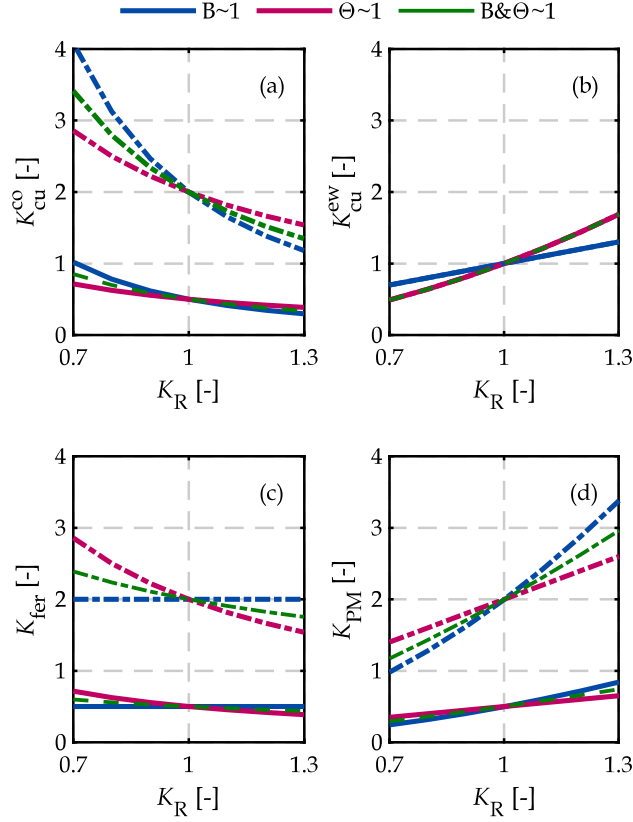
Fig. 33: Assessment of the power loss scaling factors using different scaling choices for a downscaling scenario with a torque scaling of 0.5 (solid lines for the two first choices and dashed line for the hybrid choice) and upscaling scenario with a torque scaling of 2 (dash-dotted lines).

Table 5: The scaling choices corresponding to a lower loss for each loss component of the scaled machine

	$K_R < 1$	$K_R > 1$
P_{cu}^{co}	$\Theta \sim 1$	$B \sim 1$
P_{cu}^{ew}	$\Theta \sim 1$	$B \sim 1$
P_{fer}	$B \sim 1$	$\Theta \sim 1$
P_{PM}	$B \sim 1$	$\Theta \sim 1$

3.2 Numerical validation of the scaling laws based on the finite element method

In this section, a numerical validation using FEM of the geometric scaling laws based on different choices is presented. For this aim, the workflow, shown in Fig. 34, is adopted. Due to the high number of scaled designs that can be investigated, the study is confined to illustrative cases of geometric scaling factors, as indicated in Table 6. Different scaled designs have been considered to demonstrate the application of the scaling laws, for the geometric choices $B \sim 1$

and Θ ~1. As for the hybrid choice, the same scaling factors as the choice B~1 have been applied for the sake of simplicity and synthesis. No rewinding scaling is herein applied (K_W = 1). These scaling factors are selected to examine examples of upscaling and downscaling cases. Regarding the choice Θ~1, a choice is made to scale the air gap following (16). It is worth noting that the section is not intended to exhaustively examine and discuss different scaled designs. Ultimately, the section is aimed to illustrate the trustworthiness and applicability of the scaling laws. For more details, the reader is referred to [28], where a thoroughly discussed numerical validation of the choice B~1 using different geometric scaling factors is reported. This section can be considered as a continuation of the last study by proposing a numerical validation for the other scaling choices under investigation in this work. This is because, literature centered on the scaling of PMSM does not demonstrate numerical validation of the scaling choice Θ ~1, and B&Θ~1. The scope of this numerical validation is centered on electromagnetic parameters, namely torque, flux linkages, iron loss, and permanent magnet losses. No thermal validation is carried out as part of this work.
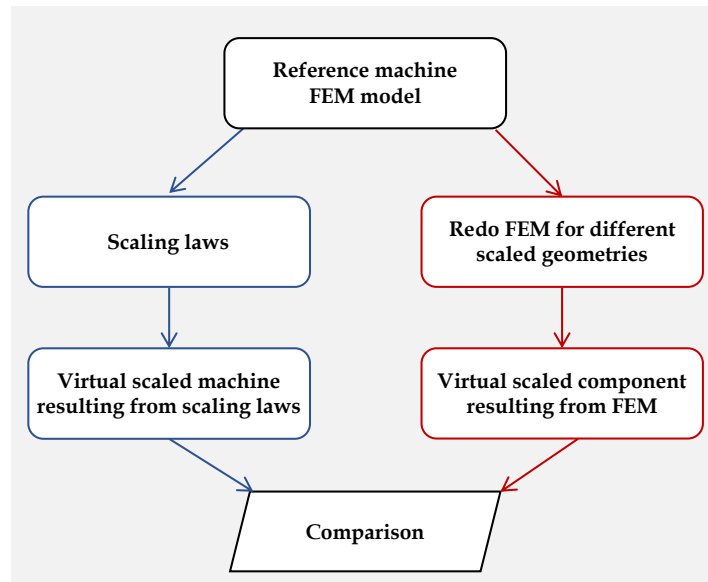
Fig. 34: Adopted workflow for the numerical validation

Table 6: Scaling factors involved in the numerical validation

	Scaling choice [-]	Axial scaling factor K_A [-]	Radial scaling factor K_R [-]	Torque scaling factor K_T [-]
Downscaling	B~1	0.78	0.80	0.50
	Θ~1	0.41	1.10	0.50
	B&Θ~1	0.78	0.80	0.45
Upscaling	B~1	1.40	1.20	2
	Θ~1	1.65	1.10	2
	B&Θ~1	1.40	1.20	2.20

3.2.1 Presentation of the reference machine

The reference machine used in this study is a traction interior PMSM, with a maximal power of 80 kW, a maximal torque of 280 Nm, and a base speed of 2728 rpm. The design of the

machine is similar to the 2012 Nissan Leaf traction machine [193]. The main geometrical parameters of the machine are presented in Appendix IV.6, based on the data published in [194]. The geometry of the machine is implemented and simulated using Ansys Maxwell in 2D transient mode.

3.2.2 Numerical validation of the upscaling case

A comparison between the outcomes of FEM and the scaling laws is discussed in this section for the upscaling cases. The section starts with examining the outcomes of the scaling choices based on the choices $B\sim1$ and $B\&\Theta\sim1$. The results for the choice $\Theta\sim1$ are addressed in a subsequent step, as they result from a distinct scaled design featuring a different air gap in comparison to the scaled design defined using the first two mentioned scaling choices.

Fig. 35 shows a comparison between the outcomes of the scaling laws using the choice for $B\sim1$ and $B\&\Theta\sim1$ choices and FEM. By consulting the figure, it can be seen that the results of the scaling laws for the considered choice are the same as FEM in terms of torque, flux linkages, and iron loss scaling. Differences in terms of the permanent magnet loss in Fig. 35.e are observed. This is mainly due to the difference in terms of the model formulation that has been used to derive the scaling law and the model incorporated in the software. Due to the low contribution of the previously-mentioned loss component, the difference in terms of the scaling will not have a significant impact on the efficiency.
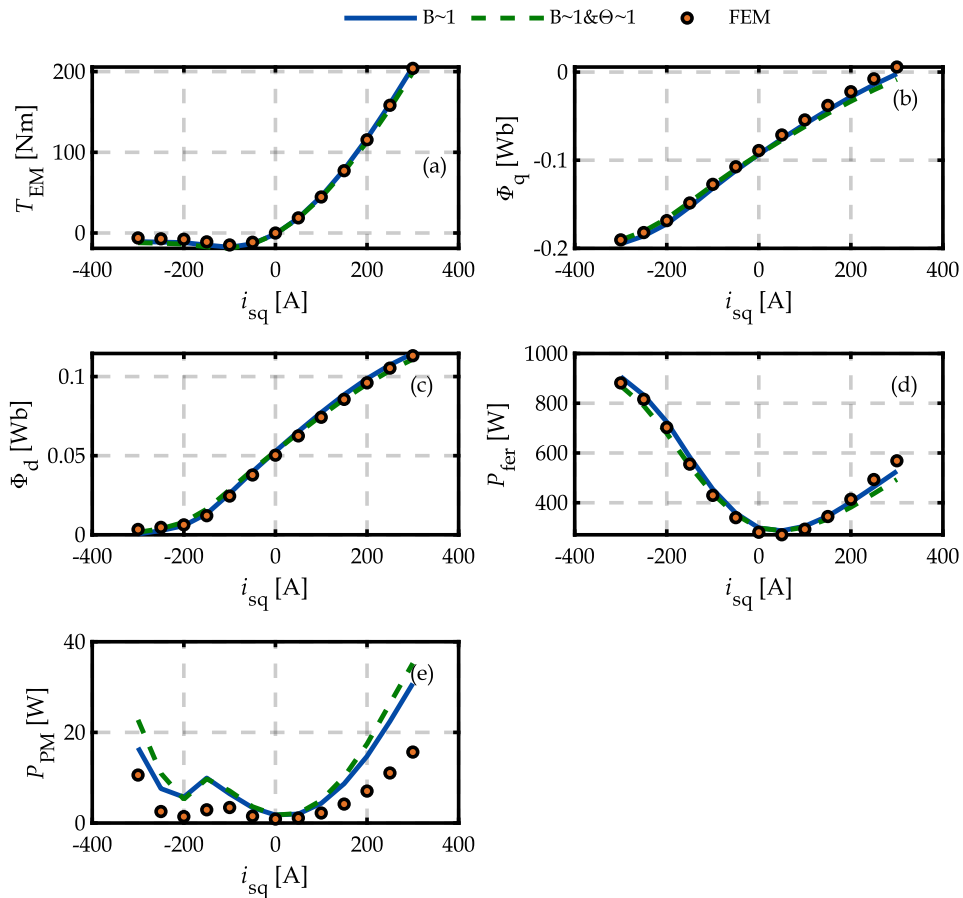
Fig. 35: Validation of the upscaling case considering the choice $B\sim1$, and $B\&\Theta\sim1$ for a current $i_{sd} = 0$

Fig. 36 depicts the comparison between the scaling laws based on the choice $\Theta\sim1$ and FEM. Similarly, the results of the scaling laws are close to those of FEM, except for the permanent magnet loss scaling.
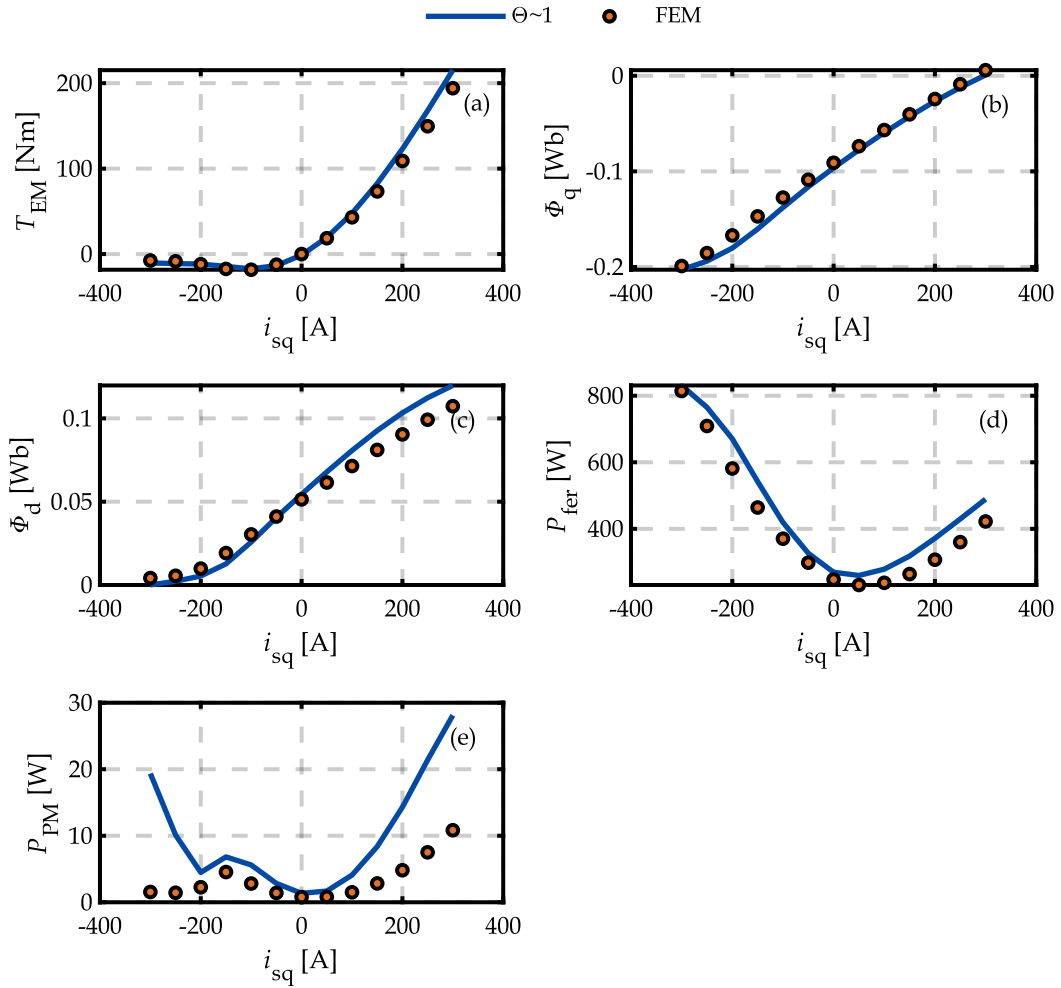
Fig. 36: Validation of the upscaling case considering the choice $\Theta\sim1$ for a current $i_{sd} = 0$

3.2.3 Numerical validation of the downscaling case

The comparison results for the downscaling case are reported in this section for the choices $B\sim1$, and $B\&\Theta\sim1$ in Fig. 37, and the choice $\Theta\sim1$ in Fig. 38. Similar to the upscaling case, the scaling demonstrates a good match with FEM.
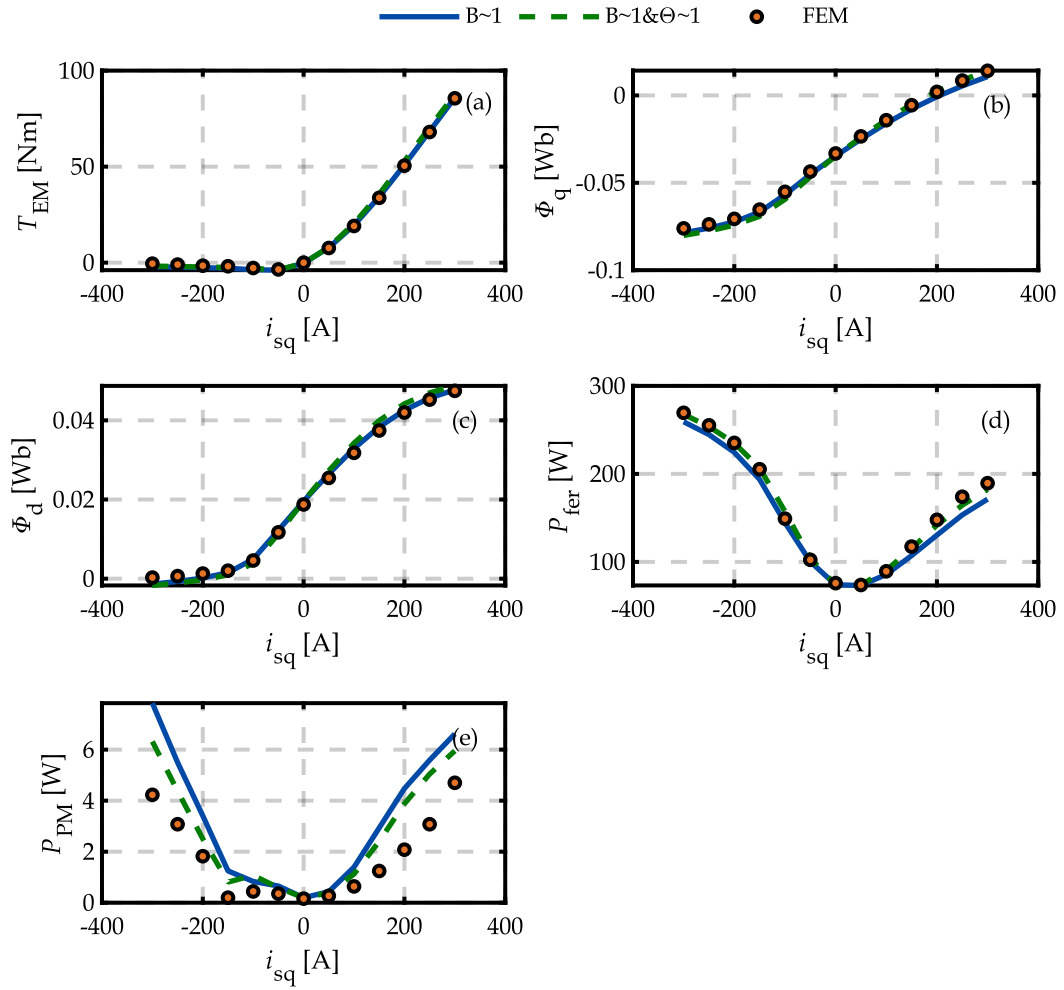
Fig. 37: Validation of the downscaling case considering the choice $B{\sim}1$, and $B\&\theta{\sim}1$ for a current $i_{sd} = 0$
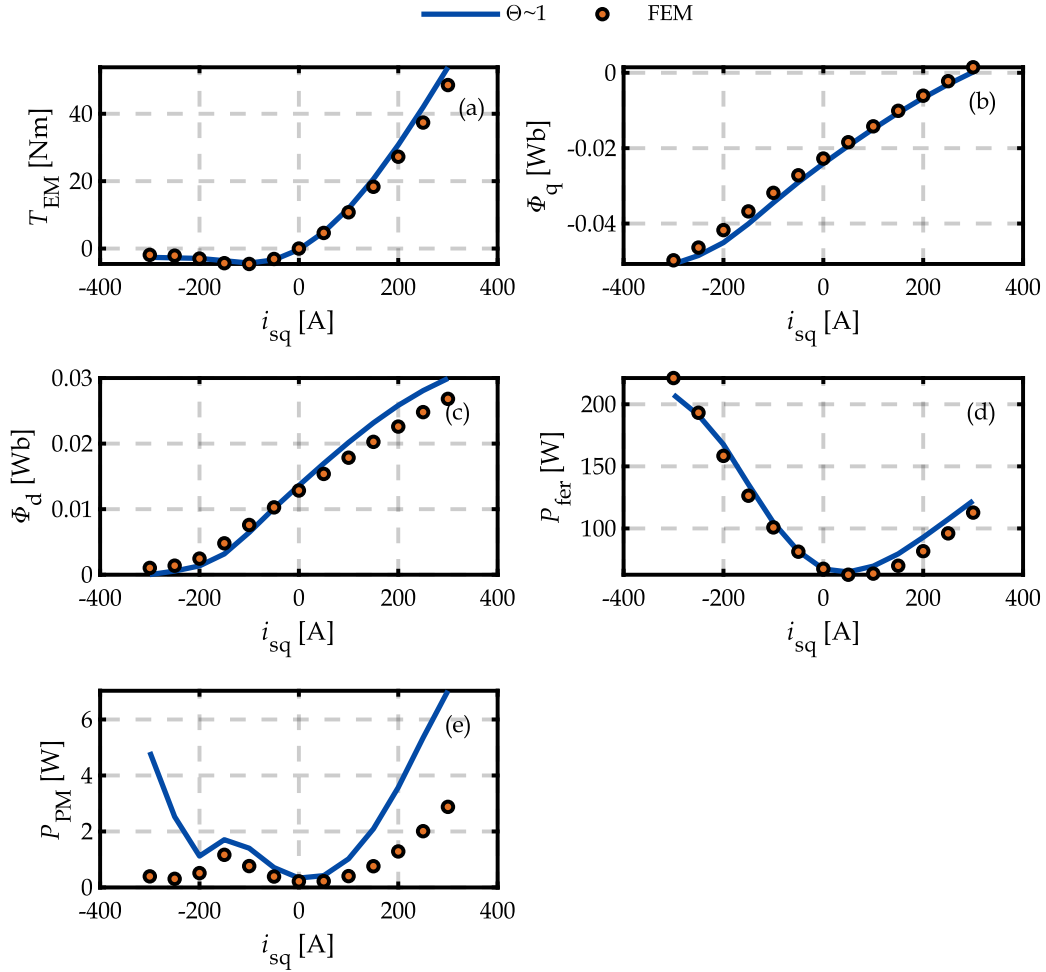
Fig. 38: Validation of the downscaling case considering the choice $\theta \sim 1$ for a current $i_{sd} = 0$

3.3 Comparison of linear losses-to-power scaling law versus geometric scaling laws

Following a thorough discussion and validation of the geometric scaling laws, this section aims to compare the efficiency map scaling of a reference machine using linear scaling and geometric scaling laws. For this aim, the efficiency of the reference machine, presented in Section 3.2.1, is initially benchmarked using FEM across the operating points in the torque-speed plane, as depicted in Fig. 39.a. Note that the Maximum Torque Per Ampere (MTPA) control paradigm is used for establishing the efficiency map [95]. The comparison between the computed efficiency map and the experimental one exhibits a good match as shown in Fig. 39.b.

In the following sections, the efficiency map of the reference design is subjected to upscaling with a torque scaling factor K_T of 2 and downscaled with a factor of 0.5. These torque scaling factors are selected as illustrative cases to conduct a comprehensive comparison between linear scaling and the other scaling choices for upscaling and downscaling cases. For this comparison, all scaled designs, established using geometric scaling laws, share the same base speed as the reference machine. This is necessary to ensure a fair comparison since linear scaling maintains the base speed throughout the scaling process. Correspondingly, the

rewinding scaling factor K_W is defined to preserve the same base speed. For simplicity reasons, non-integer values of K_W are herein allowed.
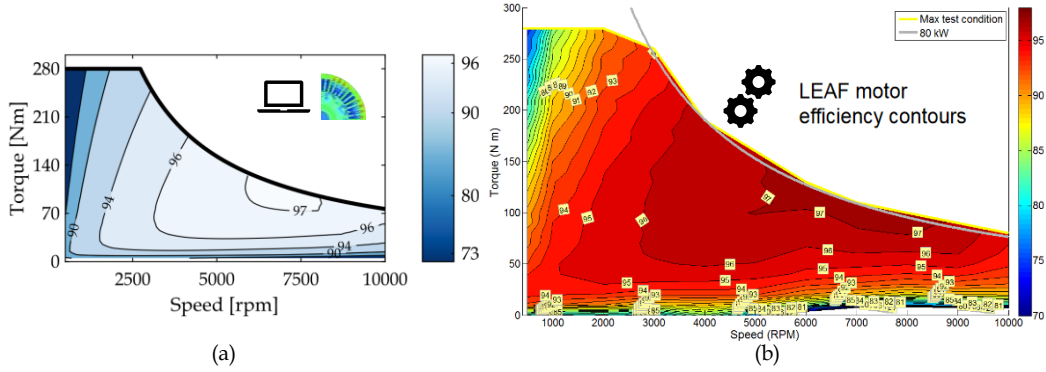
Fig. 39: Efficiency map of the reference electrical machine in [%] in the torque-speed plane: (a) map established using finite element analysis; (b) map built using experimental tests [38].

3.3.1 Upscaling case

To demonstrate the difference between linear scaling and geometric scaling laws regarding efficiency map scaling for upscaling cases, an illustrative case is initially presented. The scaling factors for this case are presented in Table 7.

Table 7: Scaling factors for the upscaling case

	K_T	K_A	K_R	K_W	K_{cu}^{co}	K_{cu}^{ew}	K_{fer}	K_{PM}
Linear scaling	2	$\emptyset$	$\emptyset$	$\emptyset$	2	2	2	2
$B{\sim}1$	2	1.39	1.20	0.60	1.39	1.20	2	2.88
$\Theta{\sim}1$	2	1.39	1.20	0.66	1.67	1.44	1.67	2.40
$B\&\Theta{\sim}1$	2	1.27	1.20	0.66	1.52	1.44	1.82	2.63

The results of the efficiency map scaling are presented in Fig. 40. By consulting Fig. 40. a-d, it is evident that the area of maximal efficiency (97%) is broader for the three choices of geometric scaling than for linear scaling. This confirms that the linear scaling is pessimistic in terms of efficiency estimation for larger machines. The second column of Fig. 40 shows the difference in terms of efficiency Δ_η between the results obtained with linear scaling and each choice of geometric scaling laws. Negative values of Δ_η indicate that linear scaling underestimates the efficiency as compared to geometric scaling and vice versa. The most conspicuous observation that emerges from these figures is that the region with low speed and high torque, where the copper losses are predominant, exhibits the largest difference between the scaling choices. This discrepancy is particularly noticeable in Fig. 40.e, where the maximal absolute value of Δ_η reaches 7.7%, when comparing linear scaling with the choice $B{\sim}1$. This substantial difference can be attributed to the large difference in the copper losses scaling factors between the two aforementioned scaling choices, as indicated in Table 7.
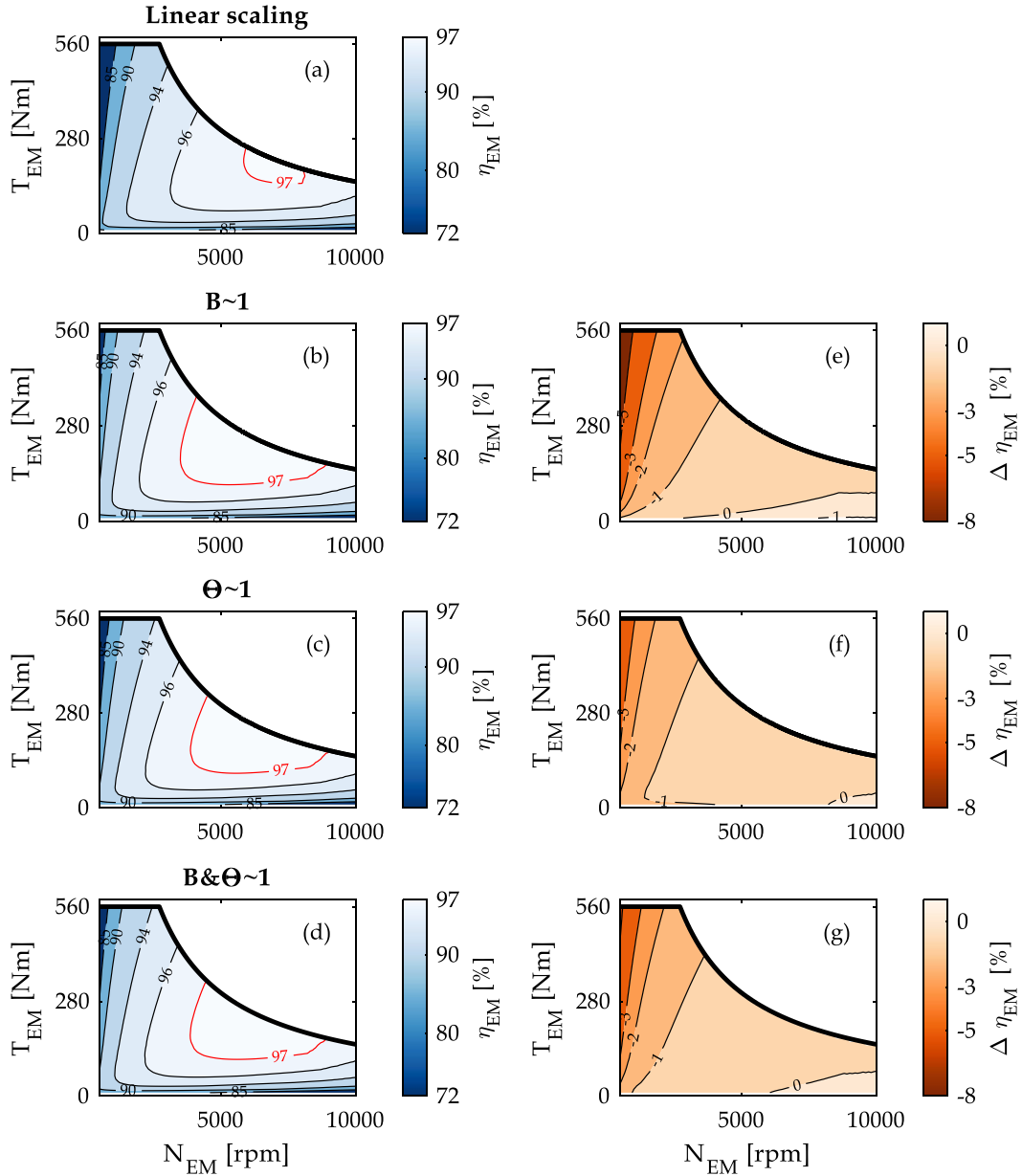
Fig. 40: Efficiency maps η_{EM} in [%] in the torque-speed plane using linear and geometric scaling laws for an upscaling case with a torque scaling factor of 2. The second column represents the efficiency difference Δ_η in [%] between linear and each choice of geometric scaling laws. Negative values for Δ_η mean that linear scaling underestimates the efficiency as compared to geometric scaling and vice versa.

Concerning the remaining choices, the maximal difference in terms of efficiency Δ_η is comparatively lower. For the choice $\Theta\sim1$, the maximal value of Δ_η reaches 4.7%, whereas, for the hybrid choice, it amounts to 5.5%. Interestingly, the difference between linear scaling and the scaling choices decreases at high-speed regions, where the iron losses are dominant. In certain areas of the map, the difference cancels out. This is because the scaling factor for the iron loss of the geometric scaling laws is close to the linear scaling one, as shown in Table 7. It is worth mentioning that Appendix IV.4 includes a quantification of the difference between linear scaling and the scaling choices for each power loss component across the torque-speed plane.

3.3.2 Downscaling case

Similar to what has been done in the previous section for the upscaling case, a downscaling case of the reference machine with a torque scaling factor of 0.5 is herein presented.

Table 8: Scaling factors for the downscaling case

	K_T	K_A	K_R	K_W	K_{cu}^{co}	K_{cu}^{ew}	K_{fer}	K_{PM}
Linear scaling	0.50	$\emptyset$	$\emptyset$	$\emptyset$	0.50	0.50	0.50	0.50
$B{\sim}1$	0.50	0.78	0.8	1.60	0.78	0.80	0.50	0.32
$\Theta{\sim}1$	0.50	0.78	0.8	1.43	0.63	0.64	0.63	0.40
$B\&\Theta{\sim}1$	0.50	0.87	0.8	1.43	0.70	0.64	0.56	0.36

By examining Fig. 41, the findings reveal that linear scaling resulted in a more efficient machine design than those obtained by the different choices of geometric scaling laws. The maximal efficiency of the machine is 97% using linear scaling, against 96% obtained with geometric scaling. This substantiates the statements made in Section 2, confirming that linear scaling is optimistic in terms of efficiency estimation for small power rating machines. For further consideration of this issue, Fig. 41.e-f show the difference in efficiency Δ_η [%] between the scaling choices, considering linear scaling as a reference. Note that a positive value of Δ_η means that the linear scaling result in a more efficient operating point than geometric scaling laws and vice versa. Similar to the outcomes observed in the upscaling case, the regions characterized by low-speed and high-torque demonstrate the largest discrepancy among the scaling choices. This efficiency disparity can be as high as 10% when comparing linear scaling with the geometric scaling laws based on the choice $B{\sim}1$. The scaling choice $\Theta{\sim}1$ demonstrates comparable results with the linear scaling, with a maximal value of Δ_η approximately equal to 4%. Once more, this observation is confined to regions characterized by low speed and high torque values. Although the large differences observed in the aforementioned regions, it should be noted that these latter regions encounter infrequent usage in the context of automotive applications. These regions are mainly engaged during acceleration phases. This detail will be further discussed in Chapter IV when addressing the system-level investigations. Additionally, similar to what was observed in the upscaling case, the values of Δ_η diminishes at high speed regions for all three comparison cases.

Note that the current analysis on the comparison between linear losses-to-power scaling law and geometric scaling laws is expanded in Appendix IV.5 with a sensitivity analysis, including distinct geometries and different torque scaling factors.
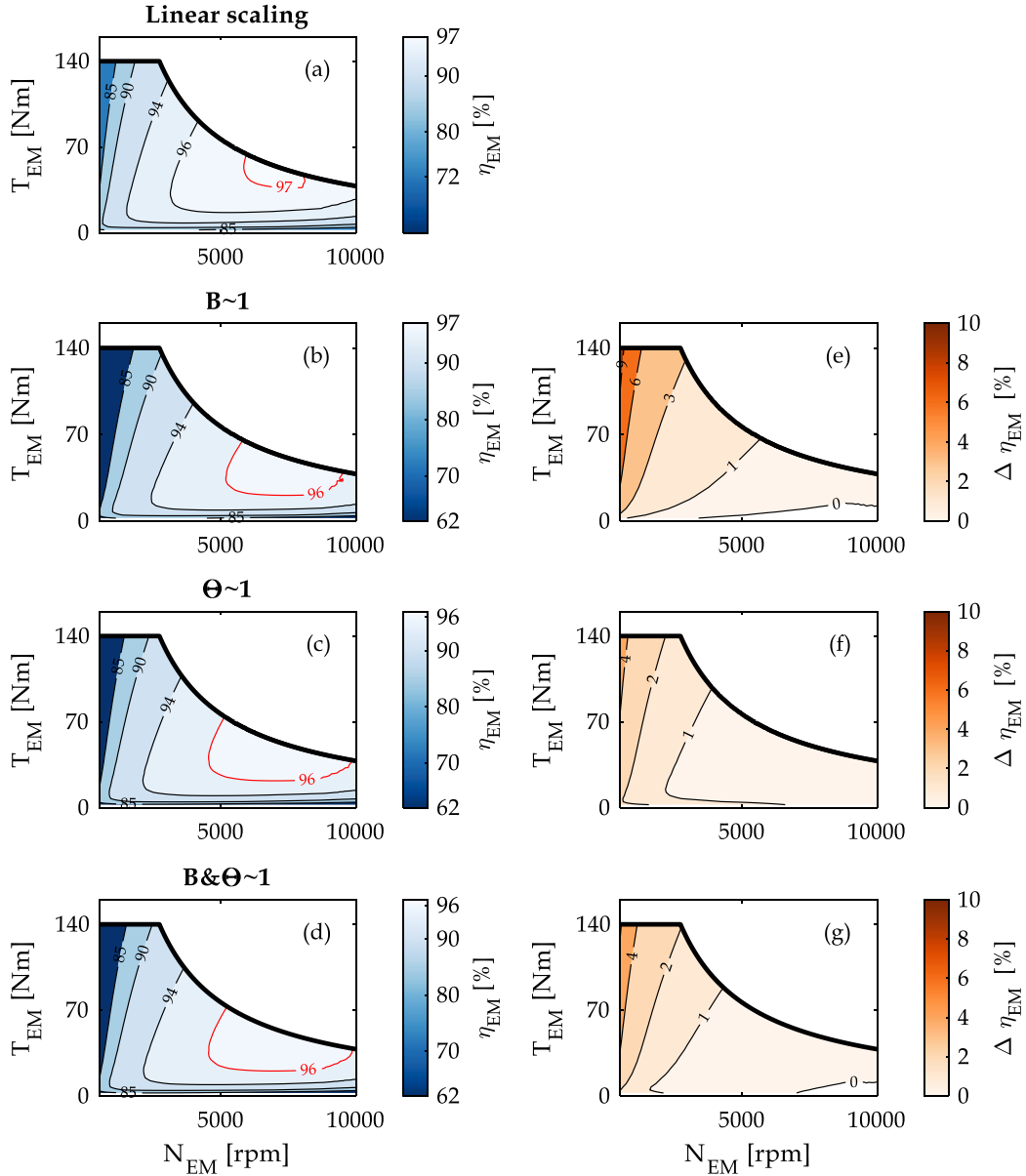
Fig. 41: Efficiency maps η_{EM} in [%] in the torque-speed plane using linear and geometric scaling laws for a downscaling case with a torque scaling factor of 0.5. The second column figures represent the efficiency difference Δ_η in [%] between linear and each choice of geometric scaling laws. Positive values for Δ_η mean that linear scaling overestimates the efficiency as compared to geometric scaling and vice versa.

3.4 Conditions of linear losses-to-power scaling of PMSM

This section derives the conditions that result in linear losses-to-power scaling of the PMSM, followed by a feasibility analysis of these conditions. This is achieved by a new organization of the scalable model of the PMSM following the Energetic Macroscopic Representation (EMR) formalism. This involves maintaining a reference PMSM model fixed but complemented with two electrical and mechanical Power Adaptation (PA) elements, as depicted in Fig. 42 [155], [156]. The key novelty lies in the incorporation of geometric scaling laws based on different scaling choices within the power adaptation elements. This enables scalability through adjustments solely to the input and output variables of the reference model. By

68

following this approach, the non-linearity of the losses is included in the scaling process by introducing an equivalent loss term ΔP, as shown in Fig. 43. This provides a novel functionality of the power adaptation elements of the EMR methodology, which are historically used to perform linear scaling manipulations (Fig. 43) [157]. An overview of the prior use of the power adaptation element of EMR is presented in Appendix III.2. By consulting Fig. 43, a criterion that leads to a linear scaling case can be already observed, which involves the elimination of the ΔP term. If the latter condition is feasible, it can be therefore concluded that the linear scaling of PMSM is a particular case of the geometric scaling laws. The derivation of this condition is elaborated in the following section.
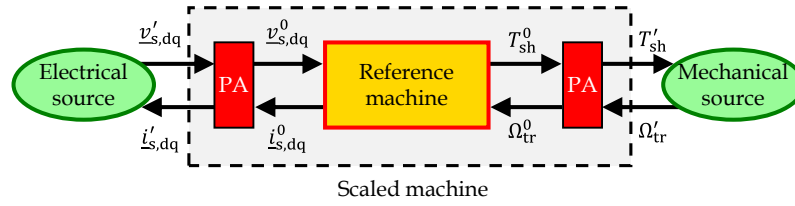
Fig. 42: Proposed structural methodology of the scaled machine
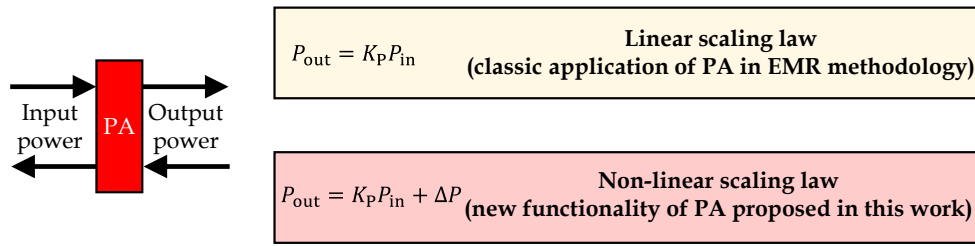
K_P: power scaling factor; ΔP: equivalent loss term due to the scaling process

Fig. 43: New proposed functionality of Power Adaptation (PA) element

3.4.1 EMR-based scaling laws of PMSM

The EMR-based scaling laws of PMSM are depicted in Fig. 44. A comprehensive explanation of the derivation of the power adaptation elements using the three choices of the geometric scaling laws is provided below.
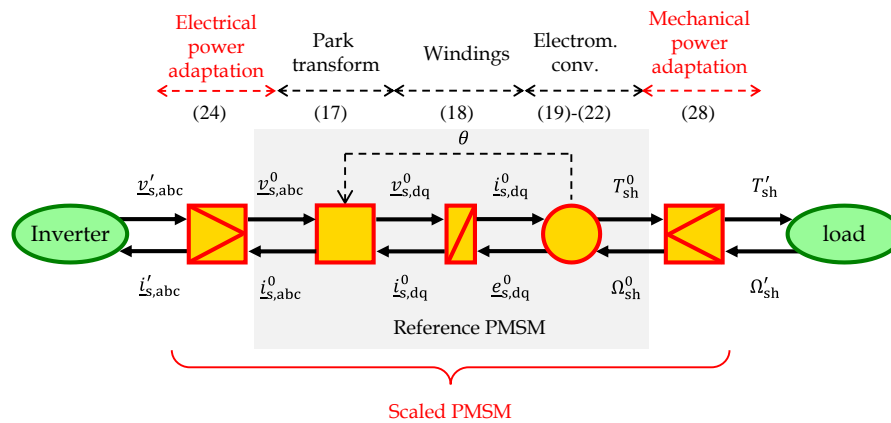
Fig. 44: EMR-based scaling laws of PMSM

3.4.1.1 Reference PMSM

The analysis assumes that the PMSM is only considered in the Park framework. The model of the reference machine (17)-(22) is represented by EMR using three elements (Fig. 44): Park-Concordia transform (red rectangle) for the transition from the three-phase *abc* frame to *dq* frame, the winding dynamic (orange rectangle pictograms with an oblique bar), and the electromagnetic conversion (orange circle pictogram). The three-phase voltage $\underline{v}^0_{s,abc}$ and speed Ω_{sh} are the inputs of the reference model, while the back-emf $\underline{e}^0_{s,dq}$ and shaft torque T^0_{sh} are its outputs. The shaft torque is determined by subtracting the equivalent torque loss terms, namely the iron core torque T^0_{fer}, magnet torque T^0_{PM}, and mechanical loss torque T^0_{mech}, from the electromagnetic torque T^0_{EM}. Note that the equation numbers are recalled in EMR, which are above each pictogram in Fig. 44. As a reminder, superscript 0 refers to the variables of the reference machine. Furthermore, the underscore subscript indicates a vector of parameters, for example $\underline{v}^0_{s,dq} = [v^0_{s,d}, v^0_{s,q}]^T$.

$$\begin{cases} \underline{v}^0_{s,dq} &= [P(\theta)]\underline{v}^0_{s,abc} \\ \underline{i}^0_{s,abc} &= [P(\theta)]^{-1}\underline{i}^0_{s,abc} \end{cases} \tag{17}$$

$$\frac{d}{dt}\underline{\psi}^0_{s,dq} = \underline{v}^0_{s,dq} - (R^0_{co} + R^0_{ew})\underline{i}^0_{s,dq} - \underline{e}^0_{s,dq} \tag{18}$$

$$T^0_{EM} = N_p\left[\psi^0_{s,d}i^0_q + \psi^0_{s,q}i^0_d\right] \tag{19}$$

$$T^0_{sh} = T^0_{EM} - T^0_{fer} - T^0_{mag} - T^0_{mech} \tag{20}$$

$$\begin{cases} T^0_{fer} = P^0_{Fe}/\Omega_{sh} \\ T^0_{PM} = P^0_{PM}/\Omega_{sh} \end{cases} \tag{21}$$

$$\begin{cases} e^0_{s,d} = -N_p\Omega^0_{sh}\psi^0_{s,q} \\ e^0_{s,q} = N_p\Omega^0_{sh}\psi^0_{s,d} \end{cases} \tag{22}$$

3.4.1.2 Electrical power adaptation derivation

The derivation of the electric power adaptation element is based on a new organization of the geometric scaling laws of PMSM outlined in Section 3.1. For this aim, the voltages $\underline{v}'_{s,dq}$ of the scaled machine can be expressed in a unified way for the three scaling choices as a function of the parameters of the reference machine and the scaling factors.

$$\underline{v}'_{s,dq} = K_A K_R^n K_W \frac{d}{dt}\underline{\psi}^0_{s,dq} + K_W^2\left(\frac{K_A}{K_R^2}R^0_{co} + \frac{1}{K_R}R^0_{ew}\right)\frac{K_R^m}{K_W}\underline{i}^0_{s,dq} + K_A K_R^n K_W\underline{e}^0_{s,dq} \tag{23}$$

where *n* and *m* are exponents that are defined based on the scaling choices and presented in Table 9. The electric PA is derived by refining (23) to get the voltages $\underline{v}^0_{s,dq}$ applied to the reference model. To this end, a voltage scaling factor K_v^{PMSM} and an equivalent resistance ΔR^0 is introduced (24)-(26). Furthermore, a current scaling factor K_i^{PMSM} is introduced as the ratio between the scaled and reference currents. The PA is described in EMR by an orange square pictogram with the symbol ">" inside. The sign means that the scaled PMSM power is greater

than the reference PMSM power. In the case of downscaling, the symbol "<" needs to be employed to indicate the opposite scenario.

$$\begin{cases} \underline{v}_{s,dq}^0 = \left(\underline{v}_{s,dq}'/K_v^{PMSM}\right) - \Delta R^0 \underline{i}_{s,dq}^0 \\ \underline{i}_{s,dq}' = K_i^{PMSM}\, \underline{i}_{s,dq}^0 \end{cases} \tag{24}$$

$$\Delta R^0 = \frac{1}{K_R^x}\left(\frac{R_{co}^0}{K_R} + \frac{R_{ew}^0}{K_A}\right) - R^0 \tag{25}$$

$$\begin{cases} K_v^{PMSM} &= K_A K_R^n K_W \\ K_i^{PMSM} &= \dfrac{K_R^m}{K_W} \end{cases} \tag{26}$$

in which x, n, and m are exponents that depend on the scaling choice and are summarized in Table 9. Finally, equation (24) can be rewritten in the three-phase frame *abc* as follows:

$$\begin{cases} \underline{v}_{s,abc}^0 = \left(\underline{v}_{s,abc}'/K_v^{PMSM}\right) - \Delta R^0 \underline{i}_{s,abc}^0 \\ \underline{i}_{s,abc}' = K_i^{PMSM}\, \underline{i}_{s,abc}^0 \end{cases} \tag{27}$$

Table 9: Overview of the exponents used for the power adaptation elements

	$B \sim 1$	$\Theta \sim 1$	Hybrid choice
x in (25)	1	0	0.5
n in (26)	1	0.5	1
m in (26)	1	1.5	1.5
α in (29)	$n+m$	$n+m$	$n+m$
β in (30)	0	1	0.5
γ in (31)	2	1	1.5
ε in (32)	1	1	0.5

3.4.1.3 Mechanical power adaptation derivation

The mechanical power adaptation element is derived from (20). To achieve this, the shaft torque of the reference machine T_{sh}^0 is scaled by the torque K_T^{PMSM}. However, since the power loss scaling factors differ from K_T, an equivalent torque ΔT must be subtracted to find the right value of the scaled torque (29)-(31). As a reminder, the scaling factors of torque and power loss are presented in Table 3 and Table 4, respectively. Furthermore, it is assumed that the reference and the scaled machines operate at the same speed.

$$\begin{cases} T_{sh}' &= K_T^{PMSM} T_{sh}^0 - \Delta T \\ \Omega_{sh}' &= \Omega_{sh}^0 \end{cases} \tag{28}$$

$$\begin{cases} K_T &= K_A K_R^\alpha \\ \Delta T &= \Delta T_{fer} + \Delta T_{PM} + \Delta T_{mech} \end{cases} \tag{29}$$

$$\Delta T_{fer} = K_T^{PMSM}\left(\frac{1}{K_R^\beta} - 1\right) T_{fer}^0 \tag{30}$$

$$\Delta T_{PM} = K_T^{PMSM}\left(K_R^\gamma - 1\right) T_{PM}^0 \tag{31}$$

$$\Delta T_{\text{mech}} = K_{\text{T}}^{\text{PMSM}}(K_{\text{R}}^{\varepsilon} - 1)T_{\text{w}}^0 \tag{32}$$

in which α, β, γ, and ε are exponents that depend on the scaling choice and are summarized in Table 9. ΔT_{fer}, ΔT_{PM}, and ΔT_{mech} represent the equivalent iron, magnet, and mechanical loss torques, respectively.

3.4.1.4 Scaled losses

Based on the electrical and mechanical PA elements, the losses P_{loss} of the scaled PMSM can be straightforwardly deduced by considering the power loss of the reference machine and introducing equivalent loss terms ΔP (33)-(35). This is achieved thanks to the new organization of the scalable model, following the rules of the EMR methodology.

$$P'_{\text{loss}} = P'_{\text{cu}} + P'_{\text{fer}} + P'_{\text{PM}} \tag{33}$$

$$\begin{cases} P'_{\text{cu}} &= K_{\text{T}}^{\text{PMSM}}P_{\text{cu}}^0 + \Delta P_{\text{Cu}} \\ P'_{\text{fer}} &= K_{\text{T}}^{\text{PMSM}}P_{\text{fer}}^0 + \Delta P_{\text{fer}} \\ P'_{\text{PM}} &= K_{\text{T}}^{\text{PMSM}}P_{\text{PM}}^0 + \Delta P_{\text{PM}} \\ P'_{\text{mech}} &= K_{\text{T}}^{\text{PMSM}}P_{\text{mech}}^0 + \Delta P_{\text{mech}} \end{cases} \tag{34}$$

$$\begin{cases} \Delta P_{\text{cu}} &= K_{\text{T}}^{\text{PMSM}}\Delta R^0 \left(i_{\text{s,a}}^{0\,2} + i_{\text{s,b}}^{0\,2} + i_{\text{s,c}}^{0\,2}\right) \\ \Delta P_{\text{fer}} &= \Delta T_{\text{fer}}\Omega_{\text{sh}}^0 \\ \Delta P_{\text{PM}} &= \Delta T_{\text{PM}}\Omega_{\text{sh}}^0 \\ \Delta P_{\text{mech}} &= \Delta T_{\text{mech}}\Omega_{\text{sh}}^0 \\ \Delta P_{\text{tot}} &= \Delta P_{\text{cu}} + \Delta P_{\text{fer}} + \Delta P_{\text{PM}} + \Delta P_{\text{mech}} \end{cases} \tag{35}$$

According to the values of both axial and radial scaling factors, the equivalent loss terms ΔP can be either positive or negative. This can be observed by examining (25), and (30)-(32). A positive value of ΔP means that the scaling process result in greater losses than a linear losses-to-power scaling and vice versa. The extra copper losses ΔP_{cu}, due to the addition of the equivalent resistance ΔR^0, can be seen as the difference between the input electric power of a scaled machine using geometric scaling laws and a linearly scaled machine, as described in (36).

$$\Delta P_{\text{cu}} = \underline{v}'_{\text{s,abc}}\underline{i}'_{\text{s,abc}} - K_{\text{T}}^{\text{PMSM}}\underline{v}_{\text{s,abc}}^0\underline{i}_{\text{s,abc}}^0 \tag{36}$$

Similarly, the sum of the extra magnetic loss terms, i.e. ΔP_{fer}, ΔP_{PM}, alongside the mechanical loss ΔP_{fer}, can be considered as the ratio between the mechanical power of the machine scaled using geometric scaling laws and the linearly scaled machine, as shown in (37).

$$\Delta P_{\text{fer}} + \Delta P_{\text{PM}} + \Delta P_{\text{mech}} = T'_{\text{sh}}\Omega'_{sh} - K_{\text{T}}^{\text{PMSM}}T_{\text{sh}}^0\Omega_{sh}^0 \tag{37}$$

3.4.2 Derivation of the conditions of linear losses-to-power scaling of PMSM

Through the examination of equations (36), and (37), it can be concluded that a relationship between the geometric and linear scaling exists. In simpler terms, if it is feasible to eliminate the equivalent terms ΔR (25), and ΔT (29), it becomes conspicuous that both scaling methods yield the same power loss scaling. This is further evidenced by redrafting the power scaling laws of geometric scaling laws, mentioned in (34), to be expressed in (38) as a function of the power loss scaling of linear scaling. The aforementioned equation provides a clear indication that to achieve a case where losses scale linearly with power, it is necessary to eliminate the equivalent loss terms ΔP. To accomplish this, it is sufficient to find the scaling factors in (25), (30)-(32) that enable the complete cancellation or minimization of the ΔP terms, as depicted in (39). In other words, if a combination of the axial and radial scaling factors that eliminate ΔP exists, the linear losses-to-power scaling is then considered as a particular case of the geometric scaling laws. Note that this particular case can result from the three scaling choices presented in Section 3.

$$
\begin{cases}
P'_{\text{cu}} & = & P^{\text{LS}}_{\text{cu}} + \Delta P_{\text{Cu}} \\
P'_{\text{fer}} & = & P^{\text{LS}}_{\text{fer}} + \Delta P_{\text{fer}} \\
P'_{\text{PM}} & = & P^{\text{LS}}_{\text{PM}} + \Delta P_{\text{PM}} \\
P'_{\text{mech}} & = & P^{\text{LS}}_{\text{mech}} + \Delta P_{\text{mech}}
\end{cases}
\tag{38}
$$

Find K_A, and K_R that cancel out

$$
\begin{cases}
\Delta P_{\text{Cu}} & = & 0 \\
\Delta P_{\text{fer}} & = & 0 \\
\Delta P_{\text{PM}} & = & 0 \\
\Delta P_{\text{mech}} & = & 0
\end{cases}
\tag{39}
$$

As can be seen in (39), there are four independent equations with two unknown variables to be found. For simplicity reasons, it is assumed that the contribution of the equivalent terms related to the iron, permanent magnet, and mechanical losses are marginal as compared to the copper loss. Therefore, $\Delta P_{\text{fer}}, \Delta P_{\text{PM}}$, and ΔP_{mech} can be initially disregarded. The impact of this assumption will be assessed in the next section. Consequently, the determination of the conditions for linear scaling necessitates finding a combination of the geometric scaling factors K_A and K_R that makes ΔR, and hence ΔP_{cu}, equal to zero.

The second condition of linear scaling is the assumption of a fixed base speed through the scaling process. This can be accomplished by appropriately defining the rewinding scaling factor K_W, based on the performed geometric scaling. Indeed, the base speed Ω_b PMSM is related to the voltage limit of the DC bus $v^{\text{limit}}_{\text{DC}}$ and can be approximately expressed as in (40). Assuming that $v^{\text{limit}}_{\text{DC}}$ is preserved, which is a reasonable assumption considering different vehicle classes share the same DC bus voltage rating, the base speed scales following (41).

$$
\Omega'_b \propto \frac{v^{\text{limit}}_{\text{DC}}}{\sqrt{\left(\psi'_{\text{s,d}}\right)^2 + \left(\psi'_{\text{s,q}}\right)^2}}
\tag{40}
$$

$$
\Omega'_b = \frac{1}{K_A K_R^\delta K_W} \Omega^0_b
\tag{41}
$$

in which $\delta \in \{0.5, 1\}$, depending on the selected scaling choice of the geometric scaling laws, as indicated in Table 2 for the flux linkage ψ scaling. Based on (41), the rewinding scaling factor should be defined as in (42), to preserve the base speed. This finding has not confirmed previous research, which postulates that the DC bus voltage needs to be scaled to maintain the base speed through the scaling process using linear scaling [182], [195]. For instance, in [182], the authors assumed that the DC bus voltage needs to be scaled with K_T^{PMSM}, or with the root square of K_T^{PMSM} in [195], without providing any further explanation for these assumptions. Based on (42), the voltage K_v^{PMSM} and current K_i^{PMSM} scaling factors, indicated in (24), can be reformulated as in (43).

$$K_W = \frac{1}{K_A K_R^{\delta}} \tag{42}$$

$$\begin{cases} K_v^{PMSM} & = & 1 \\ K_i^{PMSM} & = & K_T^{PMSM} \end{cases} \tag{43}$$

3.4.3 Simulation-based validation of the derived conditions

To assess the reliability of the derived conditions discussed earlier, Fig. 45 presents the difference in terms of efficiency $\Delta\eta_{EM}$ between two efficiency maps computed using linear and geometric scaling methods. The efficiency map defined with geometric scaling is established using the scaling factors, presented in Table 10, that result in ΔR, thus equivalent copper loss ΔP_{Cu}, equals to 0 for the three geometric scaling factors. For simplicity, non-integer values of K_W are herein allowed. The assumption of disregarding ΔP_{fer}, ΔP_{PM}, and ΔP_{mech} is initially evaluated in Fig. 45. a-c. This followed by a second assessment in Fig. 45. e-f that incorporates the preceding equivalent loss terms.

Table 10: Scaling factors that cancel out ΔR

	K_T	K_A	K_R	K_W
$B\sim1$	2	3.146	0.7973	0.3986
$\Theta\sim1$	2	0.700	1.6093	1.1261
$B\&\Theta\sim1$	2	0.4620	1.7970	1.2045

Fig. 45. a-c reveal that $\Delta\eta_{EM}$ is zero accros the entire torque-speed plane of the scaled machine, for the three geometric scaling choices. This means that linear losses-to-power scaling is achieved using the defined combination of the geometric scaling factors in Table 10. Fig. 45. e-f shows $\Delta\eta_{EM}$ including ΔP_{fer} ΔP_{PM}, and ΔP_{mech} to assess their impact. As it can be observed from the previous figure, $\Delta\eta_{EM}$ is less than 0.5% in absolute terms for most operating points. The largest discrepancy, up to 2%, between linear and geometric scaling occurs in confined areas characterized by high-speed and low-torque values, wherein mechanical and iron losses predominate. However, it is worth emphasizing that, in the context of automotive applications, the concerned areas are seldom used except for braking phases, essentially due to the resistive forces imposed by the environment of the vehicle. This result has further strengthened the confidence in the assumption of disregarding ΔP_{fer}, ΔP_{PM}, and ΔP_{mech} is not impactful. It is then enough to find the combination of the geometric scaling factors that results in

ΔP_{cu} equal to zero. The linear losses-to-power scaling method applied to PMSM can be therefore deemed sufficient for this upscaling case study.
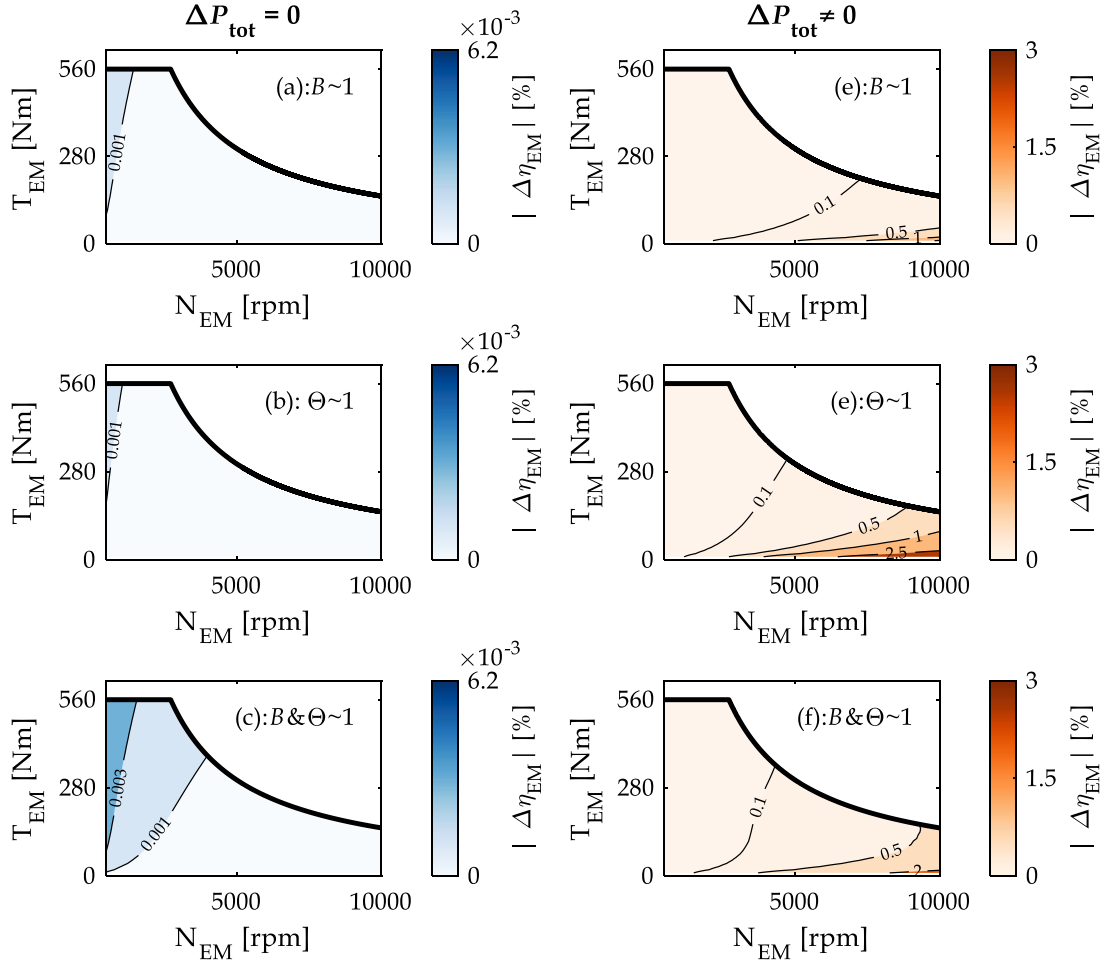
Fig. 45: Difference in terms of electric machine efficiency $|\Delta\eta_{EM}|$ between linear scaling and geometric scaling laws for an upscaling case with a torque scaling factor of 2. The figures in each row represent $|\Delta\eta_{EM}|$ between linear scaling and a particular choice of geometric scaling laws. Each column figure pertains to the assumption of either disregarding or including the equivalent loss terms ΔP_{tot}.

To generalize the last condition of $\Delta R=0$ using different torque scaling factors K_T^{PMSM}, Fig. 46 shows the results of the equivalent resistance term ΔR in per-unit (ΔR [Ω]/ ($R_{co}^0 + R_{ew}^0$) [Ω]) as a function of different combinations of geometric scaling factors. The figure also depicts the contour lines of the torque scaling K_T values as a function of the geometric scaling, with values ranging from 0.5 to 2. Regarding the upscaling case, the sign of ΔR varies according to the combination of the selected geometric scaling factors. A positive value (blue color in Fig. 46) of ΔR means that the linear scaling underestimates the copper loss, particularly for lengthy machines, and vice versa. Most importantly, certain combinations of axial and radial scaling factors nullify ΔR. The intersection between the contours of K_T^{PMSM} (purple color in Fig. 46) and the contour line ΔR of zero values defines the geometric scaling factors that result in a linear scaling of the losses. Fig. 46. a-c suggests that all cases of upscaling lead to linear scaling of the losses, regardless of the applied torque scaling factor. This is true for the three scaling choices of geometric scaling. However, the opposite is not true for the downscaling cases, in

which only a torque scaling factor K_T of 0.9 results in a linear scaling case, as illustrated in Fig. 46.a-b for the choices $B\sim1$ and $\Theta\sim1$. Below the aforementioned scaling factor, the value of ΔR is always positive, leading to the conclusion that no combination of geometric scaling factors results in linear losses-to-power scaling for the downscaling cases. For the hybrid choice, Fig. 46.c shows that there are no combinations of the geometric scaling factors that cancel out ΔR for the downscaling cases. Based on these findings, it is concluded that geometric scaling laws exhibit a particular case that results in linear power-to-losses scaling solely for the upscaling cases. However, the last statement does not hold for the downscaling cases. To generalize this statement, the same analysis is conducted in Appendix IV.6, using a second machine as a reference. Note that this second machine has a completely different design as compared to the initial one utilized in the analysis above.
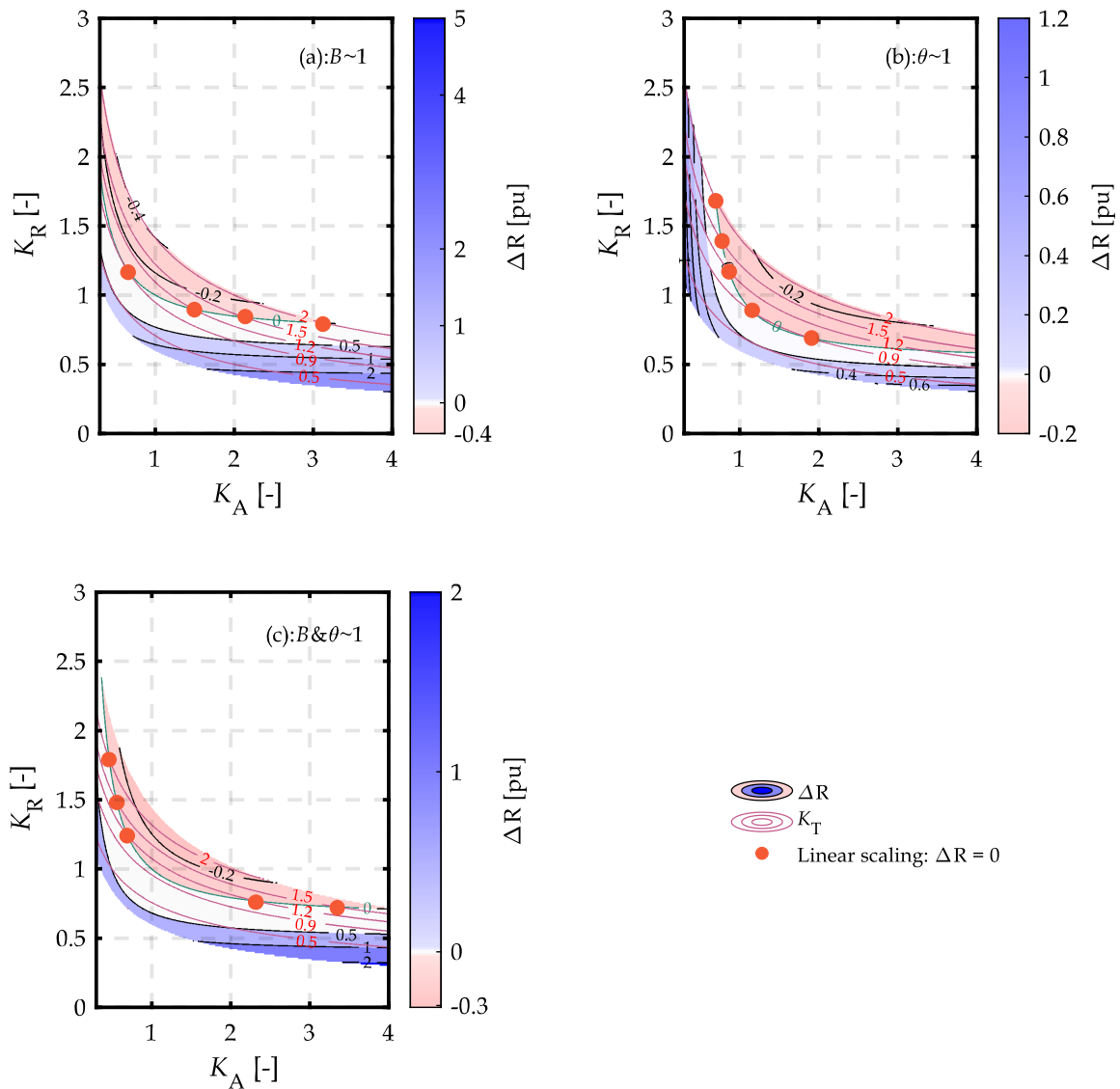
Fig. 46: Equivalent resistance term ΔR (black contour lines) in per-unit and torque scaling factor K_T^{PMSM} [-] (purple contour lines) as a function of axial K_A and radial K_R scaling factors.

Up to this point, it has been demonstrated that there are geometric scaling factor combinations that numerically yield linear scaling cases for the upscaling scenarios. However, the feasibility of these combinations, considering both axial and radial scaling factors, needs to be assessed. To accomplish this, the constraints outlined in (44) are set as boundaries during the scaling process. These constraints ensure that undesirable geometries of the machine, such as tubes and disk-shaped machines, are avoided. This is considered by keeping the equivalent axial stack length to the diameter of the air gap ratio (l_a/D_g ratio) within the range indicated in (44). The boundaries indicated in the preceding equation allow for avoiding mechanical problems, related to vibrations due to the first critical speed [102]. Furthermore, the maximal allowable current density J' is maintained below 23 A/mm², which can be handled by the existing cooling technology of traction machines. Fig. 47 shows combinations of geometric scaling factors, i.e. axial K_A and radial K_R factors, that yield different torque scaling factors K_T^{PMSM}.
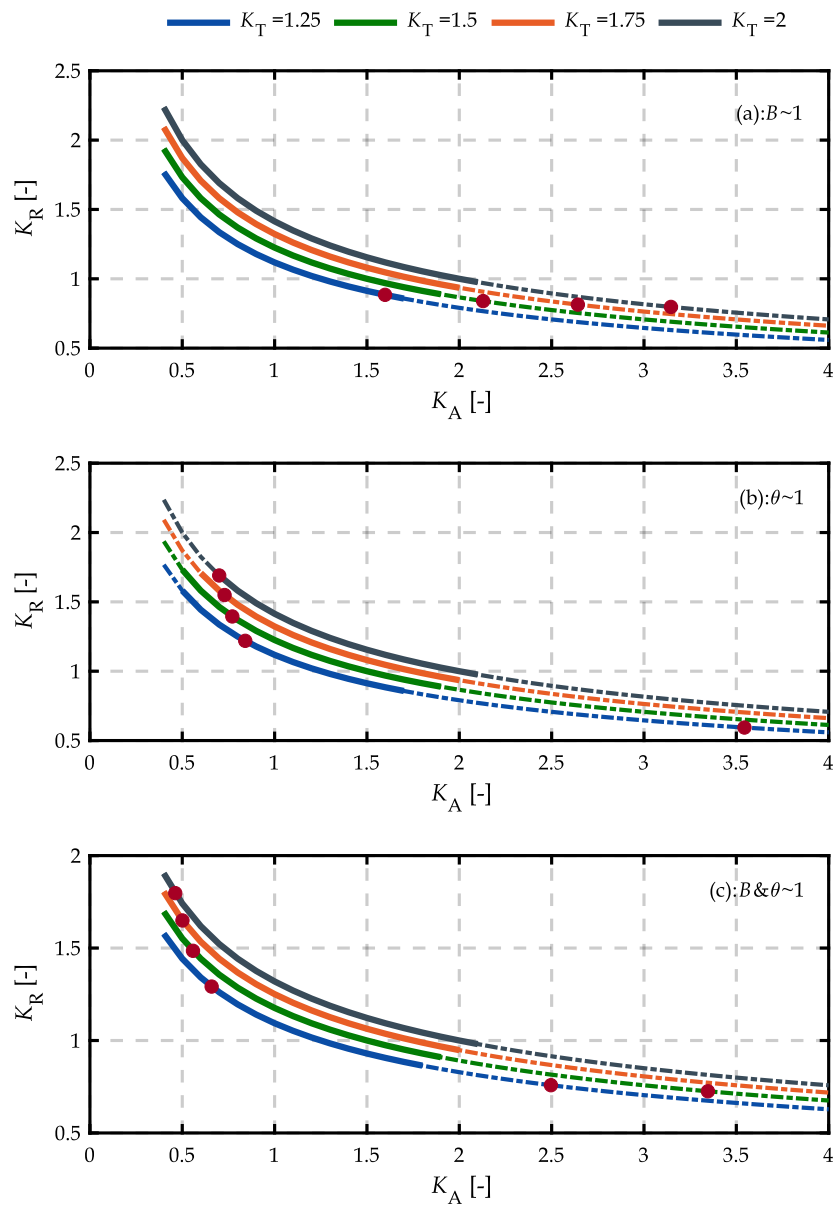
Fig. 47: Assessment of the feasibility of the geometric scaling factors combinations that result in linear power-to-losses scaling cases for different torque scaling factors. The solid lines represent the feasible

geometric scaling factors, while the dashed lines represent unfeasible geometric factors. The red marker indicates the geometric scaling factors that result in linear scaling cases for each torque scaling factor and scaling choice.

$$\begin{cases} 0.4 \leq \dfrac{l_a'}{D_g'} = \dfrac{K_A}{K_R}\dfrac{l_a^0}{D_g^0} \leq 2.5 \\ \quad J' \leq 23 \ \text{A/mm}^2 \end{cases} \tag{44}$$

The solid lines in Fig. 47 depict the feasible geometric scaling factors, whereas the unfeasible ones are described in dashed lines. This assessment is carried out for the three scaling choices of geometric scaling. From Fig. 47.a, which deals with the scaling choice $B{\sim}1$, it can be seen that a linear scaling case is solely achieved for a torque scaling factor K_T of 1.25. This is illustrated by the red marker that overlays the solid line, representing feasibility. Nonetheless, for K_T above 1.25 and considering the same scaling choice, no feasible geometric scaling factors that yield a linear scaling case have been found. The red markers in Fig. 47.a suggest the necessity of large axial factors, which can be achieved due to the length-to-diameter associated with the first critical speed. Conversely, the examination of Fig. 47.b and Fig. 47.c reveals that there exists at least a viable combination of K_A, and K_R that can result in linear scaling cases for different torque scaling factors. This can be explained by the fact that ΔR scales differently for each scaling choice, as shown in (25), which leads to a different mathematical solution for K_A, and K_R. It is of high importance to emphasize that the analysis presented in this section is specifically based on the geometry of the reference machine utilized for this study. In case a new reference machine with other geometric parameters is considered, different conclusions might be drawn. Consequently, generalizing the statements made in this section is challenging. However, it is important to note that the presented methodology is general and can be conducted using different machines. To substantiate the last statement, Appendix IV.6 presents the same analysis conducted in this section but uses another design of PMSM as a reference machine.

4   Scaling laws of IGBT-based voltage source inverters

Compared to electric machines, investigation on the scalability of voltage source inverters has received comparatively less attention. The concept of applying geometric scaling to power electronics is less straightforward. Instead, the concept of modularity finds widespread application. This is exemplified by manufacturers providing power modules, wherein semiconductor devices are either paralleled or connected in series to increase the current or the voltage of the power converter [77]. If the requirements are altered, it becomes necessary to either replace the semiconductor components with other ones selected from a catalog, reassess the parallel or series connections, or even reconsider the topology of the power electronic converter. Therefore, these later solutions result in different discrete sets of values for voltage and current rating.

This section aims to make a comparison between linear losses-to-power scaling and the available scaling laws of IGBT-based inverters in literature. As a reminder, the retained scaling methods for inverters in this study are depicted in Fig. 30 and consist of the scaling law that preserves the temperature rise and the power density, data-driven scaling laws, and linear

scaling. The analysis in the subsequent sections is centered on two-level inverters due to their prevalence in the automotive industry. The section concludes by deriving and assessing the conditions that result in a linear power scaling case of the inverters through the EMR-based scaling laws.

4.1 Theoretical background of the scaling laws of inverters

4.1.1 Preserving temperature rise and power density

Kasper et al. derived a general scaling law for the efficiency scaling of power electronics converters based on a hybrid choice that consists in preserving the temperature rise and power density of the reference and scaled converters [180]. To derive the efficiency scaling law, the converter is assumed to be a cube with a surface S_{conv}, with a volume V_{conv}, leading to the relationship between the surface and volume in (45). Based on the last equation, the temperature rise Θ is expressed as a function of the volume (46). Under the assumption that temperature rise is preserved during the scaling process (47), a relationship between the output power $P_{conv,out}$ of the reference and scaled converters as a function of the volume scaling can be deduced (48). The latter scaling law, under the assumption of a consistent power density ρ_{conv} throughout the scaling process (49), can be reformulated as depicted in (50). This scaling choice is referred to as $\rho \& \Theta \sim 1$ in the sequel.

$$S_{conv} = 6V_{conv}^{2/3} \tag{45}$$

$$\Theta = \frac{P_{losses}}{S_{conv}} = \frac{P_{losses}}{6V_{conv}^{2/3}} \tag{46}$$

$$\Theta' = \Theta^0 \Rightarrow \frac{P'_{losses}}{6V_{conv}^{2/3'}} = \frac{P^0_{losses}}{6V_{conv}^{2/3^0}} \tag{47}$$

$$\frac{P'_{conv,out}}{P^0_{conv,out}} = \frac{(1 - \eta^0_{VSI})}{(1 - \eta'_{VSI})} \frac{\eta'_{VSI}}{\eta^0_{VSI}} \left(\frac{V'_{conv}}{V^0_{conv}}\right)^{2/3} \tag{48}$$

$$\rho'_{conv} = \rho^0_{conv} \Rightarrow \frac{P'_{conv,out}}{V'_{conv}} = \frac{P^0_{conv,out}}{V^0_{conv}} \tag{49}$$

$$\eta'_{VSI} = \frac{\eta^0_{VSI} \left(\frac{P'_{conv,out}}{P^0_{conv,out}}\right)^{1/3}}{1 + \eta^0_{VSI} \left(\left(\frac{P'_{conv,out}}{P^0_{conv,out}}\right)^{1/3} - 1\right)} \tag{50}$$

4.1.2 Data-driven scalable loss model

This scaling choice relies essentially on knowledge of the parameters of a group of power electronics converters with the same technology. The derivation of this scaling can be achieved by fitting the data from measurements or catalogs. Then, models can be deduced to describe a general tendency and relationships between variables. For instance, a "scalable inverter power module" model is established in [177] based on datasheet data of 650V IGBT automotive

power modules with nominal collector current ratings from 50A up to 800 A. The proposed model in the last previously mentioned reference expresses the different parameters of the inverter as a function of either the nominal collector current I_{cn} or the magnitude of the AC current $\hat{I}_s$ determined from the electric machine mapping, as illustrated in (51). The parameters of the fitted model, e.g. the on-state resistance r_{on}, the turn-on $E_{on,T}$, turn-off $E_{off,T}$, and recovery E_{rec} energies, have been tuned based on the data of 7 inverters that belong to the same family series, using the same technology of semiconductor components.

$$\begin{cases} r_{on,T} &= & 990.07\, I_{cn}^{-1.003} \\ r_{on,D} &= & 675.61\, I_{cn}^{-1.004} \\ E_{on,T} &= & 9.1964\ 10^{-6}\hat{I}_s^2 + 0.0156\hat{I}_s + 0.6221 \\ E_{off,T} &= & 2.4259\ 10^{-8}\ \hat{I}_s^3 - 5.7183\ 10^{-6}\hat{I}_s^2 + 0.0357\ \hat{I}_s + 1.87 \\ E_{rec} &= & 2.8029\ 10^{-6}\ \hat{I}_s^2 + 0.0139\ \hat{I}_s + 0.9973 \end{cases} \tag{51}$$

In [97], further developments to the aforementioned scaling method are proposed by adding the chip area of the semiconductor devices and normalizing all the parameters of the inverter based on this latter, instead of the current rating. However, it is worth noting that for commercially available power modules, the chip areas are seldom provided in the datasheets.

4.2 Comparison of linear losses-to-power scaling law and other scaling laws

To assess the accuracy of linear losses-to-power scaling of inverters, three 650 V IGBT-based-automotive inverters from the Infineon Hybrid Pack family are selected. These inverters are similar to those studied in [177] for comparison reasons. These inverters have a range of nominal collector currents of 400 A, 600 A, and 800 A, which can correspond to a continuous electric power between 50 kW and 107 kW [196]. This makes them suitable for exploring the scalability of losses. The main parameters are presented in Table 11. The reference inverter selected for the analysis is the FS600R07A2E3 power module with a rated current of 600 A, which suits the reference machine presented in 3.2.1. This reference inverter is used to examine the effects of both upscaling the current rating of the inverter by a factor of 0.67 (FS800R07A2E3) and downscaling it by a factor of 1.33 (FS400R07A1E3). For this aim, the reference machine is scaled with the same power scaling factors. This enables acquiring the voltages, and current setpoints needed for computing the losses of the inverters, which are detailed in the next section. Additional information can be found in the modules' datasheet [197].

Table 11: Main parameters, extracted from the datasheets of the inverters

Power module	I_{cn} [A]	v_{CE} [V]	$r_{on,IGBT}$ [mΩ]	$r_{on,Diode}$ [mΩ]	$v_{ce0,IGBT}$ [V]	$v_{ce0,Diode}$ [V]
FS400R07A1E3	400		2.18	1.85		
FS600R07A2E3 (ref)	600	650	1.44	1.05	0.69	0.79
FS800R07A2E3	800		1.08	0.79		

In the following, the comparison process is structured in two steps. Initially, a benchmark step of the three inverters is conducted, employing the theoretical models and using data extracted from the datasheets for computing the losses. The outcomes of the benchmarking will be compared with the linear losses-to-power scaling results. Subsequently, the second step involves assessing and comparing the other different scaling choices, aiming to identify the most precise scaling choices. In this comparison, all the scaling choices are compared on the same basis, against the benchmarking study assuming a constant junction temperature of 125°C. It is worth mentioning that the thermal aspect is out of the scope of this work.

4.2.1 Linear scaling accuracy assessment via benchmarking study

4.2.1.1 Losses benchmark

This section presents the theoretical model used to benchmark the losses of the inverters. Assuming a sinusoidal pulse width modulation, i.e. the output current waveforms are sinusoidal, the average conduction losses over a switching period P_{cond} in one switch is expressed in (52) as was reported in [98].

$$P_{cond,xy} = \left(\frac{1}{2\pi} + \frac{s_x \, \cos\varphi}{8}\right) v_{ceo,x} \widehat{I}_s + \, + \left(\frac{1}{8} + \frac{s_x \, \cos\varphi}{3\pi}\right) r_{on,x} \widehat{I}_s^{\,2} \tag{52}$$

with x is a subscript $\in$ {IGBT, diode} for the concerned switch, y is a second subscript $\in$ {on, off, rec} refereeing to the turn-on and turn-off states of the IGBT and the turn-off state of the diode known as reverse recovery (rec), s refers to the switching function, φ is the phase angle between voltage and current, v_{ceo} is the on−state threshold voltage, $\widehat{I}_s$ is the amplitude of AC phase current, and $r_{on,x}$ is the on−state resistance.

The average turn-on and turn-off switching losses P_{sw} of the transistor and the diode reverse recovery (rec) loss are calculated as shown in (53) [98].

$$P_{sw,x} = \frac{f_{sw}}{\pi}\left(E_{x,y}(\widehat{I}_s)\right)\left(\frac{V_{DC}}{V_{ref}}\right)^{k_v} \tag{53}$$

where x is a subscript describing the concerned switch, y is a second subscript $\in$ {on, off, rec} refereeing to the state of each switch in question, f_{sw} is the switching frequency, E energy dissipated during the turn on/off/recovery of the switch, V_{DC} is the applied DC bus voltage, V_{ref} is the reference DC voltage, and k_v is a switching loss factor. The energy $E_{x,y}$ can be modeled by a second-order polynomial equation, which depends on the current $\widehat{I}_s$ (54). The energy parameters in (54) are identified based on the datasheets and presented in Table 12.

$$E_{x,y} = a_{INV}\widehat{I}_s^{\,2} + b_{INV}\widehat{I}_s + c_{INV} \tag{54}$$

Table 12: Parameter identification of the energies of the studied inverters at 125°C in [J].

	FS400R07A1E3
$E_{\text{on,IGBT}}$	$3.97\ 10^{-6}\ \widehat{I_s}^2 + 12.18\ 10^{-2}\ \widehat{I_s} + 0.29$
$E_{\text{off,IGBT}}$	$2.16\ 10^{-5}\ \widehat{I_s}^2 + 32.29\ 10^{-2}\ \widehat{I_s} + 1.27$
$E_{\text{rec,Diode}}$	$-2.82\ 10^{-5}\ \widehat{I_s}^2 + 30.13\ 10^{-2}\ \widehat{I_s} + 0.94$
	FS600R07A1E3
$E_{\text{on,IGBT}}$	$-9.55\ 10^{-6}\ \widehat{I_s}^2 + 31.39\ 10^{-2}\ \widehat{I_s} + 0.55$
$E_{\text{off,IGBT}}$	$-7.55\ 10^{-6}\ \widehat{I_s}^2 + 43.39\ 10^{-2}\ \widehat{I_s} + 1.81$
$E_{\text{rec,Diode}}$	$-1.62\ 10^{-5}\ \widehat{I_s}^2 + 26.53\ 10^{-2}\ \widehat{I_s} + 0.66$
	FS800R07A2E3
$E_{\text{on,IGBT}}$	$1.07\ 10^{-5}\ \widehat{I_s}^2 + 27.68\ 10^{-2}\ \widehat{I_s} + 0.83$
$E_{\text{off,IGBT}}$	$3.07\ 10^{-6}\ \widehat{I_s}^2 + 44.26\ 10^{-2}\ \widehat{I_s} + 1.36$
$E_{\text{rec,Diode}}$	$-1.72\ 10^{-5}\ \widehat{I_s}^2 + 32.08\ 10^{-2}\ \widehat{I_s} + 0.99$

Note that the losses generated by the driver, snubber circuits, and capacitive and inductive parasitics are assumed to be negligible. Therefore, they are not included in the scaling process.

4.2.1.2   Comparison results

Fig. 48 presents the efficiency maps of the scaled inverters, established using the theoretical models and linear scaling, for both upscaled and downscaled cases. By consulting, Fig. 48. a-d, it is clear that the linear scaling proves to be effective in predicting the maximal efficiency of the scaled inverters. This contrasts with the observations made in Section 3.3 for the scaling of electrical machines. These results hold for both upscaling and downscaling cases. As far as the downscaling case is concerned, the difference in terms of efficiency $\Delta\eta_{\text{INV}}$ between linear scaling and the benchmark, illustrated in Fig. 48. e, falls below 1% in absolute terms across the majority of the map. It should be noted that a negative value of $\Delta\eta_{\text{INV}}$ means that linear scaling underestimates the efficiency, and vice versa. However, a small discrepancy of up to 2% in absolute terms is observed in low-speed regions below 1000 rpm. Regarding the upscaling case, Fig. 48. f indicates that $\Delta\eta_{\text{INV}}$ is less than 0.5% in absolute value in the majority of the map. Considering the observations and outcomes derived from this comparison, it can be concluded that linear scaling yields satisfactory results in terms of efficiency map scaling. Note that similar results have been obtained in a published conference paper [26], where additional inverters from the same family series are employed.
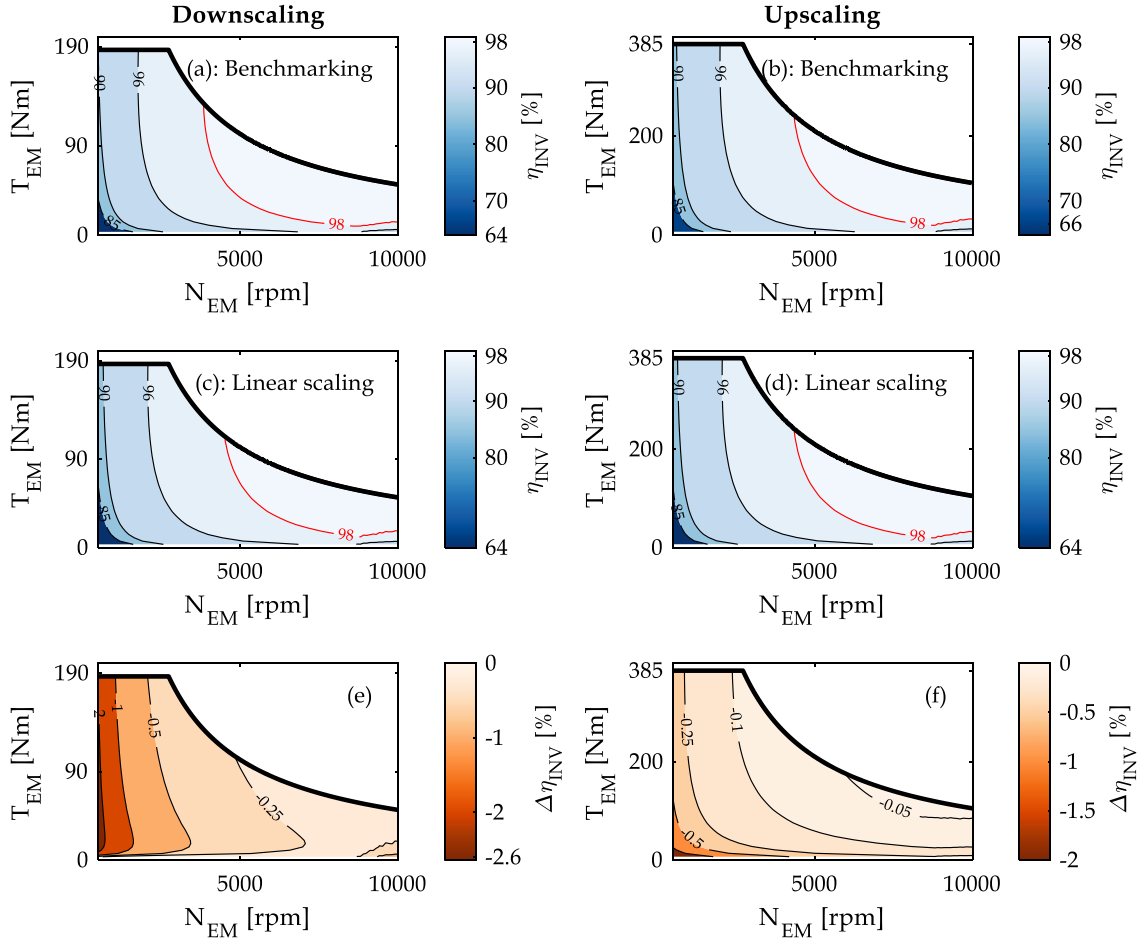
Fig. 48: Linear scaling vs. benchmarking study of the efficiency. The negative value of the difference in terms of efficiency $\Delta\eta_{INV}$ means that linear scaling underestimates the results.

4.2.2 Alternative inverter scaling choices accuracy assessment via benchmarking study

This section examines the difference in terms of efficiency between the benchmark and the hybrid choice ρ_{VSI}&Θ~1, as well as the data-driven choice. This allows the assessment of whether alternative scaling choices of the inverter yield better results as compared to the linear scaling method of the inverter.

Fig. 49 discusses the results obtained with the choice ρ_{VSI}&Θ~1. For the downscaling case, it can be seen from Fig. 49. a that the area of maximal efficiency is narrower as compared to the benchmarking results shown in Fig. 48. a. The difference in terms of efficiency $\Delta\eta_{INV}$, illustrated in Fig. 49. c, is mainly negative across the majority of the map regions. This means that the choice ρ_{VSI}&Θ~1 underestimates the efficiency relative to the benchmark. Broadly, an average difference of 1% in absolute value is attained across the efficiency map, except for regions characterized with speed values below 1000 rpm, where the maximal difference can reach up to 5%. Regarding the upscaling case, the values of $\Delta\eta_{INV}$ are positive, meaning that the choice ρ_{VSI}&Θ~1 overestimates the efficiency as compared to the benchmark. The observed values of $\Delta\eta_{INV}$ fall with a range from 0.25% to 0.75%, which represents a notable reduction compared to the downscaling case.
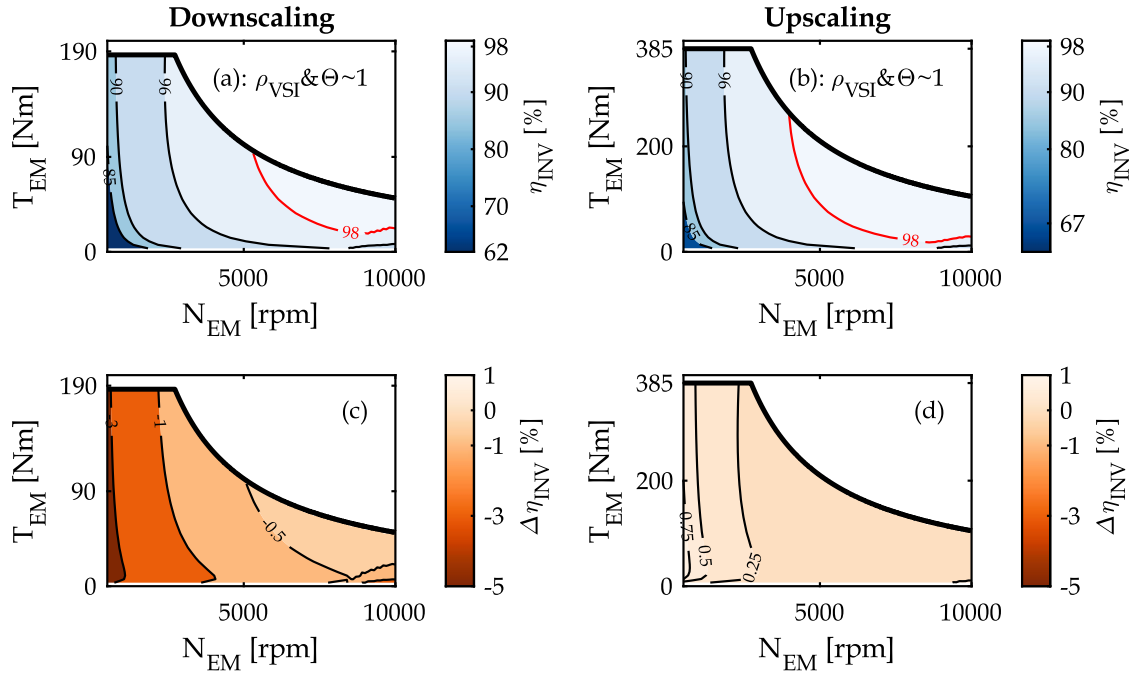
Fig. 49: Comparison of the efficiency map scaling between the choice that consists in preserving the power density and the temperature rise and the benchmark. Negative values of $\Delta\eta_{INV}$ means that the choice $\rho_{VSI}\&\Theta\sim1$ underestimates the efficiency as compared to the benchmark and vice versa.

Fig. 50 presents the findings obtained with the data-driven scaling choice. Broadly, the $\Delta\eta_{INV}$ is relatively negligible for the upscaling and downscaling cases. Better results have been achieved for the downscaling case as compared to the linear scaling and the hybrid choices. This is evidenced by the non-significant values of $\Delta\eta_{INV}$ of less than 0.5%, obtained at low speed and high torque regions, as shown in Fig. 50.a. In the same regions, the linear scaling and hybrid choices exhibit $\Delta\eta_{INV}$ of -2% and -3%, respectively.

To summarize, the comparison outcomes of the studied scaling method of the inverter with the benchmark lead to the conclusion that linear scaling results in satisfactory results for the upscaling and downscaling cases with an average discrepancy of less than 0.5% for both cases. This is achieved considering power scaling factors of 0.67 and 1.33. When comparing the outcomes of the hybrid choice $\rho_{VSI}\&\Theta\sim1$ against the linear scaling, it can be concluded that linear scaling yields results that are relatively closer to the benchmark, particularly in the downscaling case. Relative to the data-driven method, the linear scaling method of inverters results in comparable results. Consequently, the linear power-to-losses scaling for IGBT-based inverters is deemed sufficient for employment in the early design phases of EDS. Table 13 provides an overview of the advantages and flaws of each scaling choice.
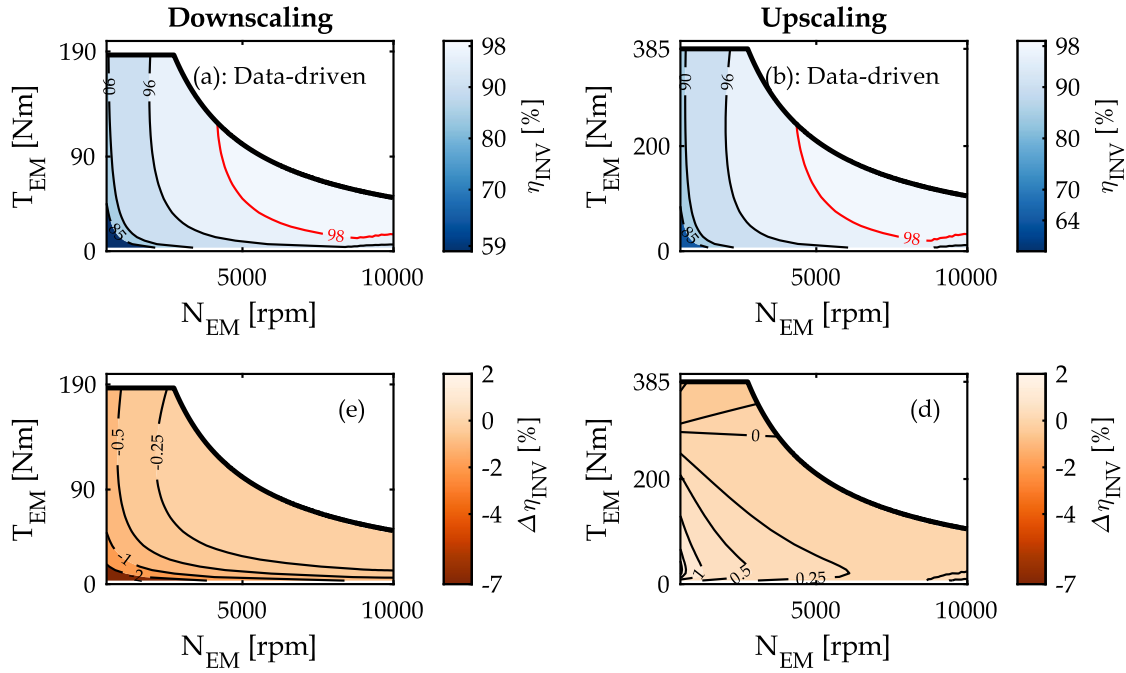
Fig. 50: Comparison of the efficiency map scaling between the data-driven choice and the benchmark.
Positive values of $\Delta\eta_{INV}$ means that the data-driven choice overestimates the efficiency as compared to
the benchmark, and vice versa.

Table 13: Comparison of the scaling choice for voltage source inverters

Scaling choices	Advantages	Flaws
Linear losses-to-power	• Effortless: easy and fast calculation • Simple input requirements: only the overall or loss efficiency map is needed to perform the scaling process • Satisfactory results for upscaling and downscaling cases	• No geometric/volume information • Unknown parameters scaling
Preservation of the temperature rise and power density	• Same as linear scaling with additional information related to the volume scaling	• Poor accuracy at low-speed and high-torque regions, particularly in downscaling cases • Unknown parameters scaling
Data-driven	• Accurate results	• Need for a pre-processing phase to define the fitted model for each parameter • Accuracy-dependency on the number of inverters used to tune the parameters of the fitted model

4.3 Conditions of linear losses-to-power scaling of IGBT-based inverters

This section aims to derive the conditions that result in a linear scaling of the inverter. As previously demonstrated for the PMSM in Section 3.4, this is achieved through the EMR-based scaling laws, which are presented in Fig. 51.
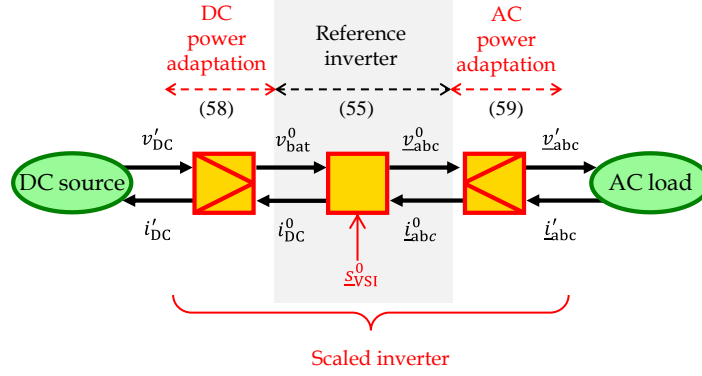
Fig. 51: EMR-based scaling laws of inverters

4.3.1 EMR-based scaling laws

4.3.1.1 Reference inverter

An average model, taking into account the switching P_{sw}^0 and conduction P_{cond}^0 losses, over a switching period, is adopted for the reference inverter because of its computational efficiency [198]. Consequently, the inverter is controlled by an average switching functions $\underline{s}_{VSI}^0$ that links the current and voltage of the DC source to those of the load (PMSM in this work), as illustrated in Fig. 51. The model of the reference inverter (55), (57) is represented in EMR by an orange rectangle pictogram with a red input control signal $\underline{s}_{VSI}^0$. The inputs of the reference model are the voltage of the battery v_{DC}^0, the three-phase currents of the load $\underline{i}_{abc}^0$, and the switching functions $\underline{s}_{VSI}^0$. The outputs of the model are the current i_{DC}^0, and the three-phase voltages $\underline{v}_{abc}^0$. Note that the equation numbers are recalled in EMR, which are above each pictogram in Fig. 51.

$$\begin{cases} \underline{v}_{abc}^0 & = & \underline{s}_{VSI}^0 \, v_{bat}^0 \\ i_{DC}^0 & = & \eta_{VSI}^{0\gamma} \, \underline{s}_{VSI}^{0T} \, \underline{i}_{abc}^0 \end{cases} \text{, with } \gamma = \text{sign}(i_{DC}) \tag{55}$$

$$\underline{s}_{VSI}^0 = [s_a, s_b, s_c]^T \tag{56}$$

$$\eta_{VSI}^0 = \frac{P_{out}^{VSI,0}}{P_{out}^{VSI,0} + P_{loss}^{VSI,0}} = \frac{P_{out}^{VSI,0}}{P_{out}^{VSI,0} + \left(P_{cond}^0 + P_{sw}^0\right)} \tag{57}$$

4.3.1.2 Structuration of the DC side power adaptation element

The DC voltage of the source v_{DC}' scales using a voltage scaling factor, denoted as $K_{v,DC}^{VSI}$. By analyzing (55), it can be seen that the definition of the DC current i_{DC}^0 is impacted by the scaling of the losses. Therefore, the scaling of the DC current is formulated as a function of a

current scaling factor $K_{i,DC}^{VSI}$, and an equivalent current Δi_{DC} that accounts of the non-linear scaling of the losses.

$$\begin{cases} v_{DC}^0 & = & \dfrac{1}{K_{v,DC}^{VSI}} v_{DC}' \\ i_{DC}' & = & K_{i,DC}^{VSI} i_{DC}' + \Delta i_{DC} \end{cases} \tag{58}$$

4.3.1.3 Structuration of the AC side power adaptation element

As the losses do not affect the AC side, following the adopted model in (55), it is therefore assumed that the current and the voltages of the AC part of the inverter scale linearly using a voltage $K_{v,AC}^{VSI}$ and current scaling factors $K_{i,AC}^{VSI}$.

$$\begin{cases} \underline{v}_{abc}' & = & K_{v,AC}^{VSI} \underline{v}_{abc}^0 \\ \underline{i}_{abc}^0 & = & \dfrac{1}{K_{i,AC}^{VSI}} \underline{i}_{abc}' \end{cases} \tag{59}$$

The definition of the DC and AC scaling factors of the voltage and current will be defined in Chapter IV when addressing the interconnection between the voltage source inverter and the PMSM.

4.3.2 Conditions of linear losses-to-power scaling of inverters

By examining the equations incorporated within the DC power adaptation elements of the inverter (58), it is possible to establish conditions for achieving linear losses-to-power scaling of the inverter.

The first condition is to preserve the DC bus voltage rating. This is possible by adjusting $K_{v,DC}^{VSI}$ as shown in (60). This condition allows keeping the same voltage rating between the reference and scaled inverters. Furthermore, this is essential to preserve the base speed of the machine, which is one of the requirements of linear scaling of electric drive systems.

$$K_{v,DC}^{VSI} = 1 \tag{60}$$

The second condition is to nullify the equivalent current Δi_{DC} that represent the non-linear scaling of the losses (61). From the analysis performed in Section 4.2.1, it is already proved that the impact of this term is marginal. The following analysis is intended to elucidate the conditions leading to perfect linear scaling of the losses.

$$\Delta i_{DC} = 0 \tag{61}$$

To find the condition that results in (60), the scaling of the conduction and switching losses can be formulated as a function of equivalent loss terms ΔP_{cond}, (62), and ΔP_{sw} (63), and a power scaling factor K_P^{VSI} (64). These latter can be added if needed, following what was done for the PMSM.

$$P'_{\text{cond}} = K_P^{\text{VSI}} P_{\text{cond}}^0 + \Delta P_{\text{cond}} \tag{62}$$

$$P'_{\text{sw}} = K_P^{\text{VSI}} P_{\text{sw}}^0 + \Delta P_{\text{sw}} \tag{63}$$

with the power scaling factor of the inverter K_P^{VSI} is expressed as follows

$$
\begin{aligned}
K_P^{\text{VSI}} &= K_{v,\text{DC}}^{\text{VSI}} K_{i,\text{DC}}^{\text{VSI}} \\
&= K_{i,\text{DC}}^{\text{VSI}} \qquad \text{if (60)}
\end{aligned} \tag{64}
$$

Therefore, the conditions that lead to a linear scaling of the losses according to the power are indicated in (65).

$$
\begin{cases}
\Delta P_{\text{cond}} &= 0 \\
\Delta P_{\text{sw}} &= 0
\end{cases} \tag{65}
$$

To ensure the last condition (65), it is essential to comprehend how the parameters involved in the power loss model of the inverter (52)-(54), presented in Section 4.2.1.1, vary according to changes in the power rating. The switching functions $\underline{s}_{\text{VSI}}$ and the power factor $\cos\varphi$ do not change during the scaling process, if the voltages of the reference and scaled inverters are linearly scaled. It remains to know how the on-sate resistance and the threshold voltage scale. To address this, two scaling factors $K_{r_{\text{on}}}$, and $K_{V_{\text{ce0}}}$ for the on-state resistance and the threshold voltage, respectively, are defined as given in (66), and (67).

$$K_{r_{\text{on}}} = \frac{r'_{\text{on}}}{r_{\text{on}}^0} \tag{66}$$

$$K_{V_{\text{ce0}}} = \frac{V'_{\text{ce0}}}{V_{\text{ce0}}^0} \tag{67}$$

To end up with a linear power-to-losses scaling of the conduction losses (65), (66), and (67), should meet the following conditions mentioned in (68) and (69). These conditions will be subsequently checked and discussed based on the datasheet of different power-rated inverters in the next section.

$$K_{r_{\text{on}}} = \frac{1}{K_{i,\text{DC}}^{\text{VSI}}} \tag{68}$$

$$K_{V_{\text{ce0}}} = 1 \tag{69}$$

Regarding switching losses, the parameters f_{sw}, V_{DC}, V_{ref}, and k_v are assumed unchanged during the scaling process. A scaling factor K_E for the dissipated energies, during the turn-on, and turn-off states, of the switches is expressed in (70). To achieve a linear switching losses-to-power scaling (65), (70) should be equal to 1, which results in the conditions reported in (71) for the scaling of the parameters a_{VSI}, b_{VSI}, and c_{VSI}, defined in (54).

$$K_E = \frac{E'}{E^0} \tag{70}$$

$$\begin{cases} a'_{\text{VSI}} &= \dfrac{1}{K_{\text{i,AC}}^{\text{VSI}}} a_{\text{VSI}}^0 \\ b'_{\text{VSI}} &= b_{\text{VSI}}^0 \\ c'_{\text{VSI}} &= K_{\text{i,AC}}^{\text{VSI}} c_{\text{VSI}}^0 \end{cases} \tag{71}$$

To introduce a geometric layer into the linear scaling method, the examination of equation (48), which describes an efficiency scaling law based on the choice of preserving the temperature rise, serves as a starting point. To this end, it is essential to recall that linear scaling assumes that the efficiency of the inverter is preserved, i.e. $\eta'_{\text{VSI}} = \eta_{\text{VSI}}^0$ within the torque-speed plane of the electric drive. By incorporating this assumption into (48), a scaling law for the volume can be derived as a function of the power scaling as described in (72). This leads to the conclusion that linear scaling is a particular case of the scaling choice that preserves the temperature rise.

$$V'_{\text{VSI}} = \left(\frac{P'_{\text{VSI,out}}}{P_{\text{VSI,out}}^0} \right)^{3/2} V_{\text{VSI}}^0 \tag{72}$$

4.3.3 Validation of the derived conditions based on datasheet data

The validation of the earlier derived conditions is conducted based on the inverter presented in Table 11. The inverter FS600R07A2E3 with a current rating of 600 A is selected as a reference, resulting in upscaling and downscaling cases of the current rating of 1.33, and 0.67 respectively. The voltage rating of the inverter under investigation is the same. From Table 11, it can be observed that the scaling conditions for the on-state resistance and the threshold voltages defined in (68), and (69) are upheld. This can be attributed to the use of identical power switches in parallel by inverter manufacturers to achieve a given current rating [77]. Consequently, a linear power-to-losses scaling of the conduction losses can be achieved. However, the identified parameters of the turn-on energies shown in Table 12 indicate that the conditions outlined in equation (71) are not met, leading to the conclusion that a linear switching loss-to-power scaling cannot be achieved. This is true for the upscaling and downscaling cases. This can be explained by the fact that the experimental characterization of the dissipated energy of different power-rated inverters is conducted with different test conditions, specifically the gate resistance [199], as defined in the datasheets [197]. Even though the conditions for the switching losses are not met, the impact of the efficiency is marginal. This is demonstrated in Section 4.2.1.2 of this chapter, where a comparison between linear scaling and the benchmark of different inverters is conducted. The result of this comparison demonstrates an average discrepancy of efficiency of less than 0.5% for upscaling and downscaling cases. This outcome holds significance for the assessment of energy consumption later in Chapter IV.

5 Conclusion

In this chapter, a comprehensive analysis and a thorough comparison are conducted of the scaling laws of the electric drive systems, encompassing IGBT-based inverters and PMSM. This comparison assessed the efficiency map scaling considering different scaling choices not only for PMSM but also for inverters. This contributes to the current literature on the scaling

of, PMSM and inverters by providing a clear understanding of the effect of each scaling method for each component. Significant emphasis is paid to the examination of the linear scaling method for both components of the electric drive, as the existing literature currently lacks a comprehensive understanding of its fundamental principles and resultant outcomes in terms of loss scaling. Regarding PMSM, linear scaling has been compared to geometric scaling laws based on three scaling choices that consist of preserving the magnetic field density, the temperature rise in the windings, and a hybrid choice that combines the aforementioned choices. Regarding IGBT-based converters, linear scaling is compared against an efficiency benchmarking of three commercialized inverters of the same series family. Moreover, the analysis encompasses other scaling choices available in literature, such as data-driven power loss scaling, and scaling laws based on preserving power density and temperature rise between the scaled and the reference inverters. Additionally, a new organization of the scalable models of both IGBT-based and PMSM has been proposed using the EMR formalism by keeping the reference model of the components fixed but complemented by power adaptation elements. A new formulation of the modeling equations of power adaptation is herein proposed in this work to include the non-linearity aspect of the scaling process. This contribution enhances the utilization of power adaptation within the EMR formalism. This new structuration of the power adaptation elements highlights conditions that result in a linear scaling case of the PMSM and the inverters.

The findings of the comparative analysis in this chapter are summarized as follows:

- The difference in terms of efficiency scaling between linear geometric scaling methods of PMSM depends on the operating regions within the torque-speed plane. This finding is of high significance to understanding the reliability of the linear scaling method for energy consumption in Chapter VI when investigating driving cycles with varying operating point distributions.
- The efficiency map scaling comparison between linear losses-to-power scaling and geometric scaling laws based on different scaling choices of PMSM reveals that the efficiency discrepancy is greater in high-torque and low-speed regions, where copper losses prevail. This efficiency disparity is more pronounced in downscaling cases, particularly when comparing linear scaling and geometric scaling that preserves the magnetic field density. In the last aforementioned region, the difference in terms of efficiency is less significant when comparing linear scaling with geometric scaling based on the preservation of the temperature rise. The same applies to the comparison of linear scaling with the hybrid choices. This is explained by a large difference in terms of the copper loss scaling. The frequency of usage of these regions will be assessed in Chapter IV to evaluate whether this difference will impact the energy consumption results.
- The efficiency difference between linear and geometric scaling laws decreases at high-speed regions of the machines, where the iron and mechanical losses dominate. This is true for upscaling and downscaling cases and the different scaling choices.
- The geometric scaling choice that preserves the temperature rise poses challenges to be implemented due to saturation concerns. It has been found that a fourth

scaling factor, for either the air gap or the length of the magnets, is needed to use this scaling choice. This point lacks clarity in earlier literature and is highlighted in this work.

- The efficiency map scaling comparison between losses-to-power scaling and efficiency benchmarking of commercialized inverters demonstrate comparable results. This is attributed to the linear scaling of conduction losses and the non-significant impact of nonlinearities in the switching losses throughout the scaling process. The last statement is true for upscaling and downscaling cases.

- A methodology is presented to incorporate a geometrical information layer into the linear losses-to-power scaling method of PMSM. The linear scaling method is demonstrated as a particular case of the geometric scaling laws. There exists at least one combination of axial and radial scaling factors that yield a particular case of linear scaling of losses. Nonetheless, the last statement holds for solely upscaling cases. It has been demonstrated for such scaling cases that no geometric combinations resulted in linear scaling cases.

- A volume scaling of the inverter is derived for the linear scaling method.

Chapter III

Scaling of planetary gearboxes

1 Introduction

Although the literature review reveals that many studies have made considerable efforts to study the scalability of electric machines and power electronic converters, scarce contributions have been made to the scalability of gearboxes. One of the few contributions to scaling laws for gearboxes has been proposed by Pott in [200]. Simple scaling laws have been found by altering the torque and speed based on a common general scaling factor. Budinger et al. in [141] have derived scaling relationships of the main parameters of different types of gearboxes as a function of torque and speed scaling factors. A more extensive derivation of scaling laws has been proposed by Saerens et al. [31]. Scaling laws of different types of gearboxes are proposed based on the main design parameters, e.g. length, diameter, number of stages, and gearbox ratio. The derived scaling laws in the aforementioned reference make it possible to predict maximal output torque, mass, and inertia and have shown a good correlation with the catalog of different manufacturers. Furthermore, Weinberger et al. in [201] have investigated a scaling methodology to downsize a wind turbine planetary gearbox that maintains dynamic similarity between the reference and scaled gearboxes.

Previous studies have exclusively focused on geometric scaling to achieve a new desired torque demand or to have insights into the mass and inertia of the scaled gearbox. However, scaling laws for gearboxes taking into account the losses are still lacking. Efficiency and power loss are fundamental metrics for all mechanical transmissions. Nowadays, high efficiencies of 96%-98% are attained in the rated operating point [202]. At partial load regions, the efficiency drops significantly [153]. Therefore, there is a need to benchmark the efficiency and power loss across the possible operating points of the gearbox. This is of high importance to quantify the energy consumption of automotive applications, in which the operating points are widely dispersed across the torque-speed plane. Nevertheless, efficiency benchmarking of gearboxes through experimental testing or numerical methods is still time and effort-consuming. To date, no scaling laws for predicting power losses and efficiency have been proposed in literature. The conclusion drawn in [201] substantiates the last statement, asserting that "*it is not easily possible to transfer the efficiency results from the scaled gearbox to the original gearbox*". In light of this, this chapter aims to address this gap by proposing an initial framework for scaling laws

of the power loss of gearboxes, with specific emphasis on dip-lubricated[8] planetary gearboxes. This choice is motivated by the growing interest in planetary gearboxes for automotive applications, as reported in Chapter I, due to their compact design and co-axial arrangement. Given the diverse varieties of topologies, this investigation particularly focuses on conventional planetary gearboxes with a single degree of freedom, often referred to as planetary reducers. This topology, which is illustrated in Fig. 52, is considered highly suitable for electric vehicles with a mono-drive system. While there are alternative topologies, commonly employed as power-split devices in the context of hybrid electric vehicles or recently in multi-drive systems, it is noteworthy that these alternatives are not the primary focus of this study. Ultimately, the goal of this chapter is to provide an initial framework of scaling laws that can be extended later to different topologies. Additionally, a special focus is given to high-speed planetary reducers in this work. This is because of the specifications of the automotive applications, where high-speed powertrain concepts are becoming more and more attractive due to the potential for improved power density, as previously mentioned in 4.2.2 of Chapter I [84].

Sun gear   Ring gear

Planet carrier   Planet gears
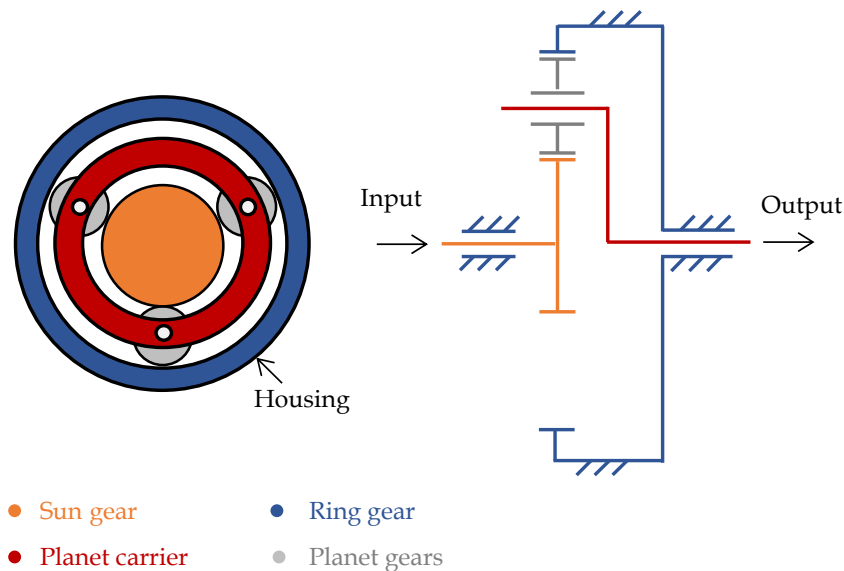
Fig. 52: Schematic of planetary reducers

As discussed in Chapter II for the electric drive systems, scaling laws can be derived through the manipulation of models based on geometric similarity and scaling choices (conservation of physical properties). Alternatively, a data-driven approach can be undertaken, involving deriving scaling laws from datasets obtained from catalogs or measurements. In the case of planetary reducers, the modeling of the losses is challenging. This is because of their particular kinematics, which result in more complex fluid flows than the ones observed in parallel-shaft gearboxes, as illustrated in Fig. 53. Due to centrifugal effects, the oil sump tends to disappear and most of the oil is splashed at the housing periphery, resulting in an oil ring [203]. Of utmost importance, the literature review shows a lack of reliable information on the power losses at high-speed values of planetary gearboxes. This makes the use of the existing models in literature questionable as they were formulated and validated at low and medium

---

[8] A dip-lubricated gearbox uses an oil sump, i.e. a reservoir of oil. As the gears rotate, the lower parts of the gears dip into the oil sump, causing oil to splash onto the parts to be lubricated.

speeds, less than 5000 rpm [203]. On the other hand, the automotive industry is witnessing a remarkable trend toward high speed. Consequently, this presents greater challenges when deriving scaling laws for gearboxes.
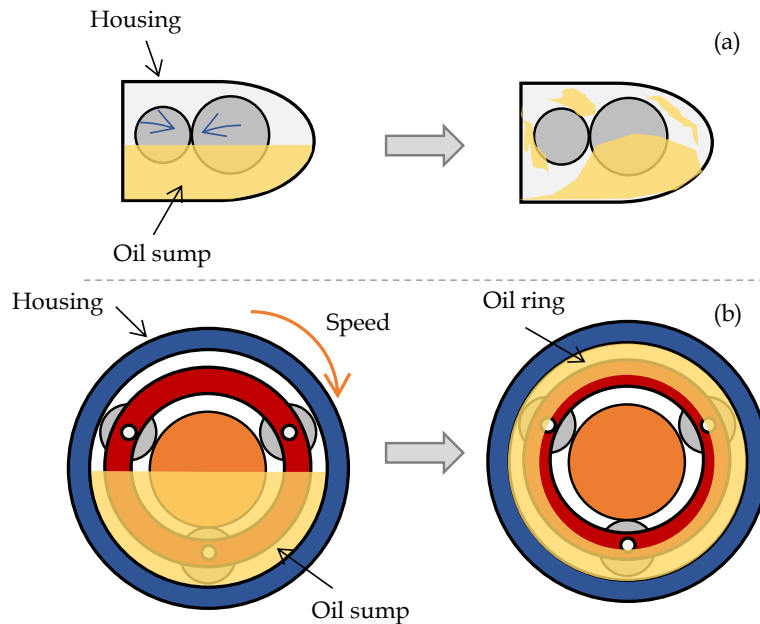
Fig. 53: Oil flow inside a dip-lubricated: (a) parallel-shaft gearboxes, (b) planetary reducers

Given the limited data on the losses of planetary gearboxes at high-speed operating points, there is a need for an experimental investigation. This aids in acquiring knowledge about high-speed power loss and serves as a starting point to derive scaling laws. Hence, a data-driven approach is herein adopted. It is worth emphasizing that it is neither the goal of this work to improve the existing models nor to validate them at high speed. Ultimately, the main purpose of this chapter consists in deriving fast scaling laws for conventional planetary reducers. This has not been presented in literature so far. The key contributions of this chapter are summarized as follows:

- Experimental characterization of the power loss components, i.e. load-independent and load-dependent losses, of dip-lubricated planetary gearboxes at high-speed values up to 14,000 rpm of the sun shaft. The available experimental data to quantify both loss components for planetary gearboxes are scarce. The current state of the art is limited to 8000 rpm (sun shaft) in terms of experimental investigation of load-independent losses [204] and 5000 rpm (sun shaft) for load-dependent losses [205]. The results were reported for oil-jet lubricated planetary gearboxes.
- Data-driven modeling of load-independent and -dependent losses based on high-level specifications of the e-axle, namely the maximal input speed, output torque, and gear ratio.
- Fast and accurate generation of efficiency maps of scaled gearboxes using data from a reference gearbox combined with scaling laws.
- Assessment of the reliability of linear losses-to-power scaling method for gearboxes, similar to the undertaken approach in Chapter II for electric drive systems. It is worth

mentioning that the application of the linear scaling method is confined to the electric drive systems and is seldom used to scale the power loss of gearboxes.

- Reorganization of the scalable model of the planetary gearbox following the concept of the EMR-based scaling laws.

This chapter is organized as follows. Section 2 presents the approach adopted to derive power loss scaling laws. Section 3 describes the power loss modeling, deduced from experimental campaigns. The scaling laws are derived and validated in Section 4. Section 5 presents the EMR-based scaling laws of the planetary gearbox.

2 Adopted approach

To obtain a scalable gearbox model, scaling laws for the following properties need to be found: maximal torque, maximal speed, gear ratio, inertia, mass, and losses. In the subsequent sections, an overview of the scaling laws available in the literature is provided, and the adopted approach to derive power loss scaling laws is described.

2.1 Overview of the available scaling laws for gearboxes in the literature

Pott in [200] derived simple scaling laws for the torque T and speed Ω according to a general scaling factor s as shown in (73) for reducers with spur gears. According to the derived scaling laws, the power scale proportionally with the scaling factor s. The scaling relationships have been derived, assuming that the maximum centrifugal force F_z exerted on the oil is consistent during the scaling process (74). Therefore, this leads to a speed relationship inversely proportional to the square of s (73). The decrease in speed as power increases can be explained based on the limiting speed to build up a fluid film. Note that for (74) to be true, the radius r has to be scaled with s and the mass m with s^3. One limitation of these scaling laws is their inability to distinguish between the effect of a change in length or diameter, which can be of high importance due to restricted available space in an automotive application. Additionally, no validation has been provided to evaluate the accuracy of these laws.

$$\begin{cases} T' &= s^3\, T^0 \\ \Omega' &= s^{-2}\, \Omega^0 \\ P' &= s\, P^0 \end{cases} \tag{73}$$

$$F_z' = F_z \;\Rightarrow m\Omega^2 r = m'\Omega'^2 r' \tag{74}$$

Budinger et al. have derived scaling laws for different types of reducers, namely parallel-shafted reducers with spur and worm gears, cycloidal drive, and planetary reducers, based on another choice that consists in preserving the bending[9] stress σ_B between the reference and scaled gearboxes (75) [141]. This choice was motivated by the need to ensure materials consistency within a family series of gearboxes. A scaling factor, denoted as x, has been introduced in the scaling process as the ratio between the geometrical dimensions of the reference y^0 and scaled y' gearboxes (76). Based on this scaling factor relationships for the volume V_{gb}, mass

---

[9] When two gears are engaged, there is a normal force pressing against the tooth, which leads to a bending action that generates a tensile stress at the root surface of the gear.

m_{gb}, and inertia I_{gb} have been found as shown in (77)-(79) respectively. Following the scaling choice (75), relationships for torque and speed are derived as given in (80), and (81) respectively. More details on the derivation of the aforementioned scaling laws are available in [141]. To assess the accuracy of the scaling laws, a comparison with data from gear manufacturers was made for worm gears, with a particular focus on mass and inertia scaling. The average deviation between the scaling laws and the catalog data for the two last parameters was found to be below 10%.

$$\sigma'_{\text{B,max}} = \sigma^0_{\text{B,max}} \tag{75}$$

$$x = \frac{y'}{y^0} \tag{76}$$

$$V'_{\text{gb}} = x^3 V^0_{\text{gb}} \tag{77}$$

$$m'_{\text{gb}} = x^3 m^0_{\text{gb}} \tag{78}$$

$$I'_{\text{gb}} = x^5 I'_{\text{gb}} \tag{79}$$

$$T'_{\text{gb}} = x^3 T^0_{\text{gb}} \tag{80}$$

$$\Omega'_{\text{gb,max}} = x^{-1} \Omega^0_{\text{gb,max}} \tag{81}$$

A more extensive derivation was proposed by Saerens et al. that considers separate scaling procedures in the axial and radial directions for different topologies of gearboxes [31]. Based on stress analysis, the maximum torque $T'_{\text{out,max}}$ of parallel shaft and planetary gearboxes, with the same gear ratio, can be scaled as given in (82):

$$T'_{\text{out,max}} = \frac{l\,d^2}{a} T^0_{\text{out,max}} \tag{82}$$

in which l refers to the core length of the gearbox, d is the outer diameter, and a represents the number of stages. The torque scaling law can be seen as a change in the volume of the gearbox divided by the number of stages. If the length and diameter are proportionally scaled with a scaling factor x assuming the same number of stages, the output torque scales with x^3. This is aligned with the scaling laws derived in [141], [200] but with more insights into the axial and radial scaling procedures. Additionally, the impact of the gear ratio k_{gb} scaling has been incorporated in the scaling laws leading to different relationships based on the topology of the gearbox as shown in (83). Besides scaling laws for torque, a scaling law for inertia is depicted in (84).

$$\begin{cases} T'_{\text{out,max}} & \propto & k_{\text{gb}}^2 \dfrac{l\,d^2}{a} T^0_{\text{out,max}} & \text{parallel shaft gearbox} \\[2ex] T'_{\text{out,max}} & \propto & \dfrac{k_{\text{gb}} - 2}{\left(k_{\text{gb}} - 1\right)^2} \dfrac{l\,d^2}{a} T^0_{\text{out,max}} & \text{planetary gearbox} \end{cases} \tag{83}$$

$$J' \propto k_{\text{gb}}^2 \frac{l\,d^4}{a} J^0 \tag{84}$$

The accuracy of the derived scaling laws has been demonstrated based on manufacturers' catalogs. All the derived laws show globally a good agreement with the data extracted from the catalogs. To validate the torque scaling law in (83) for planetary gearboxes, Fig. 54.a shows a plot illustrating maximal torque values as a function of geometric parameters and the number of stages of gearboxes from different manufacturers. An orange line can be observed which gives the design solution according to the proposed scaling laws. As can be noticed, some points are below the line. This is explained by the fact that higher-stage ratios use different stress levels and different safety factors. From Fig. 54.b, it can be observed that the orange line, which represents the derived law of inertia (84), follows closely the inertia values of the different gearboxes, extracted from manufacturers' catalogs.

(a)   (b)
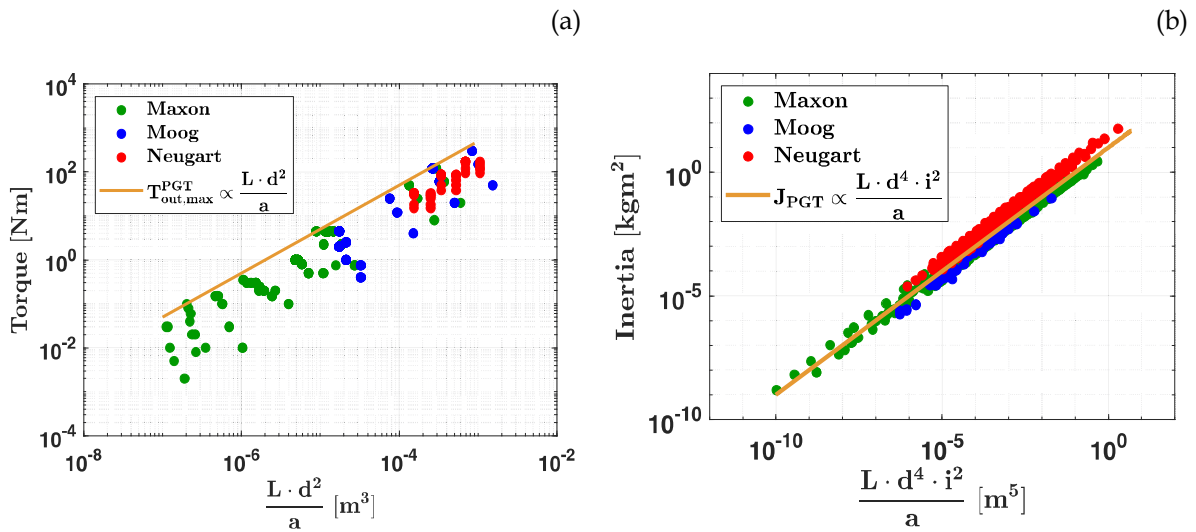
Fig. 54: Validation of the scaling laws derived for planetary gearboxes: (a) maximum output torque, (b) inertia. The scaling laws results are represented by the orange line. The figures were made by [31].

Despite the valuable contributions made by the discussed references, power loss scaling has not been addressed. The power loss scaling was left independent from the scaling process without providing any explanations.

2.2 Theoretical power loss models

Power losses P_{losses} of any geared transmission can be divided into two main groups (85), namely: 1) load-dependent power losses P_{LD}, often called mechanical losses or torque-dependent, and 2) load-independent power losses P_{LID}, also known as spin losses or speed-dependent losses [206], [207]. Load-dependent losses originate from friction in the mating surfaces at the gear meshes and bearings due to the sliding and rolling actions of the lubricant film [207]. The load-independent losses originate from the interaction between the gearbox components with the surrounding medium under no-load conditions (oil, air, or a mixture of oil and air). The load-independent power losses are caused by various phenomena such as churning or windage and squeezing [204]. Churning loss is caused by a friction moment exerted by a fluid mixture (oil and air) on the gears when they are dipping and circulating in the oil sump. When a jet or injection lubrication is used, this kind of loss is referred to as windage loss as only one single fluid phase (air) is involved. The contribution of these loss components becomes

significant with high rotational speeds [208]. Squeezing loss is caused by compressing the oil between the flanks of the engaged gears.

$$P_{\text{losses}} = P_{\text{LD}} + P_{\text{LID}} \tag{85}$$

To elucidate the challenges involved in the derivation of power loss scaling, this section provides an overview of the theoretical power loss models of mechanical transmissions. An abundance of models can be found in literature to compute the load-dependent and -independent losses. Most of the models currently used are briefly presented in the sequel.

2.2.1 Load-dependent losses

The load-dependent losses are the sum of the gear mesh losses P_{gears} that occur in the internal and external meshes of the planetary gears and the sum of the frictional losses generated by the bearings $P_{\text{br}}^{\text{LD}}$.

$$P_{\text{LD}} = \sum P_{\text{gears}} + \sum P_{\text{br}}^{\text{LD}} \tag{86}$$

The models to predict the friction at the mating contact of gears differ in terms of formulation. Models that employ a constant coefficient of friction along the contact surface or empirical formulae [122], and real-time transient analysis of elastohydrodynamic lubrication [209] can be cited. A well-known model to compute the gear mesh is the model developed by Ohlendorf (87) [122]. In this model, the gear mesh loss P_{gears} is expressed as a function of the transmitted power P_{in}, the average friction coefficient in the gear contact μ, and the gear loss factor H_{v}.

$$P_{\text{gears}} = P_{\text{in}} \, \mu \, H_{\text{v}} \tag{87}$$

The gear loss factor H_{v} can be calculated using the following expression (88):

$$H_{\text{v}} = \frac{\pi}{Z \cos \beta} \frac{(k_{\text{gb}} + 1)}{k_{\text{gb}}} \, (1 - \varepsilon_\alpha + \varepsilon_1^2 + \varepsilon_2^2) \tag{88}$$

with k_{gb} the gear ratio of the gear mesh, β the helix angle, Z refers to the tooth number of the pinion (driver gear), ε_α is the profile contact ratio (the ratio between the length of the arc of contact and circular pitch), ε_1, and ε_2 are the tip contact ratios. Note that a graphical gear nomenclature is provided in Appendix V.1 to illustrate the preceding geometrical parameters.

The average coefficient μ is assumed constant along the mesh cycle and can be calculated using the model of Höhn [122], as shown in the following equation:

$$\mu = 0.048 \left(\frac{F_{\text{bt}}/f}{\rho_c \, v_{\Sigma C}} \right)^{0.2} \eta_{\text{oil}}^{-0.05} R_{\text{a}}^{-0.25} \, X_{\text{L}} \tag{89}$$

where F_{bt} is the transverse load, f is the face width, $v_{\sum C}$ is the sum of tangential velocities at the pitch circle diameter, ρ_c is the normal radius of relative curvature at the pitch diameter, η_{oil} is the dynamic viscosity at sump temperature, R_a is the mean roughness value, and X_L is an empirical factor to adjust the coefficient of friction based on the lubricant.

The load-dependent losses of each bearing can be calculated, following the SKF[10] model, as a function of rolling T_{rr} and sliding T_{sl} frictional torques and speed Ω_{br} [210].

$$P_{br}^{LD} = (T_{rr} + T_{sl})\Omega_{br} \tag{90}$$

2.2.2 Load-independent losses

The state-of-the-art in modeling load-independent losses shows that most models in literature are based on empirical studies, and dimensional analysis [123]. Most of these load-independent models have been developed from dedicated measurement campaigns to investigate specific load-independent power loss components. The experimental results are then correlated with the models. Further works resort to computational fluid dynamic analysis for a better understanding of the behavior of the air-oil lubricant mixture [211]. Nevertheless, the last method is time and effort-consuming.

The load-independent losses of dip-lubricated planetary gearboxes are the sum of the churning loss P_{ch} due to the planet gears and the carrier, squeezing losses in the internal and external meshes, viscous loss of the bearings, and seal loss.

$$P_{LID} = \sum P_{ch} + \sum P_{sq} + \sum P_{br}^{LID} + P_{seal} \tag{91}$$

Boni et al. in [203] have derived a model to compute the churning loss of the planets and the carrier of planetary reducers, based on the work of Changenet et al. [212] (92). The churning loss generated by the sun gear was not considered in the model because it was impossible to have an oil ring thick enough to reach the sun. The aforementioned model was the first to consider the fluid flows of planetary gearboxes (e.g. the oil ring) and was validated for speed values below 3000 rpm (sun shaft).

$$P_{ch/x} = \frac{1}{2}\,\rho\,C_x\,S_x\,r_x^3\Omega_x^3 \tag{92}$$

In the last equation, the subscript x refers either to the planet gears or the planet carrier, ρ is the lubricant density, C_x is the drag coefficient, S_x is the wet surface, r_x is the pitch radius, and Ω_x is the angular speed of the considered rotating element in [rad/s]. The formulation of the drag coefficients C_c, and C_p of the carrier and the planets are defined based on dimensionless analysis [203].

---

[10] SKF, a well-known manufacturer of bearings, provides models and tools for the computation of the power loss of bearings.

$$
\begin{cases}
C_\text{c} & = & \psi_1 Re_\text{c}^{\psi_2} \\
C_\text{p} & = & \psi_3 \left(\dfrac{f}{r_\text{p}} \right)^{\psi_4} \text{Fr}_\text{p}^{\psi_5} \text{Re}_\text{p}^{\psi_6}
\end{cases}
\tag{93}
$$

In (93), the ψ terms are constant coefficients defined from experimental results over a specific speed range, f refers to the face width, Fr is the Froude number, and Re is the Reynolds number.

For dip-lubricated gearboxes, the squeezing losses can be calculated using the empirical model of Mauz [123]:

$$
P_\text{sq} = 0.0235 \, \rho \, b \, r_\text{p} \, v_\text{t}^{1.2} C_\text{m}
\tag{94}
$$

where v_t is the circumferential speed, and C_m is the splash oil factor of the considered gears.

According to the ISO standards [213], the no-load power loss of the seals P_seal can be expressed as a function of the diameter of the shaft d_sh and the rotating speed of the considered shaft N_sh in [rpm]:

$$
P_\text{seal} = 7.69 \, 10^{-6} \, d_\text{sh}^2 \, N_\text{sh}
\tag{95}
$$

The load-independent power loss of the bearings P_br^LID can be calculated, following the SKF model, as a function of the frictional moment of drag losses T_drag and speed. More details on the expression of T_drag can be found in [210].

$$
P_\text{br}^\text{LID} = T_\text{drag} \, \Omega_\text{br}
\tag{96}
$$

2.3 Motivation of the data-driven modeling approach

The theoretical models are based on detailed design parameters of the gearbox, e.g. the geometrical parameters of the gears. These parameters are often unavailable in the early development phases, which can make the computing task of the losses somewhat complex. Moreover, some models present empirical parameters (e.g. (93)) that have been defined at specific operating conditions (e.g. limited speed range, given temperature, lubricant type, etc). Therefore, any change in operating conditions, e.g. high-speed values, will raise questions about the accuracy of the model. Consequently, the empirical coefficients need to be updated based on the new operating conditions. The formulation of the models, in some cases, could also be reconsidered to take into account new phenomena related to the new operating conditions, e.g. the oil ring for planetary reducers. To lend support to the last statements, the accuracy of the models has been assessed for a commercially available planetary gearbox, with a maximal speed of 10,000 rpm, a maximal torque of 120 Nm, and a gear ratio of 8. To accomplish this, the geometric parameters of a planetary reducer have been measured using a digital

microscope from the brand Keyence at the Soete laboratory[11] at Ghent University. Using the measured dimensions of the gears, the churning losses of the planets and the carrier have been computed using (92), and (93), considering the empirical coefficients determined in [203]. Fig. 55.a shows that the results for the churning loss of the planet gears fall within a realistic range, irrespective of their accuracy. However, the churning loss of the carrier represents unrealistic results as can be observed in Fig. 55.b. This can be attributed to the fact that the empirical parameters of the model have been not tuned for the new operating condition of the studied gearboxes, e.g. high-speed values, the lubricant type, the range of values for geometric parameters, etc.
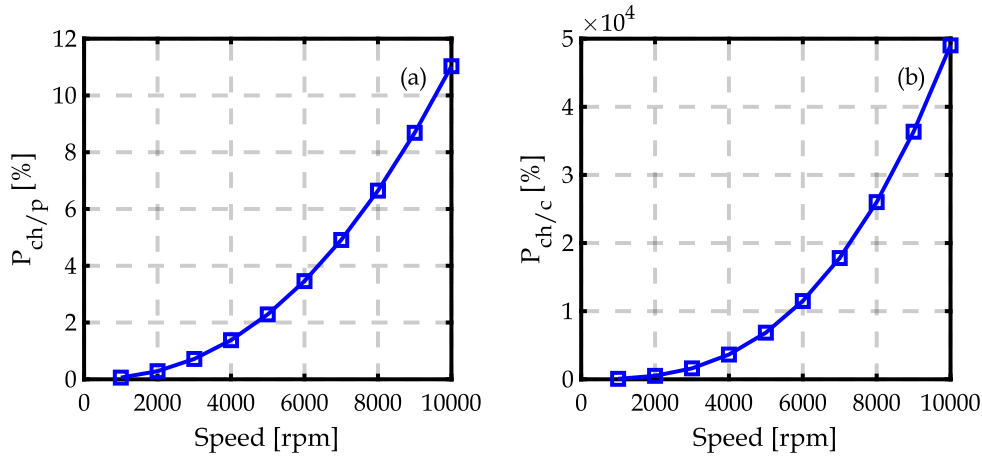
Fig. 55: Computed churning losses in [%] relative to the rated power at 50°C: (a) planets, (b) carrier.

The lack of reliable information on the modeling at high-speed values of planetary gearboxes and detailed design parameters has motivated the adoption of the data-driven modeling approach. A data-driven model is an analytical model that is defined to best fit the surface that represents the data, particularly the losses in this work. The main concept of data-driven modeling is to find straightforward relationships between the losses and top-level parameters of the gearbox (e.g. torque, speed, and gear ratio) without explicit knowledge of the design parameters. This is in line with the purpose of the scaling laws, which are intended to be used at system-level. In this context, different data-driven models have been proposed in the literature to model the overall losses of gearboxes. Examples include quadratic equations [214], [215], or exponential equations [216], including torque and speed terms. A data-driven model based on speed, torque, and gear ratio parameters will be discussed in Section 4 of this chapter based on the outcomes of the experimental campaign.

The adopted workflow of this work to derive scaling laws is depicted in Fig. 56. First an experimental campaign is conducted to benchmark the efficiency and the losses of 5 gearboxes. The results of the tests are then split into 2 sets. The first set, named the training set, is used to deduce a power loss model based on the data from solely three tested gearboxes. Next, power loss scaling laws are derived. An intermediary step consists of validating the derived scaling laws using the training set. The second set of data, named the test and validation set, contains the results of the fourth and fifth gearboxes. This set is used to validate the derived scaling laws.

---

[11] https://www.ugent.be/ea/emsme/en/research/soete
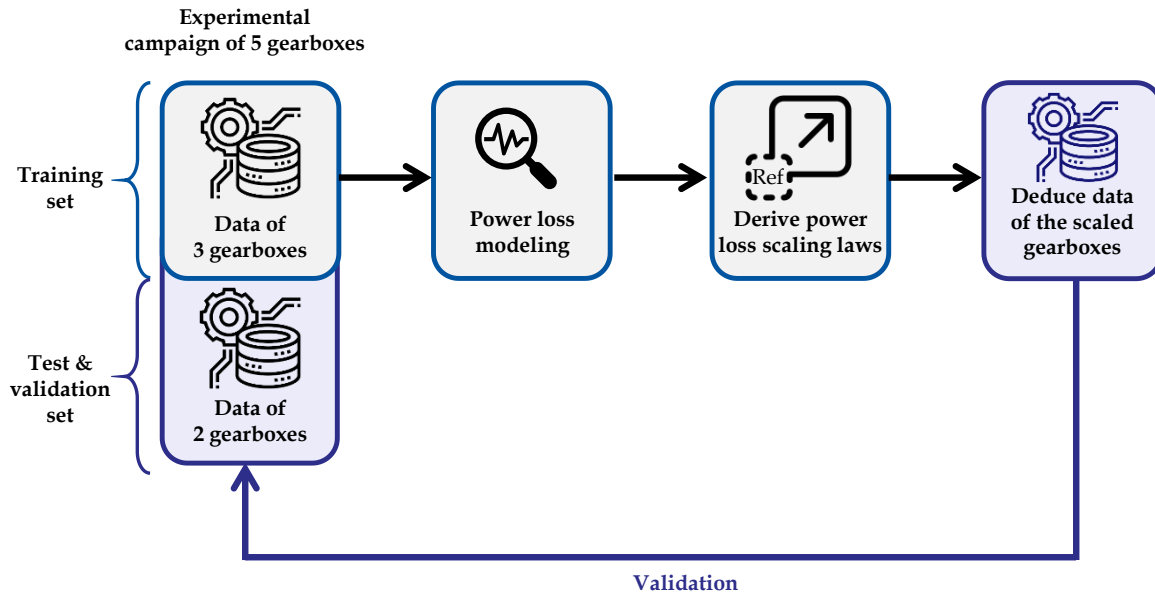
Fig. 56: Adopted workflow for the derivation of the scaling laws

3 Power loss modeling

This section deals with power loss modeling based on extensive experimental investigations. For this aim, the experimental setup is first presented and discussed, followed by a comprehensive analysis of the outcomes of the experimental campaign.

3.1 Overview of the experimental campaign specifications

3.1.1 Tested gearboxes

Five commercial planetary gearboxes, belonging to the same family series, have been considered for the experimental campaign with different speed and torque ratings and gear ratios [217]. The tested specimens consist of one single sun, a carrier with three planets, and a fixed ring gear. The sun shaft is defined as the input of the gearbox, whereas the carrier shaft is the output of the gearbox. This configuration enables higher torque at the output of the gearbox. The main parameters can be found in Table 14. Note that the torque rating of the gearboxes used in this study does not correspond to automotive applications. In effect, having access to components designated for automotive applications is challenging due to confidentiality reasons. However, the scarcity of commercially available components does not pose a significant obstacle for this work as the selected gearboxes allow for investigating different scaling cases, e.g. torque scaling, speed scaling, and gear ratio scaling. The speed rating of the selected gearboxes, on the other hand, does align with automotive applications, making them relevant for this investigation.

The training set, i.e. the first set in Fig. 56, comprises the three first gearboxes, whereas the last two gearboxes are designated for the test and validation set. This selection is justified by the substantial range of torque, speed, and gear ratios exhibited by these three first gearboxes,

which are deemed appropriate for deriving the scalable model. A sensitivity analysis of the gearbox selection will be later presented in Section 4.

Table 14: Specifications of the studied planetary gearboxes. The differences relative to the first gearbox are highlighted in bold, while the common parameters are in italics. The maximal torque can be attained for 30,000 rotations of the output shaft.

	1st gearbox	2nd gearbox	3rd gearbox	4th gearbox	5th gearbox
Nominal torque at the carrier [Nm]	39	**75**	39	**37**	**155**
Maximal torque at the carrier [Nm]	62	**120**	62	**59**	**248**
Nominal speed at the sun gear [rpm]	5000	**4500**	**4400**	5000	**4000**
Maximal speed at the sun gear [rpm]	14,000	**10,000**	14,000	14,000	**8500**
Gear ratio [-]	8	8	**4**	**7**	8
Number of teeth of the sun gear [-]	12	12	**30**	**15**	12
Number of teeth of the planet gear [-]	36	36	**29**	**37**	36
Number of teeth of the ring gear [-]	84	84	**90**	**90**	84
Number of planets [-]			*3*		
Number of stages [-]			*1*		
Gears type [-]			*Helical gears*		
Type of lubrication [-]			*Dip-lubricated*		

3.1.2   Test metrics and procedure

The test matrix consists of two test sets, namely unloaded and loaded tests, to experimentally separate load-dependent and load-independent losses. The unloaded tests are performed under no load applied to the output shaft to quantify the load-independent losses at given speed values. The loaded test is carried out to measure the overall losses at different combinations of rotational speed and torque. Both tests are carried out at different temperature values. The tested points for each individual test and gearbox are presented in Appendix V.2. To isolate the load-dependent losses, the load-independent losses can be subtracted from the results of the loaded test at the same speed, following the assumptions made in the state of the art [205]. Given that the load-dependent losses are determined through two separate sets of tests, it is noteworthy to mention that this procedure may introduce some inaccuracies. For each gearbox, the possible operating points are evaluated, while maintaining the temperature at a predefined value. The entire speed range is scanned with a step of 2000 rpm. For the loaded test, the torque is changed between minimal and maximal values, for each speed, that is selected to achieve a reasonable number of test points. A minimum of 50 points, measured over the entire operating range of each gearbox, is considered. For the sake of synthesis, all the results reported in the following sections consider a housing temperature of 50°C for both tests. This temperature choice corresponds to the rated temperature. Notwithstanding, it is worth mentioning that Appendix V.6 presents additional results obtained under different temperature values, which provide further insights into the temperature effect. All measurements are logged based on a defined temperature range of the gearbox housing, which is maintained at 50±3°C. The tested temperature of the gearbox is achieved by adjusting the operating points to either cool down or heat up the gearbox since no external temperature regulation system is accessible. The temperature of the test room is set at 23°C for all the tests, using an air conditioning system, and maintained at a range of ±1°C. Each test, in any configuration, is repeated

at least twice to confirm the consistency and the reproducibility of the measurement. The initial steps of testing for each gearbox consist in performing a run-in cycle. This test involves running the gearbox at nominal torque and speed, as the gears and bearings are used for the first time. Based on the test procedure established in [218], a test period ranging from 24 to 48 hours is sufficient to complete a run-in cycle. This test ensures that the gear teeth are smoothed and that the gearbox achieves its nominal efficiency. It also allows for determining the rated temperature of the housing. Subsequently, the gearbox is stopped and cooled down until it reaches the ambient temperature. It is then loaded once again at nominal torque and speed. If the same consistent efficiency value is achieved during this subsequent test, it signifies that the gearbox has completed its running-in process. To gain more insights into the testing procedure, Appendix V.2 provides a comprehensive flowchart that presents the different steps involved. Lastly, note that for each intended measurement point, a dataset is obtained and recorded at intervals of 1 second. Subsequently, the consecutive recordings are subjected to averaging to mitigate the influence of test measurement fluctuations, arising from control imperfections. In Appendix V.3, an assessment of the consistency of the measurement for some operating points is provided, illustrating the extent to which the theoretically constant torque and speed conditions are maintained.

3.1.3   Test bench and instrumentation

For the loaded test, the configuration, shown in Fig. 57, is used to determine the overall losses and efficiency. The input shaft (sun) of the gearbox is driven by a Siemens high-speed induction motor (model reference: 1PH8183), which can reach 15,000 rpm. The output shaft (carrier) is loaded by another induction motor from WEG (model reference: EMI160-L). Two torque sensors, the characteristics of which are given in Table 15, are used to measure the input and output torque of the gearbox. The input speed is measured using an incremental encoder from Siemens (model reference: IN256S/R Q11) with a resolution of 256 pulses/rev. Since the input and output speeds are linked with the gear ratio, only the input speed is measured. Due to the high-speed tests, a support bearing is added between the input torque sensor and the input shaft to provide better mechanical stability. Anticipating the additional losses generated by the last mentioned bearing, these losses have been computed using the SKF toolbox and subsequently subtracted from the measurement outcomes. Several temperature sensors are used to monitor the housing temperature of the gearbox at different locations, the torque sensors, and the ambient temperature. A thermal camera is added to monitor the heat distribution around the housing. Regarding the unloaded test, the load motor is dismounted from the output shaft as depicted in Fig. 58. The data of torque and speed is synchronously logged from all the measurement devices using an HBK e-Drive power analyzer. The temperature data is acquired using the Fluke Hydra Series II data logger.

Table 15: Overview of the torque sensors

Torque sensor	Location	Range [Nm]	Accuracy class [%]	Absolute fault [Nm]	Output signal
Lorenz DR2112	Input (sun)	20	0.1 f.s.	±0.02	Voltage: ±10 V DC
HBK T40B	Output (carrier)	200	0.1 f.s.	±0.2	Frequency: 15kHz
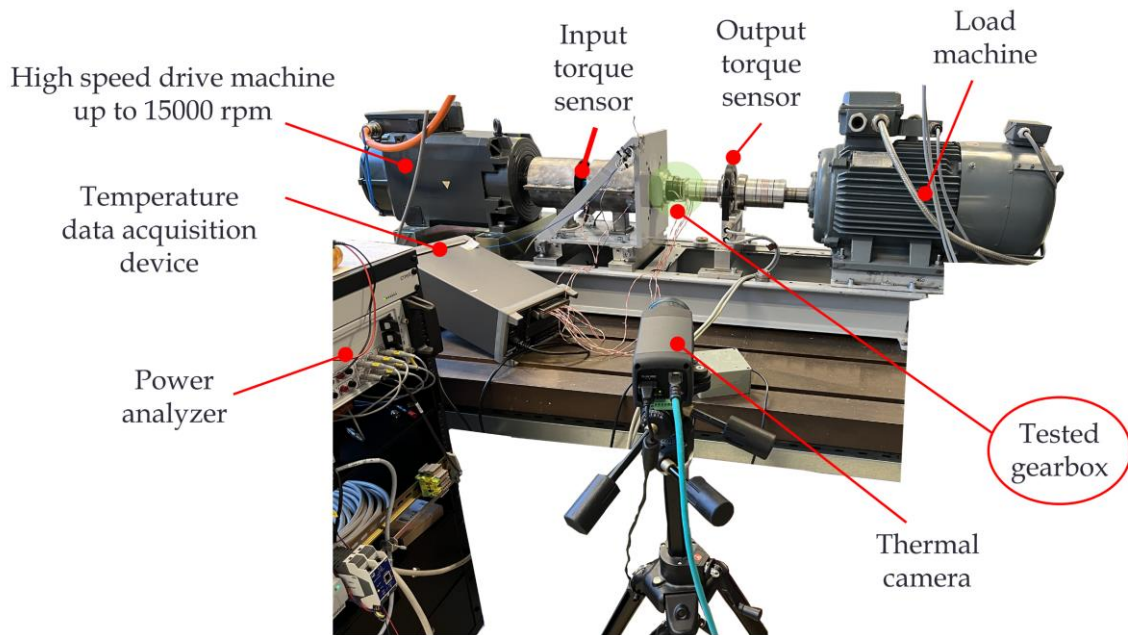
Fig. 57: Loaded configuration of the test bench
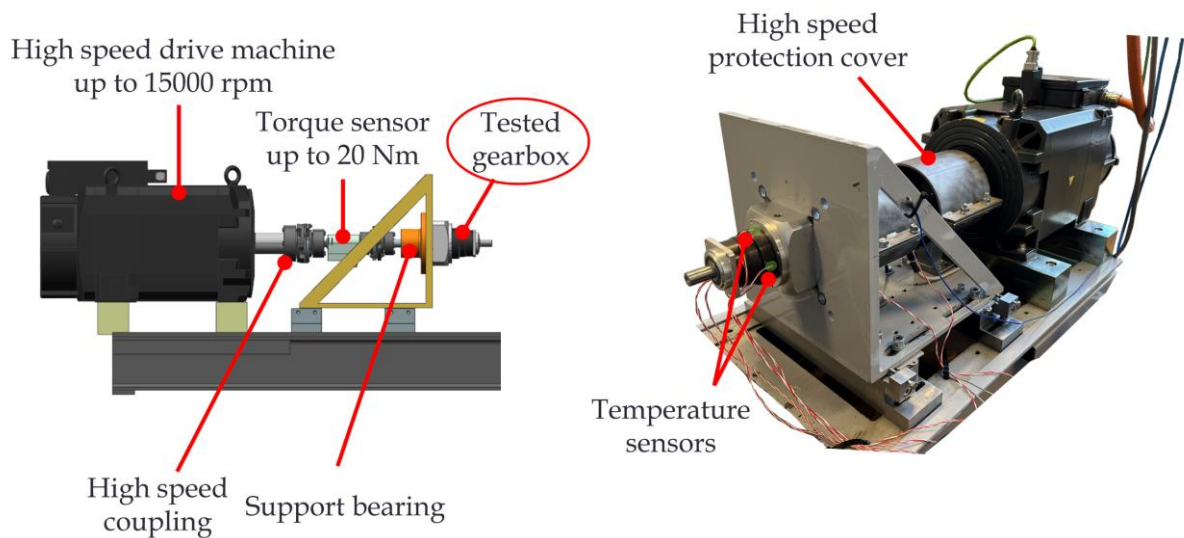
Fig. 58: Unloaded configuration of the test bench

3.1.4 Measurement accuracy

The efficiency of the gearbox η_{gb} can be calculated by comparing the output and input power (97). Since the input and output speed are linked by the gear ratio, the equation can be further simplified as the ratio of output and input torques combined with the gear ratio. However, during experimental testing, the measured efficiency is influenced by various factors, including the measurement uncertainty caused by the instrumentation, as well as the control imperfections.

The measurement uncertainty due to the instrumentation depends on the fault of the measured torques. Note that the fault of the speed measurement does not affect the efficiency, as shown in (97). The fault on the torque consists of the torque signal itself (see Table 15) and the conversion of the signals. For the voltage analog signal of the input torque sensor, the measurement uncertainty is calculated, knowing the reading error and the range error of the power analyzer. These latter are presented in Appendix V.4. The measurement uncertainty, for the captured torque using the frequency port, is introduced by the timer inaccuracies. An example of the accuracy calculation is given in Appendix V.4. The total relative fault RF_{tot} on the efficiency is thus calculated by summing up the relative faults on the torque measurements as given by (98). The absolute fault AF_{tot} is given by (99). As an illustrative case, the absolute fault of the efficiency of the first gearbox is depicted in Fig. 59. An absolute fault below $\pm 1\%$ is reached for most of the map. Only the low-speed-torque region has a higher AF_{tot}, which can be as high as $\pm 5\%$. The accuracy of the temperature sensors that are connected to the housing of the gearboxes is $\pm 0.05°C$ from $-80°C$ to $200°C$. Therefore, the temperature sensors of the housing do not affect the measurement accuracy. As the loaded and unloaded tests are conducted at different instances, the speed uncertainty and the effect of temperature on the torque sensors are assessed in Appendix V.4.

$$\eta_{gb} = \frac{P_{out}}{P_{in}} = \frac{T_{out}}{T_{in}k_{gb}} \text{ with } k_{gb} \text{ is the gear ratio} \tag{97}$$

$$RF_{tot} = \sqrt{RF(T_{in})^2 + RF(T_{out})^2} = \sqrt{\left(\frac{AF(T_{in})}{|T_{in}|}\right)^2 + \left(\frac{AF(T_{out})}{|T_{out}|}\right)^2} \tag{98}$$

$$AF_{tot} = RF_{tot}\, \eta_{gb} \tag{99}$$
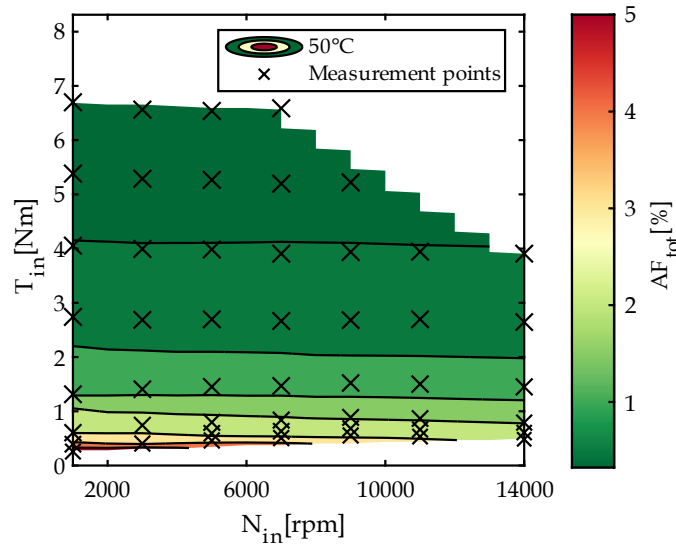
Fig. 59: Absolute fault of efficiency due to instrumentation, benchmarked within the input speed-torque plane of the first gearbox.

Due to control imperfection, the controllers cannot keep a perfectly constant speed and torque during the test. It is therefore challenging to achieve high accuracy in the efficiency measurements of gearboxes. As an illustrative case, the impact of the control imperfection of

torque and speed is assessed in Fig. 60 for the first gearbox. To this end, random points are selected for the analysis. The results show that the region characterized by low speed and low torque is mainly affected, with a maximum deviation from the average efficiency of 1%. Together with the measurement uncertainty due to the instrumentation, the overall efficiency uncertainty can reach up to 6% in low torque and speed regions. Note that a complete assessment of the remaining gearboxes is provided in Appendix V.4.
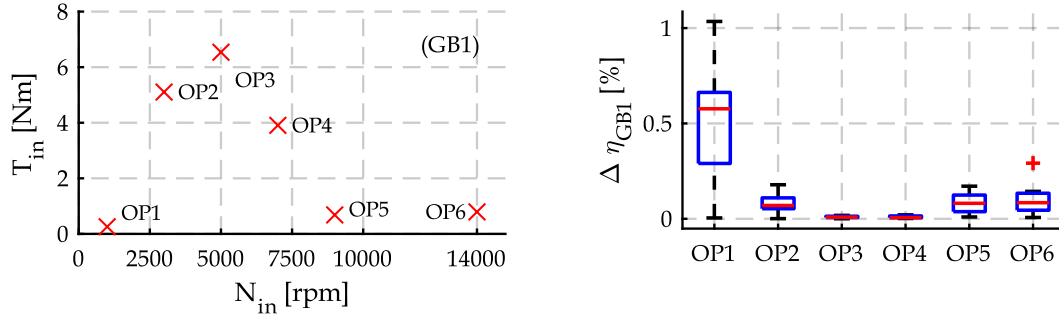
Fig. 60: Control imperfection impact on the efficiency of the first gearbox: the figure on the left represents an example of the measured points in the input (sun) speed and torque plane, while the figure on the right represents the deviation from the averaged efficiency.

3.2 Results of the experimental campaign

3.2.1 Efficiency and overall losses

Fig. 61 shows the loaded test results, for the efficiency and the overall losses for each gearbox as a function of the input torque T_{in} and speed N_{in}. As a reminder, the sun gear is considered as input and the subsequent experimental results are reported for an operating temperature of the gearbox of 50°C. It is worth mentioning that the effect of the gearbox temperature is assessed in Appendix V.6, considering two additional temperature values corresponding to cold and hot operating scenarios. Concerning the test under consideration, Fig. 61 reveals that the efficiency maps of the tested gearboxes share a similar contour shape. The results indicate that the efficiency is not equal in the entire working area for all five cases. The highest efficiency is measured at high torque values and drops at partial load. A conspicuous observation is that the efficiency of the gearbox is highly impacted by the speed, with efficiency decreasing as the speed increases. The last statement is substantiated by the results of the overall power losses (second column of Fig. 61), where the dependency on speed is noticeable. Interestingly, the 3rd gearbox has greater losses than the other four gearboxes, as shown in Fig. 61.f, even though the gear ratio is lower. This will be explained in the following sections.

Due to the number of gearboxes tested, the analysis of the load-dependent and independent losses in the following sections will be solely presented for the three first gearboxes. This is because these gearboxes are used to derive the power loss model, while the last two are chosen as case studies to validate the scalable model.

Fig. 61: Efficiency η and overall losses P_{losses} of the tested gearboxes at 50°C as a function of the input (sun) speed and torque. Note that each row shows the results of a given gearbox. The black dots refer to the measured points.

3.2.2 Load-independent losses

The experimental results of the unloaded test for the three gearboxes are shown in Fig. 62. The power losses demonstrate a non-linear variation according to the input speed, as shown in (92). This is consistent with the results of earlier unloaded experiments reported in [205] and applies even to higher speed values. Thereby, the load-independent losses can be expressed as:

$$P_{\text{LID}} = bN_{\text{in}}^c \qquad (100)$$

in which b, and c are parameters to be identified.
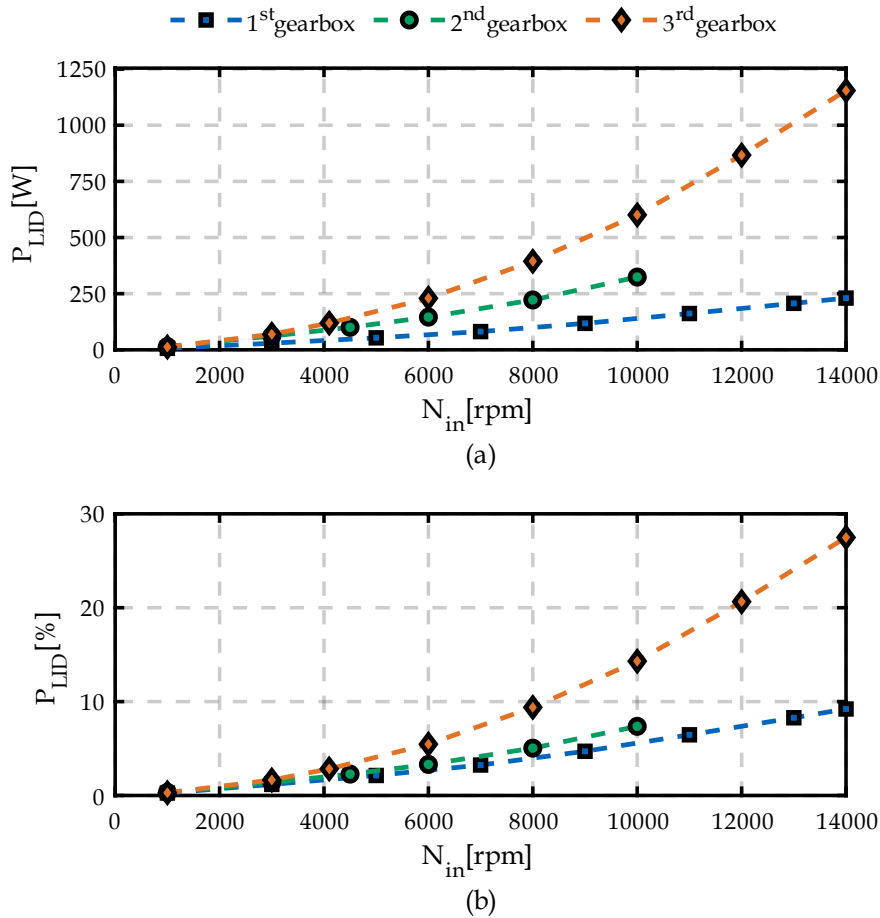
Fig. 62: Load-independent losses P_{LID} at 50°C as a function of the input speed: (a) represents the losses in [W], (b) depicts the contribution of the losses relative to the rated power of each gearbox in [%].

The most remarkable result to emerge from the data is the high contribution of the load-independent losses P_{LID}, which is illustrated in Fig. 62.b in percentage relative to the rated power of each gearbox. The figure indicates that the load-independent losses represent 28% of the rated power of the 3rd gearbox at 14,000 rpm, which is significant. For the two first gearboxes the contribution of P_{LID} is below 10%. The reasons for this can be related to the rotational speed of the planet carrier (output shaft) and the planets. In the case of the 3rd gearbox, the output shaft spins faster as compared to the two first gearboxes, due to a lower gear ratio (see

Table 14). This leads to an increase in the carrier churning losses, which has a large contribution to the load-independent losses even for low-speed rated gearboxes [211]. Furthermore, the planet gears spin approximately at 14,000 rpm (relative to the sun, see the teeth number in Table 14), leading to more churning loss. The churning power loss model presented in (92) lends support to the last statements as the power loss of the rotating gears is proportional to speed, regardless of the specific speed exponent factor. Furthermore, the high speed of the planet gears for the 3rd gearbox results in greater oil-squeezing losses. The model shown in (94) for the squeezing losses is consistent with the previous statement. The difference in losses between the first and second gearboxes is due to differences in geometry. This can be seen in the aforementioned models as they contain geometrical parameters such as the face width and pitch radius of the gears.

3.2.3 Load-dependent losses

To isolate the load-dependent losses P_{LD}, the load-independent losses are subtracted from the overall losses, following the procedure presented in [205]. Fig. 63 depicts the measured P_{LD} at the same operating conditions as in Fig. 61 and Fig. 62.

The results reveal that P_{LD} varies almost linearly with torque and speed. In other words, the findings demonstrate that the load-dependent losses for the tested planetary gearboxes are power-dependent rather than torque-dependent. The lefthand side column of Fig. 63 lends support to the last statement, as the contours of the loss map are not perfectly horizontal. As such, torque-dependent losses can be solely represented by horizontal contours. This is in good agreement with the model of the gear mesh power loss presented in (87), as the losses in question depend on the input power. Based on these statements, the load-dependent losses P_{LD} can be expressed as a function of input torque, speed, and a parameter called a that needs to be identified:

$$P_{LD} = aT_{in}N_{in} \tag{101}$$

The remarkable result to emerge from the data presented in the second column of Fig. 63, is the low contribution of the load-dependent losses as compared to the load-independent losses (Fig. 62.b). For instance, P_{LD} represents 2% of the rated power as compared to 28% of P_{LID} in the case of the third gearbox at 14,000 rpm. This emphasizes the high contribution of load-independent losses and shows the necessity for accurate modeling to better predict this loss component.
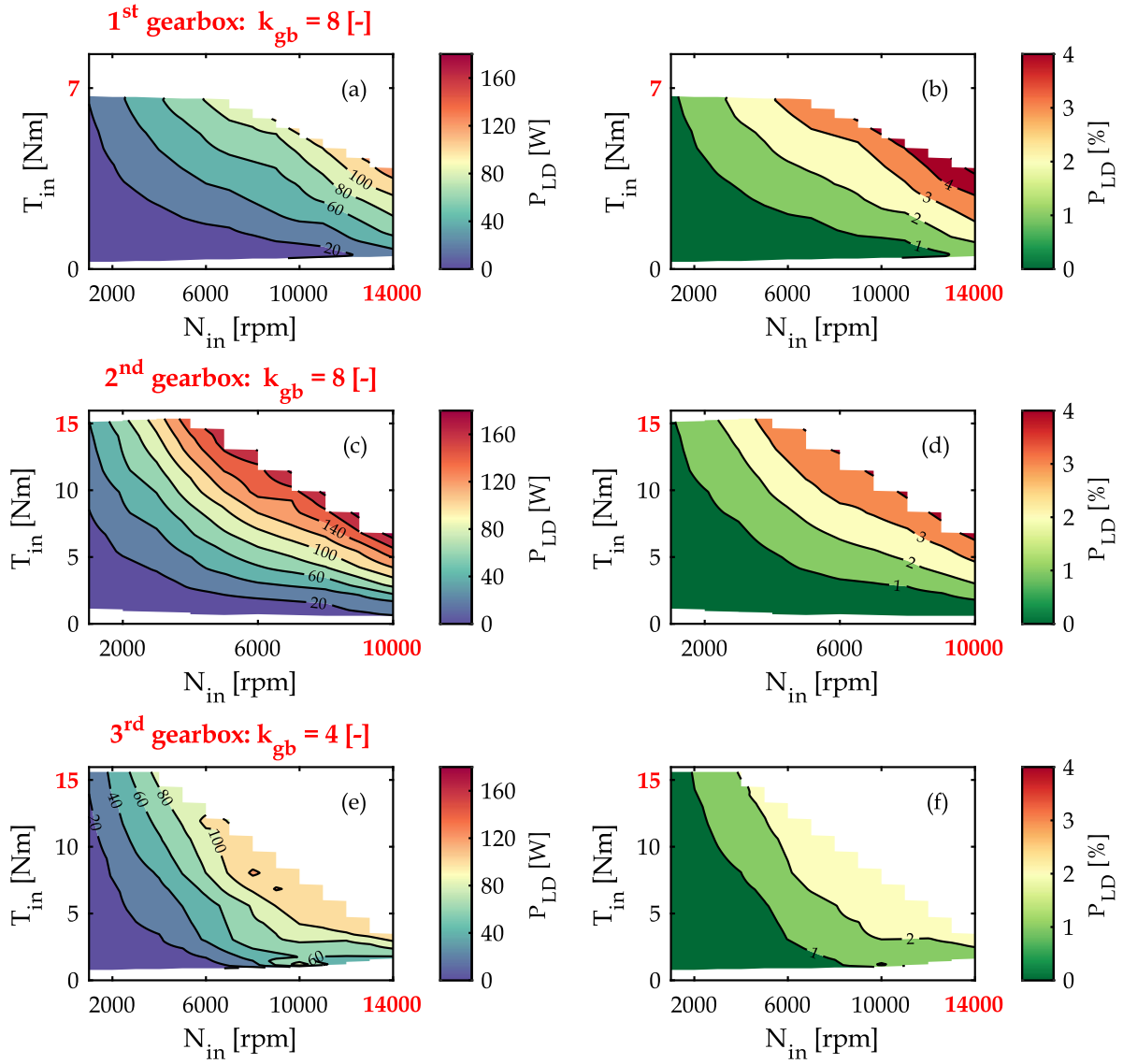
Fig. 63: Load-dependent losses P_{LD} at 50°C as a function of the input speed and torque: the first column figures represent the losses in [W], and the second column figures depict the contribution of the losses relative to the rated power in [%] of each gearbox.

3.3 Losses modeling for each individual gearbox

Based on the results of the experimental campaign, an overall loss model based on power and speed dependency is proposed. It follows from (100), and (101)) that the overall loss can be expressed as given by (102).

$$P_{\text{losses}} = P_{\text{LD}} + P_{\text{LID}} = aT_{\text{in}}N_{\text{in}} + bN_{\text{in}}^c \tag{102}$$

Next, the parameter identification is applied to the model, with the help of the experimental data for each gearbox. The parameters of the model are defined by solving the minimization problem stated in (103).

Find $X = [a, b, c]^T$ which minimizes the fitness function

$$f(X) = \sum_{i=1}^{m} \sum_{j=1}^{n} \left(P_{\text{losses,ij}}^{\text{exp}}\big(N_{\text{in}}(i), T_{\text{in}}(j)\big) - P_{\text{losses,ij}}^{\text{model}}\big(N_{\text{in}}(i), T_{\text{in}}(j)\big) \right)^2 \tag{103}$$

in which m is the length of the speed matrix, n is the length of the torque matrix, $P_{\text{losses,ij}}^{\text{exp}}$ is the total power losses experimentally measured at the operating points $\big(N_{\text{in}}(i), T_{\text{in}}(j)\big)$, and $P_{\text{losses,ij}}^{\text{model}}$ is the power loss calculated by the model depicted in (102) at the same operating points. The minimization problem is solved, considering the entire speed and torque ranges for each gearbox, using the curve fitting toolbox of Matlab [219]. For each gearbox, the number of measured data taken into account for the minimization problem falls within the range of 50 to 70 points. Table 16 shows the parameters identified for the three gearboxes. The single most striking observation to emerge from Table 16, is that the c coefficient that represents the exponent term of the load-independent losses (N_{in}^c) varies between 1.43 and 1.91. These findings do not confirm prior research on the load-independent losses, which reveal a cubic speed relation (see (92)) [203], [220]. However, this is in line with the results published in [221] for spur gears.

Table 16: Model parameters identification for the three tested gearboxes. The specifications of each gearbox are given in parentheses: ($N_{\text{in}}^{\text{max}}$ [rpm]/ $T_{\text{out}}^{\text{max}}$ [Nm]/ k_{gb} [-])

	a [-]	b [Nm]	c [-]
1st gearbox: (14000/62/8)	2.073 10^{-3}	2.692 10^{-4}	1.43
2nd gearbox: (14000/120/8)	2.367 10^{-3}	6.02 10^{-4}	1.43
3rd gearbox: (14000/62/4)	1.996 10^{-3}	1.392 10^{-5}	1.91

The first column of Fig. 64 shows the relative difference in the overall losses ΔP_{losses} in percentage between the proposed model and the measurement. The results indicate a good agreement with the experimental results of the three gearboxes for most regions of the map. This is evidenced by an average value of ΔP_{losses} of 5.5%, considering the entire loss map. Fig. 64.a and Fig. 64.e show a higher value ΔP_{losses}, reaching up 20%, observed in restriceted area characterized by low-speed and high-torque for the first and the third gearboxes, respectively. This is because the losses in the aforementioned regions are insignificant compared to the transmitted power (Fig. 61) and the smallest difference between the model findings and the experimental tests will have an impact. The last statement is supported by the second column of Fig. 64 which presents the difference in terms of efficiency $\Delta\eta$. The figures suggest a good correlation between the computed and measured efficiency, for the three gearboxes. None of the differences in ΔP_{losses} are impactful, as $\Delta\eta_{\text{gb}}$ is predominantly less than 1% for most of the map area. The largest difference is found in a small area along the borders of the map for the 3rd gearbox, where $\Delta\eta_{\text{gb}}$ is up to 3.8 %. From the comparison, it can be concluded that the minimization procedure was able to find a good match with the measurements for the three gearboxes.

Fig. 64: Assessment of the difference in percentage between the proposed model and the experimental data in terms of overall losses ΔP_{losses} and efficiency $\Delta \eta_{gb}$. Note that each row figure shows the results of a given gearbox.

4 Power loss scaling laws of high-speed planetary reducers

This section deals with the derivation and validation of the scaling laws deduced based on the results of the experimental campaign. It concludes with an assessment of the applicability of the linear losses-to-power scaling for high-speed gearboxes, and a comparison against the proposed scaling power loss scaling laws.

4.1 Overall model

Following the parameter identification of the proposed model in Section 3 of this chapter, a general model for the three first gearboxes is herein derived. The goal is to have one global model valid for the three gearboxes, in which high-level specifications, namely the maximal output torque, the maximal input speed, and gear ratio, can be easily incorporated. To this

end, analytical expressions for the parameters *a*, *b*, and *c* are derived based on the gearbox parameters, as shown in (104). Regarding the load-independent losses, the expressions, for *b* and *c*, are analytically deduced based on the maximal input speed, and the gear ratio. This choice is made because the load-independent power loss term in (102) is linked to speed and gear ratio. As per Table 16, the *b* coefficient depends on both speed and gear ratio. Therefore, the *b* coefficient is expressed as a function of these last two parameters. However, it is important to note that the *c* coefficients solely depend on the gear ratio and are not influenced by the maximal speed. Regarding the load-dependent losses, the parameter *a* is averaged since its values are approximately the same for all three gearboxes (see Table 16).

$$
\begin{aligned}
a &= a_{\text{avr}} \\
b &= f(k_{\text{gb}}, N_{\text{max}}) &= b_1 + b_2 k_{\text{gb}} + b_3 N_{\text{max}} \\
c &= f(k_{\text{gb}}) &= c_1 + c_2 k_{\text{gb}}
\end{aligned}
\tag{104}
$$

where b_1, b_2, b_3, c_1 and c_2 are new coefficients that are fitted based on the data set out in Table 16. In other words, the coefficients shown in Table 16 are used to fit the new coefficients of the new proposed model. Thereafter, the overall losses model given by (102) can be redrafted as in (105).

$$
\begin{aligned}
P_{\text{losses}} &= P_{\text{LD}} + P_{\text{LID}} \\
&= a_{\text{avr}} T_{\text{in}} N_{\text{in}} + (b_1 + b_2 k_{\text{gb}} + b_3 N_{\text{max}}) N_{\text{in}}^{c_1 + c_2 k_{\text{gb}}}
\end{aligned}
\tag{105}
$$

Table 17: Parameters identification for the overall model

a_{avr} [-]	b_1 [Nm]	b_2 [Nm]	b_3 [Nm/rpm]	c_1[-]	c_2[-]
$2.1443\ 10^{-3}$	$9.234\ 10^{-4}$	$6.382\ 10^{-5}$	$-8.32\ 10^{-8}$	2.39	-0.12

The accuracy of the results of the model proposed above is assessed in Fig. 65. No significant differences are observed while comparing the overall model results with the experimental data. The derived overall model will serve as a starting point for establishing the power loss scaling laws.

4.2 Derivation of power loss scaling laws

4.2.1 Reorganization of the overall model

The power loss scaling laws are herein derived by redrafting the overall model (105) as a function of three scaling factors: an output torque scaling K_{T}^{GB}, an input speed scaling factor K_{N}, and a gear ratio scaling K_{kgb}. The scaling factors are expressed as the ratio between the parameters of the scaled and the reference gearboxes, as depicted in (106). Note that the superscript 0 refers to the reference gearbox and the apostrophe ' is used for the scaled gearbox.

$$
\begin{cases}
K_T^{GB} &= \dfrac{T'_{out,max}}{T^0_{out,max}} \\[2mm]
K_N &= \dfrac{N'_{in,max}}{N^0_{in,max}} \\[2mm]
K_{kgb} &= \dfrac{k'_{gb}}{k^0_{gb}}
\end{cases}
\tag{106}
$$

The power losses of the scaled gearbox P'_{losses} can be deduced by replacing the scaling factors (106) in the overall model (105). This yields the following equation:

$$
P'_{losses} = a_{avr}\left(\frac{K_T^{GB}}{K_{kgb}} T^0_{in}\right)\left(K_N N^0_{in}\right) + \left(b_1 + b_2 K_{kgb} k^0_{gb} + b_3 K_N N^0_{max}\right) K_N N_{in}^{c_1 + c_2 K_{kgb} k_{gb}}
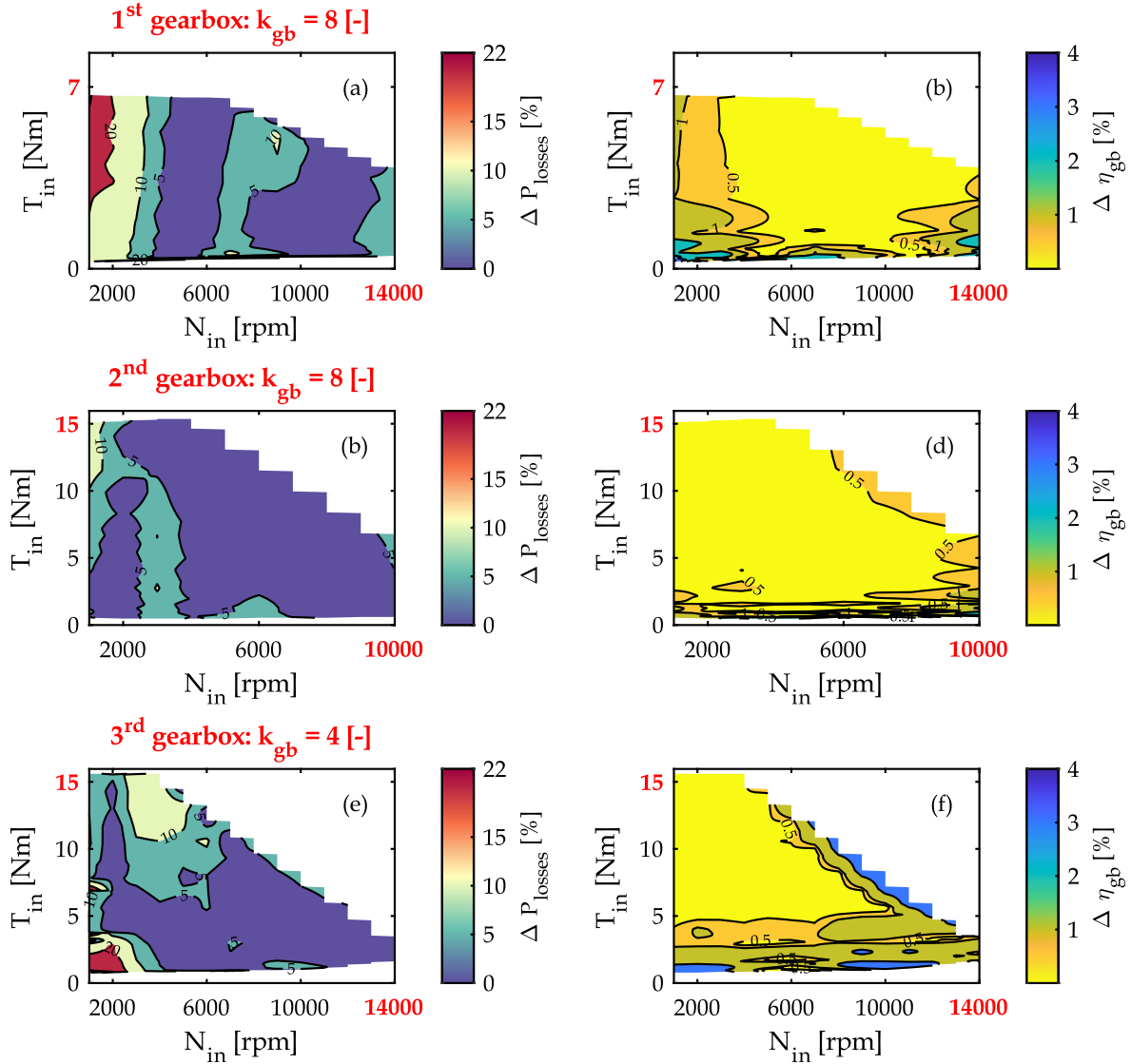\tag{107}
$$
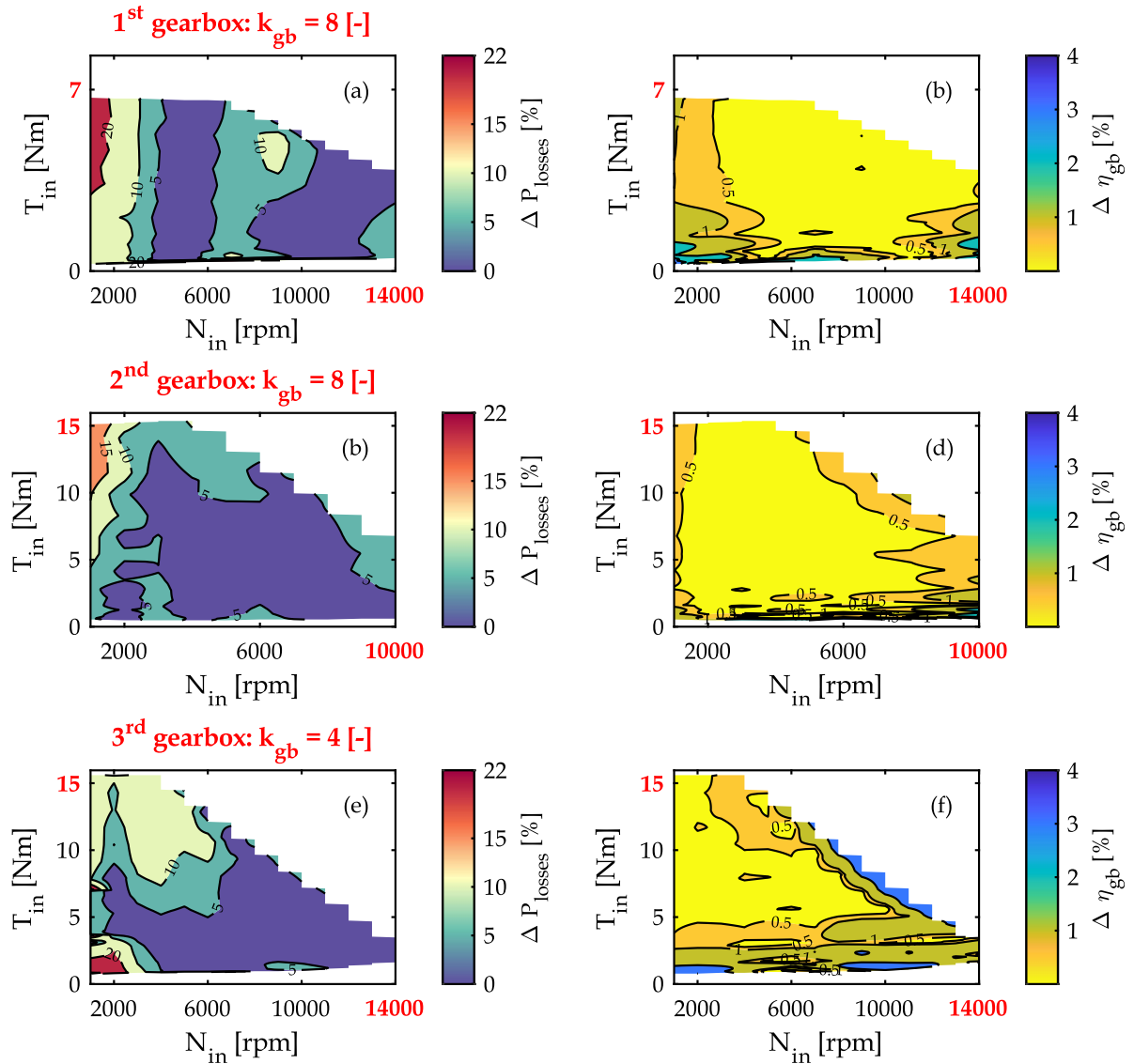
Fig. 65: Assessment of the difference in percentage between the overall model and the experimental data in terms of overall losses ΔP_{losses} and efficiency $\Delta \eta_{gb}$. Note that each row figure shows the results of a given gearbox.

In case both maximal output torque and maximal input speed are conserved, and the gear ratio is changed, the input torque of the gearbox needs to be scaled. To consider this case, the input torque is scaled by the gear ratio scaling factor K_{kgb} in (107). This is best illustrated in the example of the 1st and 3rd gearboxes (see Table 14). Next, the power losses P'_{losses} of the scaled gearbox are expressed as a function of the power losses of the reference gearbox and the scaling factors, as follows:

$$P'_{\mathrm{losses}} = \frac{K_{\mathrm{T}}^{\mathrm{GB}} K_{\mathrm{N}}}{K_{\mathrm{kgb}}} P_{\mathrm{LD}}^0 + \left(K_{\mathrm{kgb}} K_{\mathrm{N}} P_{\mathrm{LID}}^0 + \Delta P_{\mathrm{LID}} \right) \tag{108}$$

in which ΔP_{LID} is an extra equivalent load-independent term, added to end up with the same expression presented in (107), following has been done for the electric drive system in Chapter II. This equivalent loss term can be written as:

$$\Delta P_{\mathrm{LID}} = K_{\mathrm{N}} K_{\mathrm{kgb}} N_0^{c_1 + c_2 k_{\mathrm{gb}}^0} \left[b_1 \left(\frac{N_0^{c_2 k_{\mathrm{gb}}^0 (K_{\mathrm{kgb}} - 1)}}{K_{\mathrm{kgb}}} - 1 \right) + b_2 k_{\mathrm{gb}}^0 \left(N_0^{c_2 k_{\mathrm{gb}}^0 (K_{\mathrm{kgb}} - 1)} - 1 \right) \right.$$
$$\left. + b_3 N_{\mathrm{max}}^0 \left(\frac{K_{\mathrm{N}}}{K_{\mathrm{kgb}}} N_0^{c_2 k_{\mathrm{gb}}^0 (K_{\mathrm{kgb}} - 1)} - 1 \right) \right] \tag{109}$$

4.2.2 Methodology for power losses/efficiency maps computation using scaling laws

Using the power loss model (108) presented in the previous section, it is possible to establish losses or efficiency maps of a new gearbox using solely the data of a reference gearbox. The proposed methodology in this work proceeds in the same way as [169], in which a scaling procedure of the efficiency map of synchronous electric machines was proposed. To this end, three steps are required, as illustrated in Fig. 66. Step I involves obtaining the possible operating points of the scaled gearbox and the considered scaling factor values, and redefining them in the frame of the reference gearbox, based on the predefined scaling factors. Step II consists in computing the losses of the reference gearbox using (102). Lastly, Step III allows scaling the losses of the reference gearbox using the scaling laws defined in (108). These steps are repeated for all the possible operating points to establish the losses/efficiency map.
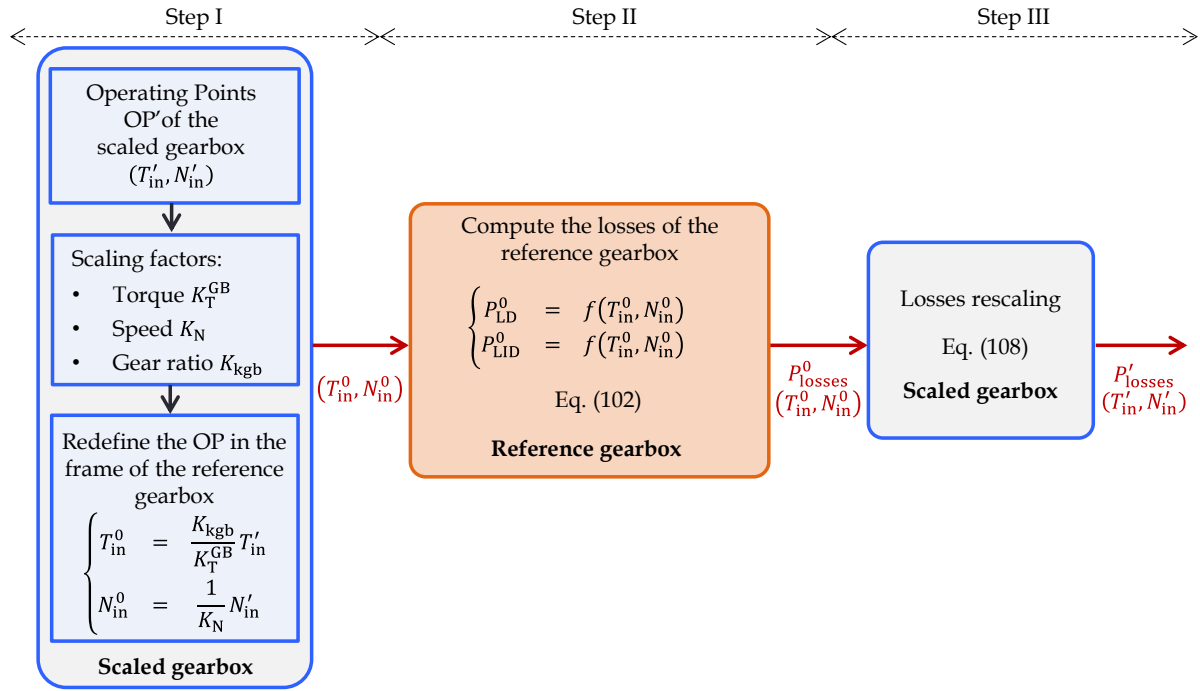
Fig. 66: Methodology to establish the power losses/efficiency maps of the scaled gearbox based on the data of a reference gearbox

4.3 Scaling laws validation

The validation framework consists of three steps as depicted in Fig. 67. First, the accuracy of the derived scaling laws is assessed using the gearboxes included in the training set (1st to 3rd gearbox). Next, in the second step, validation is carried out using the gearboxes belonging to the training and test validation. As a reminder, the methodology demonstrated in Fig. 66 is applied to compute the losses and the efficiency maps for the scaled gearboxes. The 1st gearbox serves as a reference for this evaluation. The scaling factors used for the first two validation steps are summarized in Table 18. Lastly, the final validation step involves a sensitivity analysis of the selection of gearboxes included in the training set.

Table 18: Overview of the applied scaling factors

	Torque scaling factor K_T^{GB} [-]	Speed scaling factor K_N [-]	Gear ratio scaling factor K_{kgb} [-]
Scaling case ①: 1st to 2nd gearbox	1.93	0.71	1
Scaling case ②: 1st to 3rd gearbox	1	1	0.5
Scaling case ③: 1st to 4th gearbox	0.95	1	0.875
Scaling case ④: 1st to 5th gearbox	4	0.61	1
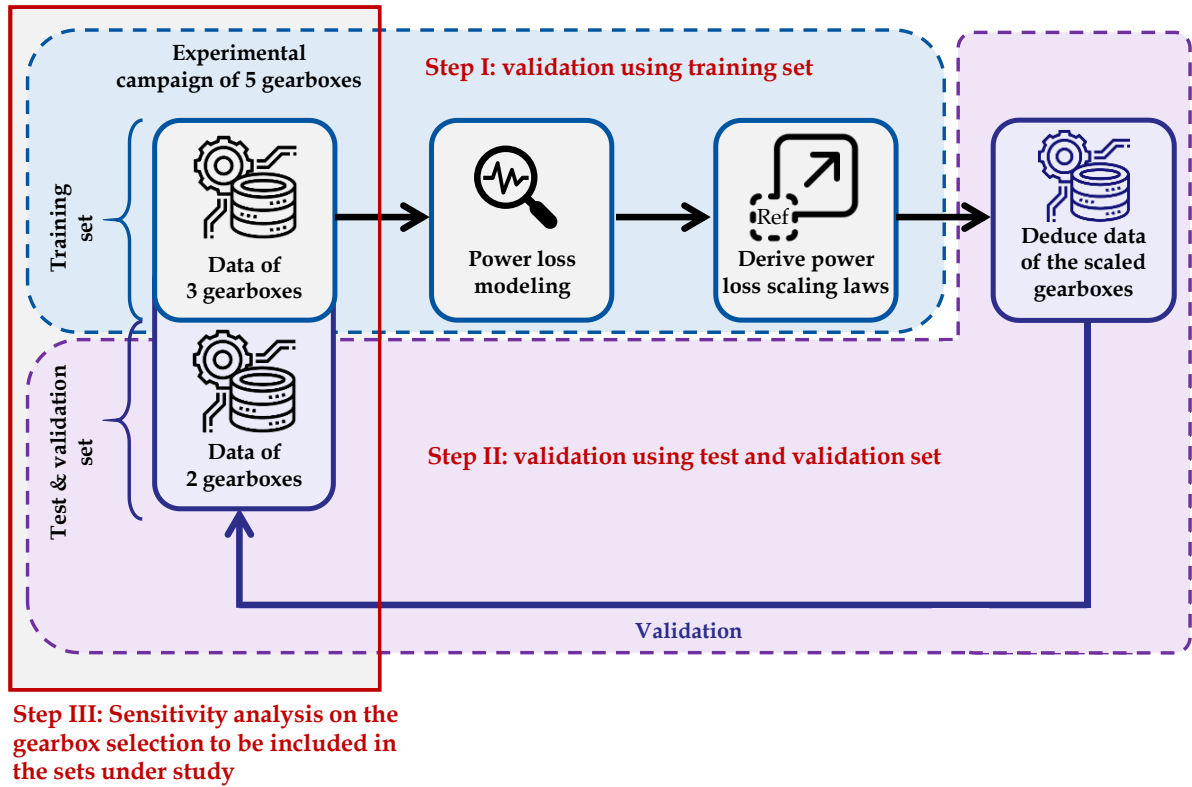
Fig. 67: Validation workflow for the derived power loss scaling laws

4.3.1 Validation based on the training set

The scaling results for the two first case studies ① and ② are herein presented. Fig. 68 shows a comparison between the results of the scaled overall power loss and efficiency map (using the scaling laws combined with the experimental efficiency map of the reference gearbox) and the experimental results of the other gearboxes. Fig. 68.a and Fig. 68.c indicate a good correlation between losses predicted using the scaling laws with the measured power losses. The average relative error is about 8%. A slight discrepancy at low speed and high torque region is observed in Fig. 68.c. This error could be explained by the fact that the experimental results have emerged from different tests. Thereby, some testing conditions may differ such as the temperature of the gearbox (50±3°C). Notwithstanding this difference in terms of power losses, the results in terms of efficiency prediction are not impacted. In the majority of the map areas, the efficiency difference $\Delta\eta$ is below 1% for the two case studies, except for a slight discordance of 3% in Fig. 68.d along the map borders. In light of the outcomes of this initial validation step, it is convenient to conclude that the scaling laws predict the efficiency with satisfactory accuracy for this first validation step.
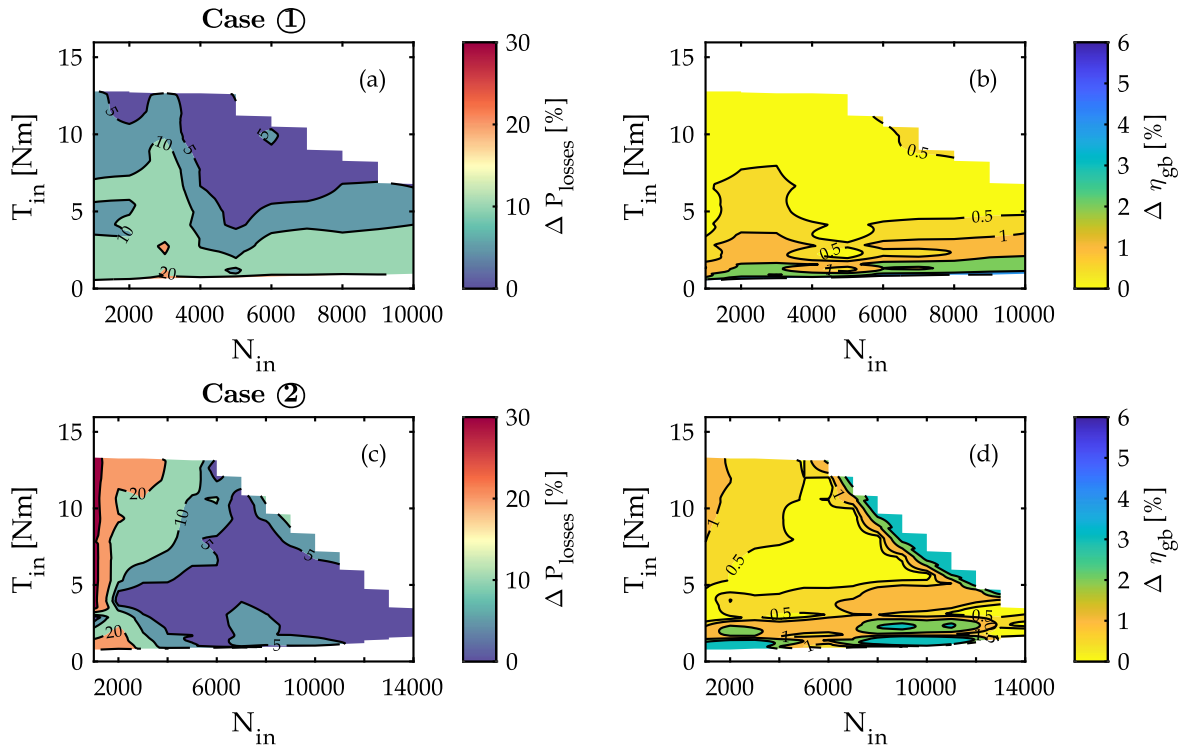
Fig. 68: Assessment of the relative difference in percentage between the scaling laws results and the experimental data in terms of overall losses ΔP_{losses} and efficiency $\Delta\eta$. Note that each row of figures shows the results of a given scaling case. (a)-(c) relative difference in terms of the power loss; (b)-(d) simple difference in terms of efficiency.

4.3.2 Validation based on the test and validation set

The proposed scaling methodology is applied to deduce the efficiency and power loss of the last two gearboxes included in the test and validation set. It is important to note that the data from these two additional gearboxes are not used to tune the scaling laws. Fig. 69 depicts the difference between the outcomes of the scaling laws and the experimental results. A good prediction of the losses and efficiency is achieved for both gearboxes. As far as case ③ is concerned, Fig. 69.a shows that the scalable model has a good loss prediction of the losses in most of the regions of the map, in which speed does not exceed 10,000 rpm. This is demonstrated by the relative difference in power loss in those areas being less than 6%, leading to a good efficiency prediction with a $\Delta\eta$ of less than 1%. In regions characterised by high speed and low torque, the relative difference reaches 12%, resulting in a difference in an efficiency difference of up to 6% in some restricted areas. The average error $\Delta\eta$ of in the entire map is 1.35%. This difference can be attributed to the fact that the experimental results were obtained from various tests, e.g. the temperature of the gearbox (50±3°C), and the measurement uncertainty which can reach 2% in high-speed regions (Fig. 59). Regarding case ④, Fig. 69.c indicates a good loss prediction with ΔP_{losses} under 3% in the majority regions in the map. The most striking result to emerge from the data is that the efficiency difference is below 0.3%. This is achieved despite the large scaling factors that have been applied for torque and speed (Table 18).
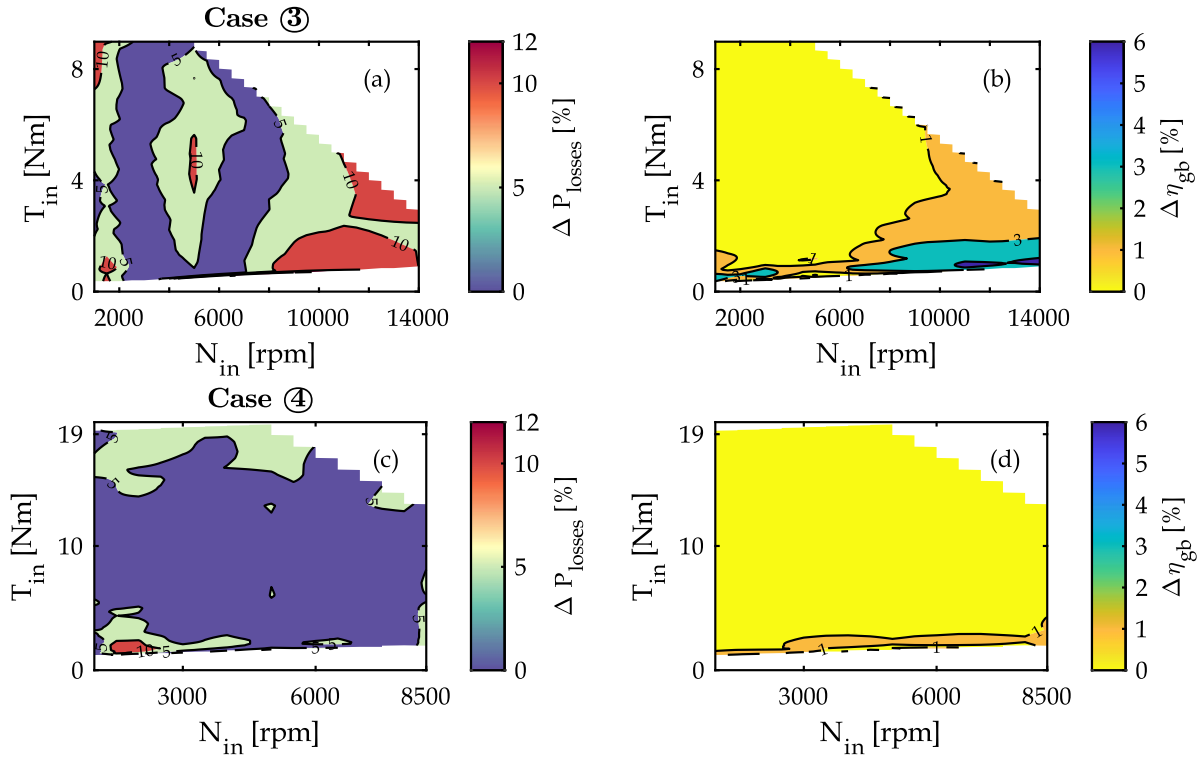
Fig. 69: Validation results of the scaling laws using the two additional gearboxes: (a)-(c) relative difference in terms of the power loss; (b)-(d) simple difference in terms of efficiency.

4.3.3   Sensitivity analysis of the gearbox selection

To carry out the sensitivity analysis, a total of 31 possible combinations can be established based on the five studied gearboxes for building the training and validation sets. To ensure feasible combinations, criteria have been defined. The first criterion consists in selecting 3 gearboxes for the training set and 2 others for the test and validation. The second criterion dictates that the gearbox selected for the training set must involve at least two gear ratio values. This makes it possible to incorporate the gear ratio scaling process in the proposed methodology. Based on the defined criteria, 7 possible combinations can be derived. However, if a sensitivity analysis of the selection of reference gearbox selection is included, the number of cases to be examined augments to 23. Due to the significant number of potential case studies, only 2 illustrative cases will be presented in the following sections. For the sake of generalizability, this section concludes with a recommendation and guidelines for selecting the gearboxes for the training set.

4.3.3.1   Effect of the reference gearbox selection

To demonstrate the impact of the gearbox selection, the same set as previously used for the analysis above is considered. As an illustrative case, the 3rd gearbox serves herein as a reference gearbox, rather than the first gearbox. The same scaling process is repeated to derive the efficiency maps of the 4th and the 5th gearboxes, incorporating new scaling factors as shown in Table 19. Fig. 70 shows the outcomes of the scaling process for the case studies ⑤ and ⑥. Similar observations can be made, as with the first gearbox as a reference, demonstrating the

120

reliability of the method. Satisfactory results below 1% in terms of efficiency difference are obtained in most of the regions of the map. Similarly, in high-speed and low-torque regions, wherein the load-independent losses prevail, a large discrepancy that reaches about 5% is found. This can be attributed to the large gear ratio used for the scaling process and the high non-linearity of the aforementioned losses.

Table 19: Overview of the applied scaling factors involved in the sensitivity analysis

	Scaling case	Torque scaling factor K_T^{GB} [-]	Speed scaling factor K_N [-]	Gear ratio scaling factor K_{kgb} [-]
Set 1	⑤: 3rd to 4th gearbox	0.95	1	1.75
	⑥: 3rd to 5th gearbox	4	0.61	2
Set 2	⑦: 5th to 2nd gearbox	0.48	1.18	1
	⑧: 5th to 3rd gearbox	0.25	1.65	0.5
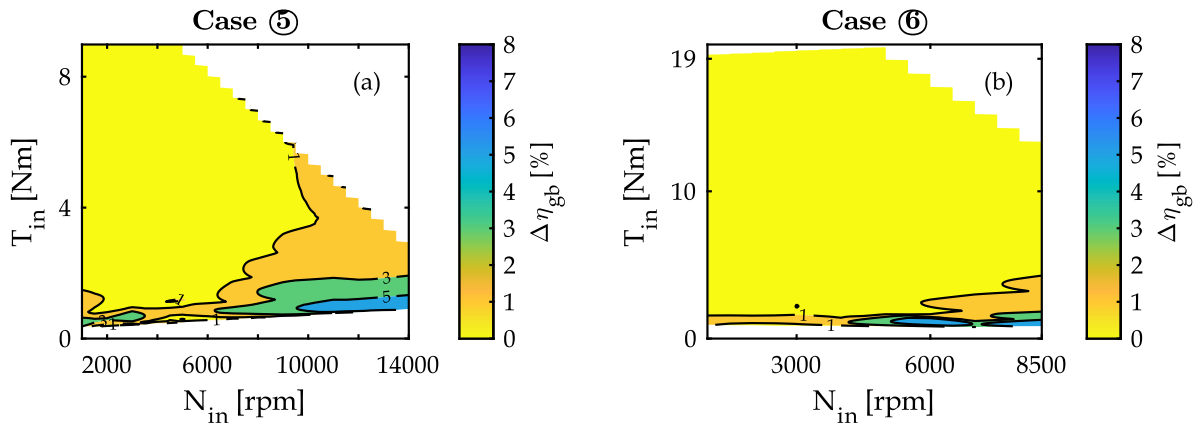
Fig. 70: Assessment of the reference gearbox change effect

4.3.3.2 Effect of the change in the training set selection

To examine the impact of the gearbox selection in the training set, a second set is considered as illustrated in Fig. 71. This represents two changes as compared to the first set. In the following analysis, the 5th gearbox is considered as a reference gearbox. The corresponding scaling factors for the test and validation set can be consulted in Table 19.

The outcomes of the scaling process are presented in Fig. 72. The scaling results for case ⑦ exhibit satisfactory results as shown in Fig. 72.a, with deviation from the experimental results below 1% in most of the regions of the torque-speed plane. This was achieved despite the large torque scaling that has been considered. However, the scaling process with the considered training set fails short to predict the efficiency of the scaling case ⑧. This is mainly attributed to the large gear ratio scaling. Indeed, the training set has been established with gearboxes with gear ratio values of 7 and 8, whereas the gear ratio of the 3rd gearbox is equal to 4.

This necessitates a large extrapolation, for which the scalable model is not trained to handle such cases, leading to incoherent results.
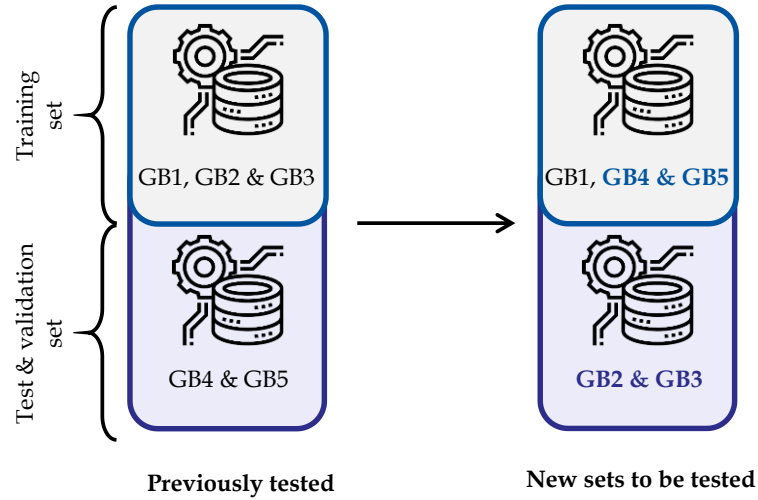
Fig. 71: Illustration of the new sets to be tested
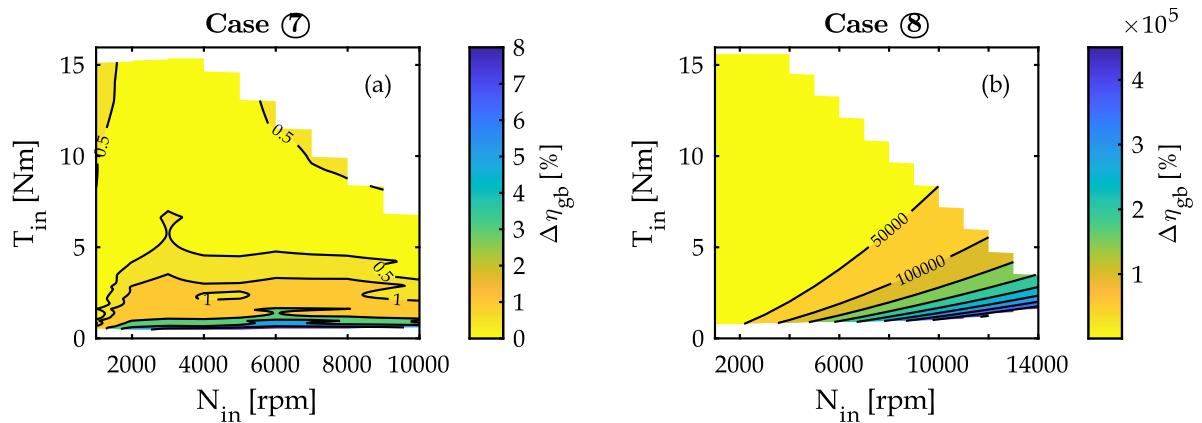
Fig. 72: Assessment of the training set change effect as compared to experimental results

For further analysis of this issue, Fig. 73 shows the c parameter in (104), as a function of the gear ratio of the studied gearboxes. The figure substantiates the statements made earlier, demonstrating that the accuracy of the model (104) is highly dependent on the gearbox selection for the training set. The first training set yields satisfactory results because the parameter of the model has been identified using gearboxes with a large variation in the gear ratio values. Consequently, the model achieves decent results without requiring extrapolation. However, in the case of the second training set, the parameters of the model have been tuned based on gear ratio values that are close to each other, specifically 7 and 8. In scaling cases where the gear ratio differs significantly from that range, the model cannot guarantee good results, due to the non-linearity of the load-independent losses. This is exemplified by case ⑧, where the 3rd gearbox reveals the highest load-dependent losses due to the high speed of the carrier. Accordingly, as a general rule, it is advised to select gearboxes with wide variations in the gear ratio, when building the training set, to guarantee satisfactory results.
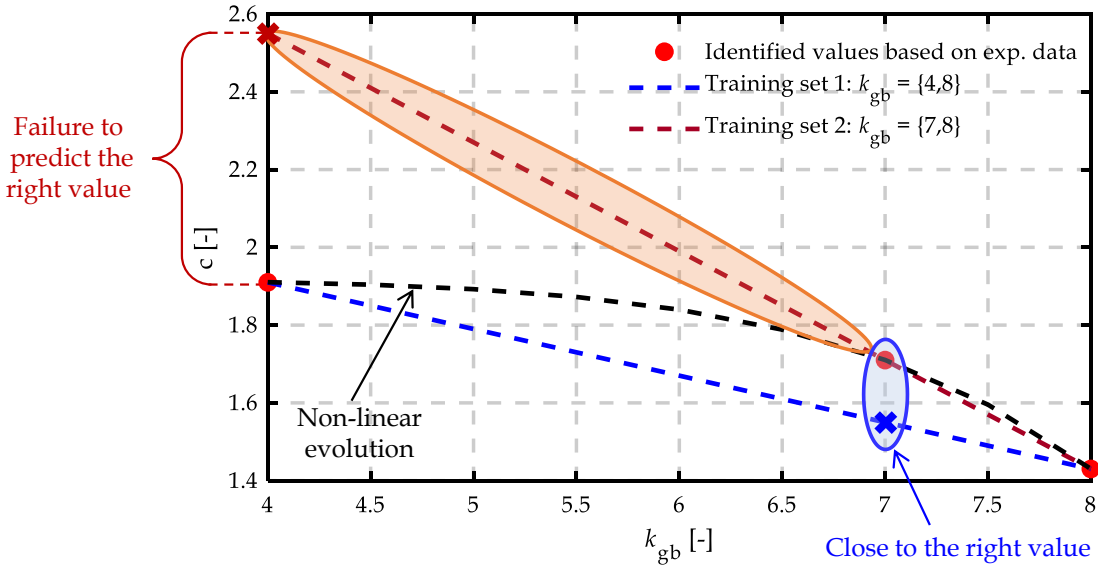
Fig. 73: Analysis of the c coefficients based on the training set selection. The black dashed line represents the evolution of the c coefficient based on the identified values for each gearbox.

4.4 Comparison of the proposed scaling laws against linear losses-to-power scaling

Similarly to what is done for the electric drive in Chapter II, the linear losses-to-power scaling is hereafter assessed for the planetary reducers. Note that the linear scaling method does not require any parameter identification or training process as compared to the proposed data-driven power loss scaling laws discussed earlier. The inputs of the linear scaling method consist of the overall loss or efficiency map of the reference component and the desired scaling factors. Scaling cases ① and ④, presented in Table 18, are first assessed. As a reminder, these case studies correspond to torque and speed scaling and the 1st gearbox serves as the reference. Contrary to the electric machine, the linear losses-to-power scaling law of the overall losses is herein reformulated to account for the maximal speed scaling of the gearbox, as expressed in (110). By consulting Fig. 74, the outcomes of the linear losses-to-power scaling for the two scaling cases can be examined. Fig. 74.a shows a good match with the experimental data of the 2nd gearbox, with Δη below to 1% in most regions of the map. However, this is not the case for the 4th gearbox as evidenced by Fig. 74.b. Only in high torque regions with torque value exceeding 15 Nm, the results are satisfactory, with a discrepancy of efficiency of less than 1%. On the other hand, in other regions of the map, the results are poor and can reach an error of up to 5% in low-torque regions. This can be attributed to the large torque (x4) and speed (x0.61) scaling factors applied in the scaling process, which have stretched the linear scaling method to its limits in terms of accuracy.

$$P'_{\text{losses}} = K_T^{\text{GB}} K_N P^0_{\text{losses}} \qquad (110)$$

Regarding the gear ratio scaling cases, the formulation of the scaling law considering solely the overall losses is challenging. This challenge arises primarily because of the

significant non-linearity observed in the evolution of losses throughout this process. To tackle this issue, the gear ratio scaling factor K_{kgb} is incorporated in the power loss scaling law following (111). This choice is driven by the experimental results, presented in Section 3, demonstrating that the overall loss increases when decreasing the gear ratio. Therefore, this leads to an inversely proportional relationship between the last two parameters. The outcomes of the scaling process following (111) are presented in Fig. 75, for the scaling cases ② and ③. From the last figure, it is apparent that the proposed scaling laws align with the experimental results for the aforementioned cases, as the efficiency difference is below 1% within a restricted area in terms of speed values below 4000 rpm. Nevertheless, the last statement does not hold with regions exceeding 4000 rpm, as a significant efficiency discrepancy of up to 30% can be reached in low torque high-speed regions. This discrepancy can be explained by the non-linearity of losses at high speed. As a result, it is convenient to say that linear scaling is not suitable for high-speed gearboxes. However, this scaling choice may find utility in low-rated speed gearboxes as decent results can be achieved in the concerned operating range.

$$P'_{losses} = \frac{K_T^{GB} K_N}{K_{kgb}} P_{losses}^0 \tag{111}$$

Based on the analysis presented above, the linear losses-to-power scaling is deemed ineffective for scaling the losses of high-speed gearboxes. This proves the utility of the data-driven power loss scaling laws derived in Section 4.2, which demonstrates high flexibility in accommodating various scaling cases and provides satisfactory accuracy.
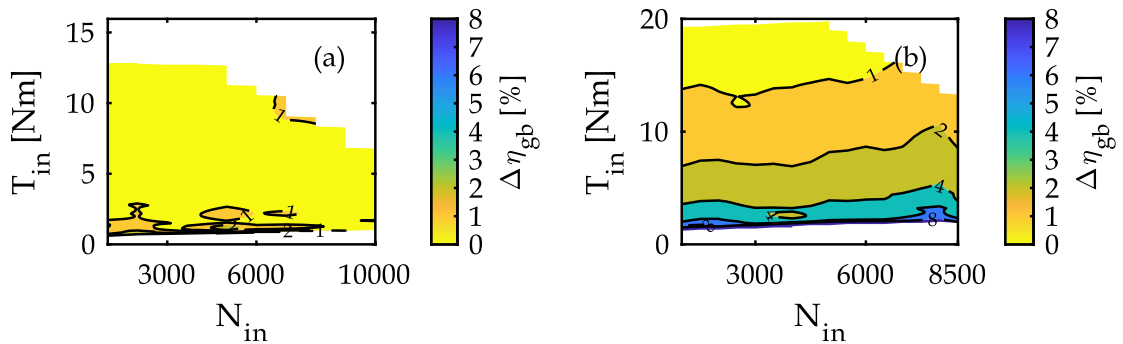
Fig. 74: Assessment of linear losses-to-power scaling outcomes for speed and torque scaling cases as compared to experimental results: (a) case study ①; (b) case study ④.
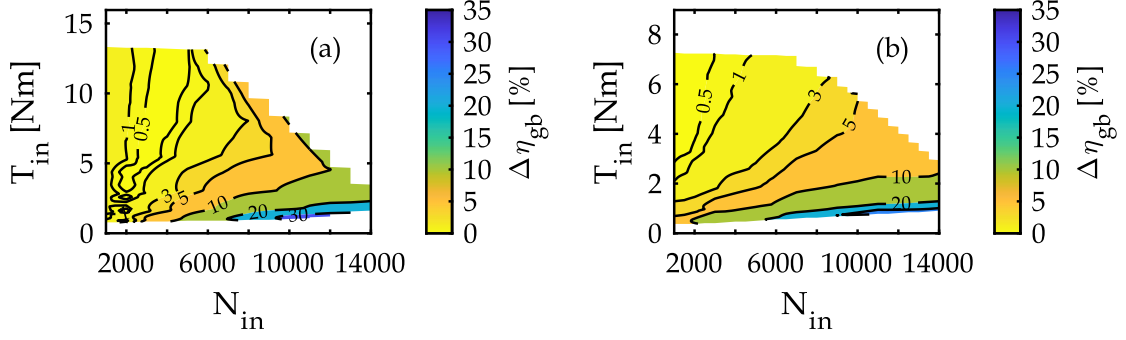
Fig. 75: Assessment of linear losses-to-power scaling outcomes for gear ratio scaling cases as compared to experimental results: (a) scaling case ②; (b) scaling case ③.

5 EMR-based scaling laws of planetary gearboxes

Following the approach elaborated in Chapter II for electric drive systems, this section presents EMR-based scaling laws for planetary gearboxes. To accomplish this, the model of planetary gearboxes (112), and (113), along with the scaling laws proposed in Section 4.2.1, are reorganized to solely scale the input and the output of the reference model. This is achieved by incorporating mechanical power adaptation elements, as illustrated in Fig. 76. As a reminder, the apostrophe ' stands for scaled parameters, while those with the superscript 0 denote the reference parameters.

$$T_{\text{sh,out}}^{\text{GB}^0} \;=\; k_{\text{gb}}^0 T_{\text{sh,in}}^{\text{GB}^0} - T_{\text{losses}} \;=\; k_{\text{gb}}^0 T_{\text{sh,in}}^{\text{GB}^0} - \frac{P_{\text{LD}}^0 + P_{\text{LID}}^0}{\Omega_{\text{gb}}^0} \tag{112}$$

$$\Omega_{\text{sh,in}}^{\text{GB}^0} \;=\; k_{\text{gb}}^0 \, \Omega_{\text{sh,out}}^{\text{GB}^0} \tag{113}$$
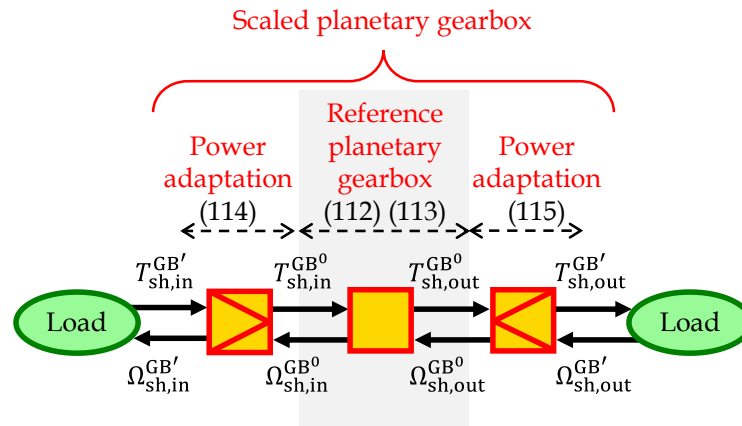
Fig. 76: EMR-bases scaling laws of planetary gearboxes

The input mechanical power adaptation is derived following (114). In this case, the input torque of the reference gearbox $T_{\text{sh,in}}^{\text{GB}^0}$ is scaled similarly to what was described in Fig. 66, while the input speed of the scaled gearbox $\Omega_{\text{sh,in}}^{\text{GB}'}$ is scaled by the speed scaling factor K_{N}. The reason behind the speed scaling will be elaborated, when dealing with the derivation of the output power adaptation element.

$$
\begin{cases}
T_{\text{sh,in}}^{\text{GB}^0} &= \dfrac{K_{\text{kgb}}}{K_{\text{T}}^{\text{GB}}} T_{\text{sh,in}}^{\text{GB}'} \\
\Omega_{\text{sh,in}}^{\text{GB}'} &= K_{\text{N}} \Omega_{\text{sh,in}}^{\text{GB}^0}
\end{cases}
\tag{114}
$$

The output mechanical power adaptation element assumes that the output torque of the reference gearbox $T_{\text{sh,out}}^{\text{GB}^0}$ scale linearly with the torque scaling factor K_{T}^{GB} (115). However, an equivalent torque ΔT_{GB} is subtracted to include the non-linear behavior of losses during the scaling process and achieve the correct value of the scaled losses. This equivalent loss term can be expressed as given in (116) based on (108), and (109). Moreover, the output speed of the scaled gearbox $\Omega_{\text{sh,out}}^{\text{GB}'}$ is scaled using the ratio between K_{kgb}, and K_{N}. K_{kgb} is introduced in (115) to account for a gear ratio scaling, whereas K_{N} represent the maximal speed scaling of the reference gearbox. To achieve the same relationship as in (113), the input speed of the scaled gearbox needs to be scaled as shown in (114), as both speeds are inherently connected.

$$
\begin{cases}
T_{\text{sh,out}}^{\text{GB}'} &= K_{\text{T}}^{\text{GB}} T_{\text{sh,out}}^{\text{GB}^0} - \Delta T_{\text{GB}} \\
\Omega_{\text{sh,out}}^{GB^0} &= \dfrac{K_{\text{kgb}}}{K_{\text{N}}} \Omega_{\text{sh,out}}^{GB'}
\end{cases}
\tag{115}
$$

$$
\Delta T_{\text{GB}} = \left(K_{\text{kgb}}^2 - K_{\text{T}}\right) \frac{P_{\text{LID}}^0}{\Omega_{\text{GB}}^0} + \frac{K_{\text{kgb}}}{K_{\text{N}}} \frac{\Delta P_{\text{LID}}^0}{\Omega_{\text{GB}}^0}
\tag{116}
$$

To validate the new model organization, a comparison between a conventional EMR and an EMR-based scaling laws is conducted as shown in Fig. 77. To clarify, a conventional EMR does not incorporate power adaptation elements in the model organization. In the following analysis, the case study ① is herein examined. The data of the scaled gearbox, i.e. the 2nd gearbox, is implemented in the model organized using the conventional EMR (Fig. 77.a). On the other hand, the data of the reference gearbox, i.e. the 1st gearbox, is implemented in the model organized through EMR-based scaling laws (Fig. 77.b). The scaling factors embedded in the power adaptation elements will enable the scaling from the 1st to the 2nd gearbox. For this comparison, trapezoid-shaped profiles for input torque and output speed, including acceleration and deceleration phases, have been imposed as illustrated in Fig. 77.c. The comparison results for the output of the scalable model of the gearbox, namely $T_{\text{sh,out}}^{\text{GB}'}$, $\Omega_{\text{sh,in}}^{\text{GB}'}$ are depicted in Fig. 78. As can be consulted from the latter figure, the difference between both simulations is negligible, almost 0%, thus demonstrating the validity of the EMR-based scaling laws.
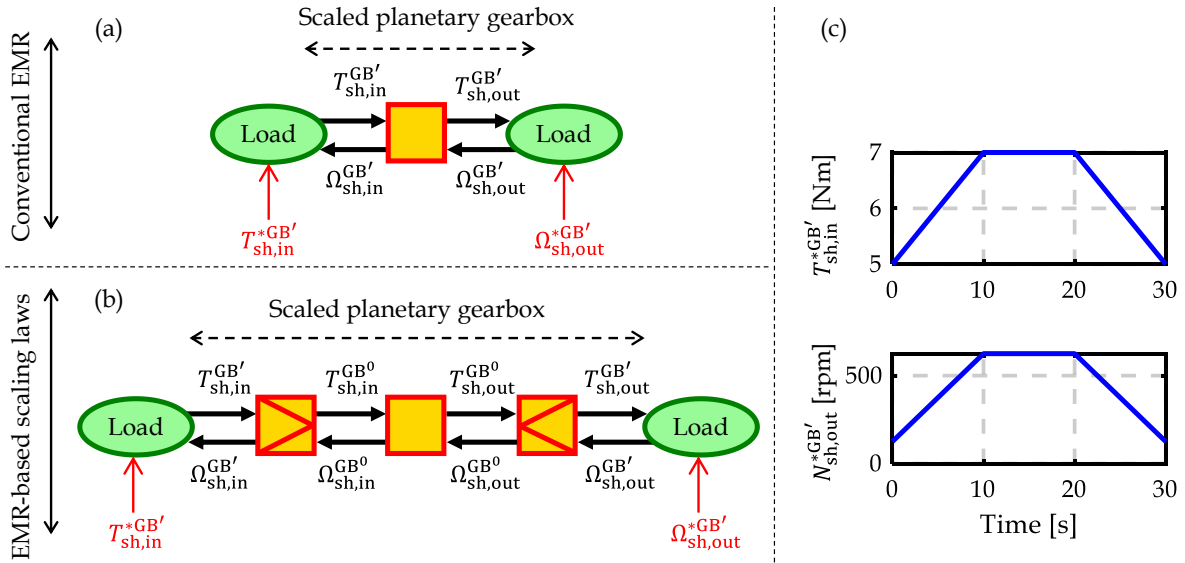
Fig. 77: Comparison between (a) conventional EMR, and (b) EMR-based scaling laws for planetary gearboxes. The red arrows in (a), and (b) are the input reference parameters illustrated in (c).
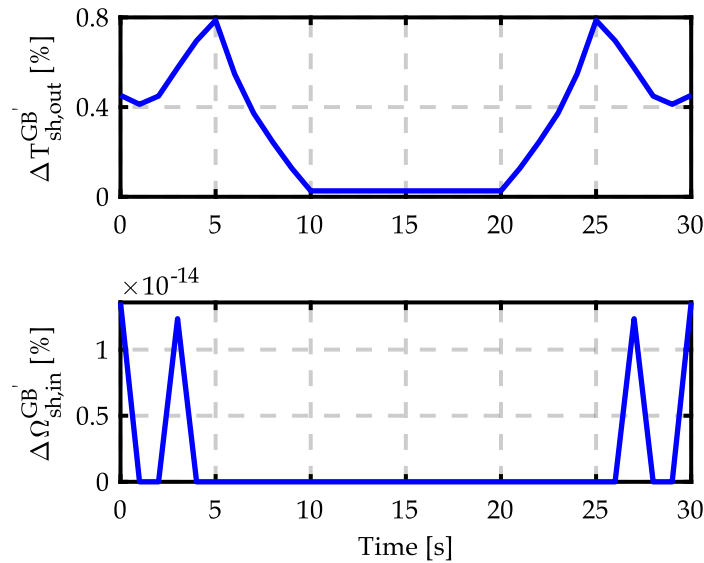
Fig. 78: Comparison results between conventional EMR and EMR-based scaling laws

6 Conclusion

The conducted work in this chapter provides an initial framework for bridging the gap in literature on the scaling laws of power losses of gearboxes, namely for dip-lubricated planetary speed reducers. This shows that the second challenge, as defined in Section 6.2 of Chapter I, is achieved. A second contribution of the work is the extensive experimental investigation of the power losses of planetary reducers at high-speed values. The emphasis on high speed is driven by the increasing interest in high-speed drivetrains in the automotive industry. Both load-dependent and load-independent losses have been experimentally characterized at speed values up to 14,000 rpm using 5 gearboxes. This experimental campaign is notable for its

127

incorporation of high-speed values as compared to the results reported on planetary gearbox testing in the current literature. However, the maximal torque rating differs from the requirements typically encountered in automotive gearboxes due to the low-rated power rating of the tested specimens. The conducted test results allow for defining a data-driven model, containing physics-based terms, i.e. speed, torque, and gear ratio parameters. Scaling laws are then derived based on maximal input speed, output torque, and gear ratio requirement using a training set, containing the data of 3 gearboxes. A second dataset, containing data from two other gearboxes has been used as a validation case for the scaling process. A methodology based on the scaling laws is subsequently proposed to create a power loss map or efficiency map of a scaled gearbox using solely the data of a reference gearbox. The results of this investigation show that scaling the torque and speed of a reference gearbox while preserving the same gear ratio leads to outstanding results. An average error of less than 0.35% for the entire operating points is obtained. However, the scaling exercise becomes more challenging when the gear ratio is incorporated because of the nonlinearity of losses at high-speed values. Although an efficiency discrepancy in high-speed regions, exceeding 10,000 rpm, up to 6% is observed in restricted areas of the map, the outcomes of the scalable model remain satisfactory. This is evidenced by an efficiency difference of less than 1% for non-high-speed areas. A sensitivity analysis is conducted, aiming to determine the impact of the reference gearbox selection in the scaling process, alongside the gearboxes incorporated in the training set. The analysis shows that the reference gearbox selection is not impactful for the scaling process, as good results have been achieved with another gearbox as a reference. However, the gearbox selection for the training process has been proven of high importance. The examination reveals that when extrapolating to regions, where the scalable model lacks training data, unsatisfactory results for some scaling cases are achieved. Speed and torque-speed scaling demonstrated satisfactory results, regardless of the training set. On the other hand, the gear ratio scaling process is shown to be sensitive to the training set selection, due to high non-linearity of load-independent losses. Incorporating a wider range of gear ratios in the scaling process will certainly improve, and broaden the current work. Further examination in the chapter assesses the application of the linear losses-to-power scaling method for planetary gearboxes. The analysis demonstrates that while the linear scaling method can guarantee good results within low-speed regions, it is not suitable for high-speed regions. The chapter concluded with a new organization of the scalable model following the EMR-based scaling laws, for ease of incorporation of the scaling laws later at system-level. To validate the reliability of the EMR-based scaling laws, a comparison is conducted versus the standard EMR, leading to negligible differences in the outcomes obtained.

Chapter IV

Comparative analysis of the effect of scaling methods of electric axle on energy consumption of electric vehicles

1 Introduction

This chapter aims to conduct a comparative analysis of the effect of the scaling method of electric axle (e-axle) components, i.e. the set of inverter, electric machine, and gearbox, on energy consumption. As stated in Chapter II, the linear scaling method is widely utilized in the current state-of-the-art in system-level investigations due to its simplicity and ease of use. Consequently, an extensive emphasis is placed in this chapter to compare the outcomes of this method against more advanced scaling laws that delve deeper into the component design. A key contribution of this chapter is to assess the reliability of the linear scaling methods in terms of energy consumption of Electric Vehicles (EV) and define the conditions under which this reliability holds. For this aim, three battery-electric vehicles, namely two passenger cars of different classes, and a medium-duty commercial truck, with varying power ratings are considered as case studies to evaluate energy consumption. The battery electric vehicles are chosen for this research as the traction function of the vehicle is ensured by at least one electric machine, making it an ideal subject for studying the effect of scaling methods on energy consumption.

Due to the considerable number of scaling methods for each component and the automotive application under investigation, there arises a necessity for a unified and comprehensive simulation framework that facilitates the incorporation of the scalability aspect at system-level. Another additional noteworthy point is that this framework should allow for an increase in the understanding of the interaction between the scaled components. The current literature lacks clarity regarding this particular matter. This originates from the fact that the theory of scaling laws is established at component-level and used at sytem-level as a set of equations combined with the reference model of the components. Consequently, a comprehensive examination of the impact of component scalability at system-level becomes challenging due to the lack of clear structuration of the models. To tackle this issue, the chapter introduces an

innovative method to structure a scalable model and control of a reference e-axle used in system-level simulations, following the Energetic Macroscopic Representation (EMR). For this purpose, the interaction between the EMR-based scaling laws presented for the PMSM and inverter in Chapter II, and for gearboxes in Chapter III is investigated. This examination enables the derivation of a new organization of EMR-based scaling laws of the entire e-axle using two equivalent power adaptation elements at the input and the output of the reference model of the e-axle, as conceptualized in Section 6.5.3 of Chapter I. Additionally, a scalable control scheme for the e-axle is proposed based on the EMR-based scaling laws. This contributes to facilitating and expediting the energy consumption assessment by easily incorporating a scalable model and control of the e-axle in simulation environments of EV. Furthermore, this contribution serves to broaden the scope of application of the EMR formalism, which is mainly used for the deduction of the control design. The key contributions of this work can be summarized as follows:

- Unified simulation framework using EMR-based scaling laws to analyze the interactions between scalable models of e-axle components and the performance of a broad range of EV with different topologies.
- A detailed examination of the energy consumption of electric vehicles, as influenced by the scaling methods for various driving cycles (urban, rural, highway).
- Thorough scrutiny of the difference between linear scaling and alternative scaling laws of the e-axle for various power scaling rates (upscaling and downscaling cases) for more informed decision-making.
- Assessment of the reliability of the linear scaling method for different topology configurations.

This chapter is structured as follows. Section 2 presents the scaling specification of this investigation. The EMR-based scaling laws of the e-axle are presented in Section 3. A sensitivity analysis of the effect of the scaling method is discussed in-depth in Section 4.

2 Scaling specifications

2.1 Presentation of the studied EV

To conduct the comparative analysis of the scaling laws, three vehicles, belonging to different classes, are considered. The driving requirements of the vehicles are conceptualized, similar to available commercialized models in the market, namely the Renault Twingo (mini-compact car) [222], Nissan Leaf (compact car) [223], and BYD ETM6 medium-duty truck [224]. The main parameters of the vehicles are presented in Table 20. All three vehicles share the same powertrain layout, namely a centralized mono-drive powertrain, which is illustrated in Fig. 79. However, the power rating specification of the e-axle differs from one vehicle to another.

Table 20: Main parameters of the studied EV

	Mini-compact car (A-segment)	Compact car (C-segment)	Medium-duty truck
Electric drive			
DC bus voltage [V]	375	375	375
Electrical machine power [kW]	45.7	80	157
Electrical machine maximum torque [Nm]	160	280	550
Drivetrain			
Overall gear ratio [-]	8.32	8.19	14.46
Chassis			
Curb vehicle weight [kg]	1168	1505	3500
Top speed [km/h]	135	144	100
Acceleration time : 0-100 km/h[s]	12.6	9.9	12.8
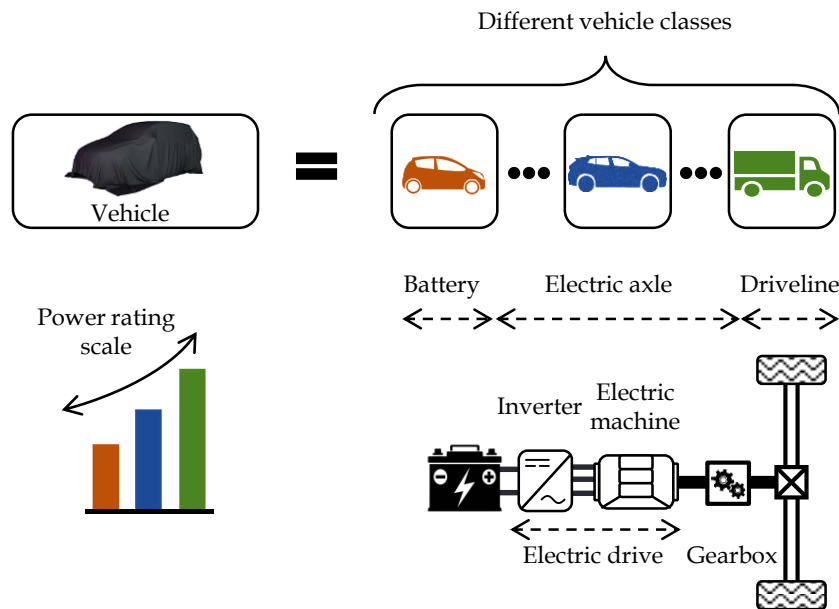
Fig. 79: Powertrain layout

2.2 Case studies

Four scaling cases are herein considered, encompassing 2 upscaling cases and 2 downscaling cases. This choice is motivated by the aim to provide a broad insight into the scaling effect, considering different power scaling factors. The adopted workflow for this investigation is depicted in Fig. 80. The starting point is the e-axle of the compact car, selected as a reference to investigate in a more balanced way the scaling effect. In other words, the reference is selected in the middle of the power rating spectrum of the case studies to constrain the extent to which scaling is required. A typical maximal power scaling factor of 2 is recommended by [169]. This recommendation is based on technical and technological considerations regarding permissible geometric modifications of the reference component. Note that, the electric machine design of this reference e-axle is the same as the 2012 Nissan Leaf traction machine (80 kW), presented in Chapter II. As for the inverter, the FS600R07A2E3 inverter from Infineon,

cf. Section 4.2 of Chapter II, is associated with the reference electric machine, as the power rating is suitable for this latter.

The upscaling cases consist of scaling the e-axle of the compact car to derive an upscaled version of the e-axle, that can be used within the same vehicle to enhance the acceleration performance. The latter scaling case is referred to as case ①. Additionally, a second upscaling, denoted as scaling case ③, is considered, which involves the scaling of the reference e-axle to correspond to the driving requirements of the medium-duty truck. The scaling case ① is considered to highlight that the scalability approach can be applied not only to study different types of vehicles but it can also be applied within the same vehicle. This choice stems from the practices of vehicle manufacturers, which offer the same model of an electric vehicle featuring different power ratings. Consequently, this practice facilitates the introduction of models with varying degrees of performance, e.g. sportier versions, or more affordable versions with reduced performance. As for the downscaling cases, the reference e-axle is downscaled to investigate a reduced-performance version of the compact car, described as case ②, and a mini-compact car, introduced as case ④. Table 21 summarizes the applied scaling factors for the four case studies.
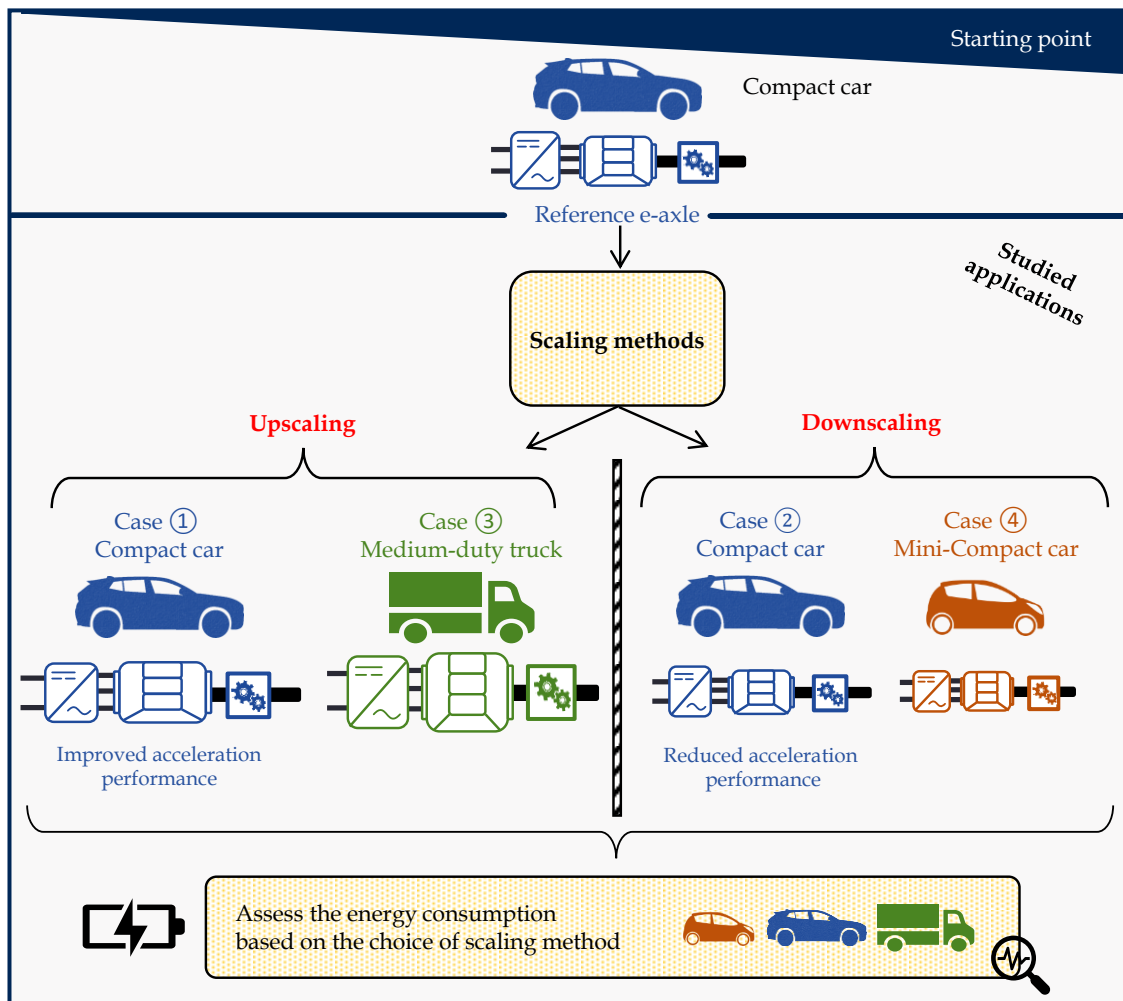
Fig. 80: Scaling specifications

Table 21: An overview of the scaling power factors

	Case ①: Compact car (improved- perfor-mances)	Case ②: Compact car (reduced-perfor-mances)	Case ③: Medium-duty truck	Case ④: Mini-compact car
Power scaling factor [-]	1.33	0.67	1.96	0.58

2.3 Driving cycles

To provide comprehensive analyses of the impact of each scaling method, diverse driving cycles with different driving patterns (urban, rural, and highway) and driving behavior (low, medium, and aggressive accelerations) have been considered (Table 22). This enables the examination to encompass a broad set of operating points dispersed across the torque-speed plane of the e-axle. Regarding the mini-compact and compact cars, 6 standardized driving cycles, widely used worldwide to benchmark energy consumption and emissions are selected [225]. Furthermore, 4 on-road driving cycles, recorded using the Nissan Leaf of the CUMIN program (cf. Section 6.3 of Chapter I), similar to the compact car, have been considered. These latter present urban and highway driving patterns to account for real-case scenarios.

Table 22: Overview of the selected driving cycles

Vehicle	Driving cycle	Average driving speed [km/h]	Top speed [km/h]	Average positive acceleration [m/s^2]	Average nega-tive acceleration [m/s^2]
Compact and mini-compact	NYCC	16.63	44.45	0.47	-0.48
	ARTEMIS urban (Art. URB)	22.29	57.32	0.53	-0.57
	WLTC 3	53.48	131.3	0.42	-0.44
	ARTEMIS rural (Art. RUR)	58.34	111.09	0.36	-0.37
	ARTEMIS Highway (Art. HWY)	97.60	131.43	0.27	-0.35
	Lille downtown (Lille DT)	19.22	46.00	0.57	-0.56
	University of Lille - Campus Villeneuve d'Ascq (ULille)	21.19	44.90	0.42	-0.48
	Lille-Tourcoing	57.38	101.66	0.22	-0.21
	Lille-Ghent	77.54	101.41	0.29	-0.32
Medium-duty truck	VECTO urban delivery	33.98	87.50	0.65	-0.65
	VECTO regional delivery	69.30	85.78	0.47	-0.50
	VECTO long haul	79.08	87.50	0.17	-0.18

Regarding the medium-duty truck, 3 driving cycles extracted from the European truck certification tool VECTO have been selected for the energy consumption analyses (Table 22) [226]. These driving cycles represent different missions of the truck, namely long haul,

regional, and urban delivery missions. Note that the speed profiles of the driving cycles, under consideration, are depicted in Appendix VI.1.

3 EMR-based scaling laws of electric vehicles

This section aims to derive a unified and flexible simulation framework to assess the performance of the different EV presented earlier, by employing a unique system-level model of the e-axle. For this aim, the modeling equations of the scaled e-axle are restructured following the EMR-based scaling laws, targeting two power adaptation elements at the input and the output of the reference model. This is achieved by capitalizing on the EMR-based scaling laws that are presented in Chapter II for electric drive systems and further elaborated in Chapter III for gearboxes. Several intermediary steps are involved, as indicated in Fig. 81.

Step 1: Deduction and simulation-based validation of the EMR-based scaling laws of the <u>**electric drive**</u>

↓

Step 2: Deduction and simulation-based validation of the EMR-based scaling laws of the <u>**electric axle**</u>

↓

Step 3: Deduction of a <u>**scalable static model**</u> using EMR-based scaling laws of the <u>**electric axle**</u>
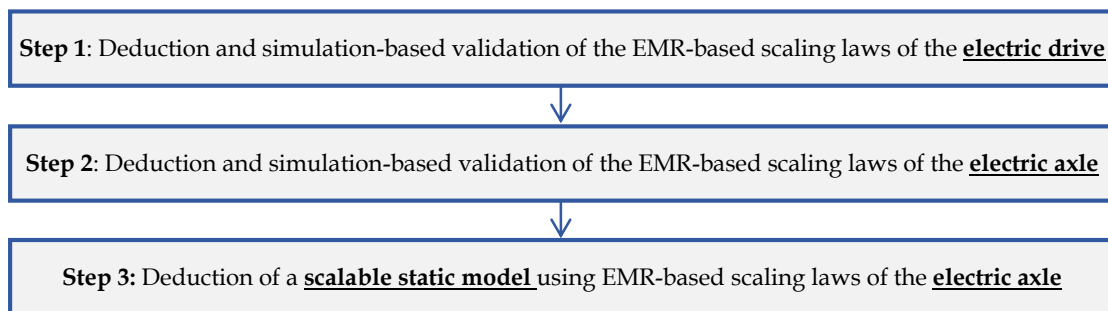
Fig. 81: Adopted workflow for the deduction of the EMR-based scaling laws

Step 1, as depicted in Fig. 82. b, consists in studying the interaction of the scalable model of the inverter and the PMSM. The focus of this step lies in simplifying the interconnected power adaptation elements. Based on the interaction examination between both components, a new structuration of the scalable Electric Drive System (EDS) model using an equivalent power adaptation element on the electrical side and another one on the mechanical side is derived. Then, a comparison is conducted between a simulation environment utilizing the proposed organization of the scalable EDS and a conventional model organization (Fig. 82. a). For clarity when referring to a conventional or a standard model organization, it means that no power adaptation elements are involved in contrast to the organization of the model following the EMR-based scaling laws concept. This involves that the scaled parameters in the conventional model organization need to be calculated beforehand in a pre-processing phase, rather than being computed online within the simulation program.

Step 2, as illustrated in Fig. 82. c, involves studying the interaction between the scalable model of the EDS and the gearbox to end up with a scalable model of the entire e-axle. Similar to Step 1, the aim is to simplify the interconnected power adaptation elements. This step includes a validation-based simulation against a conventional model organization.

Step 3, as described in Fig. 82. d, consists in deriving a scalable static model of the entire e-axle based on a reference efficiency map to perform energetic simulations of the studied vehicles. In this work, the static model is established for the e-axle in alignment with the upward tendency in current literature and industry [172], [227]. This is because the e-axle is recognized as a unified system due to its highly integrated components, often referred to as 3in1. The

presented approach in this work differs from earlier research work, which exclusively employs a static model for the EDS [16].
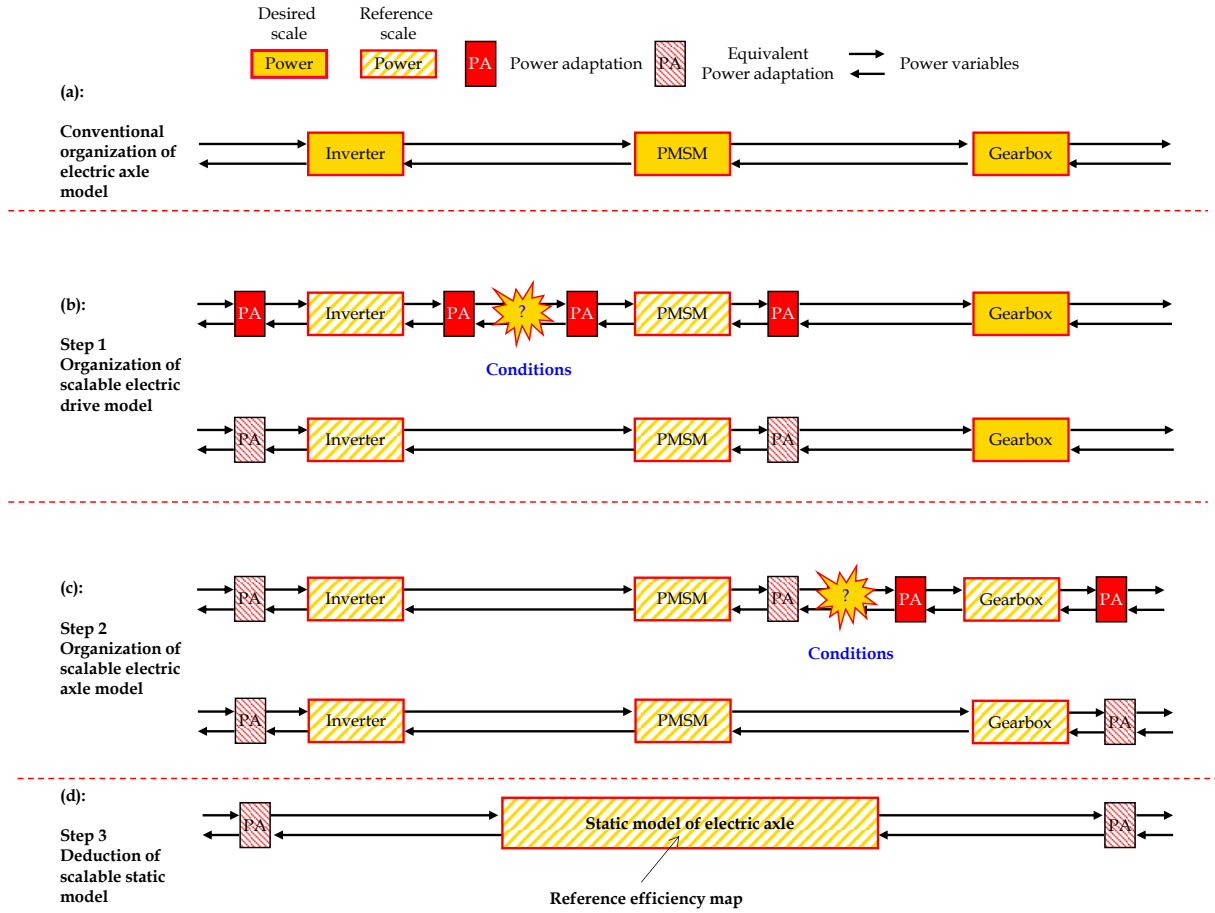
Fig. 82: Conceptualization of the EMR-based scaling laws of the electric axle

3.1 Conventional EMR for electric vehicle simulation

3.1.1 Powertrain modeling

Fig. 83 presents the EMR of the topology of the studied EV, reflecting the model organization shown in Fig. 82.a. It is worth mentioning that a description of the EMR pictograms is given in Appendix III. This EMR is deduced from a conventional organization of the powertrain components models, which are detailed in the following section. In the remainder of the chapter, the EMR, depicted in Fig. 83, is referred to as conventional EMR. To ensure consistency in notation with the previous chapters, the apostrophe "'" is employed to denote variables in the final scale.

The battery voltage v'_{bat} is expressed as a function of the current i'_{ED}, the Open Circuit Voltage (OCV), and the internal battery resistance r'_{bat}, which depends on the State of Charge (SoC_{bat}) of the battery.

$$v'_{\text{bat}} = v'_{\text{OCV}}(SoC_{\text{bat}}) - r'_{\text{bat}}(SoC_{\text{bat}})i'_{\text{ED}} \tag{117}$$

The model of the inverter is presented in Section 4.3.1.1 in Chapter II, as outlined by equations (55). The model of the PMSM is introduced in Section 3.4.1.1 of the same chapter,

described by equations (17)-(22). Note that the scaled parameters are calculated in a pre-processing phase using the scaling laws elaborated in Section 3 in Chapter II. As for the gearbox, its corresponding model is presented in Chapter III, described by equations (112)-(113).

The wheels convert the torque T'_{GB} to a force F'_{wh} and speed Ω'_{GB} to a velocity v'_{veh} using the wheel radius r_{wh} (118), assuming a kinematic bicycle model with no curves and no road-tire contact.

$$\begin{cases} F'_{wh} &= \dfrac{T'_{GB}}{r_{wh}} \\ \Omega'_{GB} &= \dfrac{v'_{veh}}{r_{wh}} \end{cases} \tag{118}$$

The total required traction force F'_{tract} is the result of the sum of F'_{wh} and the force of the mechanical brake F'_{brk} (119). The velocity of the vehicle v'_{veh} is determined by applying the second law of Newton, using the traction force F'_{tract} and the resistive force to the motion F'_{res}, and the mass of the vehicle M^{eq}_{veh} (120).

$$F'_{tract} = F'_{wh} + F'_{brk} \tag{119}$$

$$M^{eq}_{veh} \frac{dv'_{veh}}{dt} = F'_{tract} - F'_{res} \tag{120}$$

where M^{eq}_{veh} is expressed as a function of the static mass of the vehicle M_{veh} (i.e. the mass of the chassis, glider, powertrain, etc.), and the equivalent masses of the rotating elements, which depend on the inertia of the electric machine I'_{EM}, the gearbox I'_{GB}, and the wheels I'_{wh} (121).

$$M^{eq}_{veh} = M_{veh} + \frac{I'_{EM}}{r^2_{wh} k^2_{GB}} + \frac{I'_{GB}}{r^2_{wh}} + \frac{I'_{wh}}{r^2_{wh}} \tag{121}$$

The resistive force imposed by the environment F'_{res} is given as a function of the rolling resistance F'_{roll}, aerodynamic resistance F'_{aero} and the slope resistance F'_{slope} (122).

$$F'_{res} = F'_{roll} + F'_{aero} + F'_{slope} \tag{122}$$
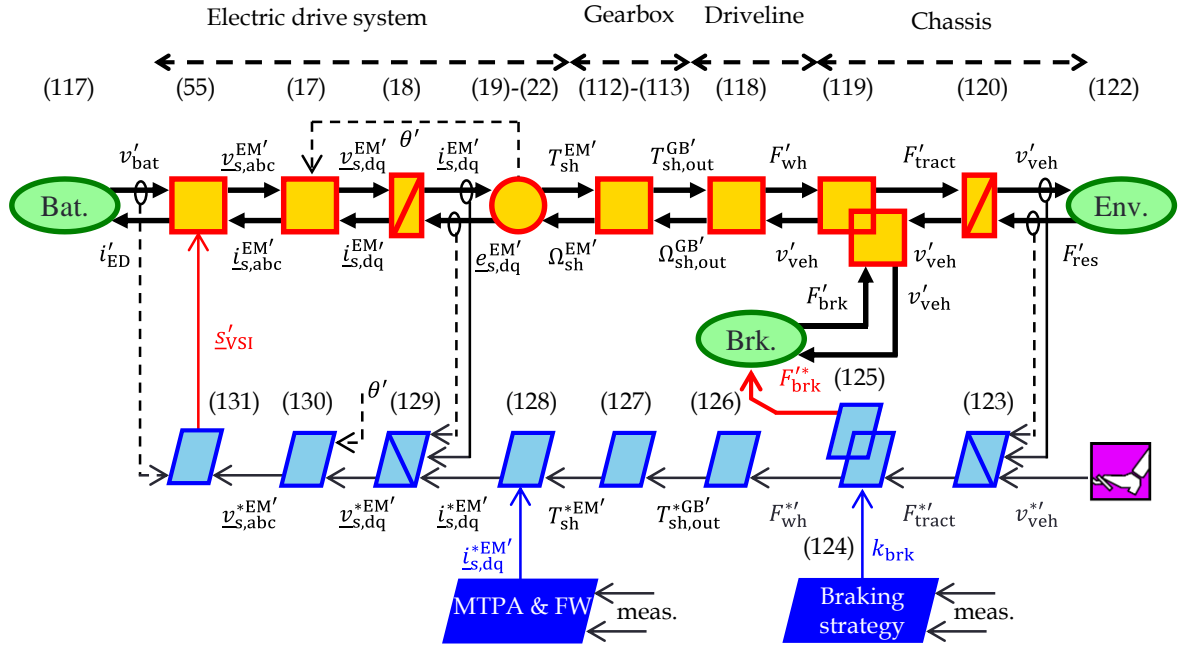
Fig. 83: Conventional EMR and control of mono-drive based- battery electric vehicles

3.1.2 Powertrain control

One of the strengths of the EMR formalism is to systematically deduce the local control structure (light blue part of Fig. 83) by following the inversion principle of the models [33]. In this case, the local control of the vehicle aims to track a reference speed profile of a given driving cycle v'^*_{veh}. This can be achieved by acting on the control variables, namely the switching functions of the inverter $\underline{s}'_{\text{VSI}}$, and the braking force F'^*_{brk}. Note that superscripts "*", and "meas" denote control and measured variables, respectively, whereas the underscored parameters represent vectors. The EMR elements that do not store energy are directly inverted from their modeling equations (light blue parallelograms), e.g. (126), (*127*), (130), and (131). A closed-loop control (light blue crossed parallelograms) using PI controllers is used to track the speed setpoints (123) and the *dq*-axes currents of the electric machine (129). A rule-based strategy (dark blue parallelogram) is herein used to define the braking criterion k_{brk} (124) to distribute the braking effort between regenerative and mechanical braking (125). Regenerative braking forces are limited to 60% of the total braking force due to the distribution of force between the front and rear axles during braking for stability reasons of the vehicle. Furthermore, constraints related to the maximal torque of the electrical machine, battery state of charge (SoC_{bat} > 99%), and maximal charging current impact the determination of k_{brk}. Note that the same braking strategy will be used for the different studied vehicles for comparison purposes. Additional details and alternative braking strategies are available in [228], [229]. The current setpoints $\underline{i}'^*_{\text{s,dq}}$ are defined using MTPA and Field Weakening (FW) strategies (128) (dark blue parallelogram). These latter are implemented in the form of a look-up table, that is computed beforehand in a pre-processing phase based on the scaled design of the PMSM. Regarding the control of the voltage source inverter, a sinusoidal pulse width modulation strategy is employed considering averaged switching functions over a period. A control strategy of the inverter is used, mandating that the zero-sequence voltage between the reference

potential of the inverter and the fictitious neutral point of the machine is set to zero [230]. More details on the modeling and control of the inverter and their associated EMR can be found in Appendix VI.3.

$$F_{\text{tract}}'^* = C_{\text{speed}}'(t)(v_{\text{veh}}^{*\prime} - v_{\text{veh}}'^{\text{meas}}) + F_{\text{res}}' \tag{123}$$

$$\begin{cases} k_{\text{brk}} & = & 1 & \text{full mechanical braking} \\ k_{\text{brk}} & = & 0 & \text{no braking} \\ 0 & \leq k_{\text{brk}} \leq & 0.6 & \text{hybrid braking (regenerative+mechanical)} \end{cases} \tag{124}$$

$$\begin{cases} F_{\text{brk}}'^* & = & k_{\text{brk}} F_{\text{tract}}'^* \\ F_{\text{wh}}'^* & = & (1 - k_{\text{brk}}) F_{\text{tract}}'^* \end{cases} \tag{125}$$

$$T_{\text{sh,out}}^{*\text{GB}'} = F_{\text{wh}}'^* r_{\text{wh}} \tag{126}$$

$$T_{\text{sh}}^{*\text{EM}'} = \frac{T_{\text{sh,out}}^{*\text{GB}'}}{k_{\text{gb}}'} \tag{127}$$

$$\left(i_{\text{s,d}}^{*\text{EM}'}, i_{\text{s,q}}^{*\text{EM}'}\right) = f(\text{MTPA \& FW}) \tag{128}$$

$$\underline{v}_{\text{s,dq}}^{*\text{EM}'} = C_{\text{current}}'(t)\left(\underline{i}_{\text{s,dq}}^{*\text{EM}'} - \underline{i}_{\text{s,dq}}^{\text{measEM}'}\right) + \underline{e}_{\text{s,dq}}'^{\text{meas}} \tag{129}$$

$$\underline{v}_{\text{s,abc}}^{*\text{EM}'} = [P(\theta)]^{-1} \underline{v}_{\text{s,dq}}^{*\text{EM}'} \tag{130}$$

$$\underline{s}_{\text{VSI}}' = \frac{\underline{v}_{\text{s,abc}}^{*\text{EM}'}}{v_{\text{bat}}'^{\text{meas}}} \tag{131}$$

3.2 Step 1: Deduction and validation of EMR-based scaling laws of electric drive systems

3.2.1 Scalable model

This section aims to derive a scalable model of the EDS, as illustrated in Fig. 82.a. This is achieved by reorganizing the equations following the concept of the EMR-based scaling laws. In Fig. 84, the EMR-based scaling laws for both the inverter and PMSM, as described in Chapter II, are recalled alongside the equation embedded in the adjoining power adaptation elements.

As a first step, the focus is placed on studying the interaction between the AC power adaptation of the inverter and the electrical power adaptation of the electric machine. To connect both elements, the conditions shown in (132) should be met. This requirement is reasonable as the output voltage of the scaled inverter $\underline{v}_{\text{abc}}^{\text{VSI}'}$ will be applied to the machine and the current requested by the scaled machine $\underline{i}_{\text{abc}}^{\text{EM}'}$ will be applied to the scaled inverter. This interaction between both components is evident in the conventional EMR, depicted in Fig. 83.

$$\begin{cases} \underline{v}_{\text{s,abc}}^{\text{EM}'} & = & \underline{v}_{\text{abc}}^{\text{VSI}'} \\ \underline{i}_{\text{abc}}^{\text{VSI}'} & = & \underline{i}_{\text{s,abc}}^{\text{EM}'} \end{cases} \tag{132}$$
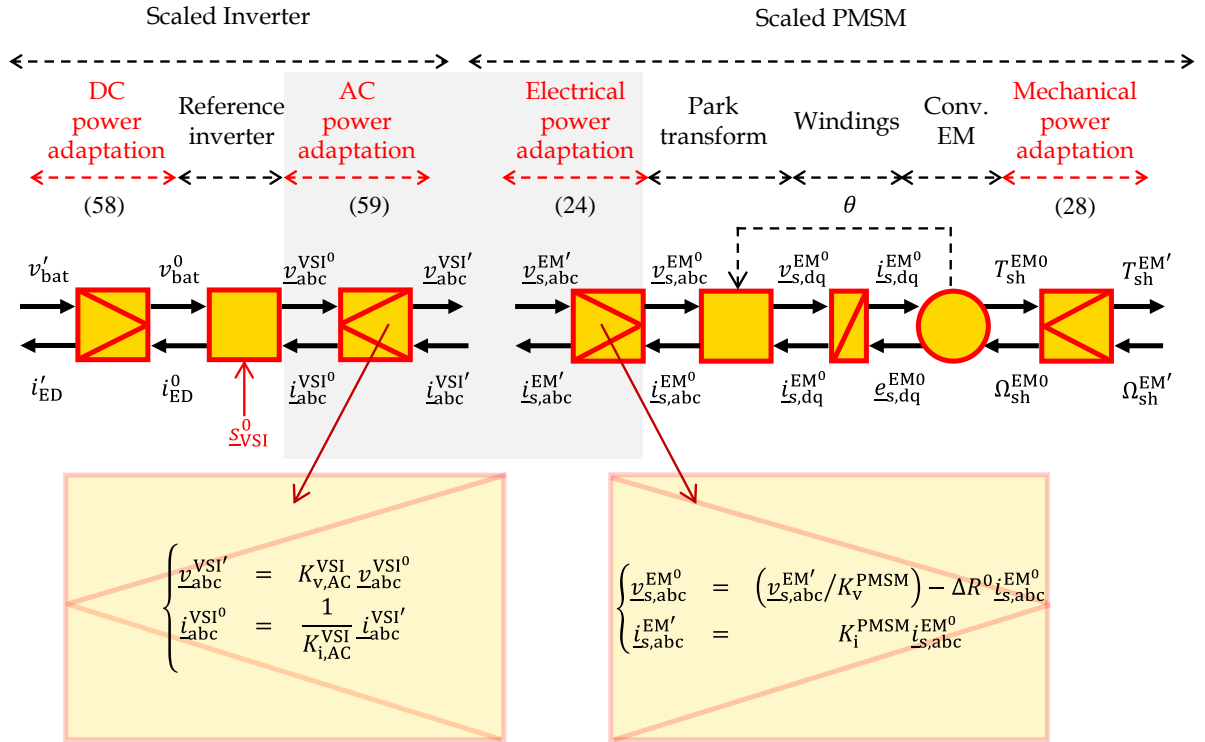
Fig. 84: EMR-based scaling laws of both inverter and PMSM

By replacing the expression of the scaled voltages and currents with their scaling laws within the framework of the reference inverter and machine, (132) can be rewritten as in (133).

$$
\begin{cases}
\underline{v}_{s,abc}^{EM^0} &= \dfrac{K_{v,AC}^{VSI}}{K_v^{PMSM}} \underline{v}_{abc}^{VSI^0} - \Delta R^0 \underline{i}_{s,abc}^{EM^0} \\[2mm]
\underline{i}_{dq}^{VSI^0} &= \dfrac{K_i^{PMSM}}{K_{i,AC}^{VSI}} \underline{i}_{s,abc}^{EM^0}
\end{cases}
\tag{133}
$$

The latter equation can be simplified by assuming an equivalent voltage scaling factor for both the machine and inverter $\left(K_{v,AC}^{VSI} = K_v^{PMSM}\right)$. This is acceptable as the voltage rating of the machine should correspond with the one of the inverter. Furthermore, it can be assumed that the current scaling of the inverter aligns with the current scaling factor of the machine $\left(K_i^{PMSM} = K_{i,AC}^{VSI}\right)$. This is because the current rating of the inverter should be at least equal to the maximum peak current of the machine, as a sizing criterion [231]. Therefore, equation (133) can be redrafted as given in (134).

$$
\begin{cases}
\underline{v}_{s,abc}^{EM^0} &= \underline{v}_{abc}^{VSI^0} - \Delta R \underline{i}_{s,abc}^{EM^0} \\[2mm]
\underline{i}_{abc}^{VSI^0} &= \underline{i}_{s,abc}^{EM^0}
\end{cases}
\tag{134}
$$

Based on (134), the two power adaptation elements can be simplified with only one intermediary power adaption element, as shown in Fig. 85. By effecting this manipulation, the most remarkable observation to emerge from the latter figure is that the definition of the reference voltages of the inverter $\underline{v}_{abc}^{VSI^0}$ and the PMSM $\underline{v}_{s,abc}^{EM^0}$ changes when transitioning from the frame (coordinate system) of the reference inverter to that of the reference machine. In other words, the interaction of both power adaptation elements will result in the manifestation of equivalent

139

parameters (voltages), but with different values. This can be explained by the fact that the scaling process of the inverter and the machine have been conducted using different scaling laws, which leads to altering the variables in distinct coordinate systems.
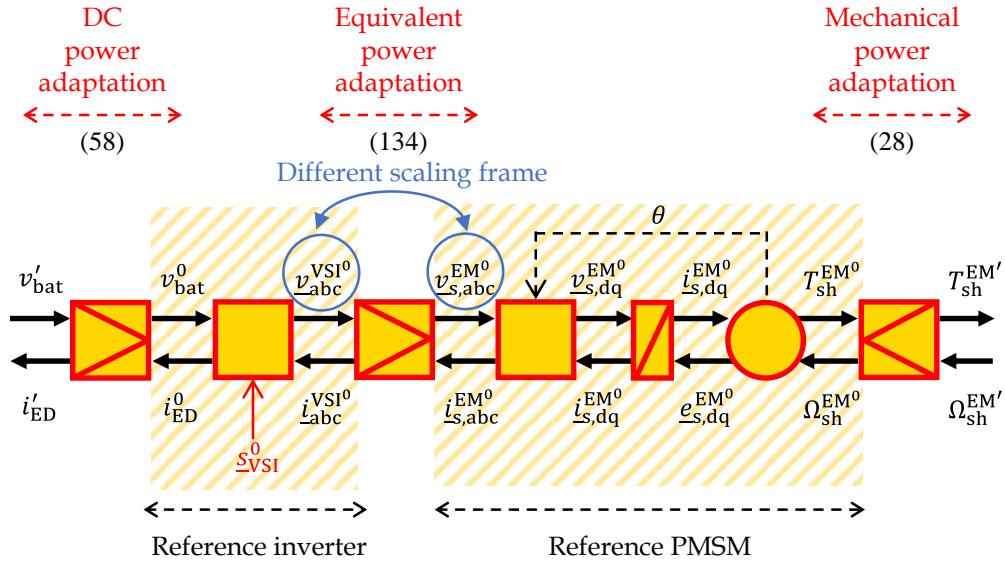
Fig. 85: Interaction between the EMR-based scaling laws of the inverter with the EMR-based scaling laws of the PMSM

From this point, the remaining challenge lies in simplifying the intermediary power adaptation to end up with only two power adaptations at the input and output of the reference model of the electric drive. By consulting (134), it is clear that the intermediary power adaptation element can be simplified if the linear scaling method is applied. This is due to the absence of the equivalent resistance ΔR according to the linear scaling method, thereby resulting in the same voltages of the inverter and the machine. Nevertheless, when different scaling methods for the inverter and the electric machine are employed, e.g. linear scaling for the inverter and geometric scaling of the machine, the simplification of the intermediary power adaptation element becomes less straightforward.

To address this challenge, the idea is to permute the intermediary power adaptation element to the DC side of the reference inverter and subsequently merge it with the DC power adaptation element. This can be accomplished by employing the permutation and merging rules of the EMR formalism [33]. The idea behind the permutation rule is to reposition elements while preserving the global behavior of the system as depicted in Fig. 86. The rule dictates that the effects, i.e. $\underline{v}_{s,abc}^{EM^0}$ and i'_{ED} in this case, needs to be established from the same causes, i.e. v'_{bat}, $\underline{i}_{s,abc}^{EM^0}$ and $\underline{s}_{VSI}^0$, as depicted in the upper part of Fig. 86. This is achieved by manipulating the modeling equation of the reference inverter, Park Transform, and the intermediary power adaptation element.

140
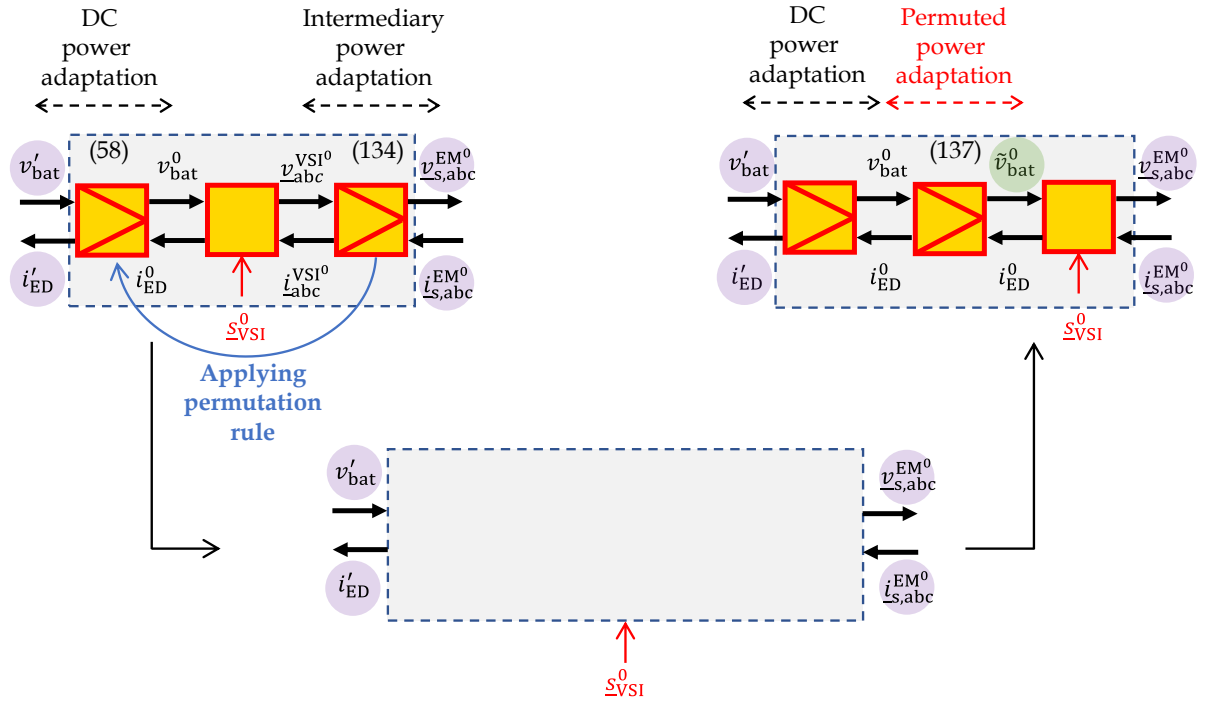
Fig. 86: Permutation of the intermediary electrical power adaptation element

Recalling the model of the reference inverter (135), the voltages $\underline{v}_{s,abc}^{EM^0}$ in (134) can be reformulated as described in (136), employing the reference switching functions and a new fictitious voltage denoted as $\tilde{v}_{bat}^0$. The latter voltage does not correspond to a physical voltage, however, it results from the permutation manipulation. In the sequel, the superscript "~" is used to denote fictitious variables resulting from the permutation manipulation. Consequently, the input of the reference inverter becomes $\tilde{v}_{bat}^0$ instead of v_{bat}^0, as illustrated in Fig. 86. The modeling equations of the permuted power adaptation are given in (137).

$$\begin{cases} \underline{v}_{abc}^{VSI^0} &= \underline{S}_{VSI}^0 v_{bat}^0 \\ i_{ED}^0 &= \eta_{VSI}^{0\gamma} \underline{S}_{VSI}^{0T} \underline{i}_{abc}^{VSI^0} \text{ with } \left[\gamma = sign(P^{VSI^0})\right] \end{cases} \tag{135}$$

$$\begin{aligned} \underline{v}_{s,abc}^{EM^0} &= \underline{S}_{VSI}^0 v_{bat}^0 - \Delta R^0 \frac{i_{ED}^0}{\eta_{VSI}^{0\gamma} \underline{S}_{VSI}^0} \\ &= \underline{S}_{VSI}^0 \left(v_{bat}^0 - \Delta R^0 \frac{i_{ED}^0}{\eta_{VSI}^{0\gamma} \underline{S}_{VSI}^{0^2}} \right) \\ &= \underline{S}_{VSI}^0 \tilde{v}_{bat}^0 \end{aligned} \tag{136}$$

$$\begin{cases} \tilde{v}_{bat}^0 &= v_{bat}^0 - \Delta R^0 \frac{i_{ED}^0}{\eta_{VSI}^{0\gamma} \underline{S}_{VSI}^{0^2}} \\ i_{ED}^0 & \qquad \text{common} \end{cases} \tag{137}$$

The second manipulation lies in merging the DC power adaptation element of the inverter with the permuted one, as depicted in Fig. 87. Similar to the permutation rule, the main idea behind the merging rules is to keep the same input and outputs of the merged elements to preserve the same global behavior of the system. The modeling equation of the new merged power adaptation element can be therefore expressed as shown in (138).
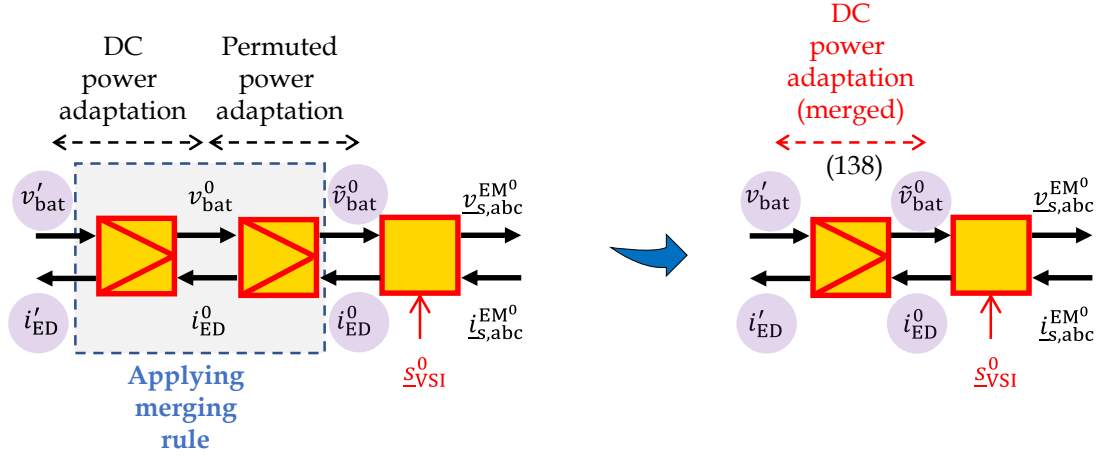
Fig. 87: Merging of electrical power adaptation elements

$$\begin{cases} \tilde{v}_{bat}^0 & = & \dfrac{1}{K_{v,DC}^{VSI}}\left(v_{bat}^0 - \Delta R\, \dfrac{i_{ED}^0}{\eta_{VSI}^{0\gamma}\underline{s}_{VSI}^{0^2}}\right) \\[4mm] i_{ED}' & = & K_{i,DC}^{VSI}\left(i_{ED}^0 + \Delta i_{ED}\right) \end{cases} \tag{138}$$

The latter equation can be subjected to further simplification as shown in (139), based on the following assumptions. Given that no DC bus voltage scaling is considered in this study, the voltage scaling of the inverter at the DC side $K_{v,DC}^{VSI}$ is equal to 1. Additionally, it is assumed that the current of the inverter and the machine scale in a similar way, resulting in an equivalent current scaling factor $\left(K_{i,DC}^{VSI} = K_i^{PMSM}\right)$. Lastly, the equivalent term Δi_{ED} can be disregarded as the assumption of linear losses-to-power scaling has been proven acceptable for the inverter as demonstrated in Chapter II.

$$\begin{cases} \tilde{v}_{bat}^0 & = & v_{bat}' - \Delta R\, \dfrac{i_{ED}^0}{\eta_{VSI}^{0\gamma}\underline{s}_{VSI}^{0^2}} \\[4mm] i_{ED}' & = & K_i^{PMSM} i_{ED}^0 \end{cases} \tag{139}$$

Considering the final aim of obtaining a scalable static model of the e-axle to perform energetic simulation, it becomes necessary to amend the aforementioned equation. This is because the information on the switching function $\underline{s}_{VSI}^0$ is only available, when employing a dynamic model of the electric machine. Therefore, the definition of $\tilde{v}_{bat}^0$ becomes challenging using a static model of the electric drive. To tackle this issue, a power balance of the reference inverter (Fig. 87) can be used (140). Based on (134), (140) can be rewritten as demonstrated in (141).

$$\eta_{VSI}^{0\gamma}\tilde{P}_{in}^{VSI^0} = P_{in}^{EM^0} \tag{140}$$

$$\begin{aligned} \eta_{VSI}^{0\gamma}\left(\tilde{v}_{bat}^0 i_{ED}^0\right) & = & \left(\underline{v}_{s,abc}^{VSI^0} - \Delta R\, \underline{i}_{s,abc}^{EM^0}\right)\underline{i}_{s,abc}^{EM^0} \\ & = & P_{in}^{VSI^0} - \Delta P_{cu} \end{aligned} \tag{141}$$

Consequently, the voltage $\tilde{v}_{\text{bat}}^0$ at the input of the reference inverter (Fig. 87) can be expressed as a function of the voltage v_{bat}', the reference electric current i_{ED}^0, the equivalent copper loss ΔP_{cu}, and the efficiency η_{VSI}^0 as follows:

$$
\begin{aligned}
\tilde{v}_{\text{bat}}^0 &= \frac{P_{\text{in}}^{\text{VSI}^0}}{\eta_{\text{VSI}}^{0\gamma} i_{\text{ED}}^0} - \frac{\Delta P_{\text{cu}}}{\eta_{\text{VSI}}^{0\gamma} i_{\text{ED}}^0} \\
&= v_{\text{bat}}^0 - \frac{\Delta P_{\text{cu}}}{\eta_{\text{VSI}}^{0\gamma} i_{\text{ED}}^0} \\
&= v_{\text{bat}}' - \frac{\Delta P_{\text{cu}}}{\eta_{\text{VSI}}^{0\gamma} i_{\text{ED}}^0}
\end{aligned}
\tag{142}
$$

This is accomplished knowing that:

$$
v_{\text{bat}}' = K_{\text{v,DC}}^{\text{VSI}} v_{\text{bat}}^0 \ \left(\text{with } K_{\text{v,DC}}^{\text{VSI}} = 1\right)
\tag{143}
$$

Finally, the EMR-based scaling laws of the entire e-axle can be derived and presented in Fig. 88.
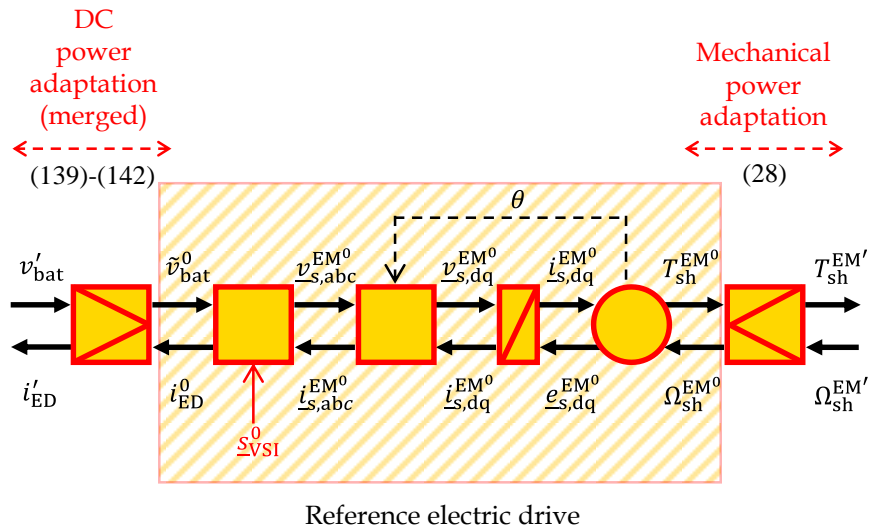
Fig. 88: EMR-based scaling laws of the electric drive

3.2.2 Scalable control scheme

This section aims to derive a scalable control scheme for the EDS. For this aim, the inversion rules are applied to the EMR-based scaling laws presented in Fig. 88. Fig. 89 depicts the EMR-based scaling laws of the EDS and the corresponding control. The mechanical PA element (28) is inverted through a direct inversion using the torque scaling factor $K_{\text{T}}^{\text{PMSM}}$, and the measured equivalent loss term $\Delta T_{\text{PMSM}}^{\text{meas}}$ as expressed by (144). This allows for a change in the definition of the reference torque setpoint from the frame of the scaled machine $T_{\text{sh}}^{*\text{EM}'}$ to that of the reference machine $T_{\text{sh}}^{*\text{EM}^0}$. Next, the control of the reference machine is realized in a similar way to what has been presented earlier in Section 3.1.2 using the conventional EMR, by employing the controllers of the reference machine to track the dq currents defined by the

143

MTPA&FW strategies. By comparing Fig. 83, and Fig. 89, it is readily apparent that the new model organization of the scaled machine following the EMR-based scalings laws provides the possibility of reusing the same control of the reference EDS for other scaled ones. The control structure of the reference EDS remains the same, including the current controllers of the reference machine and their parameters.

$$T_{\text{sh}}^{*\text{EM}^0} = \frac{T_{\text{sh}}^{*\text{EM}'}}{K_{\text{T}}^{\text{PMSM}}} + \Delta T_{\text{PMSM}}^{\text{meas}} \tag{144}$$
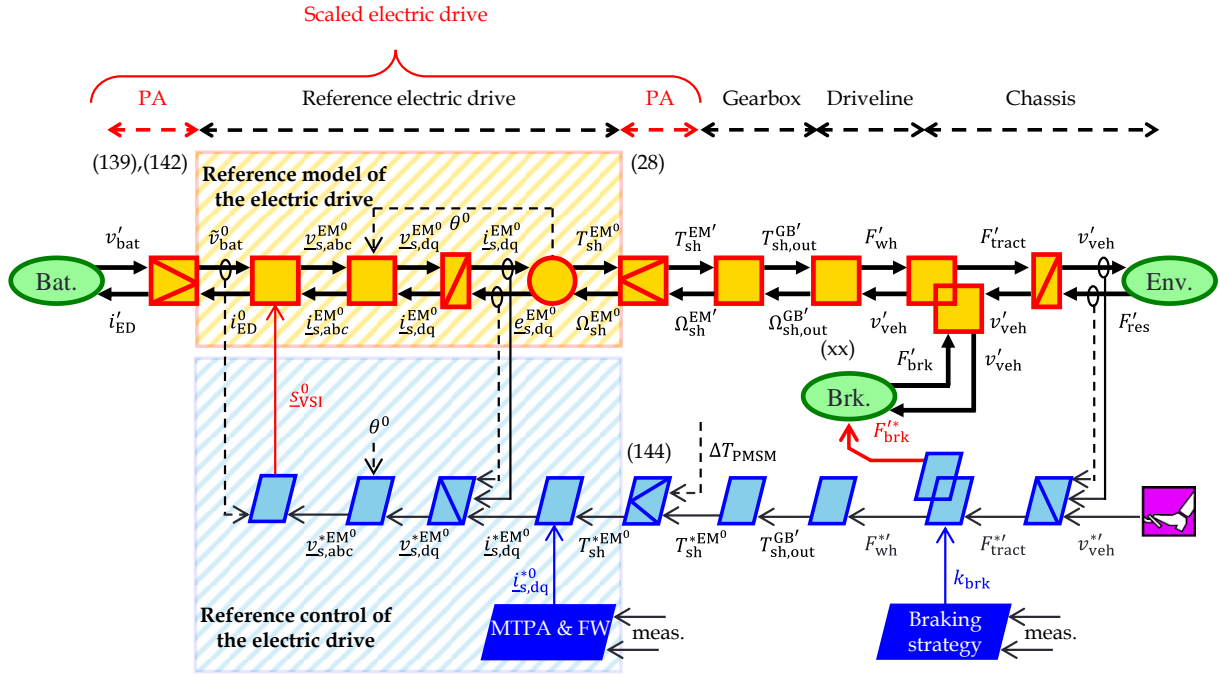
Fig. 89: EMR-based scaling laws of electric drive systems for electric vehicle simulation

3.2.3 Comparison between EMR-based scaling laws and conventional EMR for electric drive systems

To evaluate the results of applying EMR-based scaling laws, the scalable model and control of the EDS are connected to the remaining models and control of the drivetrain, as illustrated in Fig. 89. As an illustrative case, the scaling case ①, i.e. the upscaling case of the compact car, is considered to make the comparison between the EMR-based scaling laws and the conventional EMR. Due to the diverse scaling choices and to facilitate the synthesis of the results, the geometric scaling laws based on the geometric scaling choice that preserves the magnetic field density $B \sim 1$ are selected to perform the scaling process of the reference PMSM (80 kW). A scaled design is defined by applying geometric scaling laws considering a power scaling factor of 1.33 (Table 21), yielding a new power rating of 110 kW. An axial scaling factor K_{A} of 1.5 is considered as an example. The radial scaling factor K_{R} is calculated based on the power scaling requirement and the applied axial scaling factor K_{A}, following the scaling laws mentioned in Chapter II. The rewinding scaling factor K_{W} is adjusted to preserve the same rated voltage of the DC bus. The value of ΔR differs from 0 based on the selected scaling factors. The scaling process is implemented in the EMR-based scaling laws by redefining the scaling factors

in the power adaptation elements. As for the conventional EMR, the scaled parameters are calculated beforehand in a pre-processing phase. This pre-processing phase involves also the recalculation of the current controllers' parameters and the recomputation of the MTPA&FW strategies for the scaled PMSM. Regarding the voltage source inverter, the data of the reference inverter (FS600R07A2E3/80 kW) is implemented in the EMR-based scaling laws and scaled using the linear scaling method. The data of the inverter (FS800R07A2E3/110kW) is used in the conventional EMR. Linear scaling is assumed for the inverter when implementing the EMR-based scaling laws as the difference in the scaling process against the benchmarking study is demonstrated marginal (Chapter II).

Fig. 90 shows the difference between the input and output variables of the EDS obtained through conventional EMR and EMR-based scaling laws, namely the battery voltage v_{bat}, the current i_{ED}, and the torque applied on the shaft T_{sh}. Note that the speed is not part of this comparison, as no speed scaling has been considered in the scaling process of the electric machines, as shown in (28). The comparison is performed using two driving cycles with different driving patterns, specifically the Artemis highway and urban driving cycles. The comparison of the battery voltage in Fig. 90.a and Fig. 90.b shows that the voltage difference ΔV_{bat} is negligeable with a maximal difference of 0.04 V. Assessing the difference in terms of the current Δi_{ED}, the simulation results, shown in Fig. 90.c and Fig. 90.d, reveal a maximal discrepancy of 0.2 A. This difference is due to the permutation of the power adaptation elements which causes minor numerical errors, primarily resulting from induced delays employed in solving algebraic loops. This difference can be deemed negligible in magnitude. From Fig. 90.c and Fig. 90.d, it can be seen that the difference in torque ΔT_{sh} demonstrates complete parity. Given these results, it can be concluded that simulation of the powertrain using a conventional EMR and EMR-based scaling laws for electric drive systems yields the same results. The last statement can be extended to another reference machine PMSM design since identical findings have been obtained when comparing both simulation frameworks using a different reference machine design, as discussed in a published conference paper [232].
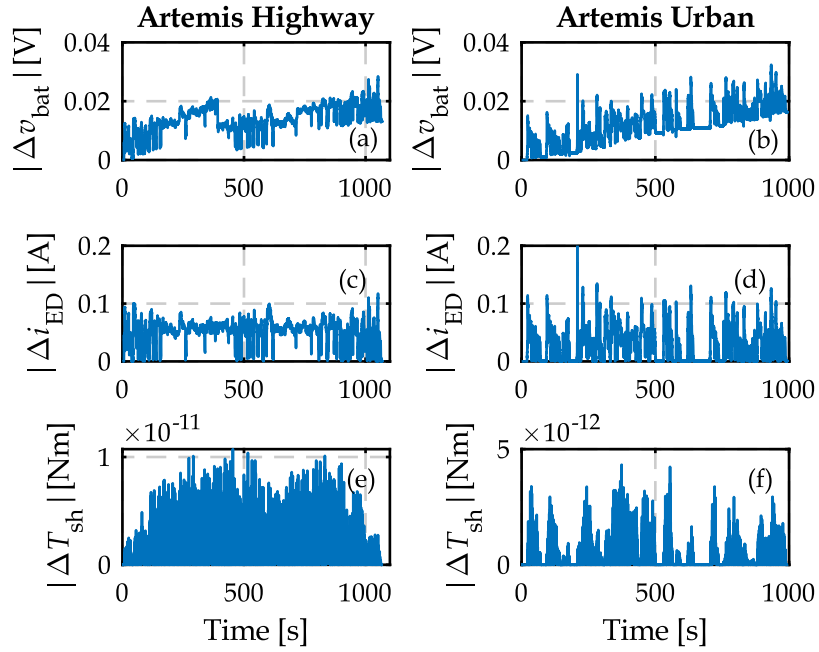
Fig. 90: Comparison between EMR-based scaling laws and conventional EMR of electric drive systems

3.3   Step 2: Deduction and validation of EMR-based scaling laws of the electric drive system and the gearbox

Similar to what is done for the inverter and the PMSM, this section examines the interaction between the EMR-based scaling laws of the EDS and the EMR-based scaling laws of the gearbox, aiming to derive EMR-based scaling laws for the e-axle as illustrated in Fig. 82.

3.3.1   General case study based on the data-driven scaling laws of the gearbox

The interaction between both scaled components is achieved by interconnecting the mechanical PA element of the EDS and the input mechanical PA of the gearbox, as depicted in Fig. 91. In effecting such manipulation, it is readily apparent that the definition of the torque $T_{sh}^{EM^0}$, and speed $\Omega_{sh}^{EM^0}$ of the reference machine changes when transitioning from the coordinate system of the reference machine to that of the reference gearbox $T_{sh}^{GB^0}$, and $\Omega_{sh}^{GB^0}$. This is similar to what is discussed earlier for the inverter and the machine. Analogous to the EDS, the same steps are followed, aiming to preserve only two power adaptation elements located at both the input and output of the e-axle.

First, the condition to interconnect the adjacent power adaptation elements is depicted in (*145*). This is expected as the torque $T_{sh,in}^{EM'}$ and the speed $\Omega_{sh}^{EM'}$ parameters of the scaled PMSM are identical to the torque $T_{sh,in}^{GB'}$ and the speed $\Omega_{sh,in}^{GB'}$ of the scaled gearbox at its input port. Next, the mechanical power adaptation element of the EDS can be merged with the input mechanical power adaptation of the gearbox as shown in Fig. 92. This results in the manifestation of an intermediary power adaptation element, which is modeled following (146). This latter can be easily simplified considering a particular case that involves four conditions as

expressed in (147). The first condition consists in assuming an identical torque scaling factor for both the electric machine and the gearbox. This condition is feasible if the gear ratio scaling is not part of the scaling process $(K_{kgb} = 1)$, leading to a second condition. The third condition requires nullifying the equivalent loss term ΔT_{PMSM}, which necessitates a linear scaling case of the EDS. The last condition assumes no maximal speed scaling for the gearbox is assumed $(K_N = 1)$.

$$
\begin{cases}
T_{sh,in}^{GB'} &= T_{sh,in}^{EM'} \\
\Omega_{sh}^{EM'} &= \Omega_{sh,in}^{GB'}
\end{cases}
\tag{145}
$$
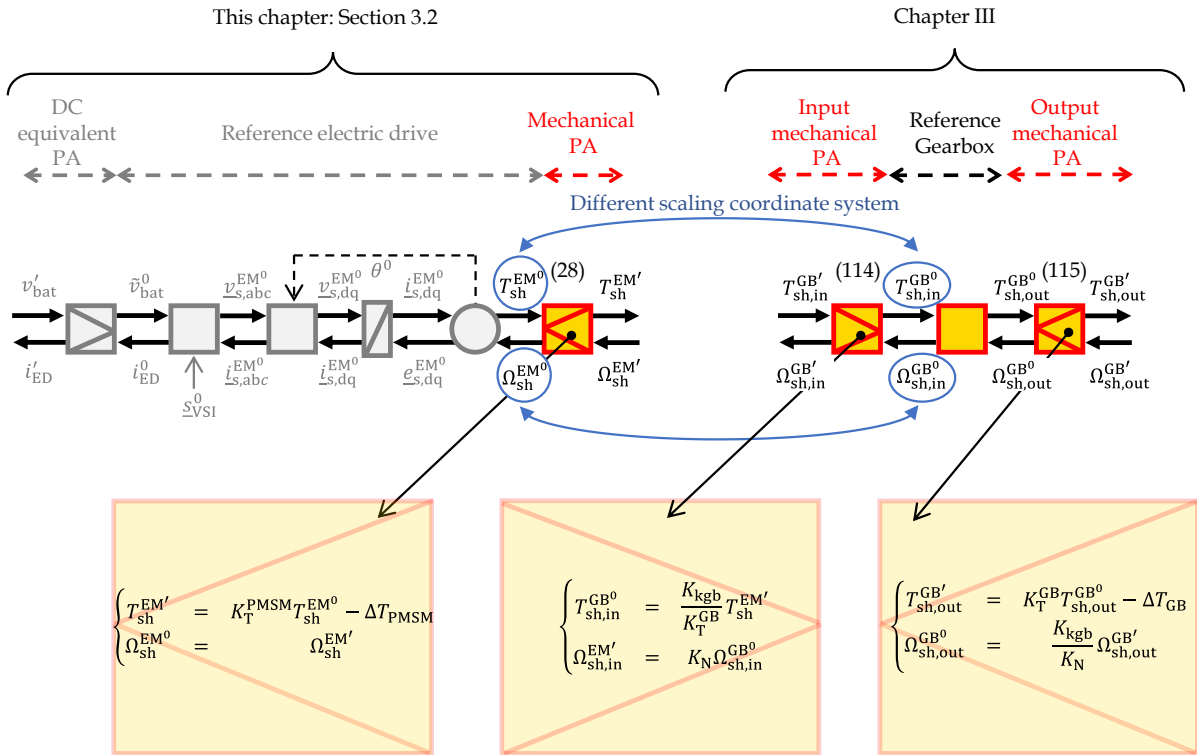
Fig. 91: Interaction between EMR-based scaling laws of the electric drive system and gearbox
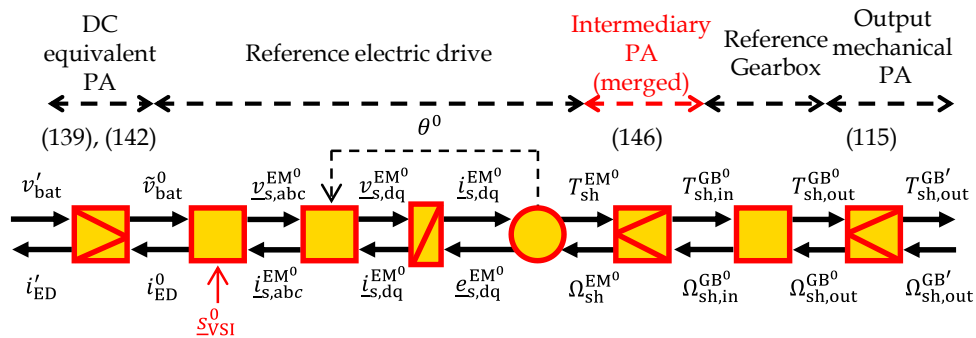
Fig. 92: EMR-based scaling laws of the e-axle with an intermediary power adaptation element

$$
\begin{cases}
T_{sh,in}^{GB^0} &= \dfrac{K_{kgb}}{K_T^{GB}} \left(K_T^{PMSM} T_{sh}^{EM^0} - \Delta T_{PMSM} \right) \\
\Omega_{sh}^{EM^0} &= K_N \Omega_{sh,in}^{GB^0}
\end{cases}
\tag{146}
$$

$$\begin{cases} K_T^{PMSM} &= K_T^{GB} \\ K_{kgb} &= 1 \\ \Delta T_{PMSM} &= 0 \\ K_N &= 1 \end{cases} \tag{147}$$

Alternatively, the intermediary power adaptation element can be permuted to the output mechanical power adaptation of the gearbox and thereafter merged, providing a general scaling case.
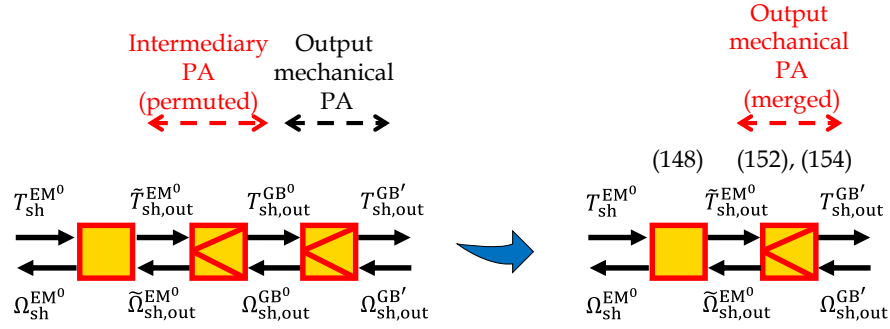
Fig. 93: Permutation and merging of mechanical power adaptation elements

As a reminder, the model of the reference gearbox is recalled in (148) using the coordinate system of the reference gearbox.

$$\begin{cases} T_{sh,out}^{GB^0} &= \eta_{GB}^0 k_{gb}^0 T_{sh,in}^{GB^0} \\ \Omega_{sh,in}^{GB^0} &= k_{gb}^0 \Omega_{sh,out}^{GB^0} \end{cases} \tag{148}$$

Replacing the expression of the torque $T_{sh,in}^{GB^0}$ (146) in (148) yields the manifestation of the output torque of the gearbox $\tilde{T}_{sh,out}^{EM^0}$ in the coordinate system of the reference gearbox :

$$\begin{aligned} T_{sh,out}^{GB^0} &= \frac{K_{kgb}}{K_T^{GB}} \left(\eta_{GB}^0 k_{gb}^0 K_T^{PMSM} T_{sh}^{EM^0} - \eta_{GB}^0 k_{gb}^0 \Delta T_{PMSM} \right) \\ &= \frac{K_{kgb} K_T^{PMSM}}{K_T^{GB}} \tilde{T}_{sh,out}^{EM^0} - \eta_{GB}^0 k_{gb}^0 \frac{K_{kgb}}{K_T^{GB}} \Delta T_{PMSM} \end{aligned} \tag{149}$$

in which $\tilde{T}_{sh,out}^{EM^0}$ is expressed as:

$$\tilde{T}_{sh,out}^{EM^0} = \eta_{GB}^0 k_{gb}^0 T_{sh}^{EM^0} \tag{150}$$

In the same way the speed $\Omega_{sh,out}^{GB^0}$ is expressed as a function of the output speed of the gearbox $\tilde{\Omega}_{sh,out}^{EM^0}$ in the coordinate system of the reference machine (151).

$$\begin{aligned} \Omega_{sh}^{EM^0} &= k_{gb}^0 \left(K_N \Omega_{sh,out}^{GB^0} \right) \\ &= k_{gb}^0 \tilde{\Omega}_{sh,out}^{EM^0} \end{aligned} \tag{151}$$

By merging the permutated intermediary mechanical power adaptation elements with the mechanical power adaptation element, a new mechanical power adaptation element at the

outside of the e-axle is derived. The scaled torque $T_{sh,out}^{GB'}$ is then expressed in (152) as a function of $T_{GB,out}^{EM0}$, and a new equivalent torque denoted as $\Delta \tilde{T}_{GB}$ due to the permutation and merging manipulations.

$$\begin{cases} T_{sh,out}^{GB'} = K_T^{GB}\left(\dfrac{K_{kgb}K_T^{PMSM}}{K_T^{GB}}T_{GB,out}^{EM0} - \eta_{GB}^0 k_{gb}^0 \dfrac{K_{kgb}}{K_T^{GB}}\Delta T_{PMSM}\right) - \Delta T_{GB} \\ \qquad\quad = K_{kgb}K_T^{PMSM}T_{GB,out}^{EM0} - \Delta \tilde{T}_{GB} \end{cases} \quad (152)$$

with $\Delta \tilde{T}_{GB}$ is expressed as follows:

$$\Delta \tilde{T}_{GB} = \eta_{GB}^0 k_{gb}^0 K_{kgb}\Delta T_{PMSM} + \Delta T_{GB} \quad (153)$$

The output speed of the reference gearbox in the coordinate system of the reference machine $\tilde{\Omega}_{sh,out}^{EM0}$ is therefore expressed as a function of the speed $\Omega_{sh,out}^{GB'}$ in the coordinate system of the scaled gearbox as depicted in (154).

$$\tilde{\Omega}_{sh,out}^{EM0} = K_{kgb}\Omega_{sh,out}^{GB'} \quad (154)$$

After following all the previously detailed steps and incorporating the procedures employed for the EDS, EMR-based scaling laws employing only two power adaptation elements at the input and the output of the e-axle are deduced and represented in Fig. 94.
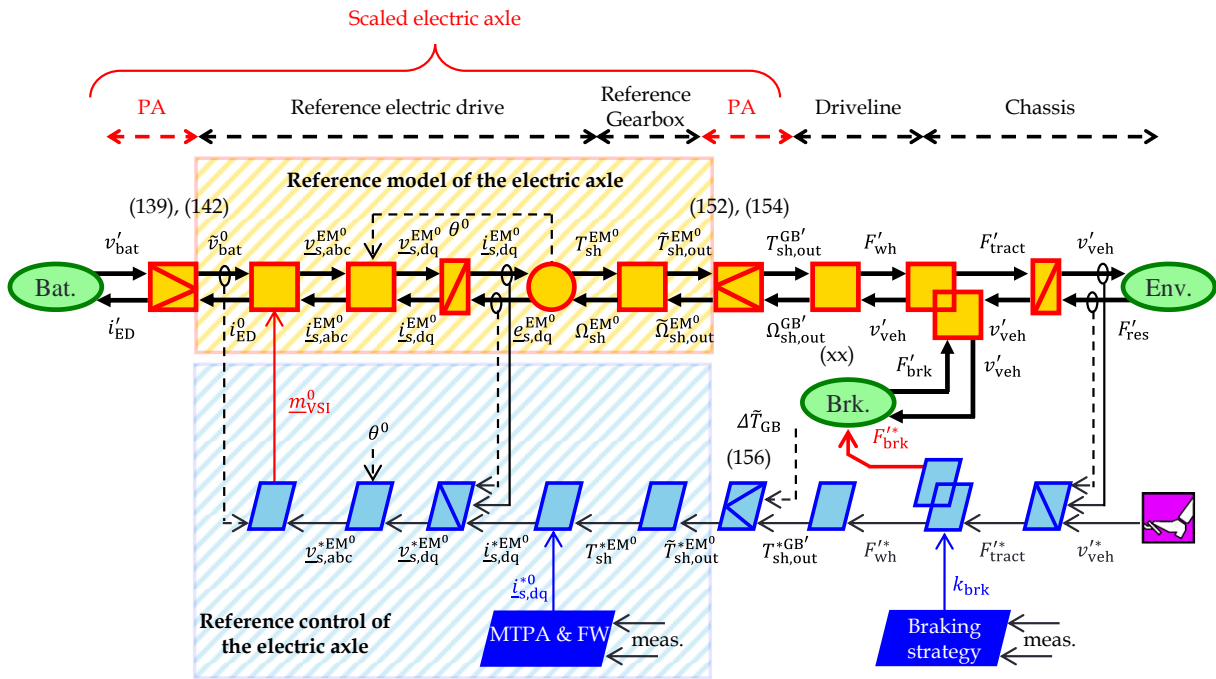
Fig. 94: EMR-based scaling laws of the electric axle

3.3.2 Particular case study considering constant efficiency and gear ratio scaling of the gearbox

Given that the scaling laws outlined in Chapter III are derived based on low-power rated gearboxes, their application is unfortunately not realistic for a power rating typical for automotive applications. The main reason for this is that the torque range of the tested gearboxes differs from the requirements typically encountered in automotive gearboxes. Consequently, applying such scaling laws to the automotive applications under investigation in this chapter requires a large torque scaling factor. To still include the scaling of the gearbox, the data-driven scaling is adapted following the assumptions retained in the current state-of-the-art literature on system-level design. These adjustments consist of scaling the gear ratio, a key parameter for system-level design of electrified powertrains [233], while assuming a constant efficiency. This means that efficiency is considered independent of the scaling process of the gearbox. An average constant efficiency that ranges from 96% to 97% is frequently employed for automotive gearboxes assuming the same number of stages, without further explanation [16], [78]. However, the last statement should not be misinterpreted as an indication that a scalable power loss model for gearboxes is needless. This is because the assumption of constant efficiency still needs to be validated particularly for high-speed automotive gearboxes.

To drive the scalable model of the e-axle following the last aforementioned assumptions, the model organization using the data-driven model is preserved with amendments to the definition of the output mechanical power adaptation elements. This adaptability emerges as the data-driven scaling provides a general case scaling. The main change consists in amending the equivalent torque $\Delta\tilde{T}_{GB}$ that represents the non-linearity of the losses (153) as shown in (155). By opting for this scaling choice, the equivalent torque ΔT_{GB} is omitted due to the non-consideration of the loss scaling of the gearbox. This can be considered as a particular case of the linear scaling method, but with a constant efficiency.

$$\Delta\tilde{T}_{GB} = \eta_{GB}^0 k_{gb}^0 \Delta T_{PMSM} \tag{155}$$

3.3.3 Deduction of a scalable control scheme of the electric axle

A new scalable control scheme is derived based on the inversion rule of the EMR. The new modeling equation of the output mechanical power adaptation element (152) is inverted by a direct inversion, as given in (156). This yields the scalable control scheme shown in the lower part of Fig. 94.

$$\tilde{T}_{sh,out}^{*EM^0} = \frac{T_{sh,out}^{*GB^0} + \Delta\tilde{T}_{GB}^{meas}}{K_{kgb}K_T^{PMSM}} \tag{156}$$

3.3.4 Comparison between EMR-based scaling laws and conventional EMR for electric axle

In relation to Fig. 81, this section aims to compare the proposed EMR-based scaling laws of the e-axle, proposed in Fig. 94, based on a comparison with a conventional EMR, similar to

what has been done in Step 1. The same inputs for the comparison as Step 1 are hereinafter considered, along with the incorporation of an example of a gear ratio scaling with a factor K_{kgb} of 0.85. This means the new scaled gear ratio is 7 instead of 8.19 (Table 20). Constant efficiency of 96% is herein considered for the gearbox, for the reasons elaborated above. As expected, both simulations lead to the same results in terms of the scaled parameters as shown in Fig. 90. This is because the same modeling equations are the same, but their organization is different.

3.4 Step 3: Deduction and validation of a scalable static model of the electric axle

3.4.1 Deduction of a scalable static model of the electric axle

In the previous steps, the scalable model and control scheme have been deduced based on a dynamic model of the PMSM. Nevertheless, to carry out energetic studies, a quasi-static model of the vehicle, which solely considers the principle dynamic of the system represented by the chassis, is generally adopted [16]. The quasi-static model is considered more suitable for performing fast quantification of the losses and the energy consumption of the vehicle. This preference is due to the advantageous computational efficiency as compared to the dynamic model, without impacting the energy consumption. To this end, a static model of the e-axle is deduced from the EMR-based scaling laws presented in Fig. 94, as depicted in Fig. 95, following the methodology proposed in [234] for EDS. In the static model, the electric dynamics are ignored, resulting in the instantaneous attainment of the reference torque (157). The reference current of the electric drive is modeled using a power balance, knowing the reference of the reference battery voltage $\tilde{v}_{\text{bat}}^0$, the reference torque and speed at the output of the gearbox $\tilde{T}_{\text{sh,out}}^{\text{EM}^0}$, and $\tilde{\Omega}_{\text{sh,out}}^{\text{EM}^0}$, as well as the efficiency of the entire electric drive axle, including the reference inverter η_{VSI}^0, PMSM η_{EM}^0, and gearbox η_{GB}^0. In this case, the efficiency can be determined using the reference efficiency maps of each component. Regarding the power adaptation elements, they remain the same as previously elaborated earlier, to consider the scaling effect for each component.

$$\tilde{T}_{\text{sh,out}}^{\text{EM}^0} = T_{\text{sh,out}}^{*\text{EM}^0} \tag{157}$$

$$i_{\text{ED}}^0 = \frac{\tilde{T}_{\text{sh,out}}^{\text{EM}^0}\tilde{\Omega}_{\text{sh,out}}^{\text{EM}^0}}{\eta_{\text{VSI}}^{0\gamma}\eta_{\text{EM}}^{0\gamma}\eta_{\text{GB}}^{0\gamma}\tilde{v}_{\text{bat}}^0} \text{ with } \gamma = \text{sign}\left(\tilde{T}_{\text{sh,out}}^{\text{EM}^0}\right) \tag{158}$$
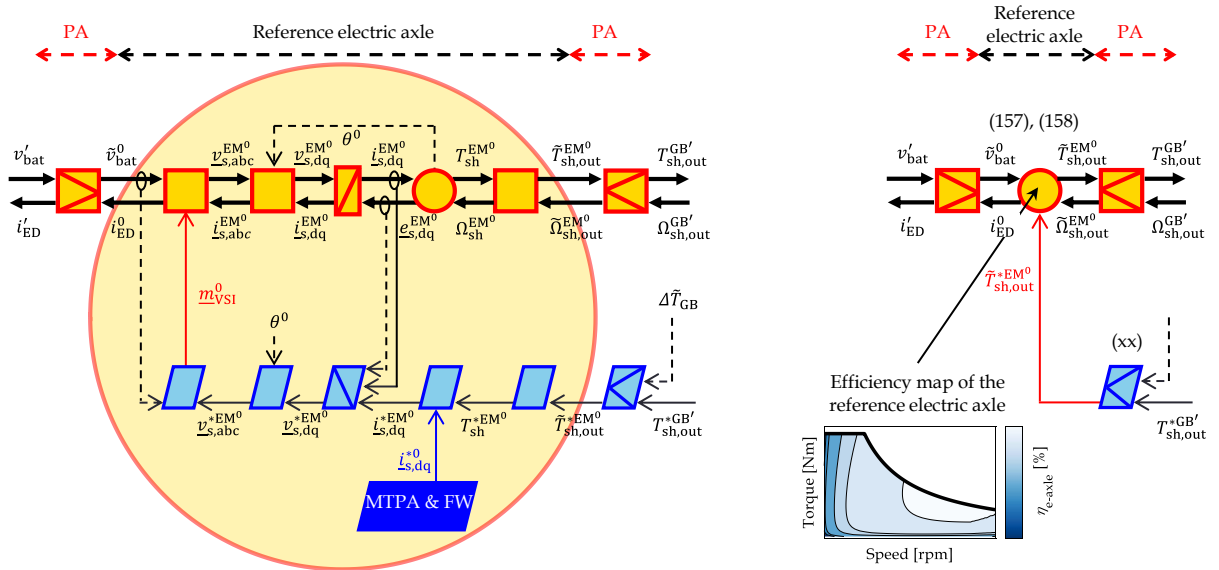
Fig. 95: Deduction of a scalable static model organization of the electric drive: (a) dynamic model, (b): static model

3.4.2 Simulation-based validation of the proposed scalable static model of the electric axle

To validate the proposed scalable static model, a comparison is performed against a conventional static model implemented in the simulation environment of EV, as shown in Fig. 96. Regarding the EMR-based scaling laws, the reference efficiency map of the e-axle is used. The input and output variables of the reference e-axle model are adjusted online during the simulation through the power adaptation elements based on the predefined scaling method and factors. However, when opting for the conventional static model organization, the efficiency map of the scaled e-axle needs to be computed offline in a post-processing phase based on the scaling requirements. Thereafter, the scaled efficiency map can be implemented in the simulation environment. The sole difference with the model structuration with power adaptation elements is that the efficiency map needs to be recomputed each time the scaling requirements are altered. This results in a laborious simulation process, particularly when different scaled design candidates need to be evaluated.
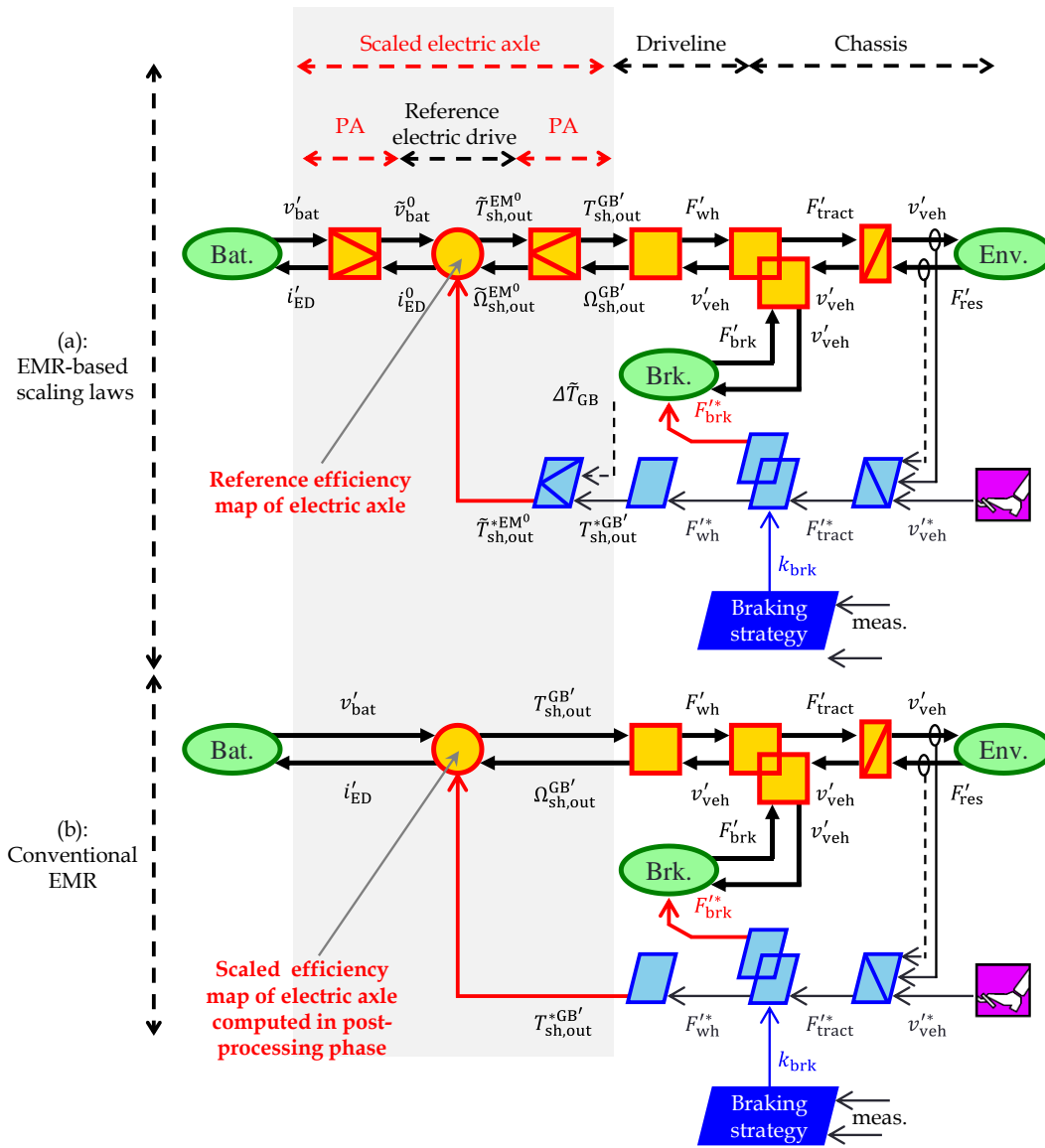
Fig. 96: Comparison between scalable static model organization for energetic simulation of battery electric vehicles

To conduct the comparison between the outcomes of the EMR-based scaling laws and the conventional EMR, the same scaling factors as presented in Section 3.3.4 are used. By consulting Fig. 97, it can be observed that no significant difference is obtained when comparing the battery voltage v'_{bat}, the current of the electric drive i'_{ED}, and the output torque of the gearbox $T^{GB'}_{sh,out}$. This demonstrates the trustworthiness of the proposed methodology.

153
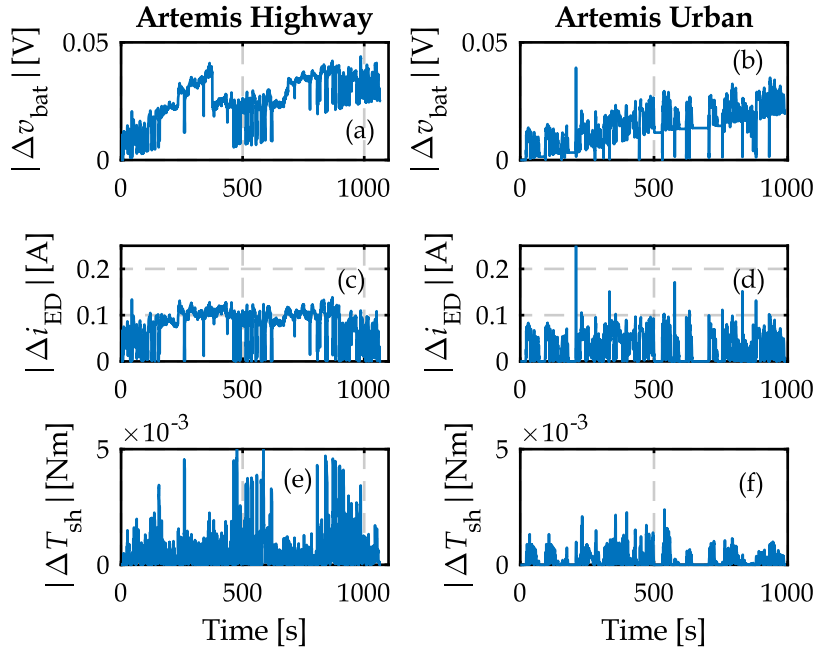
Fig. 97: Comparison between EMR-based scaling laws and conventional EMR using a static model of the electric axle

4 Effect of the scaling choices on energy consumption

This section investigates the effect of the scaling choices on the energy consumption of electric vehicles. A particular emphasis is paid to assessing the reliability of linear losses-to-power scaling for energy consumption computation of electric vehicles. This assessment is carried out through a comparison against the other scaling choices outlined in Fig. 98.

Regarding the EDS, the scaling methods of the electric machine encompass the linear losses-to-power scaling, and geometric scaling laws based on the three scaling choices elaborated in Chapter II, namely the preservation of the magnetic field density B~1, the temperature rise in the windings Θ~1, and the hybrid choice $B\&\Theta$~1. As for the inverter, the scope of the applied methods is confined to the linear losses-to-power scaling, and the benchmark study using the theoretical methods and the data extracted from the datasheets. This is because the scaling laws studied in Chapter II yield comparable results in terms of efficiency scaling. It is therefore deemed sufficient to retain only the linear scaling method and the benchmarking study for the inverter. The gearbox scaling is conducted using a constant average efficiency while altering the gear ratio, for the reasons discussed earlier.

To make the comparative analysis, the workflow depicted in Fig. 99 is followed. A particular emphasis is hereinafter paid to the scaling of the PMSM, as the efficiency scaling is demonstrated in Chapter II to be sensible to the applied scaling laws. Therefore, in the initial analysis phase, the impact of the scaling laws of the machine on energy consumption is isolated from the remaining components. The second set of analysis involves studying the impact of the scaling laws of the e-axle, combining the scaling of EDS with a scaled gear ratio. Although the outcomes of the scaling of the inverter can be predicted due to the non-significant difference

154

between the linear scaling and the benchmark study, the impact of the scaling laws of the EDS on energy consumption is isolated and analyzed separately in Appendix VI.3. The simulations are conducted using the EMR-based scaling laws discussed earlier in the previous section. When employing the linear scaling method, the equivalent loss terms embedded in the power adaptation elements, such as ΔP_{cu}, and $\Delta \tilde{T}_{GB}$, are nullified. Conversely, when employing alternative scaling methods, these terms are computed based on the earlier developments outlined in the preceding section.
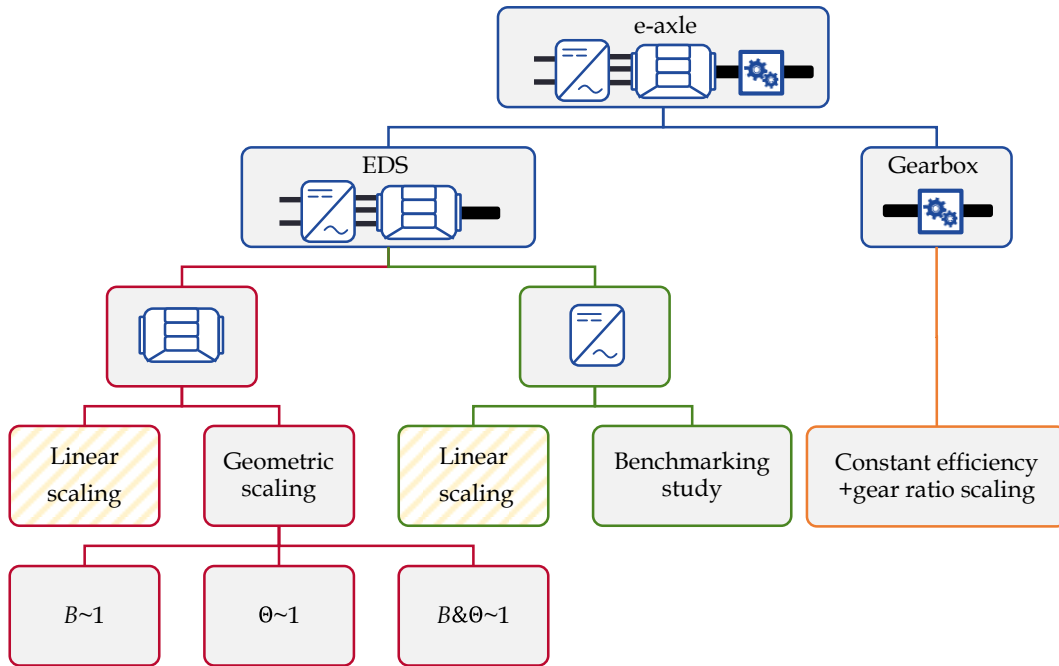
Fig. 98: Selected scaling methods for system-level analysis. Note that the methods highlighted in yellow refer to common scaling methods applied to different components.
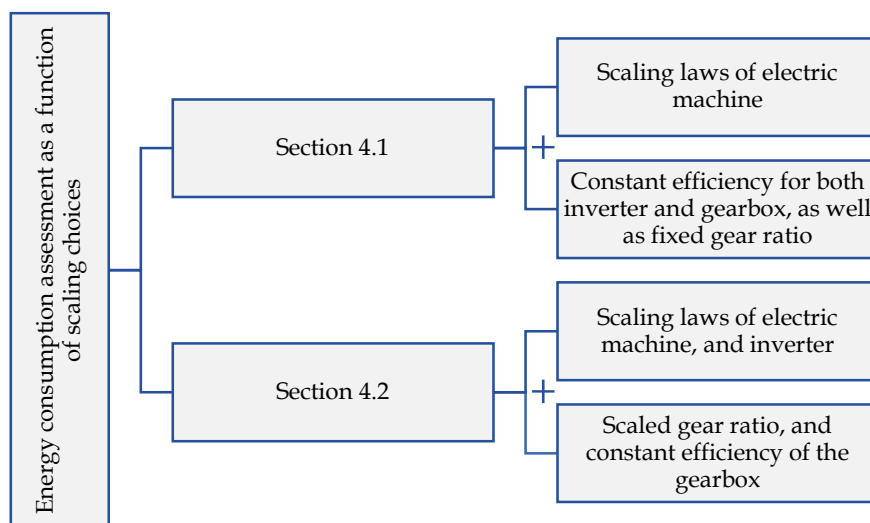
Fig. 99: Workflow for the investigation of the scaling impact of each scaling method

4.1   Effect of the scaling choices of PMSM on energy consumption

To isolate the impact of each scaling choice of the PMSM on energy consumption (Fig. 98), the efficiency of both the inverter and gearbox are assumed constant, alongside a fixed gear ratio (K_{kgb}=1). These requirements are incorporated in the power adaptation elements (142), and (155) of the EMR-based scaling laws (Fig. 96.a). In this section, particular emphasis is placed on comparing the outcomes of the linear scaling method against the different choices of the geometric scaling laws. First, the results of the comparative analysis are reported for each automotive application. The results are thereafter subjected to in-depth analysis, revealing how the operating points impact the outcomes of each scaling choice and how the geometric scaling factors of the scaled machine influence energy consumption.

4.1.1   Overview of the effect of scaling choices on energy consumption

For the different automotive applications under investigation (Fig. 80), various scaled designs of the reference PMSM machine are generated using the geometric scaling laws, featuring a range of distinct geometric variations. The axial scaling factor K_A has been varied between 0.7 and 1.5 for larger insights on the scaling impact, and to have a reasonable range that complies with the integration constraints of e-axle. The rewinding scaling factor K_W is adjusted to preserve the voltage rating of the DC bus.

Regarding the upscaling case of the compact car using a power scaling factor of 1.33 (case ①), Fig. 100 presents a sensitivity analysis of the relative difference in terms of energy consumption ΔE_{bat} $\left(\left(E_{\text{bat}}^{\text{LS}} - E_{\text{bat}}^{\text{GS}} \right) / E_{\text{bat}}^{\text{LS}} \right)$ between the Linear losses-to-power Scaling (LS) and Geometric Scaling laws (GS) based on different choices, and for the selected driving cycles. By consulting the boxplots in the figure, it can be seen that the sign of ΔE_{bat} can be either positive or negative. A positive ΔE_{bat} means that linear losses-to-power of the electric machine overestimates the energy consumption as compared to the second method and vice versa. The most remarkable observation to emerge from the data is that the urban driving cycles, e.g. NYCC, ARTEMIS Urban, Lille downtown, and ULille campus, exhibit the greatest discrepancy between the linear and geometric scaling laws. For example, ΔE_{bat} achieves its maximum value of about 1.8% for the NYCC driving cycle when opting for the scaling choice B~1 (Fig. 100.a). This result can be interpreted as the scaling choice B~1 leads to the lowest energy consumption of the vehicle for the urban driving cycles. Fig. 100.b, and Fig. 100.c reveal that ΔE_{bat} is comparatively lower, about 1%, for the urban driving cycles when choising the scaling choice that preserve the temperature rise Θ~1 and the hybrid one $B\&\Theta$~1. As for high speed driving cycles, such as ARTEMIS highway, Tourcoing, Lille-Ghent, ΔE_{bat} is non-significant. ΔE_{bat} generally falls within a range of -0.5% and 0.5%, regardless of the geometric scaling choice. The same obserbation can be made for the remaining driving cycles, namely the rural driving cycle ARTEMIS Rural and WLTC.

Regarding the downscaling case of the compact car using a power scaling factor of 0.67 (case ②), Fig. 101 demonstrates the same trend for the diverse scaling as observed in the previous scaling case. The exception is that the sign of ΔE_{bat} is consistently negative, meaning that linear scaling underestimates the energy consumption of the vehicle as compared to the

geometric scaling laws. Remarkably, Fig. 101.a shows more pronounced ΔE_{bat} when using the urban driving cycles, which can reach -10% for the NYCC driving cycle for instance. Furthermore, the scaling choice $\Theta \sim 1$ demonstrates a reduced difference in energy consumption relative to linear scaling with ΔE_{bat} being about -4% as compared to the other geometric scaling choices. No remarkable differences are observed for highway driving cycles.

To generalize this difference in terms of energy consumption between linear scaling and geometric scaling laws, Fig. 102, and Fig. 103 show a sensitivity analysis for the medium-duty truck (case ③) and the mini-compact car (case ④). The same observation as the previously examined scaling cases can be made. The maximal difference is obtained while using urban driving cycles, particularly while using the choice $B \sim 1$. For driving cycles characterized by high-speed profiles, ΔE_{bat} is non-significant.
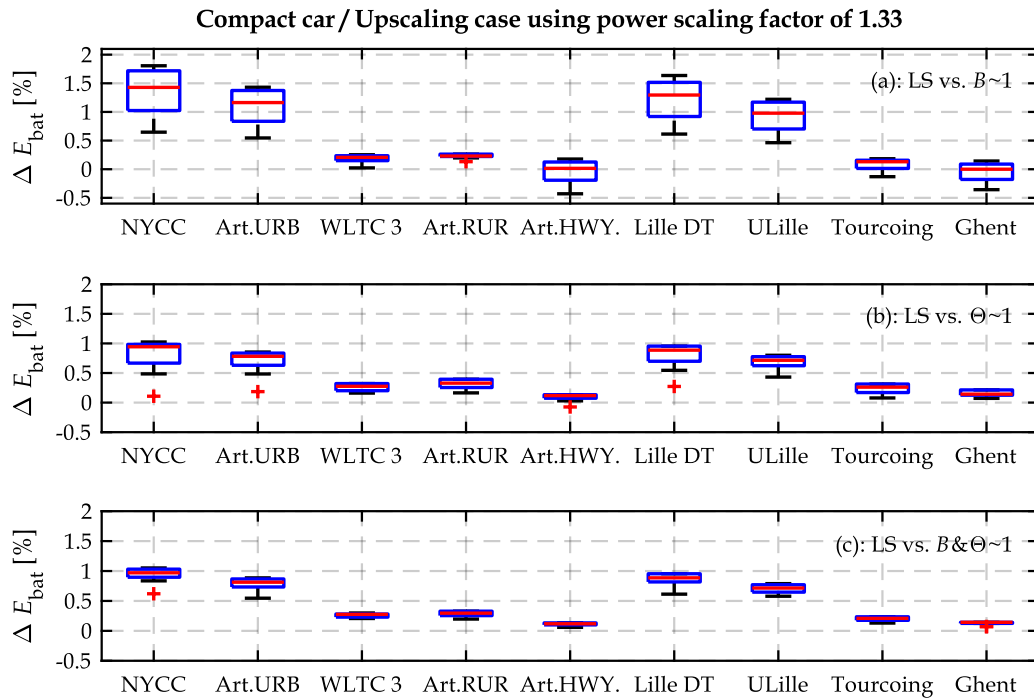
Fig. 100: Sensitivity analysis of the relative difference in terms of energy consumption ΔE_{bat} between linear scaling and geometric scaling based on different scaling choices for case ①. Note each row figure corresponds to a scaling choice of the geometric scaling laws. Positive values of ΔE_{bat} means that linear scaling overestimates energy consumption and vice versa.

Compact car / Dowscaling case using a power scaling factor of 0.67
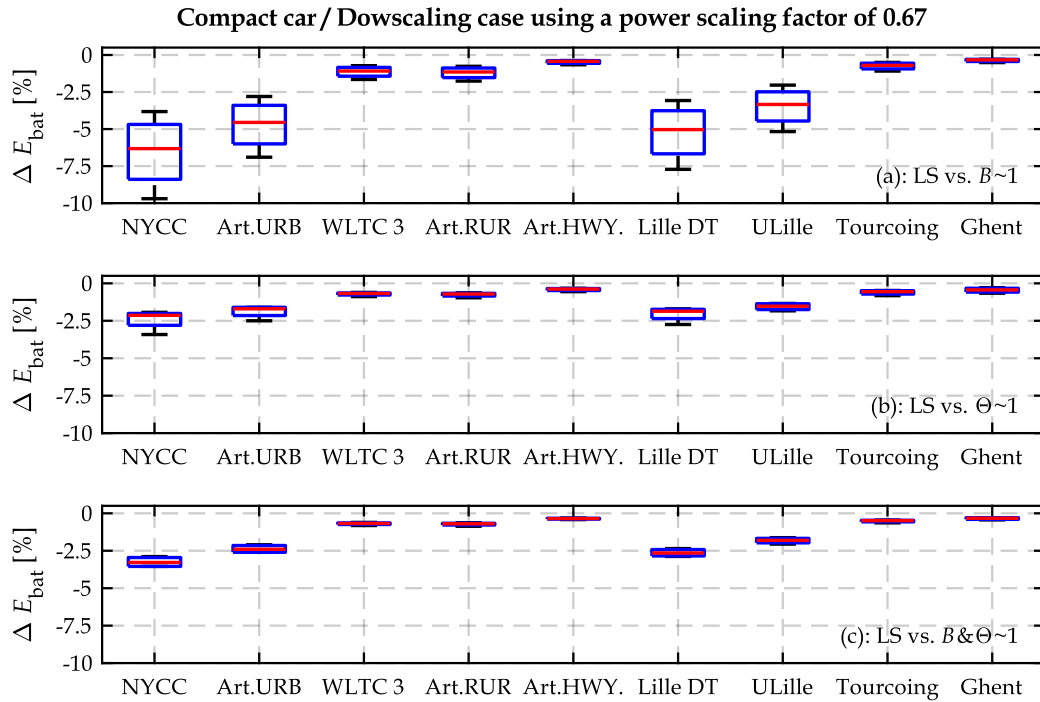
Fig. 101: Sensitivity analysis of the relative difference in terms of energy consumption ΔE_{bat} between linear scaling and geometric scaling based on different scaling choices for case ②.

Medium duty truck / Upscaling case using a power scaling factor of 1.96
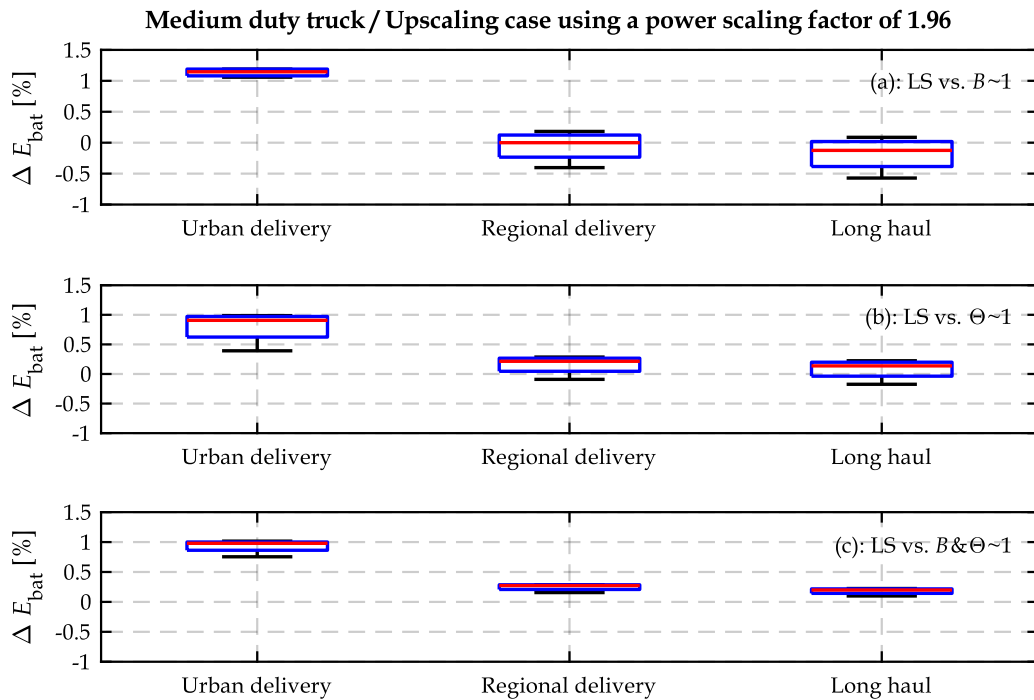
Fig. 102: Sensitivity analysis of the relative difference in terms of energy consumption ΔE_{bat} between linear scaling and geometric scaling based on different scaling choices for case ③.

Mini-compact car / Downscaling case using power scaling factor of 0.58
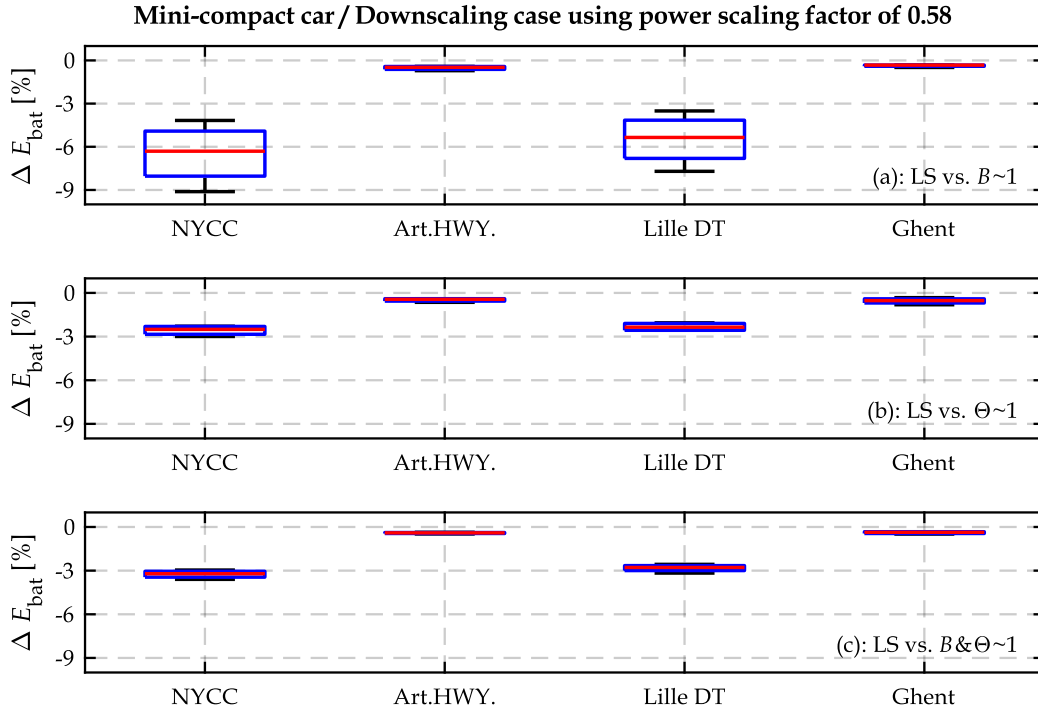
Fig. 103: Sensitivity analysis of the relative difference in terms of energy consumption ΔE_{bat} between linear scaling and geometric scaling based on different scaling choices for case ④.

4.1.2   Impact of the operating points on the outcomes of scaling choices

To elucidate the outcomes discussed earlier, it is essential to recall a key finding drawn in Chapter II. This finding underlines that the largest discrepancy in terms of the efficiency of scaled machines between linear scaling and geometric scaling manifests predominantly in regions characterized by low-speed and high-torque regions. This discrepancy diminishes in regions with high-speed values, approaching negligible values. To delve deeper into this observation, the distribution of the Operating Points (OP) in the torque-speed plane of the driving cycles is subjected to scrutiny. In the sequel, only upscaling case ① and downscaling case ② of the compact car are selected as illustrative cases to perform the analysis. For this aim, 4 regions, donated as R1, R2, R3, and R4 in Fig. 104.a, are defined based on the maximal torque T_{max} value, half of T_{max} and the base speed N_{base}. R1 represents the region characterized by low-torque and low-speed values, R2 represents the low-torque high-speed region, the high-torque low-speed region is described by R3 and R4 represents the high-torque high-speed region.

Based on the findings of Chapter II, the region R3 (Fig. 104.a) is the most critical one. In instances where this region is frequently used, one can straightforwardly conclude that a large difference in energy consumption ΔE_{bat} between linear and geometric scaling laws is expected. As far as the scaling case ① is concerned, the pie chart in Fig. 104.b shows the usage frequency of each region for the urban driving cycles. The results indicate that region R1 encounters frequent use (96% of the usage frequency), while the high-torque low-speed region R3 is hardly used (<1% of the usage frequency). This is attributed to the maximal torque T_{max} sizing requirement to satisfy the acceleration requirements from 0 to 100 km/h. Concerning the scaling

case ②, Fig. 104.d reveals a higher frequency of usage for R3, accounting for 6% of the usage frequency. Therefore, this explains the reason behind the largest difference of ΔE_{bat} for the downscaling cases when using urban driving cycles. Regarding the highway driving cycles, Fig. 104.c and Fig. 104.e indicate that R2 experiences frequent use. This observation provides an understanding of the relatively minor difference in ΔE_{bat}.
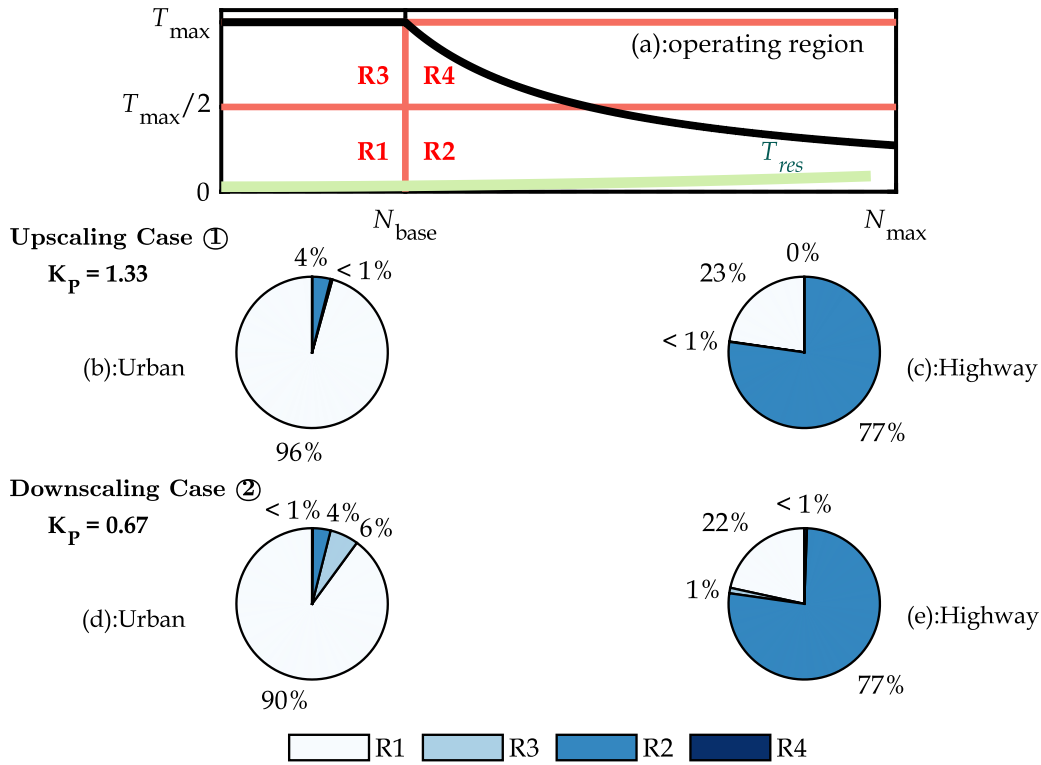
Fig. 104: Distribution of the operating points for the considered driving cycles in traction mode for case ①, and ② of the compact car. The green line in (a) represents the resistive torque imposed by the environment of the vehicle. The pie charts in the second row correspond to the upscaling case, whereas the ones in the third row represent the downscaling case.

For further discussion, a sensitivity analysis of the efficiency, considering 5 OP, as described in Fig. 105 is conducted. These operating points are selected to represent the previously mentioned regions of the torque-speed plane of the electric machine. The difference in terms of efficiency $\Delta\eta_{EM}$ between linear scaling and geometric scaling laws based on the three scaling choices is examined in Fig. 106. Positive values of $\Delta\eta_{EM}$ indicate that linear losses-to-power overestimates the efficiency as compared to the geometric scaling laws and vice versa. For the upscaling case, the results shown in the first row of Fig. 106 reveal that $\Delta\eta_{EM}$ is almost negative for all the operating points under investigation, which explains the reasons behind the overestimation of energy consumption when using linear scaling as compared to geometric scaling. An opposite trend is apparent for the downscaling case, wherein the same observation can be made, although in the opposite direction. Moreover, the sensitivity analysis reveals that opting for the choice $\Theta \sim 1$ leads to a scaled design with the lowest value of $\Delta\eta_{EM}$, specifically at OP1 as compared to other scaling choices of geometric scaling laws. In other words, a scaled design defined employing $\Theta \sim 1$ yields results that are comparatively similar to those obtained with linear scaling. This is true for the two scaling cases under investigation. This insight clarifies

160

why the difference in terms of energy consumption between linear scaling and the choice $\Theta \sim 1$ is relatively close, particularly for urban driving cycles. The same applies to the hybrid choice.
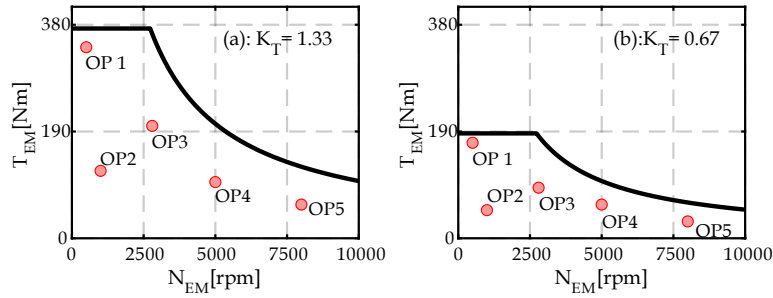
Fig. 105: Considered operating points for the sensitivity analysis
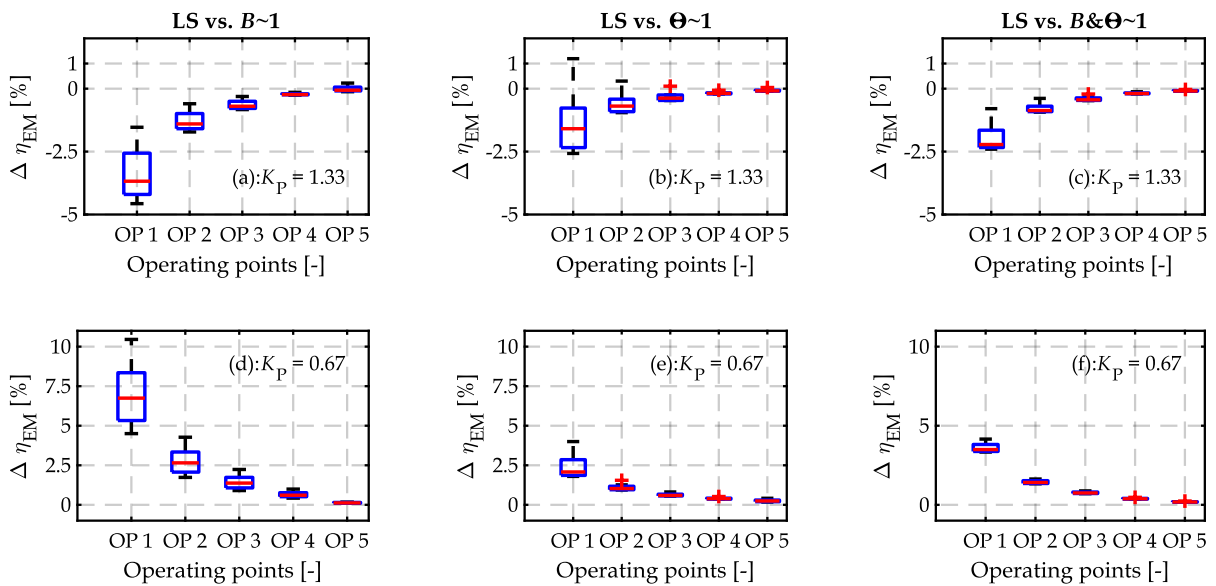
Fig. 106: Sensitivity analysis of the efficiency of the scaled electric machine: The first row corresponds to the upscaled machine for the compact car (case ①) and the second row for the downscaled machine for the compact car (case ②). Note that each column corresponds to the difference in terms of efficiency between linear scaling and the geometric scaling laws based on different scaling choices. Positive values of $\Delta\eta_{EM}$ means that linear scaling overestimates the efficiency and vice versa.

4.1.3 Impact of the geometric scaling factors on energy consumption

In this section, the impact on energy consumption of the geometric scaling factors, i.e. axial K_A and radial K_R scaling factors, is examined in comparison to a design defined by linear scaling. To this end, two scaled designs of the electric machine are defined with the geometric scaling method, each having distinct geometries to have broad insights into the scaling impact.

The difference in terms of energy consumption ΔE_{bat} for all driving cycles combined between the two scaling methods are presented in Fig. 107. By consulting the figures in the first row, Fig. 107.a-c, that represent the upscaling case ①, it is apparent that regardless of the applied geometric scaling choice the variation in ΔE_{bat} as compared to linear scaling is non-significant. This holds true except for the choice $B \sim 1$, wherein using an axial scaling K_A of 0.7

leads to a maximal deviation of 1.8% (obtained mainly when using urban driving cycles). The reason behind this is that the scaling of the loss components using this combination of scaling factors for the choice $B\sim1$ is lower as compared to the other choices, particularly for the copper loss, as shown in Table 23.

Conversely, for the downscaling case, applying an axial scaling factor K_A of 1.5 when opting for the scaling choice $B\sim1$ results in the largest discrepancy, reaching about -10%. This is attributed to the large scaling factor of copper losses associated with the aforementioned scaling choice and axial scaling factor relative to the other choices, as indicated in Table 24. For the remaining choice, similar trends are observed.
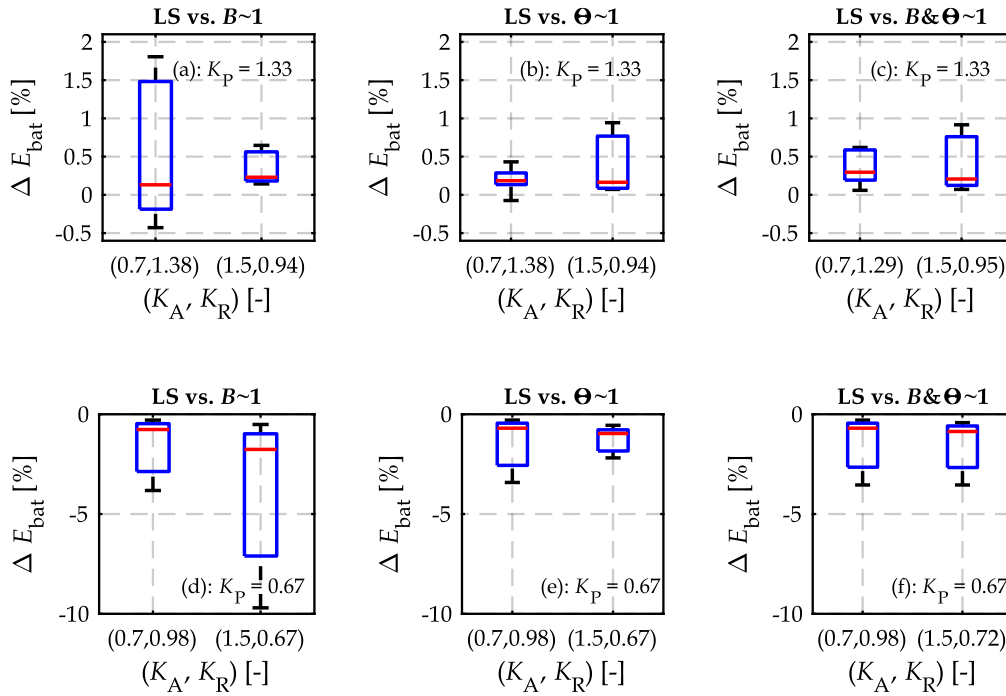
Fig. 107: Impact of geometric scaling factors on energy consumption for all driving cycles combined as compared to a linearly scaled design. Positive values of ΔE_{bat} means that linear scaling overestimates energy consumption and vice versa.

Table 23: Power loss scaling factors for the upscaling cases as a function of the scaling choices. For the radial scaling factors, the number preceding the slash is computed using the scaling choices $B\sim1$ and $\Theta\sim1$, while the value following the slash is determined using the hybrid scaling choice.

Scaling choice	Geometric combination	K_{cu}^{co}	K_{cu}^{ew}	K_{fer}	K_{PM}
Linear scaling	$\emptyset$	**1.33**	**1.33**	**1.33**	**1.33**
$B\sim1$		1.50	0.94	1.33	1.19
$\Theta\sim1$	$\begin{cases} K_A = 1.50 \\ K_R = 0.94/0.95 \end{cases}$	1.41	0.89	1.41	1.26
$B\&\Theta\sim1$		1.43	0.91	1.37	1.24
$B\sim1$		0.70	1.38	1.33	2.54
$\Theta\sim1$	$\begin{cases} K_A = 0.70 \\ K_R = 1.38/1.29 \end{cases}$	0.97	1.90	0.97	1.84
$B\&\Theta\sim1$		0.91	1.67	1.17	1.96

Table 24: Power loss scaling factors for the downscaling cases as a function of the scaling choices. For the radial scaling factors, the number preceding the slash is computed using the scaling choices $B\sim1$ and $\Theta\sim1$, while the value following the slash is determined using the hybrid scaling choice.

Scaling choice	Geometric combination	K_{cu}^{co}	K_{cu}^{ew}	K_{fer}	K_{PM}
Linear scaling	$\emptyset$	**0.67**	**0.67**	**0.67**	**0.67**
$B\sim1$		1.50	0.67	0.67	0.30
$\Theta\sim1$	$\begin{cases} K_A = 1.50 \\ K_R = 0.67/0.72 \end{cases}$	1	0.44	1	0.44
$B\&\Theta\sim1$		1.08	0.52	0.78	1.24
$B\sim1$		0.70	0.98	0.67	0.63
$\Theta\sim1$	$\begin{cases} K_A = 0.70 \\ K_R = 0.98/0.98 \end{cases}$	0.68	0.95	0.68	0.65
$B\&\Theta\sim1$		0.69	0.96	0.67	0.65

The provided analysis in this section underlines that the variation in energy consumption using geometric scaling laws as compared to linear scaling is highly impacted by the selected combination of geometric scaling factors. This means that for a given geometric combination, a large discrepancy between scaling methods is expected. This scenario can be expected when the copper loss scaling becomes larger between both methods particularly when considering driving cycles with urban patterns. In the latter case, the region R3 in Fig. 104, which demonstrates sensitivity to the application of linear scaling, is frequently utilized. Furthermore, this variation is impacted as well by the scaling direction, i.e. upscaling and downscaling cases, and depends on the geometric scaling choices.

4.1.4 Conclusion on scaling choices of PMSM

To conclude, the sensitivity analysis of energy consumption and the efficiency of scaled machines highlights the impact of the operating points on the applicability of the linear power-to-losses scaling method. Urban driving cycles, characterized by high torque and low-speed values deemed to be the cycles where the difference compared to the geometric scaling law is relatively high, particularly for the downscaling cases (about 10%). Therefore, caution is advisable when dealing with such a scenario while applying linear scaling. Notwithstanding, the sensitivity analysis reveals that a scaled design of PMSM yields a minimal difference of about 3% in terms of energy consumption (depending on the geometric scaling factors), including the three geometric scaling choices. This proves that the outcomes of linear scaling are not completely erroneous and do not significantly distort the computed energy consumption. When it comes to selecting the scaling method that yields minimal energy consumption for downscaling case scenarios and urban driving cycles, it is recommended to use the geometric scaling laws based on the scaling choice $\Theta\sim1$. This is because this choice results in a more efficiently scaled design as compared to the other geometric scaling laws (Fig. 106). For upscaling cases and when using urban driving cycles, no prominent energy difference is reached since the maximal positive values of ΔE_{bat} is about 1.8%, both achieved by the scaling choice $B\sim1$. Therefore, the impact of the scaling method for such case scenarios is relatively negligible. The last statement holds for the highway driving cycles for both upscaling and downscaling cases. To generalize the outcomes of the comparative analysis of the effect of scaling laws of PMSM, the same investigation is extended to modular drivetrain topology, exemplified by the modular cascaded machine. The details can be found in Appendix VI.4.

4.2 Effect of the scaling choices of the electric axle on energy consumption

Following the workflow illustrated in Fig. 99, the gear ratio scaling of the gearbox is included in this section. Due to the high number of case studies that can result from the geometric scaling laws of PMSM, it is decided to carry out the analysis using solely the choice $B\sim1$. Note that this decision does not compromise the generalization of the outcomes of this comparison when applying the remaining geometric scaling choices for the PMSM. This is because the trends of the PMSM scaling are already known based on the extensive analysis presented in Section 4.1. Additionally, the scaling cases ①, and ② of the compact car are herein solely examined for the sake of synthesis. It should be noted that the conclusion drawn subsequently can be extrapolated for the other scaling cases.

When dealing with the gear ratio, the maximal speed of the vehicle and the electric machine should be carefully considered. Since the maximal speed of the machine is unchanged (10,000 rpm) during the scaling process, the gear ratio scaling will influence the maximal speed of the vehicle, as illustrated in Fig. 108. In the subsequent examination, two gear ratio scaling cases are considered, with values of 6, and 10, as indicated with the red markers in Fig. 108. These values are selected as illustrative cases that encompass the downscaling and upscaling of the reference gear ratio. This is achieved through scaling factors K_{kgb} of 0.73, and 1.22, that can be implemented in the mechanical power adaptation of the EMR-based scaling laws (Fig. 95), to perform the energy consumption assessment. No change in the number of stages of the gearbox is herein assumed. Furthermore, these scaling cases of the gear ratio are subject to a constraint that ensures at least a maximal speed of 120 km/h, enabling highway driving. Note that the impact of the acceleration time is out of the scope of this comparison.

Fig. 102.a and Fig. 102.b show the energy consumption difference ΔE_{bat} for the upscaling case ① using urban and highway driving cycles, respectively. This sensitivity analysis shows the difference between using linear scaling applied to the EDS and applying geometric scaling laws based on the choice $B\sim1$ of the PMSM combined with the efficiency benchmarking of the inverter, for different gear ratios. By consulting Fig. 102.a, it is evident that ΔE_{bat} is larger for the smallest gear ratio value, considering urban driving cycles. This implies that when employing a smaller gear ratio and investigating urban driving cycles, linear scaling will overestimate the energy consumption in comparison to the second scaling method. The reason behind this is that the regions characterized by low-speed and high-torque values (R3 in Fig. 104) encounter a greater frequency of use when employing a smaller gear ratio as compared to larger values. Particularly in this region, the difference between the two scaling methods becomes more pronounced, as demonstrated earlier. For the highway driving cycles presented in this analysis by the Lille-Ghent cycle, the difference in energy consumption is non-significant using different gear ratio values. This is because the difference between the scaling methods is negligible at high-speed regions, as discussed earlier in Section 4.1.
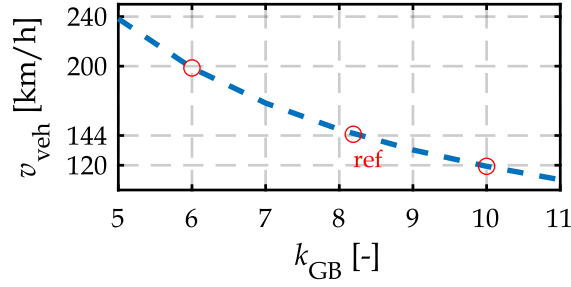
Fig. 108: Impact of the gear ratio scaling on the maximal speed of the vehicle. Red markers refer to the selected gear ratio under investigation.
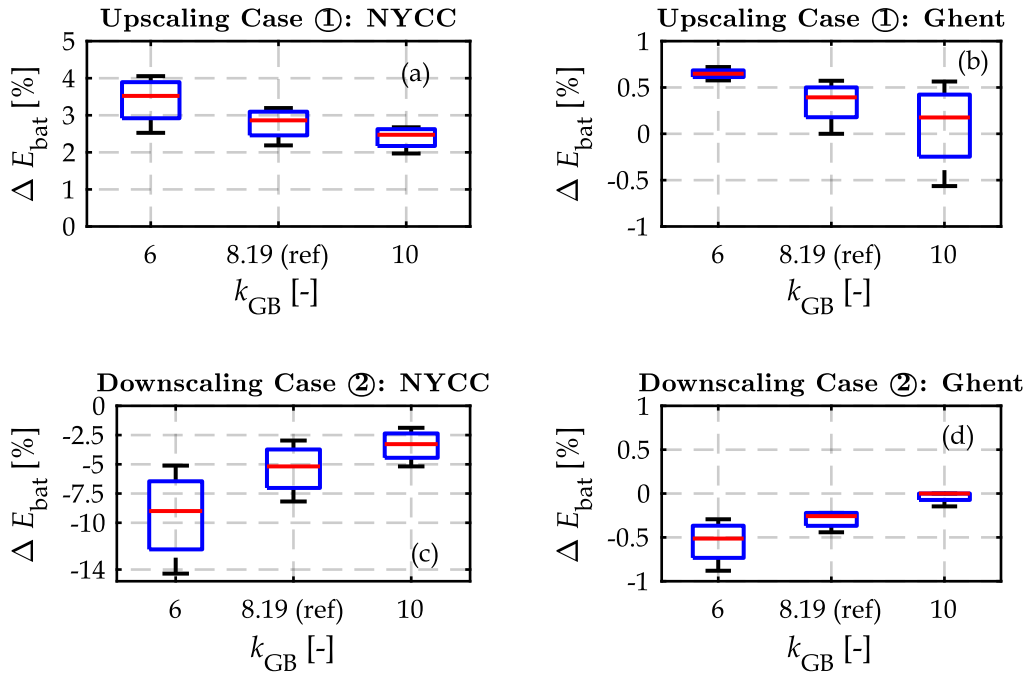
Fig. 109: Impact of the gear ratio on the difference in terms of energy consumption between linear scaling and geometric scaling laws based on the preservation of the magnetic field density $B\sim1$.

Regarding the scaling case ②, similar variations are observed of ΔE_{bat}, but in the opposite direction. This signifies that applying linear scaling for the EDS with smaller gear ratio values will result in a more significant underestimation of the energy consumption of urban driving cycles relative to the second scaling method. Concerning highway driving cycles, the differences are non-significant.

Note that the conclusion drawn from this sensitivity analysis can be expanded for the other choices of the geometric scaling laws as the patterns of the variation using such scaling laws are established earlier. For instance, based on the analysis shown in Section 4.1, it can be readily concluded that ΔE_{bat} will be smaller when using the choice that preserves the temperature rise $\Theta\sim1$ for urban driving cycles, even though applying a smaller gear ratio. This is because the sensitivity analysis depicted in Fig. 106 demonstrates that the difference in efficiency between linear scaling and the choice $\Theta\sim1$ is smaller in low-speed and high-torque regions as compared to the other geometric scaling laws of the PMSM.

5 Conclusion

This chapter presents a comparative analysis of the effect of scaling methods at system-level in terms of energy consumption, addressing the first challenge as outlined in Section 6.2 of Chapter I. To achieve this aim, the scaling laws of the electric drive (Chapter II), and the gearbox (Chapter III), are organized following the EMR-based scaling laws methodology. This is accomplished by keeping the reference model of the e-axle fixed but complimented with two power adaptation elements on the electrical and mechanical sides. By introducing EMR-based scaling in simulation environments of battery electric vehicles, a scalable model and control of the e-axle is established. This contribution provides a unified simulation framework to analyze the performance of a broad range of vehicles, incorporating the possibility of selecting different scaling methods and choices. Furthermore, valuable insights have been obtained regarding the interaction of scalable models of e-axle components. This contribution serves to broaden the scope of application of the EMR formalism, which is mainly used for the deduction of the control design. The outcomes of the EMR-based scaling laws have been compared to those obtained from conventional simulation, revealing the same results. This proves the trustworthiness of the EMR-based scaling laws methodology. Therefore, the third, fourth, and fifth research challenges, presented in Section 6.2 of Chapter I, have been completed in this chapter.

A comparative analysis of the different scaling methods is conducted in this chapter at system-level to understand their impact on energy consumption, addressing the first challenge described in Chapter I. To this end, 4 scaling cases with different power scaling rates have been considered, ranging from 0.58 to 1.96. This enables the investigation of different vehicle classes. An e-axle of 80 kW has been considered as a reference to perform the scaling process. A significant emphasis is placed on comparing the reliability of the linear scaling method of electric drive systems in terms of the computation of energy consumption because of its wide popularity in literature on system-level design. The outcomes of the aforementioned method are contrasted with scaled design candidates of electric machines with distinct geometry resulting from geometric scaling laws, combined with efficiency benchmarking of inverters. Concerning upscaling cases, the sensitivity analysis shows that linear scaling for the electric drive system yields comparative results as compared to the second scaling method, with differences spanning from 0% to 3.2% in absolute terms. These values are announced for different scaled designs of electric machines and can be regarded as comparatively low for energy consumption assessment. Regarding the downscaling cases, it is found that linear scaling consistently underestimates energy consumption. Close results have been obtained when employing the scaling choice that preserves the temperature rise and the hybrid one, with an average difference of 3%. However, a discrepancy ranging from 3% to 8% is found when applying linear scaling to the electric drive when investigating the urban driving cycle and employing the geometric choice $B{\sim}1$ for the electric machine. This difference becomes more pronounced when linear scaling is combined with low gear ratio values. Therefore, caution is recommended when dealing with downscaling cases for such specific case scenarios. For highway driving cycles, the differences in terms of energy consumption are found negligible for both upscaling and downscaling cases.

The findings of this study are important to understand the effect of the scaling method of the e-axle according to the driving patterns on the computation of energy consumption. Evidence has been provided to show that linear scaling can continue to be used in system-level simulations for fast assessment of the energy consumption of electric vehicles during the early development phases.

Conclusions and perspectives

In the following sections, the conclusions of this dissertation are summarized. The findings of each chapter are recalled. Moreover, possibilities for future research are presented at the end.

1 Conclusions

The presented work aims to develop a scaling method for the electric axle system, i.e. the set of voltage source inverter, electric machine, gearbox, and their associated control unit. The purpose of this method is to contribute to speeding up the early development phases of electrified vehicles, facilitating the exploration of diverse solutions for different classes of electric vehicles at system-level. This method is intended to furnish powertrain designers with guidelines on the impact of the adopted solutions on the energetic performance of the vehicle, before initiating detailed design phases at component-level.

Chapter I serves to contextualize the Ph.D. thesis by elucidating the challenges associated with the system-level design of electrified vehicles. The chapter provides an overview of the system-level design layers in the early development phases of automotive projects, namely, the topology, technology, component design and sizing, and control. It is pinpointed that the methods employed for the component design and sizing of the electric axle are recognized by their accuracy, however they are time and effort-consuming. This makes the incorporation of design changes to components at system-level a challenging task. To address this issue, scalability is introduced as a solution that fits the purposes of the early development phases.

Chapter II deals with the scaling of the electric drive system, specifically for IGBT-based inverters and Permanent Magnet Synchronous Machines (PMSM). The state-of-the-art demonstrates an abundance of scaling laws, each characterized by different formulations and varying design details. The objective of the chapter is to conduct a comprehensive comparative analysis to understand the impact of each scaling law on efficiency scaling. This provides insights into the selection of the scaling laws when carrying out energy consumption assessment. Linear losses-to-power scaling, or simply linear scaling, is identified as a widespread scaling method employed at system-level studies, owing to its ease and simplicity. Nevertheless, the assumption of the aforementioned scaling method can be questionable. This is because the overall losses are assumed to be linearly scaled following the power scaling factor, omitting any non-linearities in the losses or dependencies on the geometry.

For PMSM, the outcomes of the linear scaling method are compared against more sophisticated scaling laws that encompass considerations for the geometry as well as different scaling choices for magnetic, and electric loading. Three geometric scaling choices are examined based on the preservation of the magnetic field density, temperature rise in the windings, and a hybrid choice that combines the two latter. These choices result in different scaling law derivations of the parameters of the scaled machine, which are validated based on finite element simulations. The comparison with linear scaling reveals that the regions characterized by low speed and high torque values exhibit the largest discrepancy in terms of efficiency scaling. This efficiency disparity is mainly attributed to the differences in terms of copper loss scaling. At high-speed regions of the machines, where the iron and mechanical losses dominate, the efficiency difference between linear scaling and the geometric scaling laws diminishes. This holds for upscaling and downscaling cases as well as for the different scaling choices. Furthermore, a new organization of the scalable model employing the different scaling laws is proposed in a unified way employing the Energetic Macroscopic Representation (EMR). The new organization consists in keeping a fixed model of the reference machine complemented with two power adaptation elements on the electrical and mechanical sides. The scalability is achieved by manipulating the inputs and the outputs of the power adaptation elements, in which the scaling laws are incorporated. This novel organization and representation of the scalable model contribute to expanding the utilization of the EMR formalism, primarily centered around control design, by enabling the possibility of assessing the design choice impact. Owing to the EMR-based scaling laws, the conditions behind the linear scaling method are derived by examining the power adaptation elements.

Regarding the scaling of the IGBT-based inverter, the linear scaling method is compared against a benchmarking study using well-known reliable power loss models available in literature combined with data extracted from the catalog of commercialized inverters. The comparison demonstrates results that are closely aligned. This is attributed to the linear scaling of conduction losses and the non-significant impact of nonlinearities in the switching losses throughout the scaling process. The chapter includes also, a comparison with other scaling laws available in literature, such as data-driven scaling laws, and a scaling choice that preserves both temperature rise and power density. No significant difference is observed when comparing the outcomes of these latter with the efficiency benchmarking. EMR-based scaling laws are presented at the end of the chapter, elucidating the conditions to result in linear scaling cases for voltage source inverters.

Chapter III presents an initial framework for bridging the gap in literature on the scaling laws of power losses of mechanical transmission, focusing on planetary reducers. This is accomplished through an intensive experimental campaign at a reduced scale as compared to the automotive applications specifications, employing five commercialized planetary reducers. Another significant contribution of the chapter is the emphasis on benchmarking the power loss at high-speed values, up to 14,000 rpm. This focus is driven by the fact that the current literature lacks a comprehensive understanding of the losses generated under such conditions, especially considering the growing interest in high-speed drivetrains within the automotive industry. The outcomes of the experimental campaign allow for deriving data-driven scaling laws based on high-level specifications, e.g. speed, torque, and gear ratio

parameters. A methodology for scaling an efficiency map is proposed based on these latter. The results of scaling the torque and speed of a reference gearbox while preserving the same gear ratio lead to results aligned with the experimental findings. An average efficiency error of less than 0.35% for the entire operating points is obtained. However, the scaling process becomes more challenging when incorporating the gear ratio because of the nonlinearity of losses at high-speed values. Furthermore, the analysis demonstrates that the outcomes of the scaling process are highly dependent on the training set that has been used to tune the scaling laws. The sensitivity analysis reveals that when extrapolating to regions, where the scalable model lacks training data, unsatisfactory results are achieved. This is particularly observed when applying the gear ratio scaling due to the high non-linearity of load-independent losses. An EMR based on the data-driven scaling laws is proposed at the end of the chapter as well.

Chapter IV addresses the scalability of the electric axle at system-level, capitalizing on the work performed in the preceding chapters at component-level. The chapter addresses the interaction between the scaled components of the electric axle. This is achieved by studying the interconnection of the power adaptation elements of each scaled component. EMR-based scaling laws of the electric axle are established by merging and permuting the adjacent power adaptations, leading to retaining solely two equivalent power adaptation elements on the electrical and mechanical sides of the electric axle. Additionally, the new proposed organization of the scaled model of the electric axle enables the deduction of a scalable control scheme following the EMR rules. This provides a unified simulation framework to analyze the performance of a broad range of vehicles, incorporating the possibility of selecting different scaling methods and choices at system-level.

Starting from the EMR-based scaling laws, a comparative analysis of the impact of the scaling laws on energy consumption is conducted for four different battery electric vehicles using a mono-drive topology. The case studies include different power scaling factors, ranging from 0.58 to 1.96 applied to a reference electric axle of 80 kW, allowing the investigation of various types of vehicles, such as mini-compact and compact cars as well as a medium-duty truck. The sensitivity analysis reveals comparative results when applying linear scaling for upscaling cases, with differences spanning from 0% to 3.2% in absolute terms, as compared to geometric scaling laws of electric machines combined with efficiency benchmarking of the inverter. When addressing downscaling cases, the energy consumption difference between the aforementioned scaling laws becomes more noticeable, spanning from 3% to 8%. This observation is particularly pronounced when studying urban driving cycles, characterized by frequent usage of low-speed and high-torque regions. This is attributed to the large efficiency discrepancy between linear scaling and the other scaling laws in such regions. However, the difference in terms of energy consumption is not significant when employing highway driving cycles. These findings offer valuable insights into the reliability of linear scaling concerning the specific driving cycle applications and how it can impact the energy consumption assessment.

2 Recommendations for future works

The perspective of the presented work in this dissertation can be broad, encompassing both component and system levels. The recommendations for future works are delineated for each chapter within this dissertation.

Concerning Chapter II, an experimental campaign of different power-rated electric drive systems to validate the scaling laws will be of high significance. This will enable the refinement of the scaling laws. This point is already considered and under investigation within the DT4V project of the University of Ghent (cf. Section 6.4 of Chapter 1). Furthermore, another research question of significant importance is to determine the scaling process limitation, particularly for electric machines. Establishing boundaries for the scaling procedures, i.e. determining the power and geometric scaling factors beyond which the scaling laws become erroneous, is a significant contribution to the literature centered on electric machine scaling. The outcomes of the DT4V combined with a numerical campaign may provide initial insights to address the latter question. Another point that merits investigation is the inclusion of the thermal aspects in the scaling procedure. This will contribute to determining the limits of the scaling process, particularly for downscaling cases with a radial factor below 1. As for the power electronic converter scaling, it would be interesting to extend the EMR-based scaling laws to modular topologies. For instance, low voltage cascaded H-Bridge inverters with integrated battery modules are gaining increased attention due to many advantages such as efficiency improvement, fault-tolerant operation, and low voltage harmonic. Another noteworthy modular topology is multi-level inverters, which find applications mainly in high-voltage applications. This is motivated by the fact that high-voltage powertrains are gaining attention due to the possibility of speeding up the battery charging time, and potential weight saving. Therefore, it would be interesting to enhance the scaling laws of power electronic converters to incorporate voltage scaling. However, the aforementioned topologies introduce new challenges and increased complexity from both design and control perspectives.

Regarding Chapter III, the data-driven scaling law of planetary reducers could be consolidated by a second experimental campaign with gearboxes featuring additional gear ratios. This will help to improve the results of the scaling process when incorporating the gear ratio scaling. Additionally, the presented methodology should be expanded to high-power-rated gearboxes that fit the requirements of automotive applications. In this sense, the assumption of constant efficiency can be verified. Another interesting point to be investigated is modular topologies. This can be exemplified by incorporating the number of stages in the scaling process. The last parameter is of high significance in the design of high-speed mechanical transmissions, as high gear ratio values are needed.

Concerning Chapter IV, the investigation can be further expanded by making a sensitivity analysis of the impact of the reference machine choice. In Appendix IV, the scaling outcomes for another machine design show the same tendency as for the reference machine used in Chapters II and IV. However, this point needs further investigation including different machine designs to define the best reference point to perform the scaling process and cover as much as possible different transport applications. On top of that, the sizing problem of the electric axle following the scaling method can be further expanded to consider high-speed drivetrains. High-speed applications are getting more attention because of the possibility of increasing power density. However, questions related to the best sizing solution for high-speed electric axles are still to be answered to guarantee optimal energetic performance. An intriguing topic is to investigate the maximal speed of both the electric machine and gearbox at which optimal energetic performance can be accomplished, without any technological

change of the components. To achieve this goal, the scaling laws should be enhanced for better prediction of the losses at high-speed values, such as incorporating skin and proximity effects and in-depth investigation of the mechanical loss scaling.

Within the Panda European project, the application of the EMR methodology has demonstrated its utility by reducing the lead time of electrified vehicles by a percentage up to 25%. The introduction of EMR-based scaling laws in this work is expected to further enhance the potential for lead time reduction and increase the previously mentioned percentage. Quantifying that percentage is one of the perspectives of this work. For this aim, collaboration with industrial partners is required.

What is more, the utilization of scaling could find applications in complex optimization problems of automotive systems. The system-level design optimizations, in the current literature, have primarily focused on exploring different technical solutions regarding the topology, technology, sizing, and control, to minimize energy consumption. A recent growing body of literature is showing a strong interest in adding other dimensions to the optimization problem of electrified vehicles. For instance, in the context of heavy-duty vehicles (e.g. catenary battery electric trucks, trains with on-board energy storage systems, etc.), recent research studies are investigating solutions to approach the design problem for the entire fleet taking into account the traffic density, the infrastructure information, etc. The goal is to define the optimal sizing of the powertrain for the entire fleet, and not only one vehicle, for further minimization of energy consumption. Therefore, the optimization problem goes beyond the boundaries that are defined by the traditionally so-called system and expands to encompass larger dimensions (the system of systems). Additionally, another growing body of literature focuses on including life cycle analysis to include the environmental impact of the adopted solutions, leading to another dimension for the design problem. The latter examples are mentioned to emphasize the growing complexity of the system-level design. Given the ease of incorporation offered by the scalability, it is believed that scaling methodologies will find boarder applications in addressing new challenging problems in future investigations.

Appendix I: Overview of emissions standards in the transportation sector

This appendix provides a summary of the regulations that have been implemented in the major automotive markets, namely the European Union (USA), the United States of America (USA), and China over the last two decades. This summary emphasizes the worldwide commitment to decarbonizing the transportation sector and achieving a more sustainable future. An overview of the implemented regulations in chronological order is depicted in Fig. 110. What follows in this appendix is a summary of the targeted CO_2 objectives for both light and heavy-duty vehicles.

1 CO_2 emissions standards in the EU

The EU has demonstrated leadership in climate policy by putting forth stringent regulations over time for different road transportation applications [235]. This is demonstrated by Fig. 111, which illustrates the evolution of the targeted CO_2 emissions for passenger cars over time. As early as 1998, the European Commission and the European Automobile Manufacturers' Association (ACEA) made a voluntary commitment by signing an agreement to reach a target of 140 g CO2/km for new passenger cars by 2008. Nonetheless, this target was not achieved as the average emissions from passenger cars was 154 g CO2/km in 2008. The absence of significant progress prompted the adaptation of a new regulation in 2009, mandating fleet-wide targets for newly registered passenger cars of 154 g CO2/km in 2015 and 95 g CO2/km in 2019. The light commercial vehicles (vans) were concerned by another regulation, that was put forth in 2011, dictating an EU fleet-wide target of 175 g CO2/km in 2012, and later lowered to 147 g CO2/km in 2020. Subsequently in 2019, a new regulation was put forth, covering both passenger cars and vans, to strengthen the efforts of curbing emissions. The 2019 regulation upholds the 2020 targets mandated in the prior regulation, but also establishes new CO_2 reduction targets for 2025 and 2030. These latter are defined as step-wise targets with five-year intervals in between with a percentage decrease relative to the 2021 baseline:

- 15% reduction from 2025 onwards with a further 37.5% reduction required from 2030 onwards for new passenger cars.
- 15% reduction from 2025 onwards with a further 31% reduction required from 2030 onwards for new passenger cars.
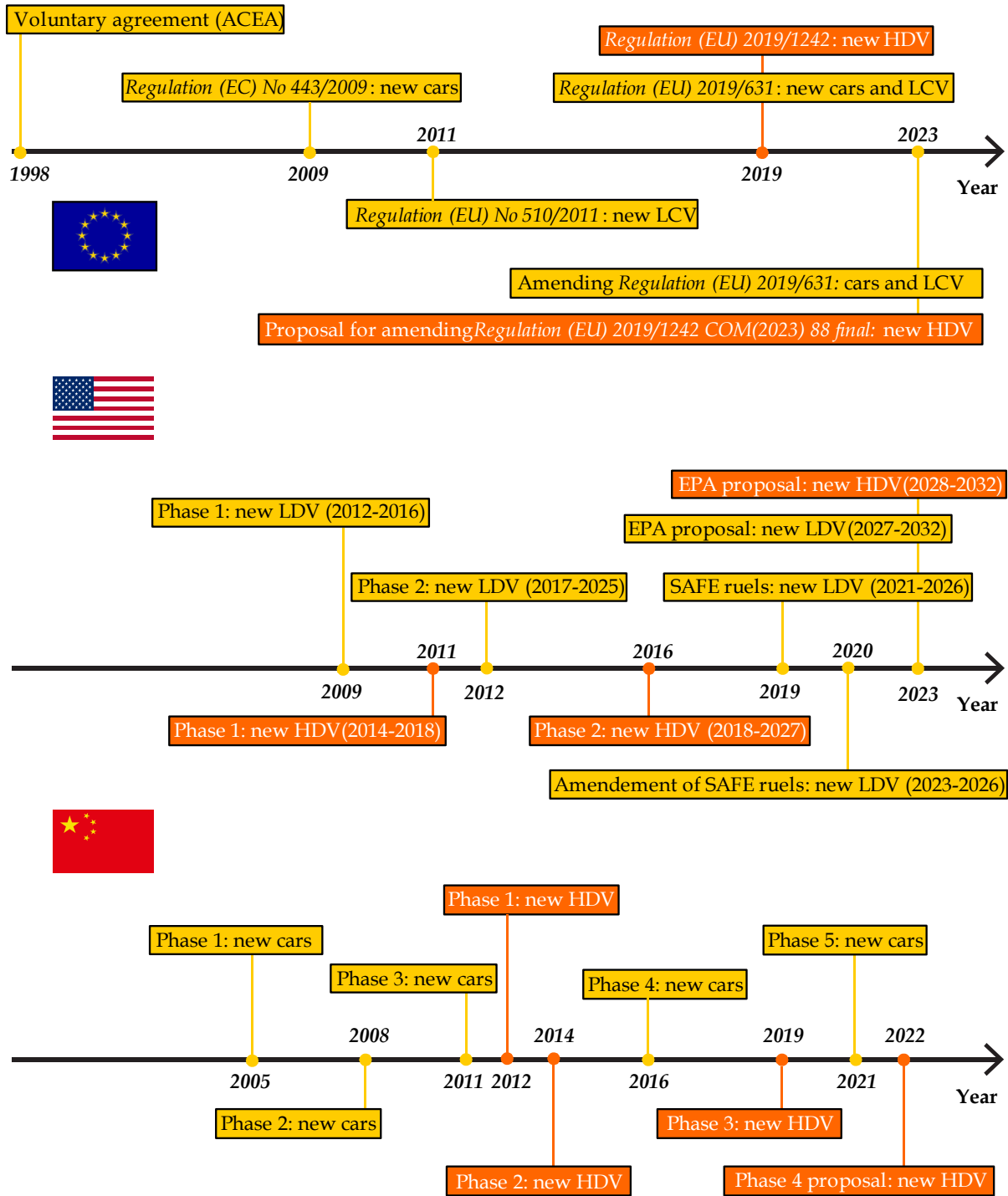
LDV: Light-Duty Vehicles, LCV: Light-Commercial Vehicles, HDV: Heavy-Duty Vehicles

Fig. 110: Timeline showing the introduction of CO$_2$ standards in the road transportation sector across major markets
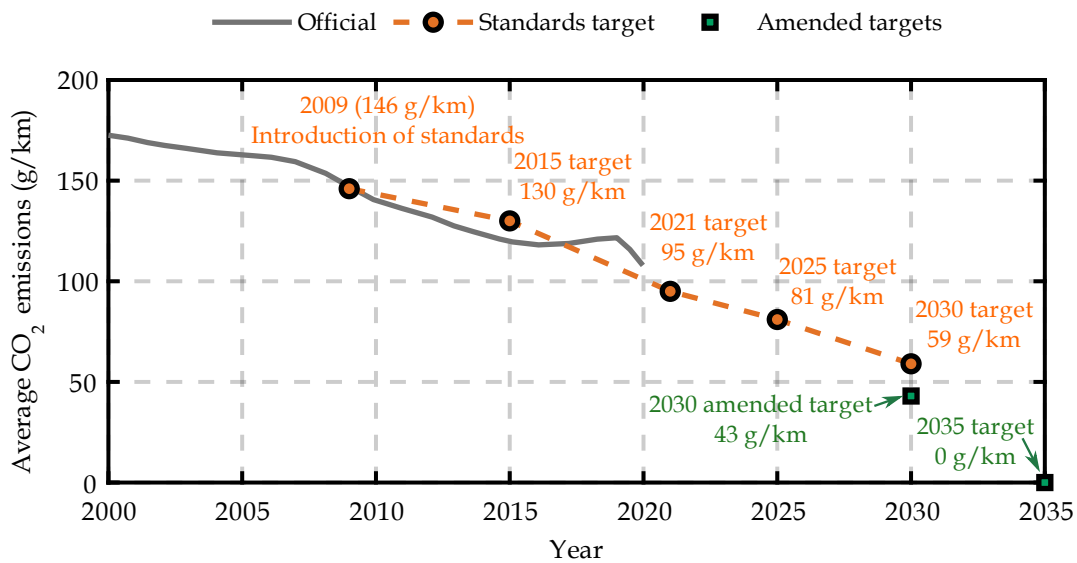
Fig. 111: CO$_2$ emissions required by standards in the European Union for passenger cars

The same year 2019 was marked by the introduction of the first-ever regulation for heavy-duty vehicles (HDV) in the EU. This regulation set a CO$_2$ mitigation target of 15% from 2025 and 30% from 2030 onward as compared to the 2019 baseline. In March 2023, the EU approved a new proposal for a revision of the regulation setting CO$_2$ emission performance standards for passenger cars and vans to ensure a clear pathway toward zero-emission mobility [236]. In the same year, the European Commission released a proposal to amend the CO$_2$ standard for HDV to stimulate faster deployment of zero-emissions vehicles in this sector [46]. The new regulation and the amendment proposal set more ambitious targets, requiring:

- 55% and 50% reduction required from passenger cars and vans, respectively, by 2030, compared to the 2021 baseline.
- 100% reduction for both in 2035 (0 g CO2/km).
- If adopted, a 90% reduction for trucks by 2040, while city buses would be required to achieve a 100% reduction by 2030.

2 CO$_2$ emissions standards in the USA

Emissions standards for Light-Duty Vehicles (LDV) in the USA have experienced changes and rollbacks over the past decade. In 2010, the Environmental Protection Agency (EPA), and the National Highway Traffic Safety Administration (NHTSA) finalized the first set of National Program standards (known as Phase 1) for Model Years (MYs) 2012-2016, requiring to achieve a fleet-wide average of 250[12] g CO2/mi by 2016 for LDV (about 169 g CO2/km normalized to NEDC) [237]. This was followed up with a second set of standards for MYs 2017-2025 in 2012 (known as Phase 2), dictating 163 g CO2/mi by 2025 (about 103 g CO2/km normalized to NEDC) [238]. Unlike the EU, the CO$_2$ regulations for new vehicles in the USA set

---

[12] This corresponds to 156 g CO2/km under the USA test cycle, which is approximately equivalent to 169 g CO$_2$/km as measured under the New European Driving Cycle (NEDC) for diesel vehicles based on the ICCT conversion tool.

annual interim targets for each MYs, instead of step-wise targets with intervals in between. In 2020, the EPA and NHTSA, under the Trump Administration, announced plans to roll back the CO_2 targets for MY 2022–2025. This is because the current was judged overly strict, leading to less affordable vehicles. This resulted in the Safer Affordable Fuel Efficient (SAFE) Vehicles Rule, which relaxed the annual reduction in emissions from 5% to 1.5% for MY 2021-2026 [239]. In 2021, the EPA under the Biden Administration suspended the SAFE rule as it was fundamentally flawed [240]. To ensure that the American LDV fleet is on track to reduce CO_2 emissions, new rules were instated to increase the stringency of the MY 2023-2026, targeting 161 g CO_2/mi in 2026. The revision required an increase in stringency of emissions reductions by 5% to 10% per year in MYs 2023 - 2026 (9.8% in 2022–2023, 5.1% in 2023–2024, 6.6% in 2024–2025, 10.3% in 2025–2026). In 2023, EPA revealed a new more ambitious standard proposal to further reduce CO_2 emissions from LDV from MYs 2027-2032 [48]. This later aims to achieve a wide average target of 82 g CO_2/mi of CO2 in MY 2032. The impact of the issued CO_2 standards over time is depicted in Fig. 112.

HDV were the subject of different standards jointly developed by the EPA and NHTSA. The standards apply to all on-road vehicles with a gross vehicle weight of more than 3856 kg with different reduction targets and were adopted in two phases. Phase 1 regulation, enacted in 2011, required CO_2 and fuel consumption reductions ranging from 6–23% (depending on the vehicle type) over MYs 2014-2018, as compared to the 2010 baseline [241]. Phase 2 regulation, introduced in 2016, applies to MYs 2018-2027 and targets a further reduction from 15-27% depending on the vehicle type, relative to the MY 2017 [242]. In 2023, EPA proposed a revision of the existing standards aimed at further reduction of emissions from heavy-duty vehicles in the MY 2027, in addition to putting forward a proposal for Phase 3 regulation with more stringent targets for MY 2028-2032 [50].
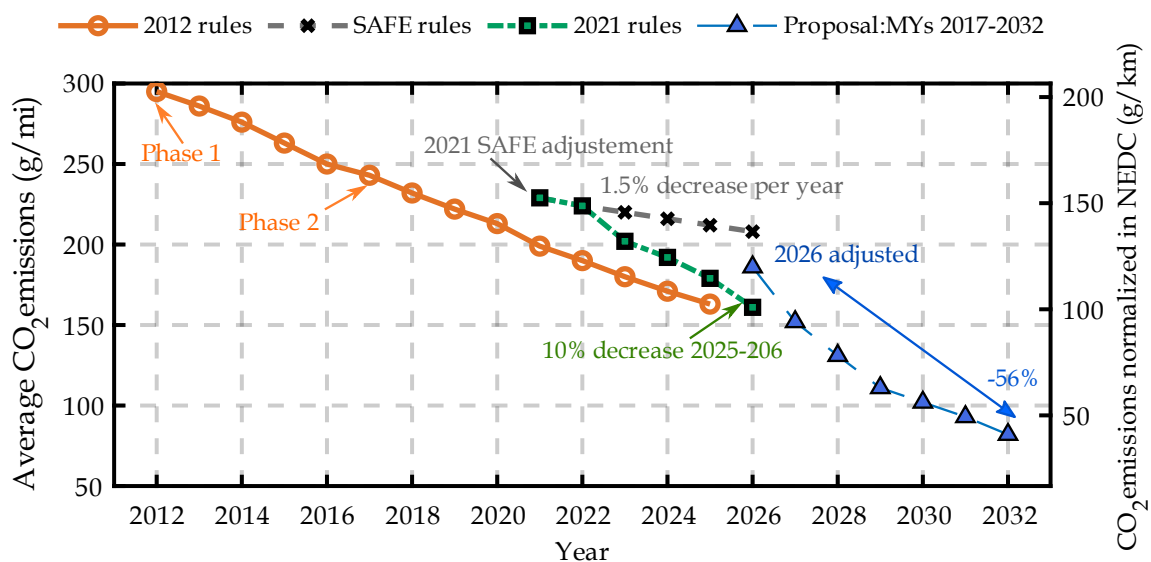
Fig. 112: Average CO_2 emissions required by standards in the United States of America for light-duty vehicles.

3 CO$_2$ emissions standards in China

China has rolled out fuel consumption standards for passenger vehicles that have progressed through five phases, resulting in the regulation of tailpipe CO$_2$ emissions [51]. In 2004, China issued its first-ever fuel economy standards for passenger cars, Phase 1 and Phase 2, which were enforced for newly certified models in 2005 and 2008, respectively. The standards address each model separately (per-model standards), requiring each vehicle model to meet specific fuel consumption thresholds. This differs from the EU, and the USA policies, whereby auto manufacturers can achieve targets by averaging emissions across their entire model fleet. In 2011, Phase 3 standards introduced Corporate Average Fuel Consumption (CAFC) targets, which established fleet average targets instead of the per-model standards already in place. A fleet target goal of fuel consumption of 6.9 L/km (about 161 g CO$_2$/km, following NEDC test procedures) was targeted by 2015. Phase 4 took effect in 2016, setting a new sales fleet average fuel consumption target of 5 L/100 km for 2020 (about 117 g CO$_2$/km). China continued to tighten its fuel economy standards through Phase 5 in 2021, setting a goal of 4 L/100 km (about 93 g CO$_2$/km) by 2025 and 3.2 L/100km (75 g CO$_2$/km) by 2030.

Furthermore, China has taken measures to restrict the fuel consumption of its HDV fleet [52]. Back in 2012, China introduced its first-ever fuel consumption standard called Phase 1, which was subsequently updated twice through Phase 2 and Phase 3, implemented respectively in 2014 and 2019. The standards set fuel consumption limits as a function of the gross vehicle weight. For instance, Phase 2 tightened the fuel consumption limits by an average of 10.5% to 14.5%, depending on the vehicle segment, as compared to Standard 1. Within Phase 3, the stringency is increased by 12.5% to 15.9%, relative to Stage 2 limits. In 2022, a Stage 4 proposal was issued, suggesting to increase the stringency by 15% compared to Stage 3. The new standard is scheduled to go into force in 2025.

Appendix II: Overview of the technical specifications of commercially available electrified vehicles

This appendix presents technical specifications of commercialized electrified vehicles gathered[13] from review papers in literature [11] or trustworthiness online databases related to electric vehicles [243]–[245].

Table 25: Traction electric machines used in commercialized electrified vehicles, data compiled by [11]

Model (year)	Max. power [kW]	Max. torque [Nm]	Max. speed [rpm]	CPSR [-]	Cooling [-]	Power density [kW/L]
Toyota Prius (2010)	60	207	13,500	4.87	Water-jacket	4.8
Nissan Leaf (2012)	80	280	10,390	3.8	Water-jacket	4.2
Tesla Model S 60 (2013)	225	430	14,800	2.96	Water-jacket with shaft cooling	-
Honda Accord (2014)	124	-	14,000	-	-	2.9
BMW i3 (2016)	125	250	11,400	3	Water-jacket	9.1
Chevy Volt (2016)	125	370	12,000	3.71	Oil cooled	-
Tesla Model 3 (2017)	192	410	18,000	4.02	-	-
Toyota Prius (2017)	53	163	17,000	5.4	Water-jacket	5.7
Nissan Leaf (2017)	80	280	10,390	3.8	Water-jacket	4.2
Chevy Bolt (2017)	150	360	8810	2.2	Oil cooled	-
BMW iX3 (2020)	210	400	15,000	3	-	-

Table 26: Traction inverters used in commercialized electrified vehicles, data compiled by [11]

Model (year)	DC-link [V]	Max. frequency [Hz]	Power density [kW/L]	Specific power [kW/kg]
Nissan Leaf (2012)	345	693	7.1	4.7
Tesla Model S 70 D (2015)	375	493	30.1	33.3
Chevy Volt (2016)	430	800	17.3	21.7
Cadillac CT6 (2016)	360-430	667	22.6	16
Toyota Prius (2016)	600	1133	23.7	13.6
Audi A3 e-Tron (2016)	396	-	9.4	7.4
Tesla Model 3 (2017)	375/400	900	-	-

---

[13] Disclaimer: It is advised that readers independently verify the information and consult the sources for any updates to the data.

Table 27: Technical specifications of battery electric vehicles released between the timeline 2019-2023, data gathered from [243]–[245]

Brand [-]	Model [-]	Year [-]	Body type [-]	Power rating [kW]	Max. torque [Nm]	Max. speed [rpm]	Gear ratio [-]	Curb weight [kg]	Maximum speed [km/h]	Acceleration 0-100 kph [s]	Drive type [-]	Battery capacity [kWh]	Voltage [V]	Range (WLTP) [km]	Air drag coefficient Cd [-]
Nissan	Leaf	2019	Hatchback	110	320	10500	8.1938	1558	144	7.9	FWD	40	-	-	0.28
Nissan	LeaF sl plus	2019	Hatchback	160	340	-	8.1938	1748	159	7.3	FWD	62	-	-	0.28
Renault	Zoé R110	2019	Hatchback	80	225	10886	-	1500	135	11.4	FWD	45.61	356	-	-
Renault	Zoé R135	2020	Hatchback	100	245	10886	-	1500	140	9.9	FWD	45.61	356	-	-
Renault	Twingo Zen	2020	Hatchback	60	160	11450	-	1178	135	12.6	FWD	22	400	190	-
BMW	i3	2019	Hatchback	125	250	-	9.655	1345	150	7.2	RWD	42.2	352	310	0.29
Volkswagen	ID.3 Perfor-mance max	2021	Hatchback	150	310	-	11.53	1805	160	7.3	RWD	58	408	416	0.267
Volkswagen	ID.3 Pro S	2021	Hatchback	110	310	-	11.53	1934	160	7.9	RWD	45	408	526	0.267
Volkswagen	e-up!	2020	Hatchback	61	210	12000	-	1229	130	11.9	FWD	36.8	-	-	0.308
Honda	e-advance 17	2020	Hatchback	113	315	-	-	1542	145	8.3	RWD	33.5	-	222	-
Peugeot	e-208 GT	2019	Hatchback	100	260	-	-	1455	150	8.1	FWD	50	-	-	-
Fiat	500e	2019	Hatchback	83	200	-	9.59	1355	141	9.5		24	364	-	0.311
Smart	fortwo	2020	Hatchback	60	160	-	-	1085	130	11.5	RWD	17.6	-	-	-
Opel	Corsa e-Edi-tion	2020	Hatchback	100	260	-	-	1530	150	8.1	FWD	50	-	359	-
Mini	Coper SE Le-vel III	2020	Hatchback	135	270	-	-	1365	150	7.3	FWD	32.6	350.4	225.3	0.3
Seat	Mii electric	2020	Hatchback	61	212	12000	-	1235	130	12.3	FWD	36.8	-	260	0.308
Skoda	CitiGO iV Ambition (SE)	2020	Hatchback	61	212	12000	-	1229	130	12.5	FWD	36.8	-	260	0.308
Volkswagen	e-Golf SE	2020	Hatchback	100	290	12000	9.747	1615	150	9.6	FWD	35.8	323	-	0.27
Chevrolet	Bolt	2022	Hatchback	150	360	-	7.05	1628	145	7.49	FWD	65	350	416.8	0.308
Dacia	Spring Elec-tric	2021	SUV	33	125	-	-	921	125	19.1	FWD	26.8	-	230	-

Kia	EV6 standard range 2WD GT-Line-S	2022	SUV	168	350	8600	-	1945	183.5	7.3	RWD	77.4	697	528	-
Hyundai	Kona 64kWh	2019	SUV	150	395	-	7.981	1685	167	7.6	FWD	64	356	-	0.29
Hyundai	Kona 39kWh	2019	SUV	100	395	-	-	1535	155	9.7	FWD	39.2	327	289	0.29
Mazda	MX-30	2021	SUV	107	271	-	-	1675	140	9.7		35.5	355	200	-
Volkswagen	ID.4 Pro	2021	SUV	150	310	-	-	2049	160	8.5	RWD	77	-	522	0.28
Audi	Q4-Sportback e-ton 40 Advance	2022	SUV	150	310	-	15.6	2045	160	8.5	RWD	55	400	-	0.27
Renault	Megane E-tech EV60	2022	SUV	160	300	11688	-	1636	160	7.4		60	400	-	-
Renault	Megane E-tech EV40	2022	SUV	96	250	11155	-	1541	150	10		40	400	-	-
Nissan	Ariya	2022	SUV	178	300	-	-	1799	160	7.5	FWD	63	-	445	-
Ford	Mustang Mach E-select AWD	2021	SUV	198	430	-	-	1969	180	6.9	RWD	75.7	-	440	0.29
Hyundai	Kona	2021	SUV	150	365	-	-	1685	167	7.9	FWD	67.5	-	484	-
Lexus	UX 300e	2020	SUV	150	300	-	-	1785	160	7.5	FWD	54.3	-	305	-
Peugeot	e-2008	2021	SUV	100	260	-	-	1548	150	8.5	FWD	50	-	330	
Volkswagen	ID.5 Pro	2022	SUV	128	235	-	-	2107	160	10.4	RWD	82	-	516	0.26
Volkswagen	ID.5 Pro Performance	2022	SUV	150	310	-	-	2107	160	8.4	RWD	82	-	516	0.26
Toyota	bZ4X	2022	SUV	150	265	-		1920	160	7.5	-	76	-	510	0.26
Kia	Soul 39.2kwh	2020	Crossover	100	395	8000	8.206	1593	156	9.6	FWD	39.2	327	277	0.35
Kia	Soul 64kwh	2020	Crossover	150	395	8000	8.206	1682	156	7.6	FWD	64	356	452	0.35
Kia	e-Niro 4	2020	Crossover	150	395	8000	8.206	1812	167	7.8	FWD	64	356	453.8	0.29
Hyundai	IONIQ	2019	Crossover	88	295	6000	7.412	1420	165	9.9	FWD	28	360	-	-
Hyundai	IONIQ STANDARD	2022	Crossover	125	350	-	-	1905	185	8.5	RWD	77.4	800	-	-

Hyundai	IONIQ LONG	2022	Crossover	138	350	-	-	2010	185	7.3	RWD	58	800	-	-
BMW	i4 eDrive40	2022	Sedan	250	430	17000	8.774	2125	190	5.7	RWD	83.9	398.5	590	0.24
Tesla	Model 3 Standard Range plus	2021	Sedan	211	375	-	-	1611	225	5.6	RWD	54	360	-	0.23
Porsche	Taycan Sport Turismo	2022	Sedan	300	345	-	-	2080	230	5.4	RWD	79.2	-	358	0.26
Hyundai	IONIQ 6 Long range	2022	Sedan	180	350	-	-	1930	190	7	RWD	77.4	-	610	0.21
Citroen	e-C4 X	2021	Sedan	100	260	10000	-	1541	150	9.7	FWD	50	-	360	0.29
XPENG	P5	2021	Sedan	155	310	-	-	1715	150	7.5	FWD	66.2	-	445	0.223
Lucid	Air	2022	Sedan	358	600	-	-	2025	200	4.2	RWD	88	-	635	0.21
Mercedes	EQE 350+	2022	Sedan	215	565	13500	-	2280	210	6.4	RWD	96	-	550	0.2
Polestar	2 Long Range Single Motor	2023	Sedan	170	330	-	-	1994	160	7.4	FWD	78	-	515	0.278
Mercedes	EQV 300	2020	Minivan	150	362	-	-	2753	160	12.1	FWD	100	-	363	-
Volkswagen	ID Buzz Pro	2022	Minivan	150	310	-	-	2486	145	10.2	RWD	82	-	410	0.285
Citroen	e-Berlingo	2021	Minivan	100	260	-	-	1664	135	11.7	FWD	50	400	279	-
Peugeot	e-Traveller Standard	2020	Minivan	100	260	-	-	1907	130	13.1	FWD	50	-	213	-
Toyota	Proace Verso	2021	Minivan	100	260	-	-	2092	130	13.1	FWD	75	-	314	-
Peugeot	e-Rifter Long	2021	Minivan	100	260	-	-	1809	135	11.7	FWD	50	-	269	-
Mercedes	EvITO	2020	Minivan	150	366	-	-	2455	160	12	FWD	100	-	332	-
Nissan	ev200	2014	Minivan	80	245	10500	-	1592	123	14	FWD	40	360	-	-

Appendix III: Energetic Macroscopic Representation - EMR
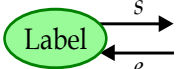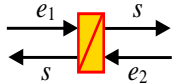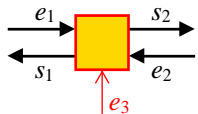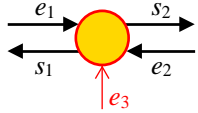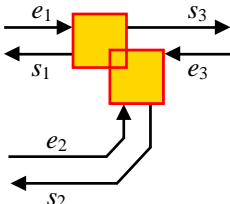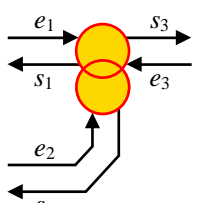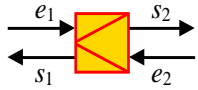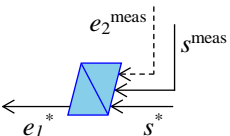
As has been demonstrated in Chapter II, Chapter III, and Chapter IV, the presented work contributes to the Energetic Macroscopic Representation (EMR) formalism by proposing a novel functionality of the power adaptation elements. This contribution allows for rapid assessment of different scaled designs during the early development phases through simulations, thereby speeding up the process. To better comprehend the novelty proposed in this work, this appendix presents a brief history of the utilization of the power adaptation elements in earlier works, alongside with basics of EMR.

1 EMR basics

EMR is a graphical formalism that was developed in 2000 to describe the models of complex energetic systems for control purposes. The EMR formalism adopts a systemic approach, relying on the natural physical causality and the action-reaction principle. Inputs and outputs of each component model are therefore defined in agreement with physical causality, ensuring appropriate interaction between the components. Furthermore, EMR translates the models of each component into graphical elements that describe its function in the system, which are elaborated in Table 28.

Table 28: EMR pictograms (adapted from [246])

Element	Pictogram	Description
Power variable	$\xrightarrow{e}$ $\xleftarrow{s}$	Pair of action and reaction variables of system model; where s denotes output variable; e input variable. The product of the latter is mandatorily power.
Signal variable	$\longleftarrow$	Mandatory signal variable in the control scheme, which is often control signal or output feedback in a closed-loop control.
	$\xleftarrow{}$	Optional signal variable, which is often disturbance measurement in the control scheme, or sometimes information in the system model.

Measurement	$()$	Measurement of variables for feedback control or disturbance compensation.
Source	Label $\quad$ s / e	Terminal of the system, which supplies or dissipates energy. The name of the source can be written inside the pictogram, e.g., battery, grid, environment, etc.
Accumulation	e_1 s / s e_2	Accumulation of energy (physical causality) with a delay, representing the dynamics of the system, e.g. an inductor, inertia, capacitor, etc.
Mono-domain conversion	e_1 s_2 / s_1 e_2 / e_3	Mono-domain conversion of energy, which can involve or not a tuning input (e_3), e.g. an inverter converts electrical DC energy to electrical AC energy with modulation functions, a wheel converts mechanical energy to mechanical energy (without tuning input), etc.
Multi-domain conversion	e_1 s_2 / s_1 e_2 / e_3	Multi-domain conversion of energy which can involve or not tuning input (e_3), e.g. an electrical machine converts electrical energy to mechanical energy (and vice versa) with reference input.
Distribution or coupling	e_1 s_3 / s_1 e_3 / e_2 / s_2	Mono-domain coupling or distribution, which describes a split or merge of different power flows, e.g. parallel connection between two electric energy storages.
Distribution or coupling	e_1 s_3 / s_1 e_3 / e_2 / s_2	Multi-domain coupling or distribution, which describes a split or merge of different power flows, e.g. electric power (current) couples with magnetic power (flux) to produce mechanical power (torque) in an electric machine, whereas the speed of the machine alongside the flux linkage is used to compute the back EMF in the machine.
Power adaptation	e_1 s_2 / s_1 e_2	To scale power between subsystems, e.g. a battery pack can be considered as a scaled equivalent of a battery cell assuming that all the cells behave in the same way. A mathematical sign ">" (greater than) or "<" (lower than) is embedded inside the square. The sign can be defined based on the desired power scaling. In this example, $P_1 = e_1.s_1 < P_2 = e_2.s_2.$
Accumulation inversion	e_2^{meas} s^{meas} / e_1^{*} s^{*}	Indirect inversion of the accumulation elements to control its output, which is a closed-loop control with reference (s^*), output feedback (mandatory s^{meas}), and disturbance rejection (optional e_2^{meas}), e.g. closed-loop speed control.

183

Conversion inversion		Direct inversion of energy conversion element; the output is the tuning input (e_3^*) of the conversion element, e.g. the inversion of the model of an inverter.
		Direct inversion of energy conversion element, in which the output is the reference for the next control block (e_1^*), e.g. the calculation of the current setpoints from the reference torque of an electric machine.
Distribution or coupling inversion		Direct inversion of coupling element (both mono- and multi-domain). A distribution or weighting factor (k_d) has to be introduced to manage the power flow, e.g. the distribution of torques in multi-drive systems.
Power adaptation inversion		Direct inversion of the power adaptation element. In this example, $e_1^* < s_1^*$.
Strategy		Strategy block to impose reference variables, distribution, and/or weighting factors to the local control scheme, e.g. the braking criterion to manage the braking of the vehicle.

To establish the local control of the system, tuning paths must be initially defined according to the objective(s) of the study. These tuning paths are the cause-effect sequence from the tuning variable(s) to the objective variable(s). Thereafter, the control paths are deduced by inverting these tuning paths. The inversion of the EMR pictograms following the defined control paths leads to a control scheme, named the Inversion Based-Control (IBC). The EMR elements that do not store energy are directly inverted from their modeling equations (light blue parallelograms). An example of such inversion is given in (159). The direct inversion rule implies as well for inverting power adaptation elements.

$$s_1(t) = ke_1(t) \Leftrightarrow e_1^*(t) = \frac{s_1^*(t)}{k} \tag{159}$$

The accumulation elements are indirectly inverted by using closed-loop controllers (light blue crossed parallelograms) using a controller $C(t)$, e.g. P, and PI controllers, as depicted in (160).

$$s_1(t) = \int e_1(t) - e_2(t)\, dt \Rightarrow e_1^*(t) = C(t)[s_1^*(t) - s_1^{\mathrm{meas}}(t)] + e_1^{\mathrm{meas}}(t) \tag{160}$$

The inversion of the energy coupling elements (light blue overlapped parallelograms) can be done through either a distribution criterion k_{d} (161) or a weighting criterion k_{w} (162) according to the coupling model. This latter is defined by another level of control called global control or Energy Management Strategy (EMS).

$$s_3(t) = e_1(t) + e_2(t) \Leftrightarrow \begin{cases} e_1^*(t) &= & k_{\mathrm{d}}(t)s_3^*(t) \\ e_2^*(t) &= & [1 - k_{\mathrm{d}}(t)]s_3^*(t) \end{cases} \tag{161}$$

$$s_2(t) = s_3(t) = e_1(t) \Leftrightarrow e_1^*(t) = k_w(t)s_2^*(t) + \left(1 - k_w(t)\right)s_3^*(t) \tag{162}$$

2   Power adaptation elements in earlier research works

2.1   Reduced-scale power hardware-in-the-loop testing

Hardware-in-the-Loop (HiL) testing involves inserting a physical part of the real system into a simulation loop. HiL simulation is generally carried out at full-scale as the aim is to subsequently integrate the tested components into the entire system. However, versatile test benches used for HiL testing in laboratory environments do not often align with the power specification of the real system due to the diversity presented in automotive applications. Therefore, a reduced-scale HiL is proposed as an intermediary step to validate the developed control laws. For this aim, power adaptation elements have been initially introduced to perform such as testing [148], [149], [247]. To exemplify the utilization of power adaptation elements, an example of reduced-scale HiL testing of a subsystem of an electric vehicle is presented in the following.

Fig. 113 shows a subsystem, compromising a battery and an electric drive, to be tested. To conduct reduced-scale HiL testing, the full-scale subsystem, intended for testing, is replaced by an experimental counterpart of the same nature, but with a reduced power specification. The remaining of the system, i.e. the drivetrain in this example, is emulated by another experimental setup, called an emulator. This latter consists of a second electric drive and a DC source, which aims to mimic the behavior of the drivetrain at a reduced-scale.
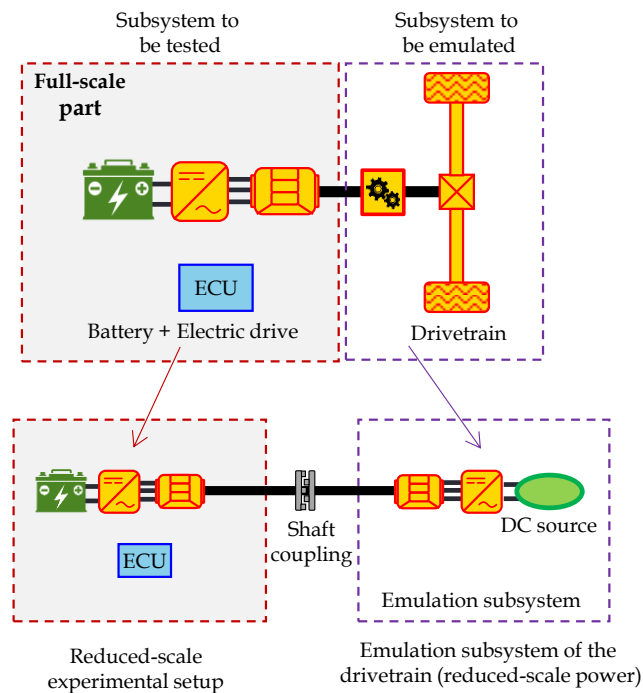
Fig. 113: Principle of reduced-scale hardware-in-the-loop testing.

185

Fig. 114 depicts an overview of the organization of the reduced-scale HiL. The tested sub-system is controlled in torque mode, wherein the input reference is adapted through a first power adaptation element, as illustrated in the lower part of Fig. 114. The power adaptation scales the full-scale torque reference T_{EM}^0, defined by the powertrain control of the vehicle, by a torque scaling factor K_T, as given in (163). This torque scaling factor is defined to respect the limitation of the experimental setup [247]. The emulator is controlled in speed mode, in which the speed reference is imposed by the model run in real-time of the full-scale drivetrain. To adhere to the speed limitation, a speed scaling factor K_Ω is incorporated at a second power adaption element, as expressed in (164). A power scaling factor K_P can be derived from the aforementioned equations as follows in (165).

$$K_T = \frac{T_{EM}'^*}{T_{EM}^{0*}} \tag{163}$$

$$K_\Omega = \frac{\Omega_{EM}'^*}{\Omega_{EM}^{0*}} \tag{164}$$

$$K_P = K_T K_\Omega \tag{165}$$

Fig. 114: Organization of reduced-scale hardware-in-the-loop testing. Variables denoted with an apostrophe ' refer to scaled parameters, while the superscript 0 represents the corresponding full-scale parameters.

The effect of the torque, speed, and power scaling factors, on the torque-speed envelope of the full and reduced scale of the electric drive is illustrated in Fig. 115
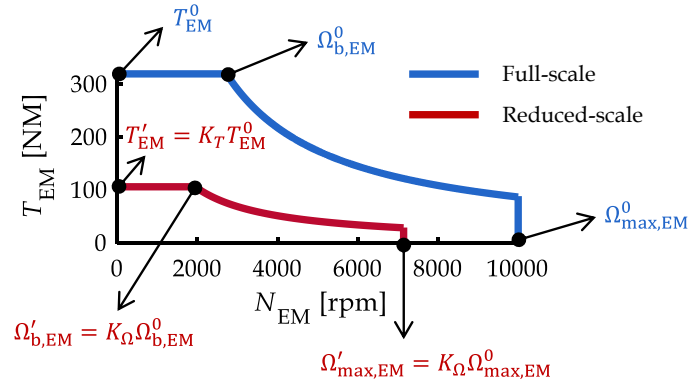
Fig. 115: Impact of the scaling factors on the torque-speed envelope of the electric drive system

2.2 Power adaptation element to alleviate the representation of complex systems

Subsequently, the utilization of power adaptation elements is expanded to alleviate the representation of complex systems, particularly in the context of railway systems. Such applications present different wagons, as illustrated in Fig. 116, leading to weight down the representation of the system.
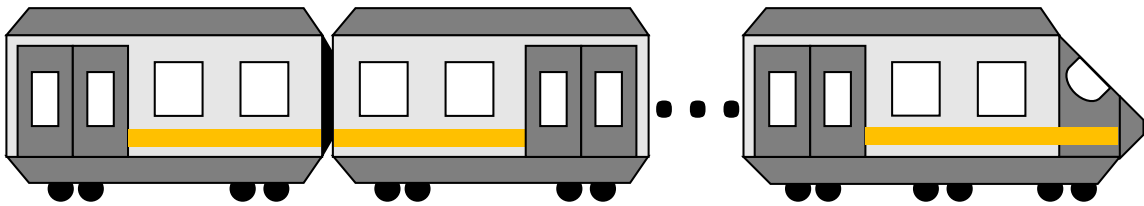

Fig. 116: Example of a railway application

For instance, a mechanical coupling element, as shown in the upper part of Fig. 117, is used to describe the sum of the forces provided by each wagon to propel the system (166). The mechanical coupling can be simplified by a power adaptation element, as shown in the lower part of Fig. 117, assuming equal forces are provided by each wagon. The governing equation of the mechanical power adaptation element is expressed as follows in (167).

$$
\begin{cases}
F_{\text{tot}} & = \quad \displaystyle\sum_{i=1}^{n} F_i \\
v_{\text{veh}} & = \quad \text{common}
\end{cases}
\tag{166}
$$

$$
\begin{cases}
F_{\text{tot}} & = \quad nF_1 \\
v_{\text{veh}} & = \quad \text{common}
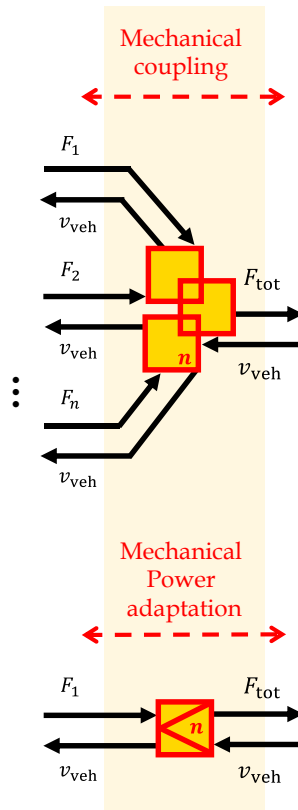\end{cases}
\tag{167}
$$

187

Fig. 117: Simplification of the mechanical coupling using power adaptation elements

Appendix IV: Further discussion on the scaling laws of electric drive systems

This appendix provides further insights into the scaling laws presented in Chapter II. This appendix is organized as follows. Section 1 derives general scaling laws of Permanent Magnet Synchronous Machines (PMSM) based on geometric variations in the axial and radial directions. A detailed comparison between linear scaling and geometric scaling laws in terms of the scaling of each individual loss component is presented in Section 2. A sensitivity analysis is presented in Section 3 to complement the efficiency scaling comparison made in Chapter II between linear scaling and geometric scaling laws. This sensitivity analysis includes distinct scaled geometries defined by geometric scaling as well as different torque scaling factors. To generalize the outcome of the comparison Section 4 compares the efficiency map scaling using the different scaling laws, considering a second reference machine design. Section 5 deals with the sizing rules of the voltage source inverters.

1   Derivation of geometric scaling laws of permanent synchronous machine

To examine the effect of the geometric scaling on the torque and the losses, basic analytical equations are first presented in the following section.

1.1   Sizing theoretical background

Typically, the magnetic tangential stress σ_{Ftan} serves as the starting point in electric machine design. Assuming sinusoidal waveforms, the air-gap flux density B_δ, and the electric load A, and the power factor $\cos \varphi$ determine the average tangential stress as given in (168) [102]. Note that in the last equation, A, and B_g are expressed in RMS values.

$$\sigma_{\text{Ftan}} = A \, B_g \, cos \, \varphi \tag{168}$$

When exerted on the rotor surface facing the air gap, the tangential stress generates the electromagnetic torque as expressed in (169), assuming a constant speed [102].

$$T_{\text{EM}} = \sigma_{\text{Ftan}} \frac{D_r}{2} S_r = \frac{\pi}{2} A \, B_g D_r^2 l_r \, cos \, \varphi \tag{169}$$

in which D_r denotes the air gap diameter, and l_r is the active length of the machine.

The electric load A can be defined as a function of the cross-section of the slot area filled with copper S_{slot}, and the stator pole pitch τ_s as in (170).

$$A = \frac{J \, S_{slot,cu}}{\tau_s} \tag{170}$$

The flux linkage can be expressed as a function of the number of turns N_{turns}, the parallel paths denoted a_p, and the integration of the magnetic field density B that crosses a rectangular area S, as shown in (171).

$$\psi = \frac{N_{turns}}{a_p} \int_S B \, dS \tag{171}$$

The resistance of the winding can be expressed as a function of the core and end-winding resistance as follows:

$$R_s = R_{s,co} + R_{s,ew} \tag{172}$$

which can be redrafted considering the resistivity ρ_s of the stator winding material, the number of slots Q_s, the number of turns N_{turns}, the number of parallel paths a_p, the total length of the winding in the active l_{co} and end-winding l_{ew} parts, and the slot area filled with copper $S_{slot,cu}$, as follows:

$$R_s = \rho_s \frac{N_{turns}}{a_p} \frac{Q_s}{3} \left(\frac{l_{co}}{\frac{1}{2} S_{slot,cu}} + \frac{l_{ew}}{\frac{1}{2} S_{slot,cu}} \right) \tag{173}$$

The copper losses P_{cu} evolve proportionally to the square of the current density J, the slot area filled with copper $A_{slot,cu}$ and the length of conductors in the core and active parts, as shown in (173).

$$P_{cu} \propto \rho_s A_{slot,cu} J^2 (l_{co} + l_{ew}) \tag{174}$$

Considering the Steinmetz model, the iron losses P_{fer} can be expressed as a function of the air gap flux density B_g, the volumetric mass density ρ_{fer}, the volume of iron V_{fer}, and the electric frequency f [102].

$$P_{fer} = k f^\alpha B_g^\beta \rho_{fer} V_{fer} \propto f^2 B_g^2 V_{fer} \tag{175}$$

in which k, α, and β denote the Steinmetz coefficients which are typically identified based on experimental tests. As an example, both α, and β are close to 2 for a FeSi material [102].

Following the model proposed by Polinder and Hoeijmakers [248], the contribution of the permanent magnet loss can be expressed as the function of the resistivity of the magnets ρ_{PM}, the geometry of the magnet (width w_{PM}, height h_{PM}, length L_{PM}), and the flux density. Note that the last model is applicable for machines in 2D cases with segmented magnets and the end effects are disregarded.

$$P_{\mathrm{PM}} = \frac{1}{12}\frac{1}{\rho_{\mathrm{PM}}}\, w_{\mathrm{PM}}^3 h_{\mathrm{PM}} L_{\mathrm{PM}} \left(\frac{\partial B}{\partial t}\right)^2 \tag{176}$$

The mechanical losses, namely the friction losses in bearings P_{br}, and the windage loss P_{w} can be evaluated based on the model proposed by Gieras [249]. The friction losses in bearings P_{br} can be evaluated using (177).

$$P_{\mathrm{br}} = k_{\mathrm{fb}} m_{\mathrm{r}} n_{\mathrm{rm}} 10^{-3} \tag{177}$$

where k_{fb} is an empirical coefficient, m_{r} is the mass of the rotor and n_{rm} is the rotor mechanical speed in rpm, the coefficient 10^{-3} is used to convert the friction torque from Nmm to Nm. The windage losses P_{win} can be approximated as in (178).

$$P_{\mathrm{win}} = 2\ 10^{-6} D_{\mathrm{ro}}^3 l_{\mathrm{stk}} n_{\mathrm{rm}}^3 \tag{178}$$

with D_{ro} is the outer diameter of the rotor, l_{stk} is the stack length, and $2\ 10^{-6}$ is an empirical coefficient defined based on experimental testing.

Evacuating heat in electrical machines is typically achieved by using the external surface of the stator to transfer the heat. The outer cooling surface of the machine can be expressed as a function of the outer diameter D_{so} and the length stack length of the stator l_{stk} (179). Assuming that the heating is mainly attributed to the copper loss in the core part, which is the major power loss contributor to the total losses for low and medium-speed rated PMSM, it can be approximated that the temperature rise in the winding Θ follows (180) [102]. The last equation supposes uniform temperature distribution throughout the entire stator.

$$S_{\mathrm{cooling}} = \pi\, D_{\mathrm{so}} l_{\mathrm{stk}} \tag{179}$$

$$\Theta = \frac{P_{\mathrm{cu,co}}}{\alpha_{\mathrm{th}}\, S_{\mathrm{cooling}}} \tag{180}$$

where α_{th} is the heat dissipation coefficient, which depends on the cooling method.

1.2 General Scaling laws

This section aims to elucidate the impact of the geometric scaling procedures, i.e. axial and radial scaling on the parameters and the properties of the scaled machines. The scaling of the relationships (168)-(178), and (180) as a function of the axial K_{A}, radial K_{R}, and rewinding K_{W} scaling factors is outlined below, regardless of the scaling choice:

$$\sigma'_{\mathrm{Ftan}} \propto A' B'_{\mathrm{g}} \tag{181}$$

$$T'_{\mathrm{EM}} \propto K_{\mathrm{A}} K_{\mathrm{R}}^2\, A' B_{\mathrm{g}}{}' \tag{182}$$

$$A' \propto K_{\mathrm{R}}\, J' \tag{183}$$

$$\psi' \propto K_{\mathrm{A}} K_{\mathrm{R}} K_{\mathrm{W}}\, B' \tag{184}$$

191

$$R'_{s,co} \propto \frac{K_A K_W^2}{K_R^2} \tag{185}$$

$$R'_{s,ew} \propto \frac{K_W^2}{K_R} \tag{186}$$

$$P'_{cu,co} \propto K_A K_R^2 \boldsymbol{J'^2} \tag{187}$$

$$P'_{cu,ew} \propto K_R^3 \boldsymbol{J'^2} \tag{188}$$

$$P'_{fer} \propto K_A K_R^2 \boldsymbol{B'^2} \tag{189}$$

$$P'_{PM} \propto K_A K_R^4 \boldsymbol{B'} \tag{190}$$

$$P'_{br} \propto K_A K_R^2 \tag{191}$$

$$P'_w \propto K_A K_R^3 \tag{192}$$

$$\Theta' \propto K_R \boldsymbol{J'^2} \tag{193}$$

From the last equations, it is evident that the scaling relationships are influenced by the change in the electric loading parameters, namely A, and J, and the magnetic loading parameter B. The aforementioned parameters, which are highlighted in bold in the preceding equations, are inherently related to the specific scaling choices made throughout the scaling process. Note that the proportional mathematical symbol $\propto$ is employed to alleviate the expressions and highlight the key parameters that significantly influence the scaling laws. Making use of the preceding equations, the scaling laws, shown in Chapter II, can be straightforwardly derived by replacing the scaling choice of the current density and the magnetic field density

2   Comparison of each loss component between linear scaling and geometric scaling laws

In Section 3.3 of Chapter II, it is found that the difference in terms of efficiency difference between linear scaling is more pronounced in regions characterized by low-speed and high-torque speed regions, while it decreases at high-speed regions. This was explained by the contribution of each loss component according to each region in the torque-speed plane. To lend support to the statement made in the concerned section, this section examines the difference between linear scaling and geometric scaling laws for each individual loss component. Note that the upscaling case presented in Section 3.3.1 of Chapter II, using a torque scaling of 2, is herein solely elaborated. The conclusion drawn from the following analysis in this section can be extended to the downscaling cases.

In this section, the relative difference in terms of power loss ΔP, between linear scaling and the geometric scaling laws based on different scaling choices, is quantified, following (194).

$$\Delta P_x = 100 \frac{\left| P_x^{LS} - P_x^y \right|}{P_x^y} \tag{194}$$

2. Comparison of each loss component between linear scaling and geometric scaling laws

$$\text{with } x \in \{cu, \text{fer}, PM, \text{mech}\}, y \in \{B\sim1, \Theta\sim1, B\&\Theta\sim1\}$$

in which x a subscript refers to the loss component in question, namely copper (cu), iron (fer), permanent magnet (PM), and mechanical losses (loss), and y is a superscript used to refer to the geometric scaling choices employed.
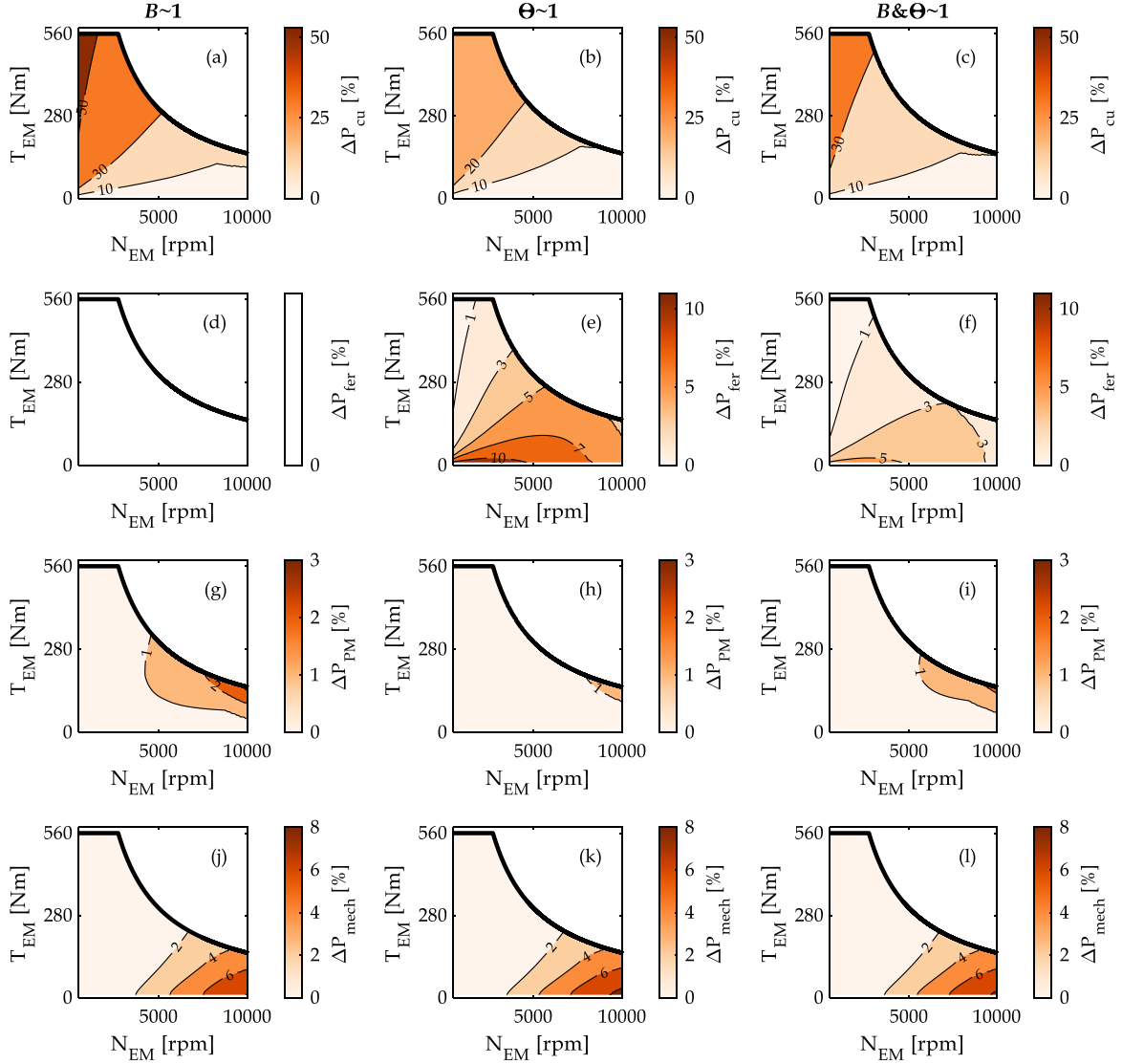

Fig. 118: Loss difference between linear scaling and geometric scaling laws for the upscaling case with a torque scaling factor of 2.

From Fig. 118. a-c, it is apparent that the difference between linear scaling and geometric scaling in terms of copper loss ΔP_{cu} is more pronounced in the regions characterized by low-speed and high-torque values. This loss disparity can be as significant as 50% in the case of the scaling choice that preserves the magnetic field density $B\sim1$, whereas it is relatively lower for the choice that preserves the temperature rise $\Theta\sim1$. The discrepancy in the scaling of the copper loss is attributed to the large difference in the copper loss scaling factor outlined in Table 4 of Chapter II. For this reason, the efficiency difference obtained in Section 3.3.1 is significant in the aforementioned regions. By consulting the remainder of the subfigures, it is evident that the loss difference, in terms of iron loss ΔP_{fer} (Fig. 118. d-f), permanent magnet loss ΔP_{PM} (Fig.

118. g-i), and mechanical loss ΔP_{mech} (Fig. 118. j-l), is relatively lower in high-speed region in comparison to the copper loss. This explains the comparable results in terms of the efficiency difference, between linear scaling and geometric scaling laws, in the last previously mentioned regions.

3 Sensitivity analysis of linear scaling versus different scaling choices of geometric scaling laws

To complement the discussion presented in Section 3.3, this section presents a sensitivity analysis that aims to quantify the difference in terms of efficiency using linear scaling and the geometric scaling laws based on different choices. The sensitivity analysis encompasses distinct geometries of the scaled machines, as well as different torque scaling factors. The ranges for the geometric scaling factors are chosen to ensure a large and still realistic variation in geometry. Table 29 provides the range within which the geometric scaling factors are varied. To avoid undesirable machine geometries and feasible scaled design the conditions set in equation (44) in Chapter II are herein considered. In this sensitivity analysis, 4 torque scaling factors K_T are considered: 0.5, 0.75, 1.25, and 2. The selection of these factors ensures a narrow torque variation close to that of the reference machine, as well as a large variation. Therefore, a comprehensive comparison between linear scaling and geometric scaling laws can be made. For the comparison, 5 Operating Points (OP) are selected to conduct the sensitivity analysis, as illustrated in Fig. 119. These operating points are chosen to represent distinct regions within the torque-speed plane of the scaled machines.

Table 29: range of scaling factors in the sensitivity analysis

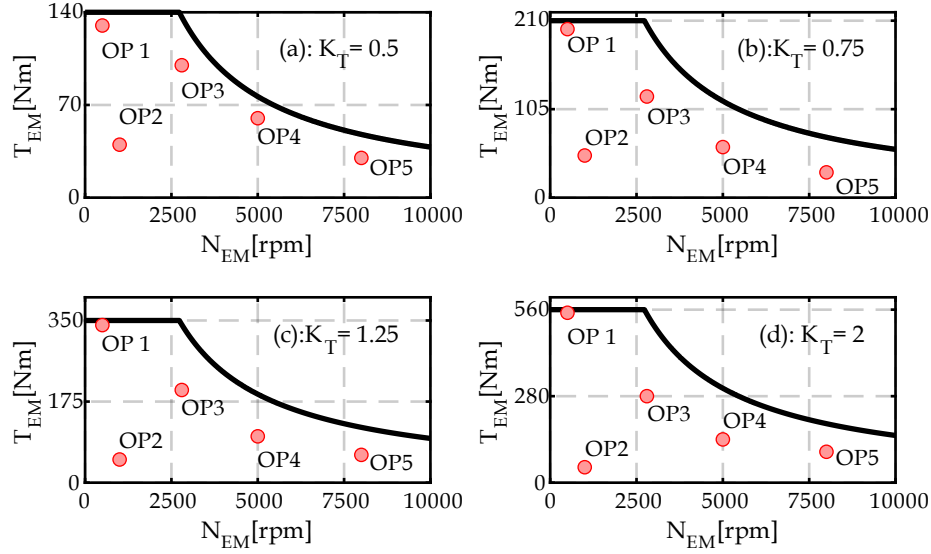| Torque scaling factor K_T [-]	Radial scaling factor K_R [-]	Axial scaling factor K_A [-]
0.50	[0.7, 1.20]	[0.32, 1.20]
0.75	[0.7, 1.40]	[0.33, 1.30]
1.25	[0.85, 1.50]	[0.45, 1.88]
2	[0.98, 1.50]	[0.73, 2.13]

Fig. 119: Operating points used for the sensitivity analysis

In Fig. 120, the sensitivity analysis presents the difference in efficiency using linear scaling and geometric scaling laws $\Delta\eta_{EM}$. The figure is quite revealing in several aspects. First, the figure substantiates the earlier statements in Chapter II, by confirming that the region characterized by low speed and torque values, exemplified herein by OP1, exhibits a significant discrepancy between linear and geometric scaling. Notably, the decreasing trend in $\Delta\eta_{EM}$ as the speed increases is observed for different scaled designs. This is particularly evident in the case of OP5, where $\Delta\eta_{EM}$ is negligible or nullified. Furthermore, it is apparent from Fig. 120 that the maximal absolute value of $\Delta\eta_{EM}$ increases when applying a large torque scaling factors, regardless of whether it is in the upscaling or downscaling direction. What is more, the comparison reveals that opting for the choice $\Theta\sim1$ leads to a scaled design with the lowest value of $\Delta\eta_{EM}$ as compared to other scaling choices of geometric scaling laws. In other words, a scaled design defined employing $\Theta\sim1$ yields results that are close to those obtained with linear scaling. This is true for the different torque scaling factors. For downscaling cases, the choice $\Theta\sim1$ results in a scaled design that is more efficient among the other choices, as this choice consistently shows the lowest value of $\Delta\eta_{EM}$. On the other hand, for upscaling cases, the choice $B\sim1$ leads to a more efficient design. The reasons behind this is explained in Section 3.1.3.4 in Chapter II, where an analysis of the power loss scaling factors is conducted.
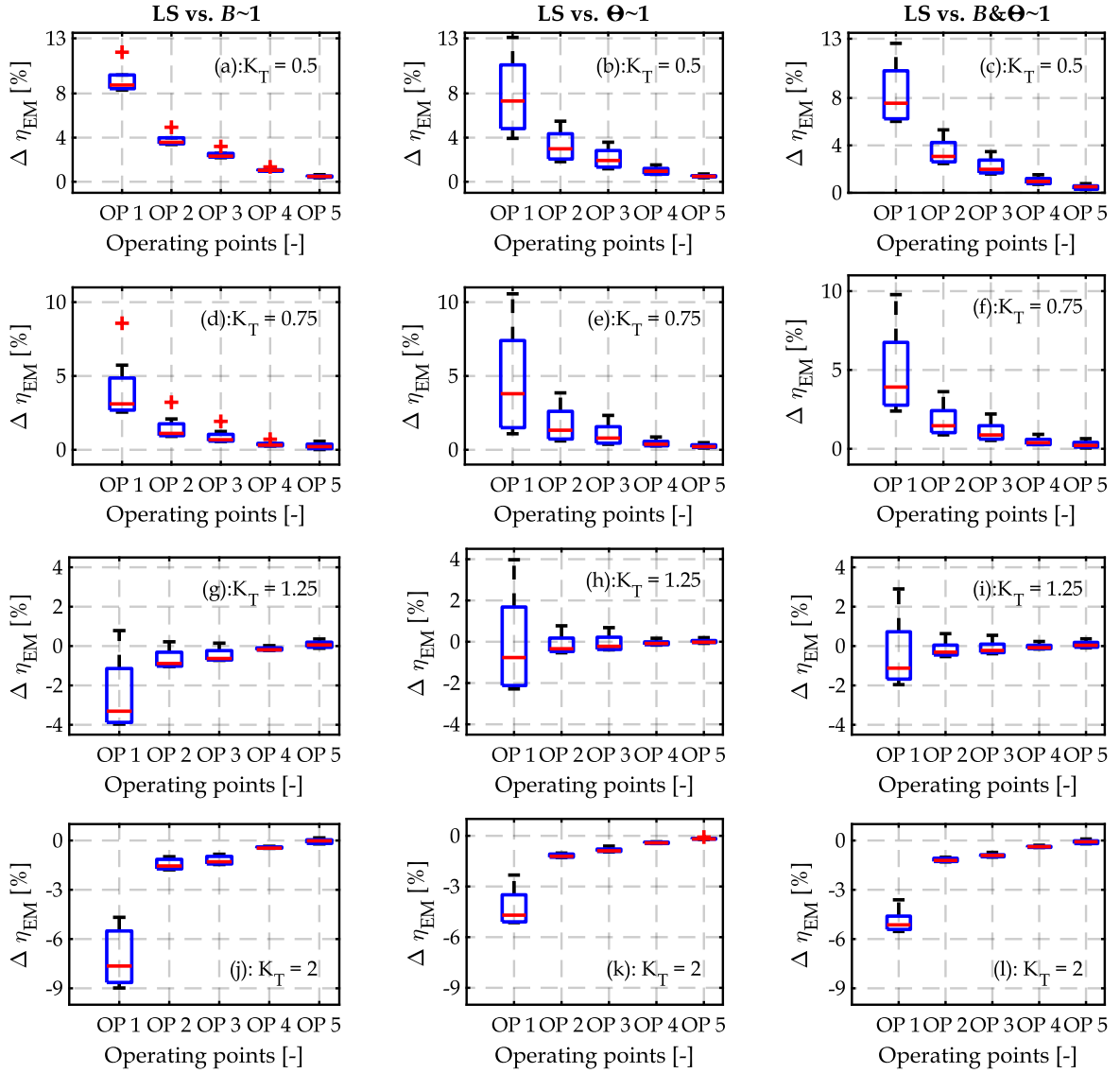
Fig. 120: Sensitivity analysis: linear scaling versus geometric scaling laws based on different scaling choices. Positive values of $\Delta\eta_{EM}$ means that linear scaling overestimates the efficiency as compared to geometric scaling laws and vice versa.

4 Generalization of the comparison of linear losses-to-power scaling and geometric scaling laws of PMSM

The outcomes of the comparison presented in Chapter II are based on a reference machine, the parameters of which are presented in Table 30. This section aims to extend the comparison presented in Chapter II between linear scaling and the geometric scaling laws using a second design of PMSM as a reference machine. The parameters of the last machine are summarized in the third column of Table 30. Note that the latter machine is designed for industrial application.

Table 30: Parameters details of the reference machines

Parameters	Reference Machine in Chapter II	Reference Machine in this appendix
Rated power [kW]	80	12.6
Continuous torque [Nm]	280	70
Base speed [rpm]	2728	1719
Maxiaml speed [rpm]	10000	3000
DC bus voltage	375	380
Outer diameter stator [mm]	200	180
Inner diameter stator [mm]	131	103.9
Number of slots/poles/phases [-]	48 /8 /3	24/4/3
Number of turns per coil/ strands per turn [-]	8 / 15	70
Winding core resistance [mΩ]	5.67	68
End-winding resistance [mΩ]	5.4	40
Peak current density [A/mm²]	14	7
Rotor type [-]	Delta-shaped	Surface-mounted
Outer diameter rotor [mm]	130	103.4
Air gap [mm]	1	0.5
Active axial length [mm]	151	120

Similar to the analysis made in Chapter II, upscaling and downscaling cases of torque scaling factors of 2 and 0.5 respectively, are considered in this comparison. The same axial and radial scaling, as indicated in Table 7 and Table 8 of Chapter II, are used to scale the second reference machine. By consulting Fig. 121, and Fig. 122, the same observations drawn in Section 3.3.1 and Section 3.3.2 of Chapter II can be made for the scaling cases using a second machine as a reference. Notably, the significant disparity in efficiency between linear scaling and geometric scaling laws is observed in regions characterized by low-speed and high torque values. As the speed increases, the efficiency disparity decreases.
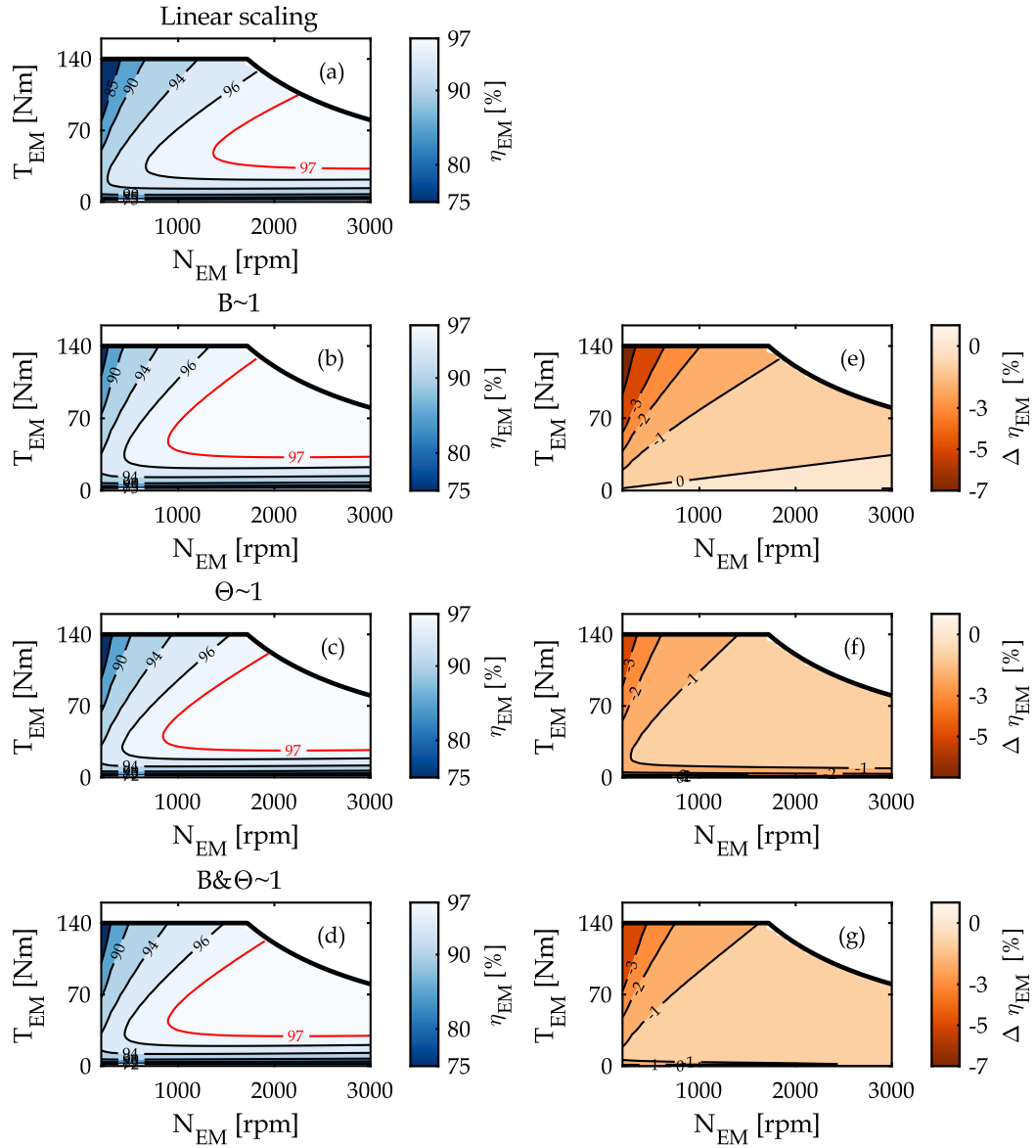
Fig. 121: Efficiency maps η_{EM} in [%] in the torque-speed plane using linear and geometric scaling laws for an upscaling case with a torque scaling factor of 2. The second column figures represent the efficiency difference Δ_η in [%] between linear and each choice of geometric scaling laws. Negative values for Δ_η mean that linear scaling underestimates the efficiency as compared to geometric scaling and vice versa.
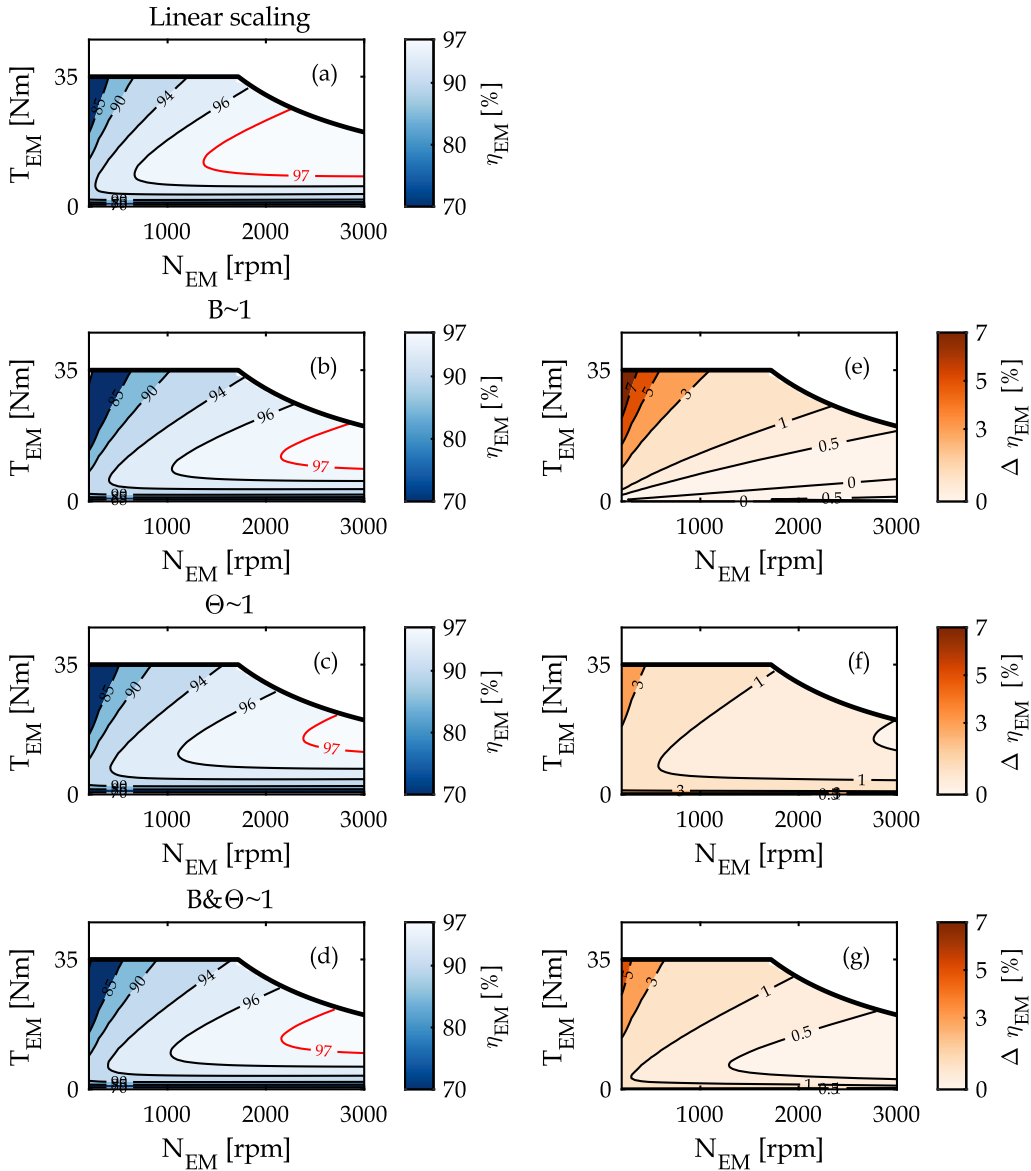
Fig. 122: Efficiency maps η_{EM} in [%] in the torque-speed plane using linear and geometric scaling laws for an upscaling case with a torque scaling factor of 0.5. The second column figures represent the efficiency difference Δ_η in [%] between linear and each choice of geometric scaling laws. Positive values for Δ_η mean that linear scaling overestimates the efficiency as compared to geometric scaling and vice versa.

Additionally, to generalize the conditions that result in linear scaling, the examination of the equivalent resistance ΔR is conducted in Fig. 123. From this figure, it can be seen that exists an intersection between the contour line indicating a value of 0 of ΔR and the torque scaling factors contour. This reveals the existence of a combination of axial and radial scaling factors that result in a linear losses-to-power scaling case, applicable to the second reference machine. It is worth noting that, the last statement holds solely for upscaling cases and does not apply to downscaling cases. The feasibility of these geometric scaling factors can be assessed following the approach outlined in Chapter II, as previously detailed for the first reference machine.
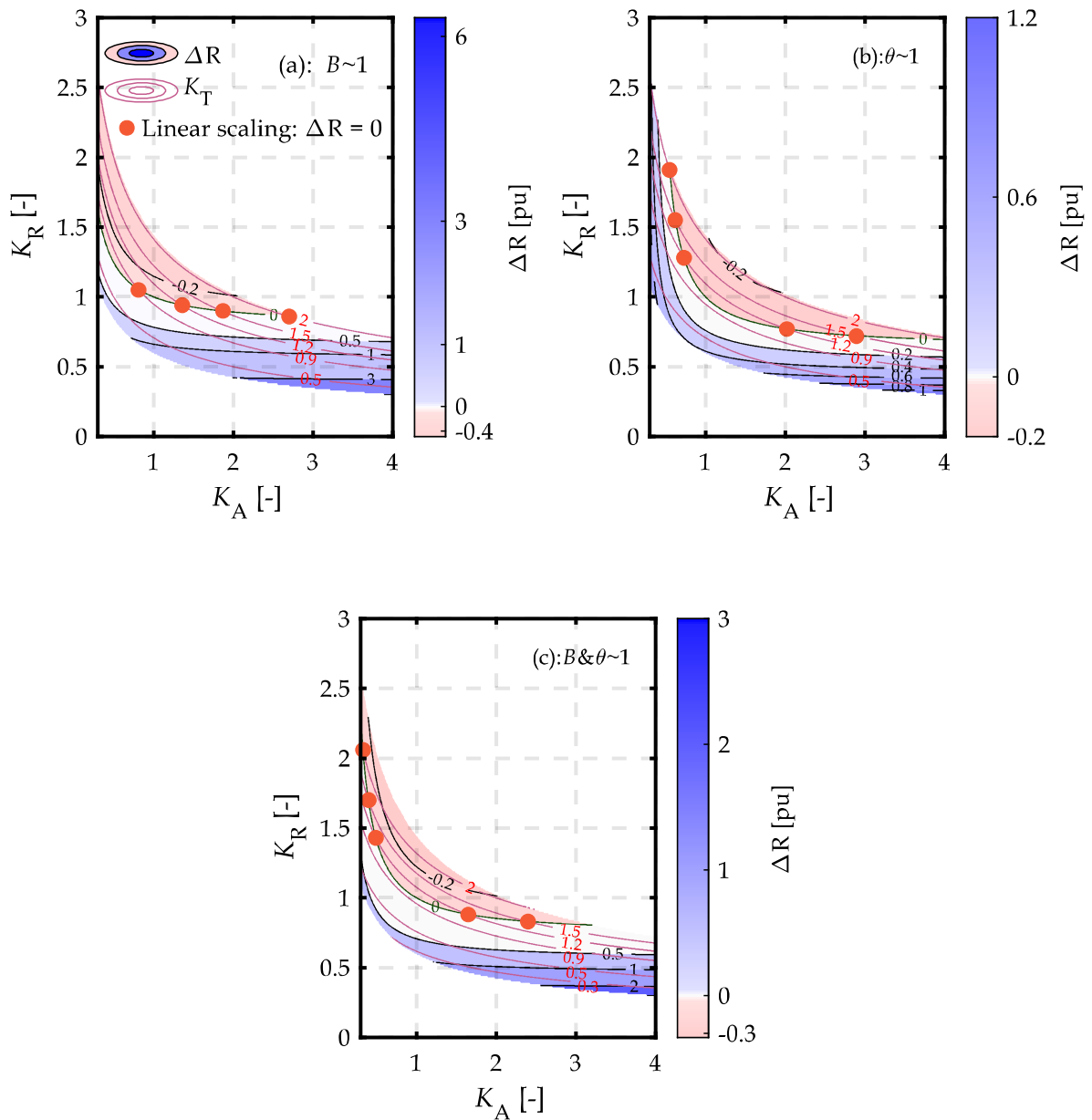
Fig. 123: Equivalent resistance term ΔR (black contour lines) in per-unit and torque scaling factor K_T [-] (purple contour lines) as a function of axial K_A and radial K_R scaling factors.

5   Theoretical background sizing of voltage source inverters

The sizing of the semiconductor components of the inverters depends on the following criteria: voltage rating, current rating, and switching frequency. These letter needs to be defined per the specifications of the electric machines.

Regarding the voltage range, the switches, i.e., transistors and the diodes, are conceived to withstand a specific voltage at their terminals. To cover various applications, manufacturers typically offer different voltage ranges in discrete values, including examples at 300V, 600V, 1200V, and 1800V. The selection of the voltage range of the switches, namely the collector-

emitter voltage v_{CE}, depends on the voltage rating of the DC source V_{DC}. Broadly speaking, a safety margin is recommended when selecting the voltage range to account for overvoltages, that can occur during the turning-off states, caused by the stray inductance of circuitry. Defining the safety factor SF for the voltage range does not follow specific rules and is typically based on experience, as evidenced by the varying values mentioned in literature, such as 1.5 as described in [250], and 2 in [231]

$$v_{CE} \geq SF \, v_{DC} \tag{195}$$

The switching frequency f_{sw} can be defined based on the maximal electric frequency f_{elec_max} of the electric machine and the sampling requirements to ensure satisfactory signal quality. The Nyquist-Shannon sampling theorem states that the sampling frequency must be at least twice the signal frequency. In automotive applications, a factor of 10 is often considered because of the risk of audible noise from the electric drive system [250]. Typical switching frequencies for IGBT-based inverters usually do not exceed 10 kHz for IGBT-based inverters.

$$f_{sw} \geq 10 \, f_{elec\_max} \tag{196}$$

Regarding the current rating, the nominal rated current of the collector I_{cn} should be at least equal to the maximum peak current of the electric machine $\widehat{I}_s$, as indicated in (197). Another sizing criterion to consider in determining the maximal current is the ability to withstand the short circuit current of the electric machine at high-speed values in fault operations [231]. In this case scenario, the VSI is short-circuited to preserve the battery. Furthermore, the maximal current depends on the junction temperature of the switches, which can vary depending on the different heat sinks or cooling technologies [231]. By utilizing a thermal model combined with loss models, proper sizing of the inverter can be achieved to ensure that it does not reach its temperature limit under extreme operating conditions and short-term power requirements.

$$I_{cn} \geq \widehat{I}_s \tag{197}$$

Appendix V: Additional details on the experimental campaign

This appendix provides further insights into the experimental campaign presented in Chapter III. This section is organized as follows. A gear nomenclature is presented in Section 1. Section 2 provides additional information on the steps followed in the experimental procedure, alongside a detailed overview of the measured points of each gearbox. The measurement consistency and the impact of control imperfection on efficiency are assessed in Section 3. Further elaboration on the measurement uncertainty is provided in Section 4. In Section 5, the measurement reproducibility is presented. Lastly, the impact of the tested temperature of the gearbox is assessed in Section 6.

1 Gear nomenclature

Fig. 124, Fig. 125, and Fig. 126 provide visual illustrations of the geometric parameters mentioned in the presented power loss model in Section 2 of Chapter III.
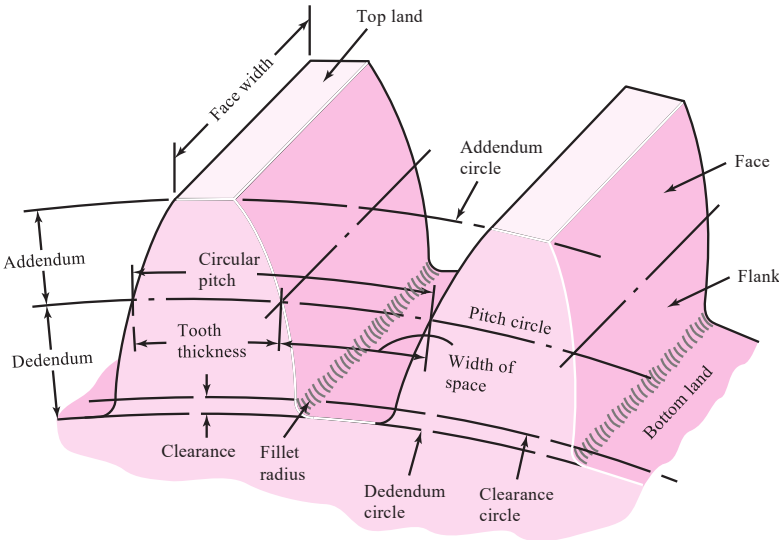

Fig. 124: Nomenclature of a-gear teeth [251]

Fig. 125: An involute helicoid [251]
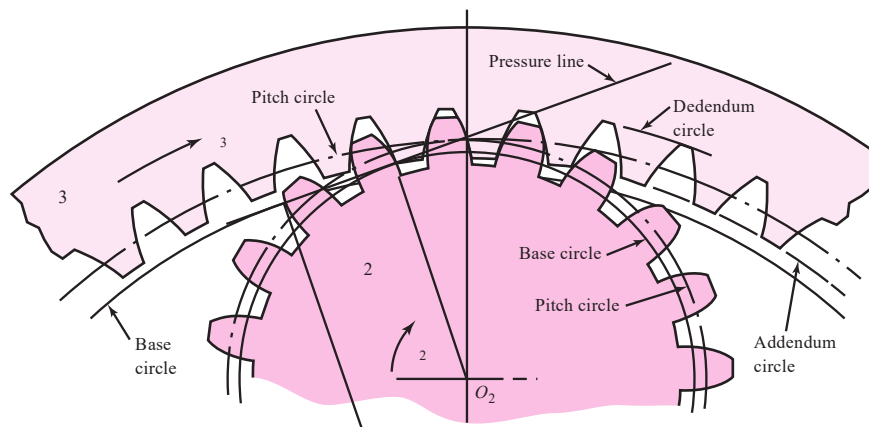
Fig. 126: Internal gear and pinion tooth action [251]

2 Procedures and tested points for each gearbox

The measurement procedure is depicted in Fig. 127. The procedure involves two main phases for each gearbox: the running-in cycle and the measurement-capturing phase. Note that the temperature of the gearbox is adjusted by changing the operating points as illustrated in the flowchart. This approach is employed due to the unavailability of an external cooling system. The tested operating points for each gearbox and load and unloaded tests are illustrated in Fig. 128.

Fig. 127: Measurement procedure

Fig. 128: An overview of the tested points for each gearbox during loaded (a)-(e) and unloaded tests (f). At the top of each subfigure (a)-(e), the total number of measured points of loaded tests is indicated. The number of measured torque points is specified for each measured speed. Lastly, the abbreviation "GB" in (f) refers to the term "gearbox".
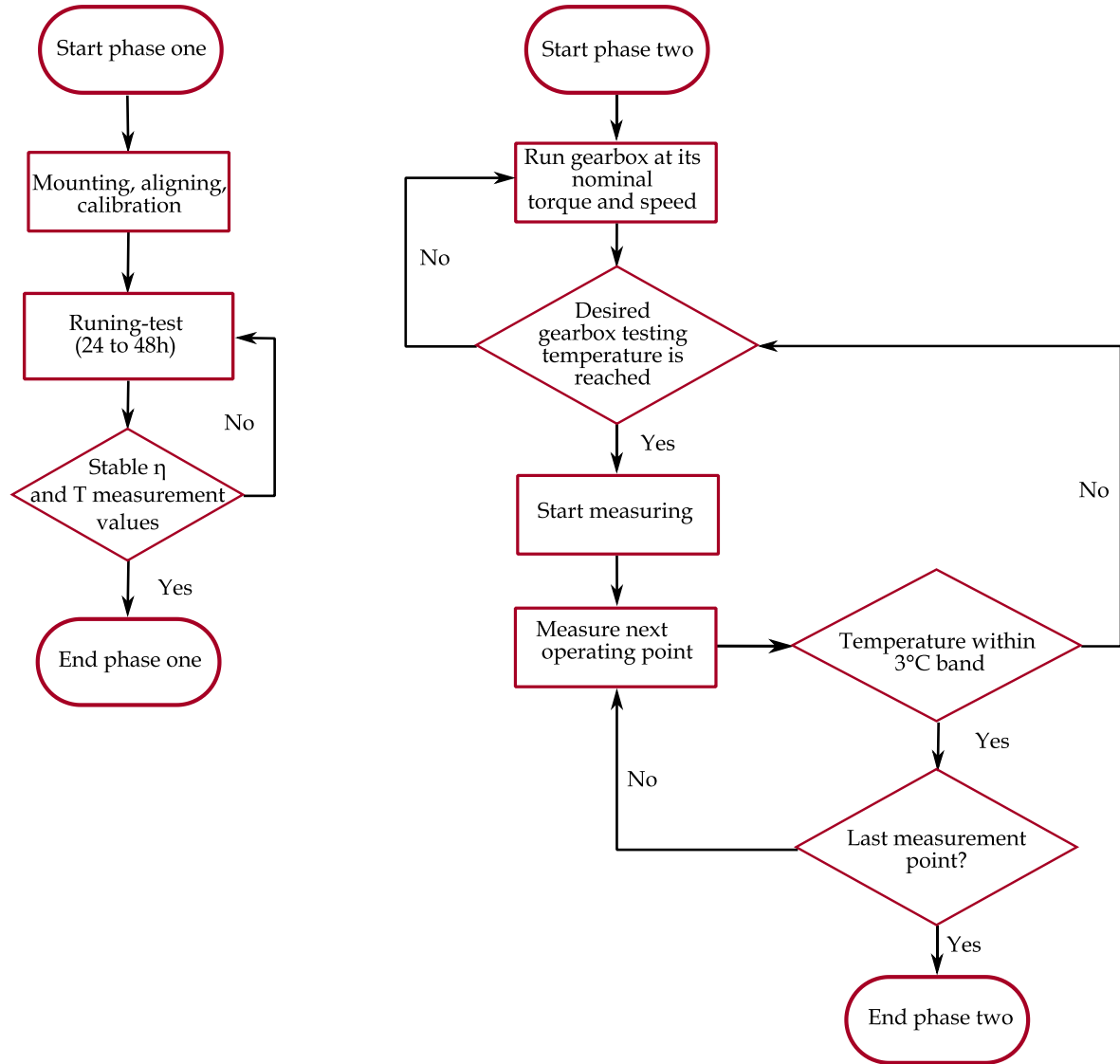
3 Measurement consistency- influence of speed and torque variations on efficiency measurement

An evaluation is herein conducted to determine the level of consistency in the measurement across some operating points. Due to a large number of tested points, the subsequent analysis is performed using representative operating points, encompassing high and low values of torque and speed. The Siemens drive machine (input side of the gearbox, see Fig. 57) is controlled in speed mode. Fig. 129 shows the speed consistency for different measured torque points combined, at low (1000 rpm), medium (5000 rpm), and high speed (14,000). As shown the speed, for different measured torque values, varies within a range of ± 0.2 rpm.
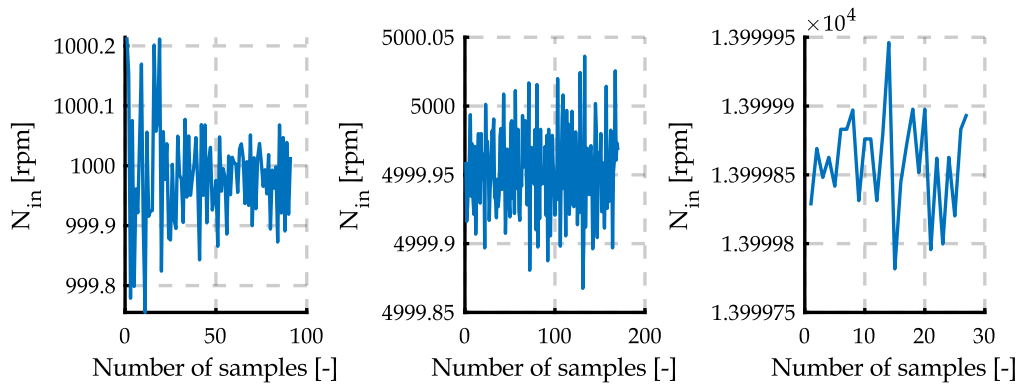

Fig. 129: Speed consistency for different measured torque points combined.

The WEG load motor (output side of the gearbox, see Fig. 57) is controlled in torque mode. Similarly, the consistency of torque is exemplified through illustrative cases of low and high torque values at both low and high-speed values as shown in Fig. 130. The output torque profile exhibits a fluctuation of 0.7 Nm at its maximum.

The impact of the control imperfection torque and speed on efficiency is assessed in Fig. 131 for the 2nd to the 5th gearbox, using randomly selected points for analysis. Note that the results for the first gearbox were presented in Chapter III. Broadly, the deviation from the average efficiency is not significant, except for the low speed and low torque region, where the deviation can reach up to 1%.
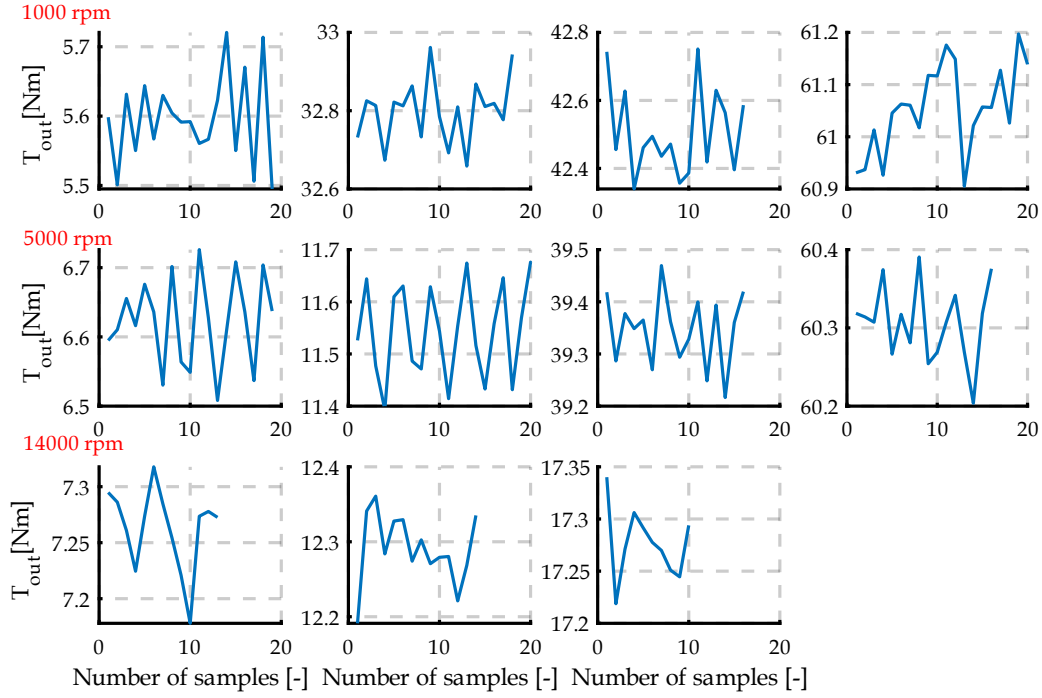
Fig. 130: Torque consistency for different measured speed operating points. The first row figures correspond to a speed value of 1000 rpm, the second row to 5000 rpm, and the last row to 14,000 rpm. This example uses measurements obtained from the loaded test of the fourth gearbox with a gear ratio of 7.

4 Measurement uncertainty due to the instrumentation

The measurement accuracy of the instrumentation was assessed following the methodology suggested by the HBK company [252]. This section provides an example to illustrate the calculation of the Absolute Fault (AF) in efficiency measurement. In this case, the torque at the sun equals 13.15 Nm, and at the carrier, a torque of 100.94 Nm is applied, and the speed of the sun equals 3000 rpm. The measured efficiency for these operating points is 95.95%.

Torque at the input side: For the torque sensor with a range of 20 Nm, the output range is 0 to 10 V. In this example, 13.15 Nm corresponds to 6.57 V. The analog signal is captured via the current channel in a voltage mode of the HBK power analyzer. The AF of the resolution converter is calculated following (198)-(201).

$$\text{DC reading error} = 0.02\% \text{ of reading} \pm 100 \ \mu V = 14.147 \ 10^{-4} \text{ V} \tag{198}$$

$$\text{DC range error} = 0.005\% \text{ of reading} \pm 50 \ \mu V = 55 \ 10^{-3} \text{ V} \tag{199}$$

$$\text{AF (V)} = 0.7071(\text{DC reading error} + \text{DC range error}) = 22.9775 \ 10^{-5} \text{ V} \tag{200}$$

$$\text{AF (Nm)} = \text{AF (V) ratio} \left(\tfrac{\text{Nm}}{V}\right) = 15.9075 \ 10^{-4} \text{ Nm} \tag{201}$$
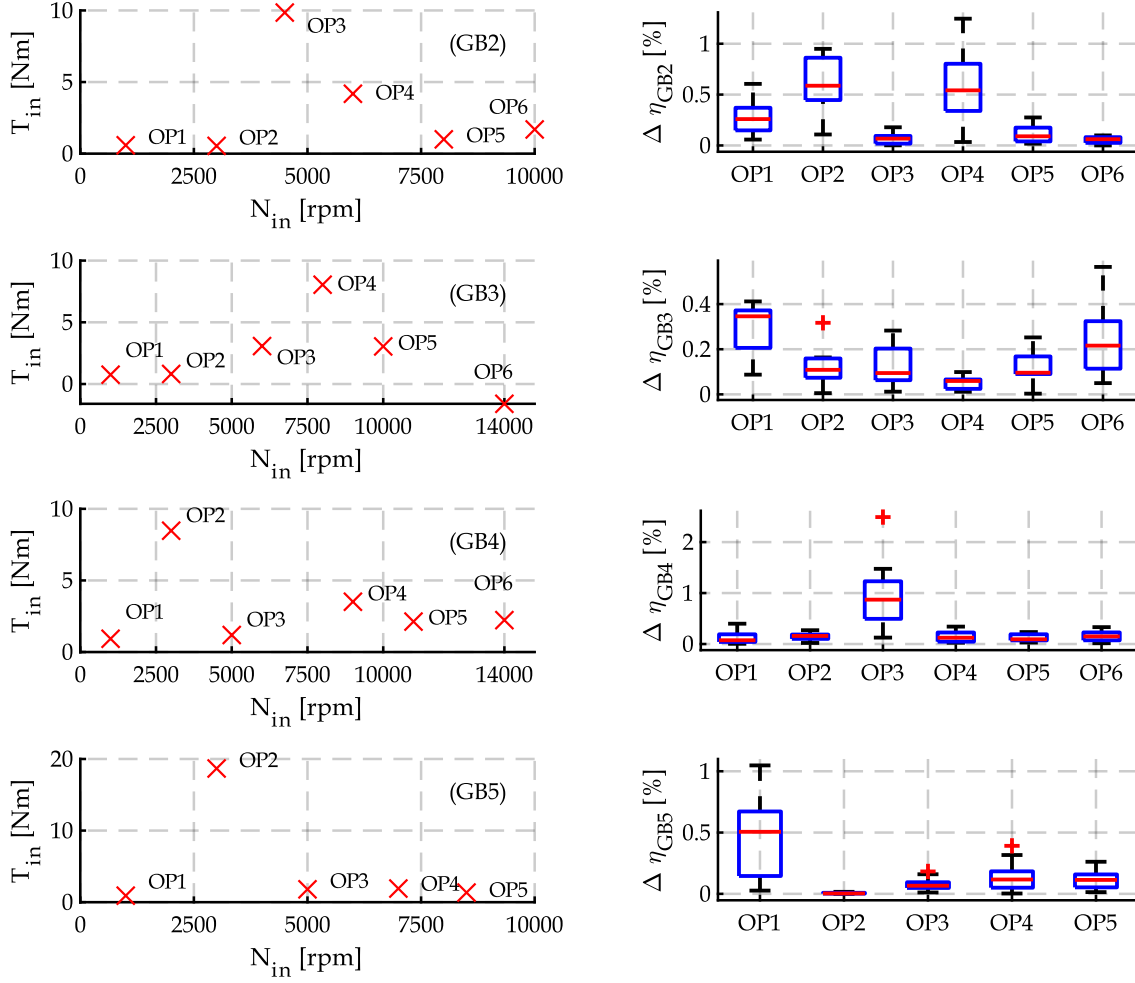
Fig. 131: Control imperfection impact on the efficiency of the tested gearboxes: the figures in the 1st column represent an example of the measured points, while the figure in the 2nd column represents the deviation from the averaged efficiency.

Torque at the output side: The fault on the resolution converter introduced by the timer inaccuracies can be calculated using the following example based on the HBK T40 torque sensor (202).

$$AF(\%) = 0.58 \text{ maximum inaccuracy (conversion for rectangular distribution)} \qquad (202)$$

in which the maximum inaccuracy is equal to 0.0008%. Considering a torque of 100.94 Nm, the AF of the reading is $4.684 \cdot 10^{-4}$ Nm.

Based on (98), (201), (202) and the absolute fault of the torque sensor mentioned in Table 15, it is possible to calculate the total relative fault RF_{tot} (203).

$$RF_{\text{tot}} = \sqrt{\left(\frac{0.02 + 15.9075 \ 10^{-4}}{13.15}\right)^2 + \left(\frac{0.2 + 4.684 10^{-4}}{100.94}\right)^2} = 0.258\% \qquad (203)$$

which yields a total fault AF_{tot} on the efficiency of

$$\text{AF}_{\text{tot}} = 0.258 \frac{95.95}{100} = 0.248\%$$

This methodology can be applied for the remainder of the operating points to benchmark the measurement uncertainty.

Speed uncertainty: When using the timer channels for measuring speed, the measurement uncertainty resulting from timer inaccuracies can be computed by (202). Based on the datasheet of the power analyzer, the maximum inaccuracy for a measurement time of 10 ms is 0.00071%. Considering a speed of 14,000 rpm, the AF of the speed reading is 0.057652 rpm.

Temperature sensitivity of the torque sensors: The temperature effect per 10 K in the nominal temperature range is summarized in Table 31. According to the HBK method, the temperature effect on the zero signal u_{TK0}, be calculated as given in (204). The temperature effect on the characteristic value u_{TKc} is calculated following (205).

$$u_{\text{TK0}} = 0.58 \, TK_0 \, T_{\text{nom}} \frac{\Delta \text{T}}{10K} \tag{204}$$

$$u_{\text{TKc}} = 0.58 \, TK_c \, T_{\text{nom}} \frac{\Delta \text{T}}{10K} \tag{205}$$

where ΔT is the temperature variation as compared to the reference temperature. According to temperature sensor measurements from the conducted tests, the maximal value of ΔT was found to be 6°C.

Table 31: Temperature effect per 10 K in the nominal temperature range

	Lorenz DR2112	HBK T40B
Reference temperature	23	23
Temperature effect on zero signal TK_0 [%]	± 0.2	± 0.05
Temperature effect on the characteristic value TK_c [%]	± 0.1	± 0.05
Measurement uncertainty due to the temperature effect on the zero signal u_{TK0} [Nm]	0.0139	0.0348
Measurement uncertainty due to the temperature effect on the characteristic value u_{TKc} [Nm]	0.0069	0.0348

5 Measurement reproducibility

In this section, an example of measurement reproducibility is provided. Due to the number of tested specimens, it is decided to show one example for the third gearbox. This choice is motivated by the fact that this last gearbox shows a larger load-independent loss as compared to other gearboxes. Fig. 132 shows the difference in terms of efficiency between two different loaded tests. A difference of less than 1% is obtained across the tested operating points. Fig. 133 shows the load-independent losses obtained through three repeated tests. As

can be observed, the measurements are reproducible, which confirms the large contribution of the load-independent losses for the concerned gearbox.
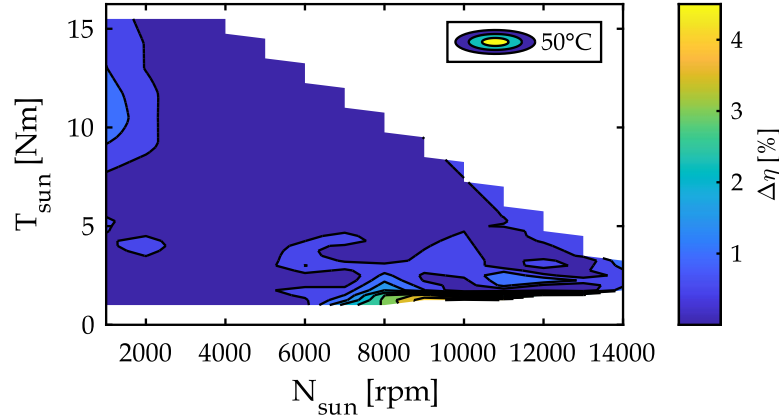

Fig. 132: Measurement reproducibility based on two loaded tests
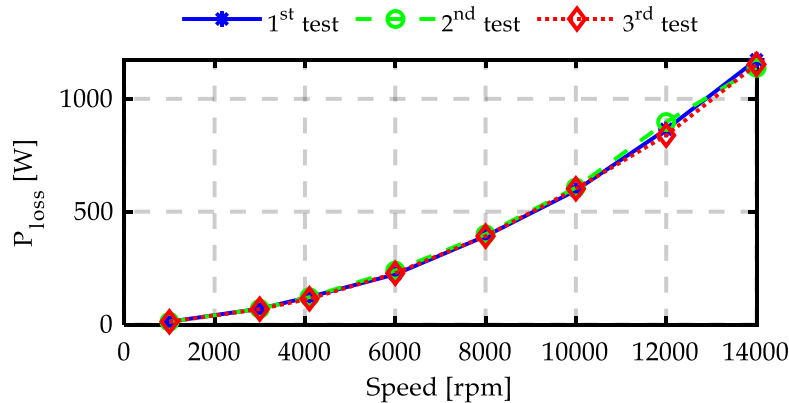
Fig. 133: Reproducibility of the load-independent loss measurements based on three tests.

6 Impact of the gearbox temperature on the efficiency and losses

In this section, an examination of the temperature of the gearbox is conducted for 30°C and 70°C in comparison to 50°C, as presented in Chapter III. In this context, Fig. 134 presents the difference in terms of efficiency and losses, donated $\Delta\eta$ and ΔP_{losses}, respectively. In this figure, the comparison results are shown for temperatures of 30°C and 50°C, considering 50°C as a reference. As can be consulted from the last aforementioned figure, the test results conducted at 50°C yielded better efficiency as compared to 30°C, as the sign of $\Delta\eta$ is positive in all the region of the maps. At high torque regions, $\Delta\eta$ is almost 1% for the studied gearboxes. The most remarkable result to emerge from the figure is that the efficiency discrepancy between the tested temperatures could be as high as 6% to 12% in high-speed regions, where load-

independent losses prevail. This is due to a significant loss difference ΔP_{losses} as shown in the second column figures of Fig. 134. For instance, an increase in temperature from 30° to 50° reduced the overall losses by approximately 300 W in high-speed regions in the case of the 3rd gearbox. Similarly, the same comparison has been conducted, considering temperatures of 50°C and 70°C, as depicted in Fig. 135. The opposite conclusion can be drawn when considering the case using 30°C.

Fig. 134: Comparison between efficiency and loss results between temperatures of 30°C and 50°C. The results from the test using 50°C are considered as a reference. Positive values of the difference in terms of efficiency mean that the test using 50°C resulted in better efficiency results. Each row in the figure corresponds to a specific gearbox.
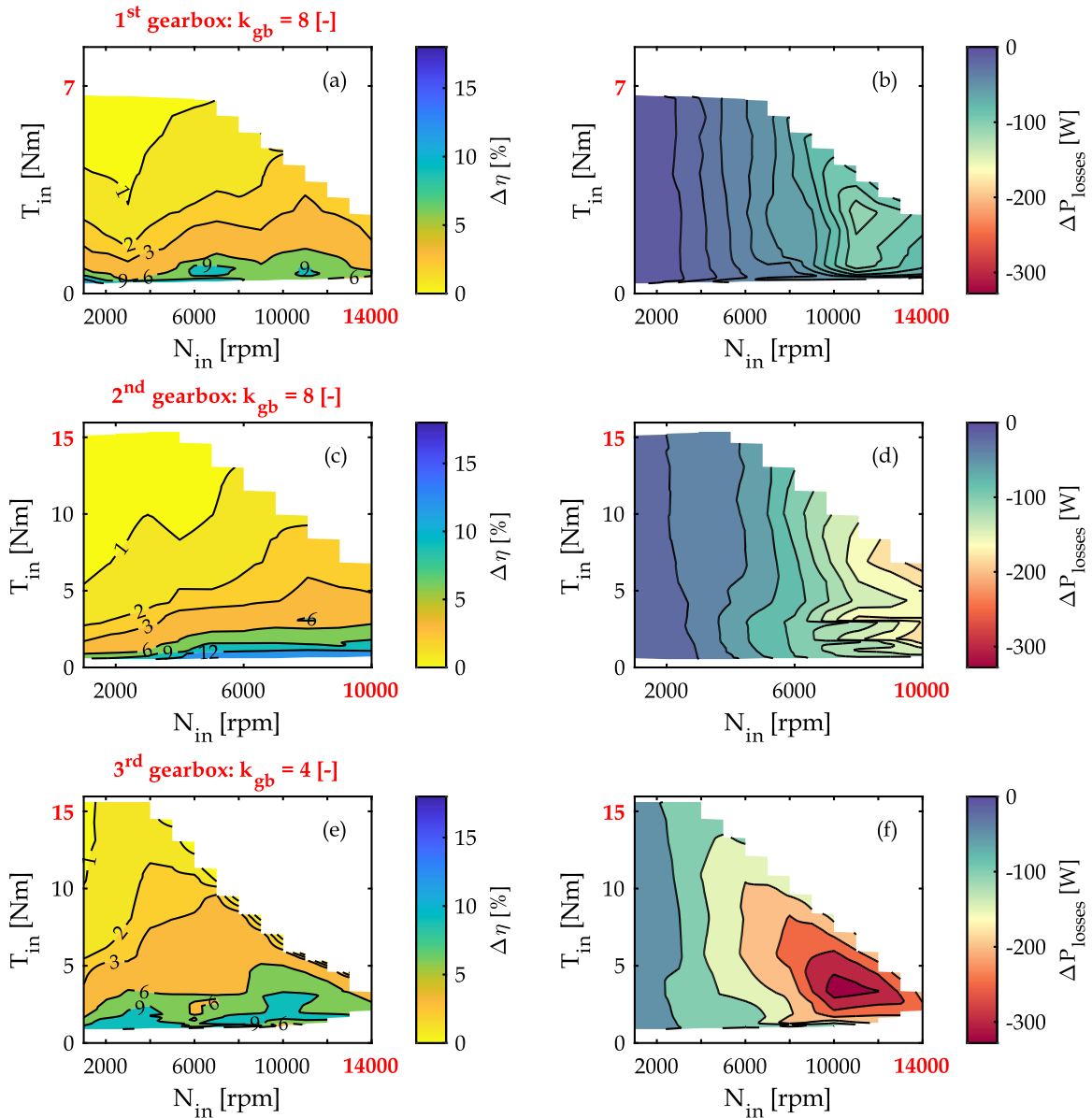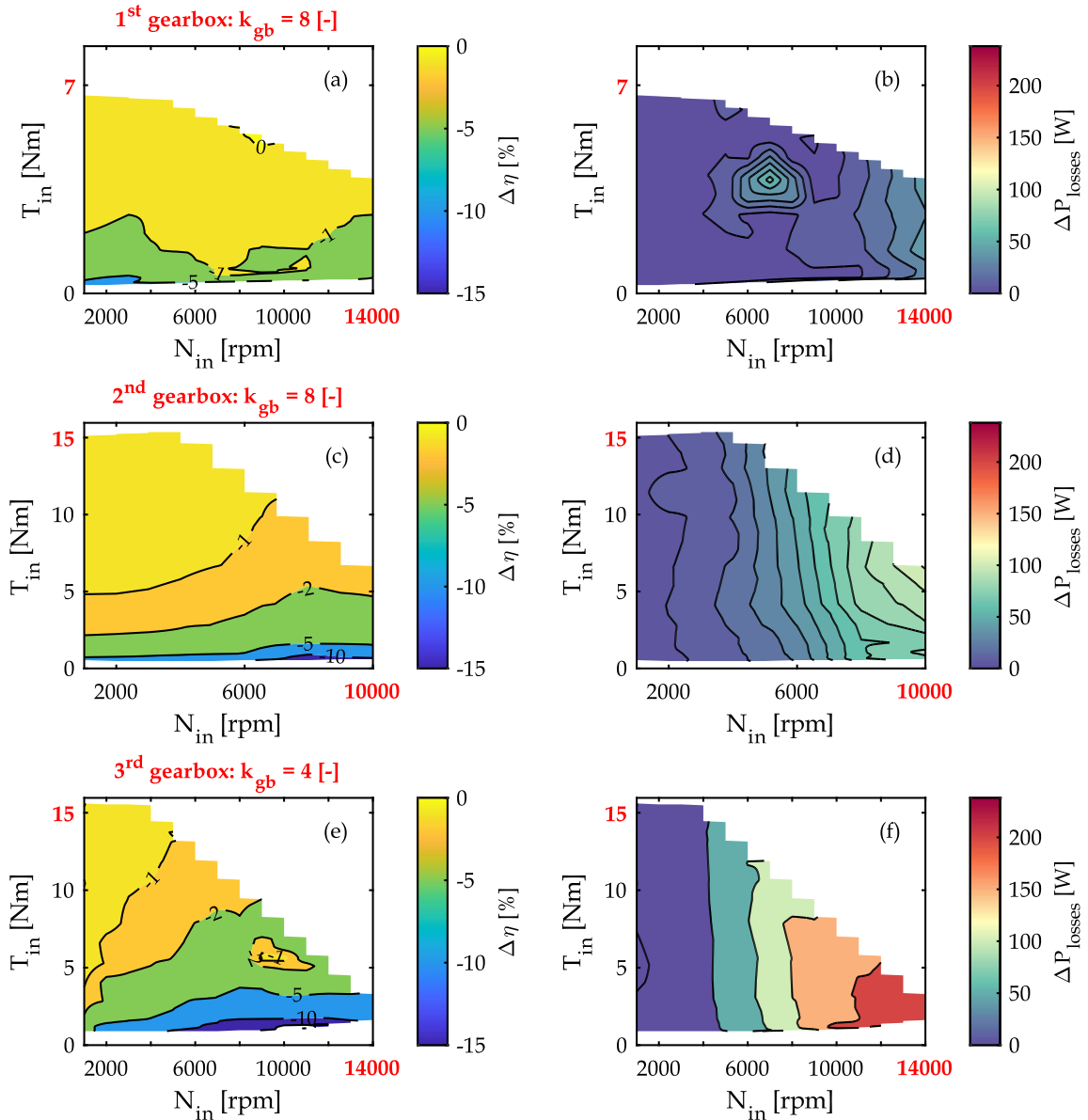
Fig. 135: Comparison between efficiency and loss results between temperatures of 30°C and 70°C. The results from the test using 50°C are considered as a reference. Negative values of the difference in terms of efficiency mean that the test using 50°C resulted in lower efficiency results. Each row in the figure corresponds to a specific gearbox.

To explain the large difference at high-speed regions, the impact of the temperature on load-independent losses is examined in Fig. 136. As can be consulted in the last figure, an increase in the oil temperature results in a decrease in the load-independent losses. This is in alignment with the results reported in [205], providing additional insights on the temperature impact at high-speed values. Interestingly, Fig. 136. b, d, and f reveal that the difference between the test conducted at 30°C and 50°C, is more significant than the difference between the test conducted at 30°C and 50°C. For instance, the three selected gearboxes exhibit a power loss reduction of about 50% at 50°C as compared to the test performed at 30°C. On the other hand, the power loss reduction is less significant when increasing the temperature from 50°C to 70°C. This is attributed to the viscosity of the oil, whose evolution with temperature is illustrated in Fig. 137. Note the presented values of viscosity are the average of three measurements

carried out using a kinematic viscometer (model reference: SVM 3001) at the Department of Green Chemistry and Technology of Ghent University. As evident by the latter figure, the viscosity drop from 30°C and 50°C is more important than from 50°C to 70°C. Therefore, this explains the large loss difference between the test conducted at 30°C and 50°C.
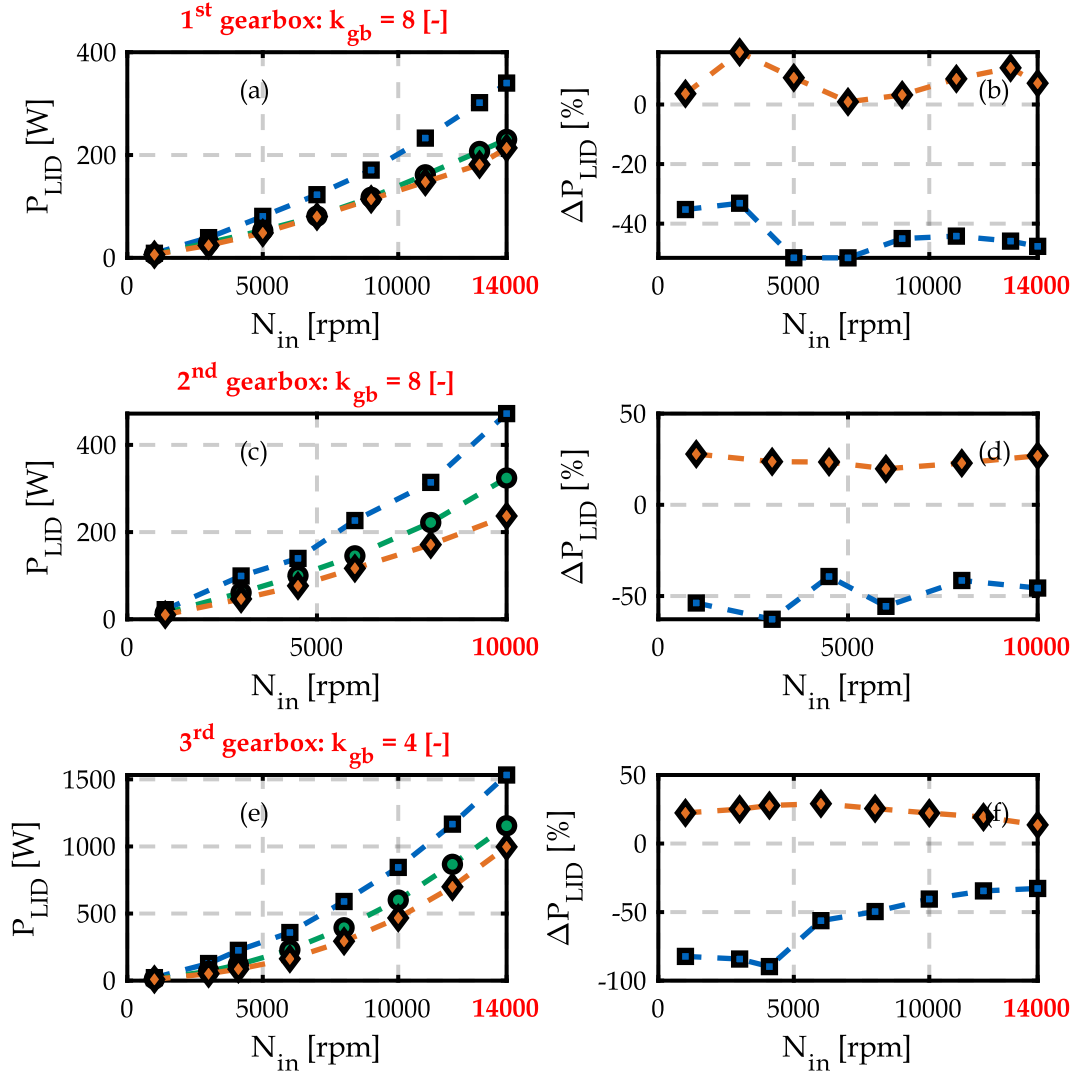
Fig. 136: Temperature impact of load-independent losses. In figures (a), (c), and (e), the 30°C temperature is represented by the blue curves, the 50°C temperature is described by the green curves, and the results for 70°C are illustrated by the orange curves. In figures (b), (d), and (f), the blues curves depict the difference between the conducted tests considering 30°C and 50°C. The orange curves represent the difference between the conducted tests considering 50°C and 70°C
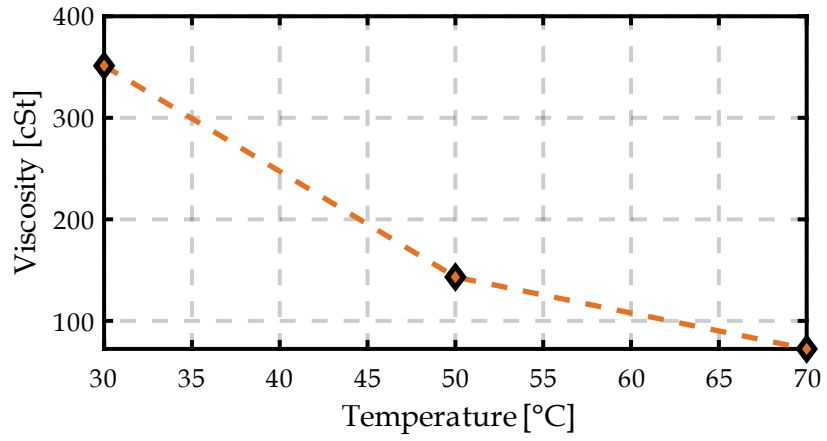
Fig. 137: Measured viscosity of the oil as a function of the tested temperature

Appendix VI: Complement to Chapter IV

This appendix presents additional details to complement some of the sections presented in Chapter IV. The appendix is structured as follows. Section 1 presents the speed profiles of the investigated driving cycles. The modeling and control details of the voltage source inverter and its associated representation using the Energetic Macroscopic Representation (EMR) are discussed in Section 2. Section 3 is dedicated to performing a sensitivity analysis on the effect of scaling laws of electric drive systems on energy consumption. Section 4 expands the analysis regarding the impact of the scaling choices on the energy consumption to modular power-trains.

1 Driving cycles

Fig. 138 depicts the speed profiles of the driving cycles used for the investigation of the passenger cars, whereas Fig. 139 presents the driving cycles employed for the truck.
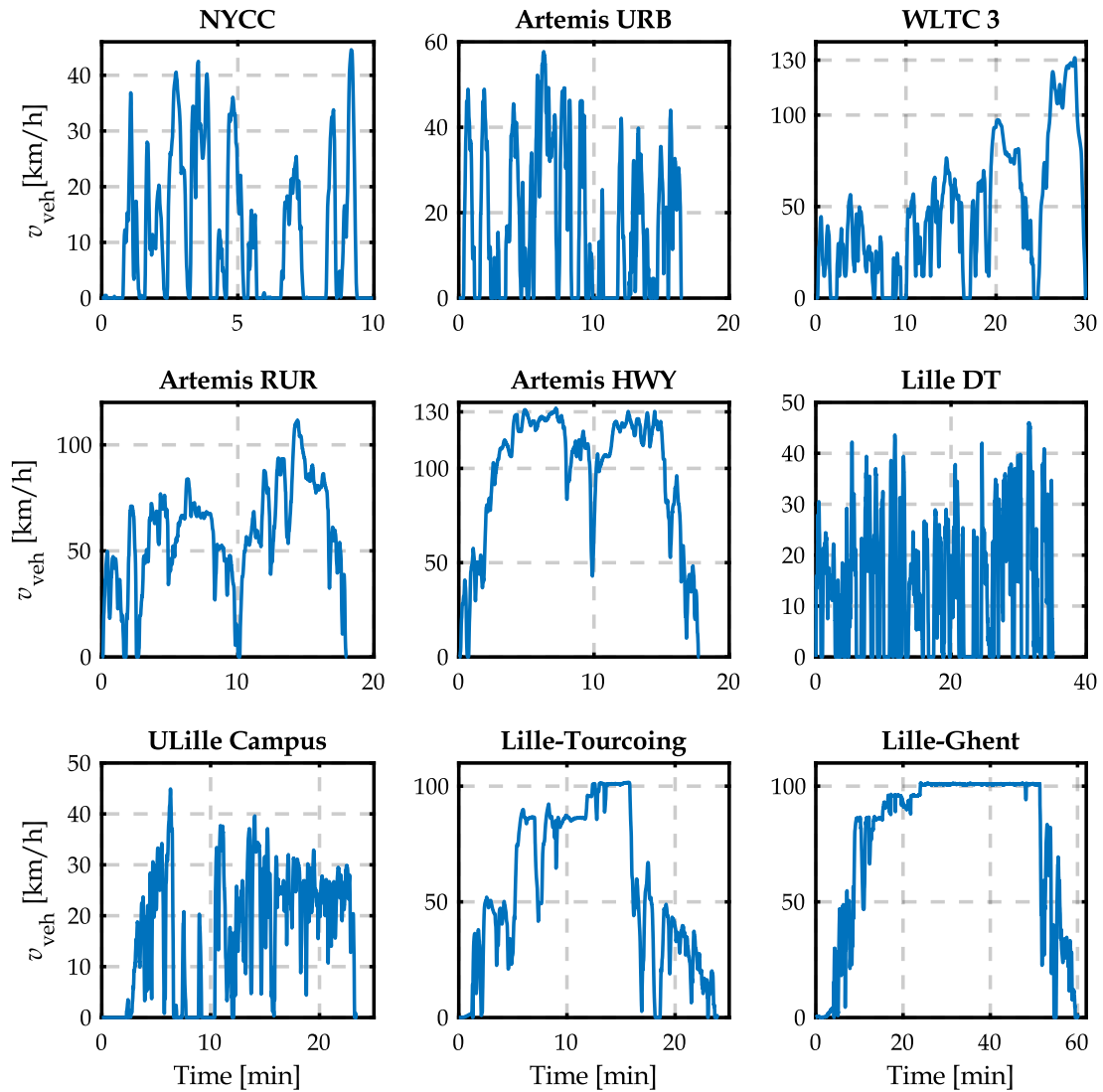
Fig. 138: Vehicle speed [km/h] as a function of time [min] for the selected driving cycles for the compact and mini-compact cars.
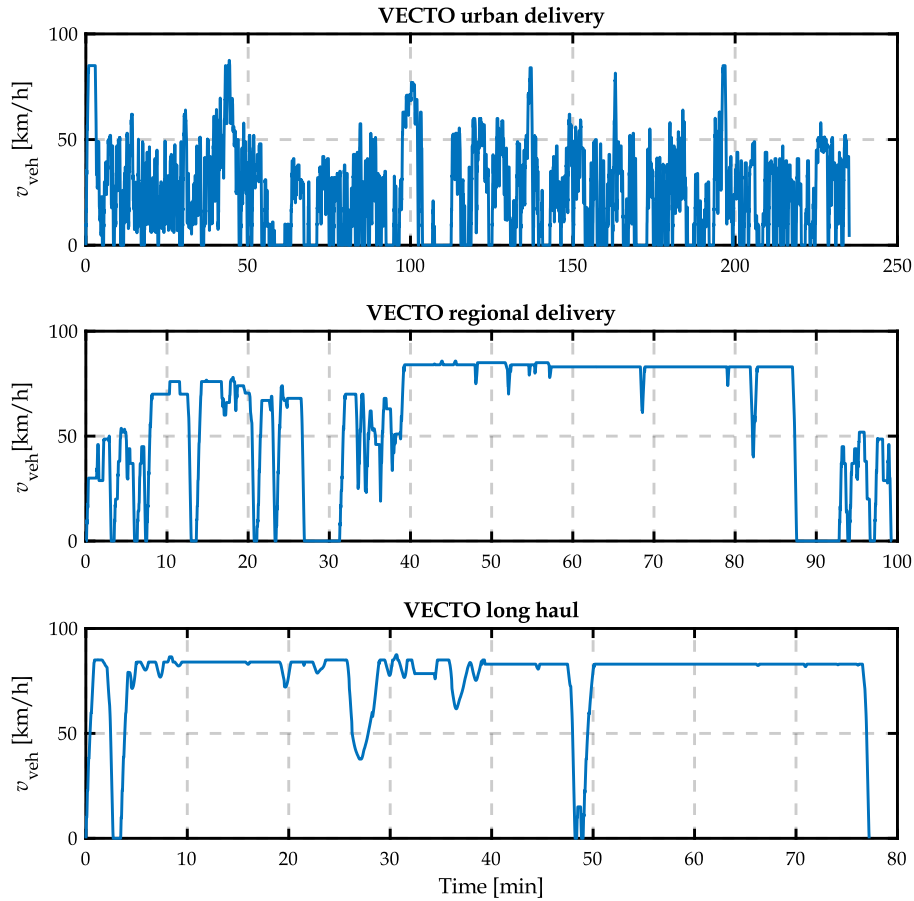
Fig. 139: Speed [km/h] as a function of time [min] of the selected driving cycles for truck.

Table 32 presents a nomenclature of the studied driving.

Table 32: Driving cycles Nomenclature

Acronym	Cycle name
Artemis	Assessment and Reliability of Transport Emission Models and Inventory Systems
NYCC	EPA New York City Cycle
WLTC	European Worldwide Harmonised Light Vehicles Test Procedure
VECTO	Vehicle Energy Consumption calculation TOol

2 Modeling and control of voltage-source inverter

A structural scheme of the three-voltage source inverter is shown in Fig. 140. Point M is defined as a reference voltage potential of the inverter, while N serves as a fictitious neutral point of the AC load. A switching function, denoted as s_{ij}, is associated with each power switch (206). This switching function assumes an ideal switching, i.e. it takes on the value 1 when the switch is in the closed state and 0 when the switch is open. Due to the ideal power switches assumption, it follows that the switches of the same leg are in complementary states (207). Therefore, only one switching function of a leg needs to be defined.

217

$$s_{ij} \in \{0,1\} \tag{206}$$

in which i refers to the leg number of the inverter $\in \{1,2,3\}$, and j denotes the number of the switch number within a given leg $\in \{1,2\}$.

$$s_{i1} + s_{i2} = 1 \; \forall \; i \in \{1,2,3\} \tag{207}$$
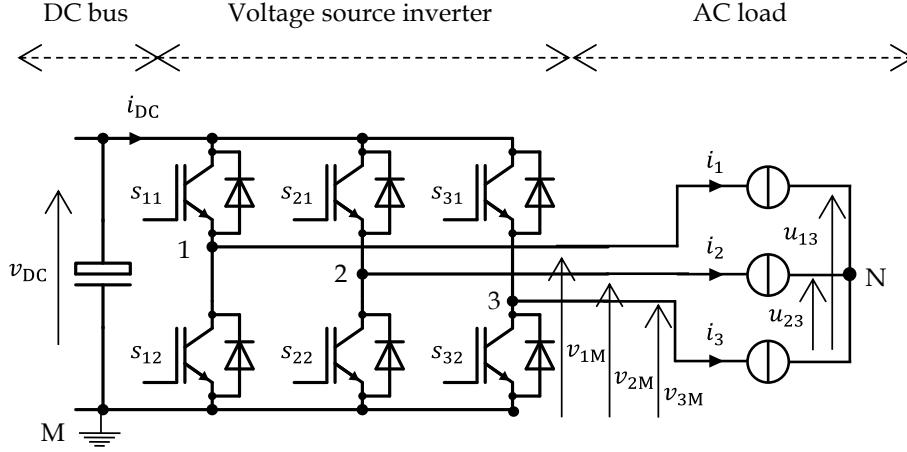
Fig. 140: Structural scheme of three-phase voltage source inverter

The analysis of the inverter structure reveals a coupling between the legs of the inverter. The equations related to this coupling are described by equations (208)-(212). As the neutral point of the load (N in Fig. 140) is often challenging to assess, the modeling and control approach relies on the use of phase-to-phase voltages.

$$\begin{cases} v_{\mathrm{DC}} & = \quad\quad \text{common} \\ i_{\mathrm{DC}} & = \quad i_{\mathrm{DC},1} + i_{\mathrm{DC},2} + i_{\mathrm{DC},3} \end{cases} \tag{208}$$

$$\begin{cases} v_{1\mathrm{M}} & = \quad s_{11} v_{\mathrm{DC}} \\ i_{\mathrm{DC},1} & = \quad s_{11} i_1 \end{cases} \tag{209}$$

$$\begin{cases} v_{2\mathrm{M}} & = \quad s_{21} v_{\mathrm{DC}} \\ i_{\mathrm{DC},2} & = \quad s_{21} i_2 \end{cases} \tag{210}$$

$$\begin{cases} v_{3\mathrm{M}} & = \quad s_{31} v_{DC} \\ i_{DC,3} & = \quad s_{31} i_3 \end{cases} \tag{211}$$

$$\begin{cases} \underline{u}_{13,23} & = \begin{bmatrix} u_{13} \\ u_{23} \end{bmatrix} = [K_{\mathrm{vu}}] \begin{bmatrix} v_{1\mathrm{M}} \\ v_{2\mathrm{M}} \\ v_{3\mathrm{M}} \end{bmatrix} \\ \\ \underline{i}_{1,2,3} & = \begin{bmatrix} i_1 \\ i_2 \\ i_3 \end{bmatrix} = [K_{\mathrm{ii},2}] \begin{bmatrix} i_1 \\ i_2 \end{bmatrix} \end{cases} \tag{212}$$

Thereupon, $[K_{\mathrm{vu}}]$ is a transform matrix from single phases to phase-to-phase voltages, and $[K_{\mathrm{ii},2}]$ is a transform matrix from two currents to three currents (213). Note that the load is assumed to be balanced.

$$\begin{cases} [K_{\mathrm{vu}}] & = \begin{bmatrix} 1 & 0 & -1 \\ 0 & 1 & -1 \end{bmatrix} \\ \\ [K_{\mathrm{ii},2}] & = \begin{bmatrix} 1 & 0 \\ 0 & 1 \\ -1 & -1 \end{bmatrix} \end{cases} \tag{213}$$

The modeling equations of the inverter can be represented by the Energetic Macroscopic Representation (EMR), as shown in Fig. 141.
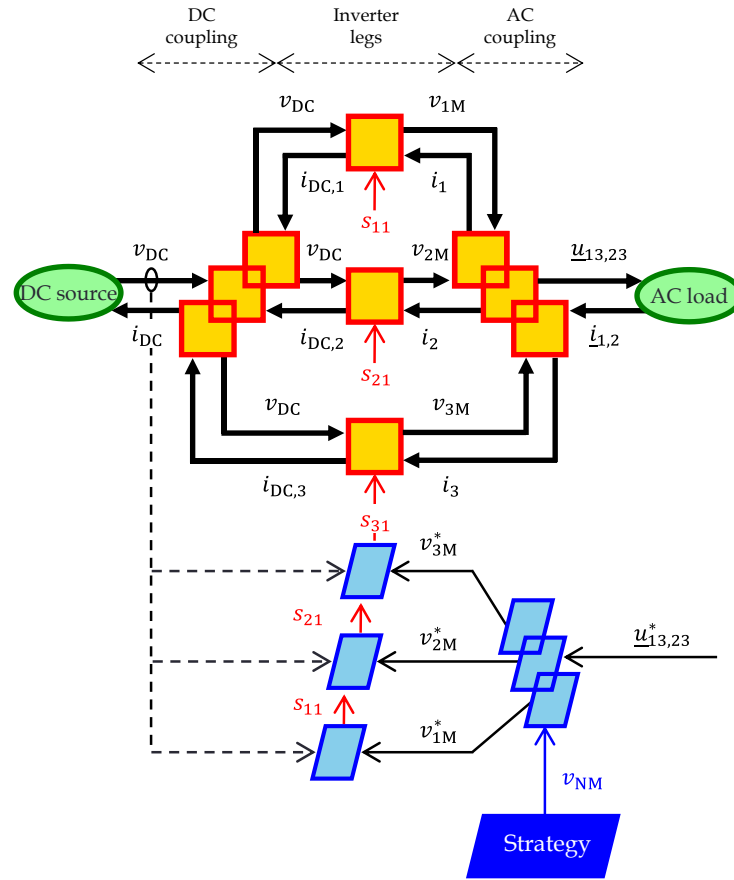
Fig. 141: EMR of a voltage-source inverter

From a control perspective, the specifications require the control of the phase-to-phase voltages, u_{13}, and u_{23}, of the AC load. These latter can be controlled using the three switching functions s_{i1}. The inversion rules of the EMR reveal the need to invert the coupling element at the AC side. For this aim, a distribution criterion using the zero-sequence voltage v_{MN} is introduced to efficiently distribute power across the legs of the inverter. The inversion of the AC coupling is carried out using (214).

$$\begin{cases} \underline{v}_{123,N} = \begin{bmatrix} v_{1N} \\ v_{2N} \\ v_{3N} \end{bmatrix} = [K_{uv}] \begin{bmatrix} u_{13} \\ u_{23} \end{bmatrix} \\ \underline{v}_{123,M} = \begin{bmatrix} v_{1M} \\ v_{2M} \\ v_{3M} \end{bmatrix} = \underline{v}_{123,N} + v_{NM} \end{cases} \tag{214}$$

in which $[K_{uv}]$ is a transform matrix from phase-to-phase to phase voltages, which can be expressed as follows:

$$[K_{uv}] = \frac{1}{3} \begin{bmatrix} 2 & -1 \\ -1 & 2 \\ -1 & -1 \end{bmatrix} \tag{215}$$

Thereafter, the switching function s_{i1} can be defined as given in (216).

$$\underline{s}_{i1} = \frac{\underline{v}_{123,\mathrm{M}}}{v_{\mathrm{DC}}} \tag{216}$$

The definition of the voltage v_{MN} depends on the defined Pulse Width Modulation (PWM) technique. In Chapter IV, a sinusoidal pulse width modulation technique is employed. This choice consists in mandating the voltage v_{NM} to be zero (217). Consequently, the phase voltages of the AC load $\underline{v}_{123,\mathrm{N}}$, referenced to point N, are equal to the phase voltages of the inverter legs $\underline{v}_{123,\mathrm{M}}$ referenced to the point M (218).

$$v_{\mathrm{NM}} = 0 \tag{217}$$

$$\underline{v}_{123,\mathrm{N}} = \underline{v}_{123,\mathrm{M}} \tag{218}$$

Therefore, the EMR shown in Fig. 141, can be amended as depicted in Fig. 142.a, incorporating the phase voltages $\underline{v}_{123,\mathrm{N}}$. This latter can be further simplified, resulting in the representation described in Fig. 142.b, as has been presented in Chapter IV.
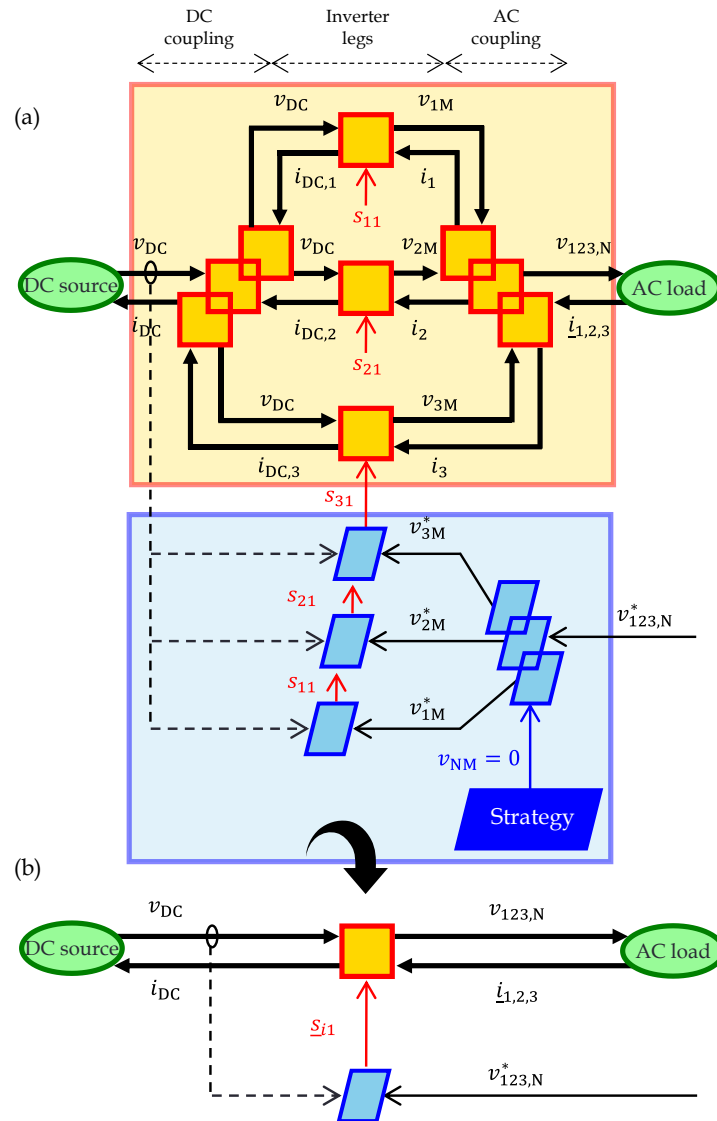

Fig. 142: EMR and control of voltage source inverter: (a) amended representation using phase voltages of the load considering a control strategy mandating v_{MN} to 0, (b): simplified representation.

3 Effect of the scaling choices of electric drive on energy consumption

A sensitivity analysis is herein conducted for the EDS. To this end, the assessment effect of scaling methods on energy consumption is expanded to encompass the voltage-source inverter, as compared to what is carried out in Section 4.1 of Chapter IV for the electric machine. The following analysis entails comparing the energy consumption using the linear scaling method for the Electric Drive System (EDS) against geometric scaling laws combined with the efficiency benchmarking of commercialized inverters as shown in Fig. 143. Because of the high number of case studies that can result from the geometric scaling laws of PMSM, the following analysis is conducted using exclusively the choice $B\sim1$ to provide an illustrative case. This decision does not compromise the generalization of the outcomes of this comparison when applying the remaining geometric scaling choices for the PMSM. This is because of the established understanding of the variation trends of the PMSM scaling presented in Section 4.1 of Chapter IV. Furthermore, the scaling cases pertaining to the compact car, i.e. case ①, and case ②, are hereinafter solely considered. For this sensitivity analysis, the inverters presented in Section 4.2 of Chapter II are employed. The FS800R07A2E3 inverter is used for case ① (upscaling), whereas the inverter denoted as FS400R07A1E3 is employed for the downscaling case ② (downscaling). These inverters are selected as they suit the power ratings of the scaled machines.
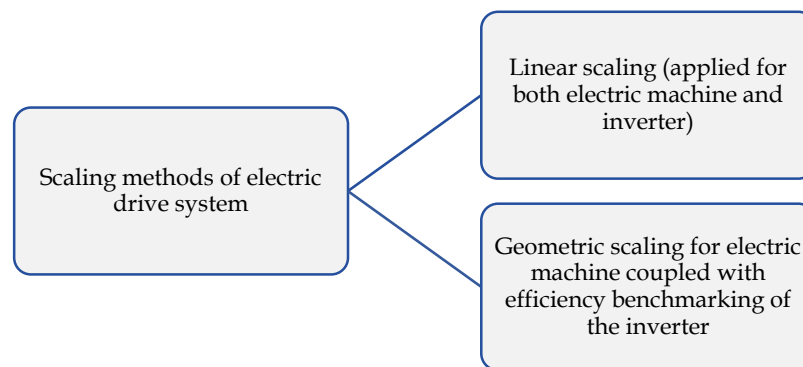
Fig. 143: Scaling methods applied for the sensitivity analysis

In Fig. 144.a, the difference in energy consumption ΔE_{bat} is presented for the scaling case ①. This is established using two exemplars of normalized and on-road urban and highway driving cycles. The figure shows the same difference trend as observed for the PMSM scaling. The sign of ΔE_{bat} is consistently positive, meaning that linear scaling overestimates the energy consumption as compared to the second scaling method of the electric drive. In comparison with the outcomes of the scaling of only PMSM, it is apparent that the maximal value of ΔE_{bat} is greater when applying linear scaling for the electric drive system. For instance, a difference of 3.2% is attained as compared to 1.8% (linear scaling is solely applied to the PMSM) for the NYCC. The explanation behind this is that linear scaling underestimates the efficiency of the inverter by about 0.5% as compared to the efficiency benchmarking, specifically in regions characterized by low torque and low-speed values (R1 in Fig. 105 of Chapter IV), as demonstrated in Fig. 48.f in Chapter II. This region experiences frequent use, which provides an

understanding of the slight increase in ΔE_{bat} when applying linear scaling to the EDS. Conversly, this trend is not noticeable for the highway driving cycles. This is because linear scaling and the efficiency benchmarking yield approximatively the same efficiency in regions characterized by high-speed values (R2 in Fig. 105 of Chapter IV), as shown in Fig. 48.f in Chapter II.

By consulting Fig. 144.b, an analogous observation can be drawn as the scaling case ①. A consistent underestimation of the energy consumption is noticed when applying linear scaling to the EDS as compared to the second scaling method. Similar to the upscaling case, the ΔE_{bat} is slightly impacted for the urban driving cycles. This is because linear scaling underestimates the efficiency of the inverter in the R1 region for downscaling cases as compared to the efficiency benchmarking (Fig. 48.d in Chapter II). This discrepancy, therefore, compensates for the difference introduced by the scaling process of the electric machine and hence mitigates the overall efficiency discrepancy of the EDS when applying linear scaling. No conspicuous difference is observed for the highway driving cycles because of the non-significant difference in terms of efficiency between linear scaling and efficiency benchmarking (Fig. 48.d in Chapter II).
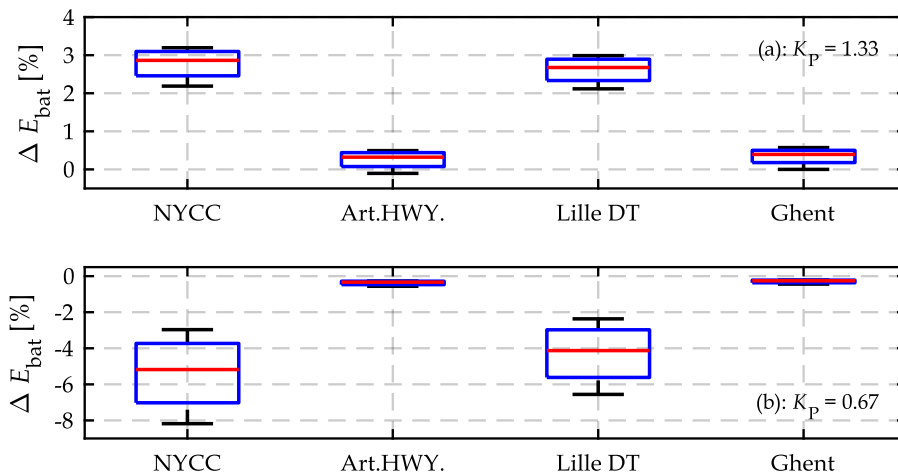
Fig. 144: Sensitivity analysis of the effect of electric drive scaling of the compact car on the energy consumption computation: (a) scaling case ①, (b) scaling case ②. This sensitivity analysis compares linear scaling applied to the electric drive against geometric scaling laws using the choice $B\sim1$ of electric machines combined with efficiency benchmarking of the inverter.

4 Expanding the scaling methodology to modular drivetrain topologies

In Chapter VI, it has been demonstrated that the linear scaling method of EDS yields results comparatively close to those attained using geometric scaling laws of PMSM combined with efficiency benchmarking of the inverter in terms of energy consumption. Nevertheless, it should be emphasized that these findings are reported for a mono-drive topology. Therefore, a central concern is whether the application of the linear scaling method is still reliable when it is applied to other topologies of the drivetrain. To address this question, this section investigates the reliability of linear scaling in terms of energy consumption using a multi-drive topology. The scope of the section is confined to the scaling of the electric machines, as earlier

demonstrated to be the origin of the difference in terms of energy consumption. To this end, constant efficiency for both the inverter and gearbox is considered to isolate the impact of the scaling laws of the machine.

4.1 Case study: Modular cascaded machines topology

The Modular Cascaded Machines (MCM) topology using two EDS, as shown in Fig. 145, is selected as a case study for the subsequent investigation. This choice is driven by the fact that this topology offers a central drive configuration, which involves either front or rear-driven wheels. This permits isolating the influence of the braking strategy from the effect of the scaling method on energy consumption. Consequently, conclusions on the reliability of linear scaling for multi-drive topology can be straightforwardly drawn. While distributed topologies (Fig. 14 in Chapter I), are possible alternatives, they comprise a second EDS mounted on another axle, enabling more energy recovery during braking phases. Certainly, this option is interesting to reduce energy consumption. Nevertheless, this complicates the investigation of how the applied scaling method influences energy consumption in multi-drive topologies.
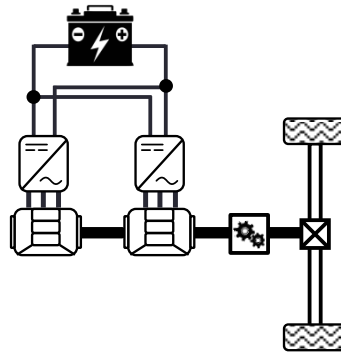
Fig. 145: Modular cascaded machine topology

4.1.1 Scaling specifications for the modular cascaded topology

This investigation aims to assess the reliability of the linear scaling method of electric machines using an alternative drivetrain, exemplified by the MCM topology, and pinpoint the conditions under which this reliability holds. For this aim, a sensitivity analysis based on the scaling methods of PMSM and the control strategy of the torque distribution of the MCM system is included in the analysis, as depicted in Fig. 146. More emphasis is herein paid to the impact of the control strategy of the MCM on the outcomes of the linear scaling methods on energy consumption. To this end, two torque distribution strategies, namely optimal torque distribution for efficiency enhancement of the MCM system, and a master-slave strategy, are considered in the following analysis. Further details concerning these strategies are presented in Section 4.1.3.

In the following, the upscaling case ① of the compact car (Section 2 of Chapter IV) is selected to extend the analysis using the MCM topology. To achieve the demanded traction power scaling of 1.33 (power scaling from a system standpoint), the reference machine is downscaled with a power scaling factor of 0.67 (power scaling from a machine standpoint).

This results in a balanced power split of 50%, serving as a representative case study. Furthermore, the downscaled machines with the MCM are considered identical, meaning that they share the same geometry. These choices are made to simplify the study and present an illustrative case, given the large design space of the MCM that includes different parameter variations and possibilities. This is exemplified by the study conducted in [115], where variations in the topology, technology, power split, geometry, and number of cascaded machines are explored.
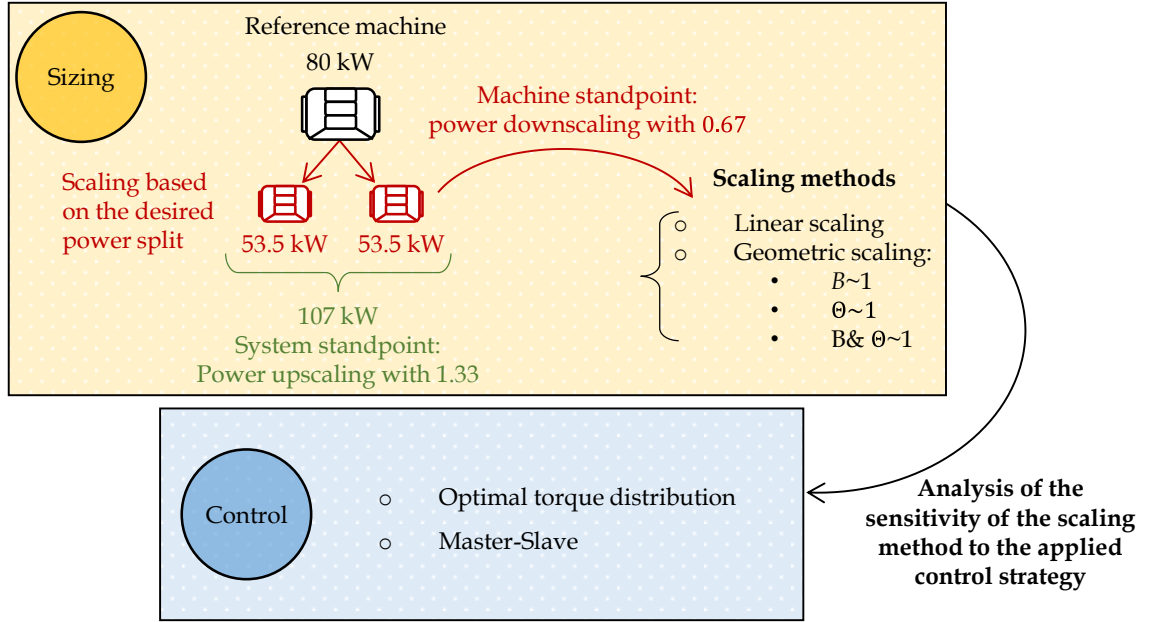
Fig. 146: Specification for the scaling of the modular cascaded topology

4.1.2   EMR-based scaling laws of the modular cascaded machines topology

The EMR-based scaling laws of the MCM are illustrated in Fig. 147. In this studied topology, the two EDS share the same DC bus voltage, and hence the same voltage v'_{bat} will be applied to both of them. The requested current from the battery i'_{ED} results from the addition of the individual currents in each EDS. Therefore, the electric coupling (overlapped squares) is modeled as in (219). As for the mechanical coupling, the overall torque is the combined results of the individual torques provided by each electric machine (226). Due to the series connection, the individual machines share the same rotational speed. The modeling of the remaining components is the same as the previously discussed topology.

$$\begin{cases} v'_{\text{bat}} & = & \text{common} \\ i'_{\text{ED}} & = & i'_{\text{ED,1}} + i'_{\text{ED,2}} \end{cases} \tag{219}$$

$$\begin{cases} T'_{\text{MCM}} & = & T^{\text{EM}'}_{\text{sh,1}} + T^{\text{EM}'}_{\text{sh,2}} \\ \Omega_{\text{MCM}} & = & \Omega^{\text{EM}'}_{\text{sh,1}} & = & \Omega^{\text{EM}'}_{\text{sh,2}} \end{cases} \tag{220}$$

Concerning the control part, the torque references of each machine, $T_{\text{sh},1}^{*\text{EM}'}$, and $T_{\text{sh},2}^{*\text{EM}'}$, are obtained through torque distribution criteria, denoted as k_{d}, as specified in (227). This latter is defined by a torque distribution strategy defined by the global control (lower part of Fig. 147).

$$\begin{cases} T_{\text{sh},1}^{*\text{EM}'} & = & k_{\text{d}} T_{\text{MCM}}^{*'} \\ T_{\text{sh},2}^{*\text{EM}'} & = & (1 - k_{\text{d}}) T_{\text{MCM}}^{*'} \end{cases} \text{ with } 0 \le k_{\text{d}} \le 1 \tag{221}$$
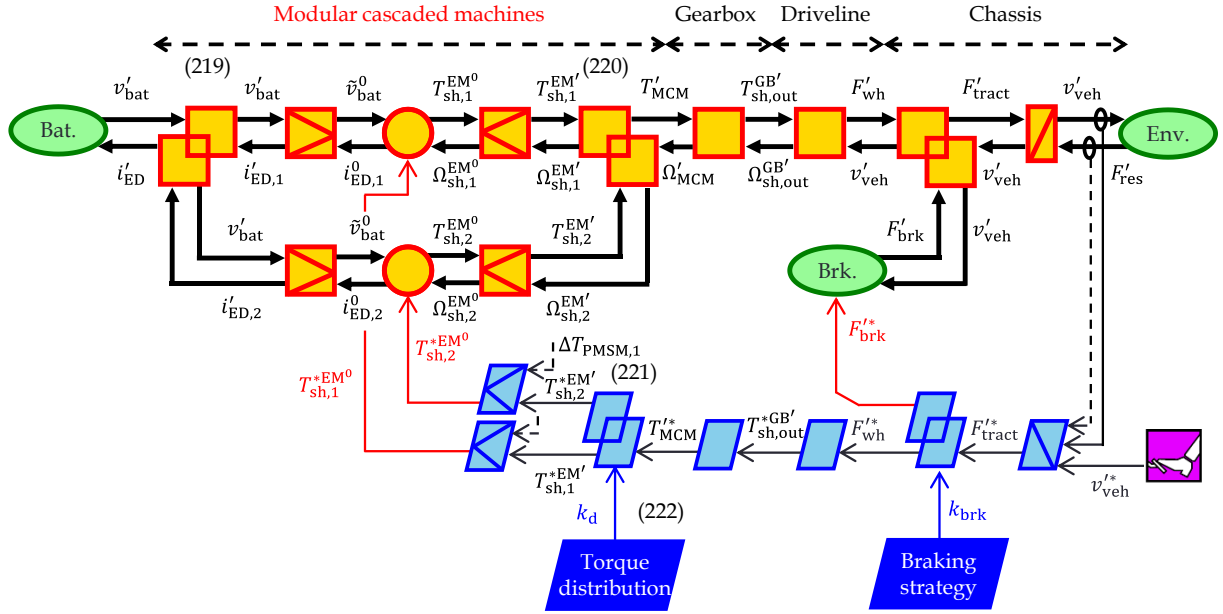
Fig. 147: EMR-based scaling laws of the modular cascaded machine topology

4.1.3 Torque distribution strategy of modular cascaded machine topology

As indicated earlier, two torque strategies of the MCM are considered. The first strategy targets a maximization of the overall efficiency of the MCM system η_{MCM} for a given speed-torque operating point through the distribution criteria k_{d}. Following the proposed method in [115], the optimization problem can be reformulated as in (225). The calculation details are provided in the next section. To include the scalability aspect, the efficiency of the individual machines $\eta_{\text{EM},1}'$, and $\eta_{\text{EM},2}'$ is redrafted as a function of the reference machine η_{EM}^0 and the equivalent loss term ΔP_{losses} that encompasses the non-linearity of the loss scaling (cf. Chapter II). Note that the term, ΔP_{losses} is zero, if the linear scaling method is applied.

$$\max\left(\eta_{MCM}(k_{\text{d}})\right) = \frac{T_{\text{MCM}}^{*'}\eta_{\text{EM},1}'^{\gamma}\eta_{\text{EM2}}'^{\gamma}}{k_{\text{d}} T_{\text{MCM}}'\eta_{\text{EM},2}'^{\gamma} + (1 - k_{\text{d}})T_{\text{MCM}}^{*'}\eta_{\text{EM},1}'^{\gamma}} \tag{222}$$

$$\begin{cases} \eta_{\text{EM}}' & = & \dfrac{K_T^{\text{PMSM}}\eta_{\text{EM}}^0 T_{\text{EM}}^0 \Omega_{\text{EM}}^0}{K_T^{\text{PMSM}} T_{\text{EM}}^0 \Omega_{\text{EM}}^0 + \eta_{\text{EM}}^0 \Delta P_{\text{losses}}} \\ \Delta P_{\text{losses}}\left(K_T^{\text{PMSM}}, K_A, K_R\right) & = & \Delta P_{\text{cu}} + \Delta P_{\text{fer}} + \Delta P_{\text{PM}} + \Delta P_{\text{mech}} \end{cases} \tag{223}$$

The second strategy is the master-slave strategy [253]. This implies that one of the machines (referred as to the slave machine) is predominantly in charge of the traction function of

the vehicle ($T_{\text{slave}}^{*\prime} = T_{\text{MCM}}^{*\prime}$), and the second machine (master machine) is inactive ($T_{\text{master}}^{*\prime} = 0$). When the driving requirement exceeds the capability of the slave machine, the master machine is engaged to satisfy these requirements. The same applies during the braking phases. Note that this strategy finds applications in commercialized electric vehicles, as reported by the benchmarking study of the BMW iX [254]. Based on this strategy, the torque distribution criterion is adjusted following (224).

$$
\begin{cases}
k_{\text{d}} & = & 1 & \text{when } T_{\text{MCM}}^{*\prime} \leq \text{T}_{\text{slave}}^{\prime\text{max}} \\
k_{\text{d}} & = & \dfrac{\text{T}_{\text{slave}}^{\prime\text{max}}}{T_{\text{MCM}}^{*\prime}} & \text{when } T_{\text{MCM}}^{*\prime} > \text{T}_{\text{slave}}^{\prime\text{max}}
\end{cases}
\tag{224}
$$

4.1.4 Efficiency of the modular cascaded machine calculations

The MCM system efficiency η_{MCM} is expressed as follows in (225).

$$
\eta_{\text{MCM}} = \frac{P_{\text{out}}}{P_{\text{in}}} = \frac{T_{\text{EM},1}\Omega_{\text{EM},1} + T_{\text{EM},2}\Omega_{\text{EM},2}}{\dfrac{T_{\text{EM},1}\Omega_{\text{EM},1}}{\eta_{\text{EM},1}^{\gamma}} + \dfrac{T_{\text{EM},2}\Omega_{\text{EM},2}}{\eta_{\text{EM},2}^{\gamma}}}
\tag{225}
$$

In the MCM system in series connection, both machines share the same rotational speed and the overall torque is the addition of the torque provided by each machine (226).

$$
\begin{cases}
T_{\text{MCM}} & = & T_{\text{EM},1} + T_{\text{EM},2} & \\
\Omega_{\text{MCM}} & = & \Omega_{\text{EM},1} & = & \Omega_{\text{EM},2}
\end{cases}
\tag{226}
$$

The torque distribution criterion k_{d} defined by the global torque split the reference requested torque from the MCM T_{MCM}^{*} as shown in (227).

$$
\begin{cases}
T_{\text{sh},1}^{*\prime} & = & k_{\text{d}}T_{\text{MCM}}^{*\prime} \\
T_{\text{sh},2}^{*\prime} & = & (1 - k_{\text{d}})T_{\text{MCM}}^{*\prime}
\end{cases} \text{with } 0 \leq k_{\text{d}} \leq 1
\tag{227}
$$

Making use of (226), (227), (225) can be redrafted as:

$$
\begin{aligned}
\eta_{\text{MCM}} & = \frac{\eta_{\text{EM},1}^{\gamma}\eta_{\text{EM},2}^{\gamma}(T_{\text{EM},1} + T_{\text{EM},2})}{T_{\text{EM},1}\eta_{\text{EM},2}^{\gamma} + T_{\text{EM},2}\eta_{\text{EM},1}^{\gamma}} \\
& = \frac{\eta_{\text{EM},1}^{\gamma}\eta_{\text{EM},2}^{\gamma}T_{\text{MCM}}^{*\prime}}{k_{\text{d}}T_{\text{MCM}}^{*\prime}\eta_{\text{EM},2}^{\gamma} + (1 - k_{\text{d}})T_{\text{MCM}}^{*\prime}\eta_{\text{EM},1}^{\gamma}}
\end{aligned}
\tag{228}
$$

4.2 Sensitivity analysis of the energy consumption of the modular cascaded topology

By consulting Fig. 148, the sensitivity analysis of the difference in terms the energy consumption ΔE_{bat} between linear scaling and the different geometric scaling laws can be examined. The results are reported for examples of normalized and on-road driving cycles with urban (NYCC, and Lille downtown) and highway (ARTEMIS, and Lille-Ghent) driving patterns. The figures in the first column show the results using the master-slave control strategy, while the second column depicts the outcomes of the comparison using the optimal torque distribution. Similar to the trend noticed in the downscaling cases for the mono-drive topology, ΔE_{bat} is consistently negative meaning that the linear scaling method underestimates the energy consumption as compared to the geometric scaling method. Furthermore, the biggest difference in ΔE_{bat} is found for urban driving cycles, similar to the finding reported earlier. The conspicuous observation to emerge from the data comparison is that the chosen torque distribution has a significant impact on the energy difference between linear scaling and geometric scaling laws, particularly for urban driving cycles. This is evidenced by the outcomes of the scaling choice $B\sim1$, as shown in Fig. 148.a, and Fig. 148.b, where the maximal value of ΔE_{bat} is reduced from -7.3% to -5% for the NYCC cycle, and from -6.2% to -4.5% using the the Lille downtown cycle. This reduction factor is comparatively less evident while opting for the other two geometric scaling choices. This is because of the difference in terms of efficiency scaling between linear scaling and the scaling choice $B\sim1$ is larger for downscaling cases as compared to the other choices. For highway driving cycles, no noticeable difference is observed when utilizing either of the control strategies.

To elucidate the effect of the control strategy on the comparison outcomes between the linear scaling and geometric scaling based on choice $B\sim1$, the operating points resulting from the master-slave, and the optimal torque distribution are analyzed. For this aim, Fig. 149 visualizes the operating points for the MCM system in a contour map, that shows the efficiency difference $\Delta\eta_{EM}$ of the aforementioned scaling methods for the NYCC driving cycles. For this illustration, a scaled design using the choice $B\sim1$ and an axial scaling factor K_A of 1.5 is herein selected, as it yields the highest value of ΔE_{bat}. Fig. 149.b clearly shows that the master-slave strategy defines operating points that are frequently situated in regions characterized by high-torque and low-speed values. In the aforementioned regions, $\Delta\eta_{EM}$ reaches its highest values. Neverthelss, this is not the case, when employing the optimal torque distribution strategy as can be seen in Fig. 149.a. In this case scenario, the operating points of both machines are located in regions where $\Delta\eta_{EM}$ is not as significant as those defined by the master slave strategy. This explains the difference ΔE_{bat} obtained using both control strategies.

Therefore, it can be concluded that linear scaling is more sensitive to control strategies that tend to define operating points in regions in high-torque and low-speed regions. This can lead to significant differences, particularly when comparing it to geometric scaling laws based on the choice $B\sim1$, in the case of the computation of energy consumption of multi-drive topology.
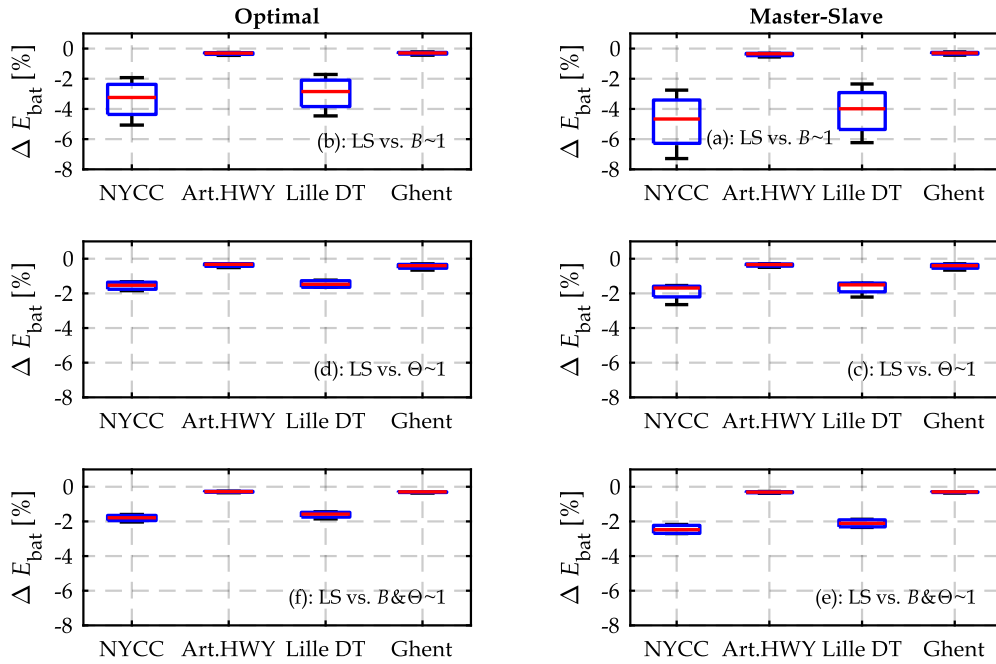
Fig. 148: Sensitivity analysis of the relative difference in terms of energy consumption ΔE_{bat} between linear scaling and geometric scaling based on different scaling choices for the modular cascaded machine topology. Negative values of ΔE_{bat} means that linear scaling underestimates energy consumption and vice versa.
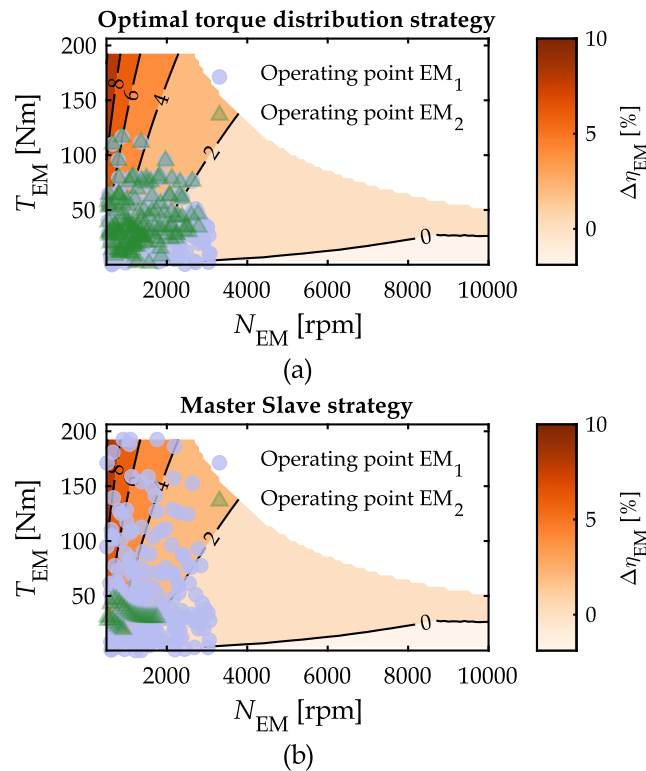
Fig. 149: Comparison of the operating points resulting from the torque distribution strategies for the NYCC driving cycle. The results are visualized in a contour map that shows the difference in terms of efficiency $\Delta \eta_{EM}$ between linear scaling and geometric scaling methods of electric machines. Note that one contour map is used as the machine used for the MCM topology is identical.

References

[1] International Energy Agency, "Global Energy Review: CO2 Emissions in 2021, Global Emissions Rebound Sharply to Highest Ever Level," 2021.

[2] United Nations Framework Convention on Climate Change (UNFCCC), "The Paris agreement." 2016.

[3] S. Singh, M. J. Kulshrestha, N. Rani, K. Kumar, C. Sharma, and D. K. Aswal, "An Overview of Vehicular Emission Standards," *MAPAN*, vol. 38, no. 1, pp. 241–263, Mar. 2023, doi: 10.1007/s12647-022-00555-4.

[4] J. Dornoff, "The stringency of the proposed Euro 7 regulation for cars and vans: An international comparison," *International Council on Clean Transportation*, Sep. 2023, doi: 10.5040/9781782258674.

[5] M. Noussan, M. Hafner, and S. Tagliapietra, *The Future of Transport Between Digitalization and Decarbonization: Trends, Strategies and Effects on Energy Consumption*. in SpringerBriefs in Energy. Cham: Springer International Publishing, 2020. doi: 10.1007/978-3-030-37966-7.

[6] International Energy Agency, "Global EV Outlook 2023: Catching up with climate ambitions," 2023.

[7] International Energy Agency, "CO2 Emissions in 2022," *IEA*, 2023.

[8] E. Masood, J. Tollefson, and A. Irwin, "COP27 climate talks: what succeeded, what failed and what's next," *Nature*, vol. 612, no. 7938, pp. 16–17, Dec. 2022, doi: 10.1038/d41586-022-03807-0.

[9] "COP28 UAE | United Nations Climate Change Conference (UNFCCC)." Accessed: Sep. 17, 2023. [Online]. Available: https://www.cop28.com/

[10] H. Hick, K. Küpper, and H. Sorger, Eds., *Systems Engineering for Automotive Powertrain Development*. in Powertrain. Cham: Springer International Publishing, 2021. doi: 10.1007/978-3-319-99629-5.

[11] I. Husain *et al.*, "Electric Drive Technology Trends, Challenges, and Opportunities for Future Electric Vehicles," *Proc. IEEE*, vol. 109, no. 6, pp. 1039–1059, Jun. 2021, doi: 10.1109/JPROC.2020.3046112.

[12] X. Hu, J. Han, X. Tang, and X. Lin, "Powertrain Design and Control in Electrified Vehicles: A Critical Review," *IEEE Trans. Transp. Electrific.*, vol. 7, no. 3, pp. 1990–2009, Sep. 2021, doi: 10.1109/TTE.2021.3056432.

[13] E. Silvas, T. Hofman, N. Murgovski, P. Etman, and M. Steinbuch, "Review of Optimization Strategies for System-Level Design in Hybrid Electric Vehicles," *IEEE Trans. Veh. Technol.*, pp. 1–1, 2016, doi: 10.1109/TVT.2016.2547897.

[14] X. Roboam, Ed., *Systemic Design Methodologies for Electrical Energy Systems: Analysis, Synthesis and Management*. Hoboken, NJ, USA: John Wiley & Sons, Inc., 2012. doi: 10.1002/9781118569863.

[15] L. Nicoletti, S. Mayer, M. Brönner, F. Schockenhoff, and M. Lienkamp, "Design Parameters for the Early Development Phase of Battery Electric Vehicles," *WEVJ*, vol. 11, no. 3, p. 47, Jun. 2020, doi: 10.3390/wevj11030047.

[16] L. Guzzella and A. Sciarretta, *Vehicle Propulsion Systems*. Berlin, Heidelberg: Springer Berlin Heidelberg, 2013. doi: 10.1007/978-3-642-35913-2.

[17] O. C. Zienkiewicz, R. L. Taylor, and J. Z. Zhu, *The finite element method: its basis and fundamentals*, 6. ed., Reprint., Transferred to digital print. Elsevier, ISBN: 978-0-7506-6320-5, 2010.

[18] L. Maccioni and F. Concli, "Computational Fluid Dynamics Applied to Lubricated Mechanical Components: Review of the Approaches to Simulate Gears, Bearings, and Pumps," *Applied Sciences*, vol. 10, no. 24, p. 8810, Dec. 2020, doi: 10.3390/app10248810.

[19] P. Boscariol and D. Richiedei, "Energy optimal design of servo-actuated systems: A concurrent approach based on scaling rules," *Renewable and Sustainable Energy Reviews*, vol. 156, p. 111923, Mar. 2022, doi: 10.1016/j.rser.2021.111923.

[20] G. Domingues-Olavarria, F. J. Marquez-Fernandez, P. Fyhr, A. Reinap, M. Andersson, and M. Alakula, "Optimization of Electric Powertrains Based on Scalable Cost and Performance Models," *IEEE Trans. on Ind. Applicat.*, vol. 55, no. 1, pp. 751–764, Jan. 2019, doi: 10.1109/TIA.2018.2864943.

[21] E. A. Grunditz, T. Thiringer, and N. Saadat, "Acceleration, Drive Cycle Efficiency, and Cost Tradeoffs for Scaled Electric Vehicle Drive System," *IEEE Trans. Ind. Appl.*, vol. 56, no. 3, p. 14, 2020, doi: 10.1109/TIA.2020.2976861.

[22] H. Pfluegl *et al.*, "OBELICS – Optimization of e-drive concepts with scalable realtime models and functional testing based on real use-cases," *Proceedings of 8th Transport Research Arena TRA, Helsinki, Finland*, p. 11, 2020.

[23] J. C. H. Bone, "Influence of rotor diameter and length on the rating of induction motors," *IEE Journal on Electric Power Applications*, vol. 1, no. 1, pp. 2–6, Feb. 1978, doi: 10.1049/ij-epa.1978.0002.

[24] E. M. H. Kamerbeek, "Scaling laws for electric motors," *Philips tech. Rev. 35*, 1975.

[25] B. Kabalan, E. Vinot, C. Yuan, R. Trigui, C. Dumand, and T. E. Hajji, "Efficiency Improvement of a Series–Parallel Hybrid Electric Powertrain by Topology Modification," *IEEE Trans. Veh. Technol.*, vol. 68, no. 12, pp. 11523–11531, Dec. 2019, doi: 10.1109/TVT.2019.2952190.

[26] L. Ramirez, A. Aroua, P. Delarue, and W. Lhomme, "Linear Scaling Evaluation of Losses for Automotive Traction Voltage Source Inverters," in *2022 IEEE Vehicle Power and Propulsion Conference (VPPC)*, Merced, CA, USA: IEEE, Nov. 2022, pp. 1–6. doi: 10.1109/VPPC55846.2022.10003330.

[27] T. Hofman, "Framework for combined control and design optimization of hybrid vehicle propulsion systems," Ph.D. dissertation, Eindhoven University of Technology, The Netherlands, 2007.

[28] S. Stipetic, D. Zarko, and M. Popescu, "Ultra-fast axial and radial scaling of synchronous permanent magnet machines," *IET Electric Power Applications*, vol. 10, no. 7, pp. 658–666, Aug. 2016, doi: 10.1049/iet-epa.2016.0014.

[29] M. Nell, J. Lenz, and K. Hameyer, "Scaling laws for the FE solutions of induction machines," *Archives of electrical engineering*, vol. 68, no. no 3., 2019, doi: 10.24425/AEE.2019.129350.

[30] F. Verbelen, A. Abdallh, H. Vansompel, K. Stockman, and P. Sergeant, "Sizing Methodology Based on Scaling Laws for a Permanent Magnet Electrical Variable Transmission," *IEEE Trans. Ind. Electron.*, vol. 67, no. 3, pp. 1739–1749, Mar. 2020, doi: 10.1109/TIE.2019.2903763.

[31] E. Saerens *et al.*, "Scaling laws for robotic transmissions," *Mechanism and Machine Theory*, vol. 140, pp. 601–621, Oct. 2019, doi: 10.1016/j.mechmachtheory.2019.06.027.

[32] M. Budinger, J.-C. Passieux, C. Gogu, and A. Fraj, "Scaling-law-based metamodels for the sizing of mechatronic systems," *Mechatronics*, vol. 24, no. 7, pp. 775–787, Oct. 2014, doi: 10.1016/j.mechatronics.2013.11.012.

[33] A. Bouscayrol, J.-P. Hautier, and B. Lemaire-Semail, "Graphic Formalisms for the Control of Multi-Physical Energetic Systems: COG and EMR," in *Systemic Design Methodologies for Electrical Energy Systems*, John Wiley & Sons, Ltd, 2012, pp. 89–124. doi: 10.1002/9781118569863.ch3.

[34] International Energy Agency, "Global energy-related CO2 emissions by sector," IEA. Accessed: May 09, 2023. [Online]. Available: https://www.iea.org/data-and-statistics/charts/global-energy-related-co2-emissions-by-sector

[35] Climate Transparency, "European Union - Climate Transparency Report: Comparing G20 Climate Action," 2022.

[36] C. Shirley and R. Gecan, "Emissions of Carbon Dioxide in the Transportation Sector," *Congressional Budget Office*, 2022.

[37] Climate Transparency, "China - Climate Transparency Report: Comparing G20 Climate Action," 2022.

[38] International Energy Agency, "An energy sector roadmap to carbon neutrality in China," 2021.

[39] International Energy Agency, "Transport," IEA. Accessed: May 10, 2023. [Online]. Available: https://www.iea.org/topics/transport

[40] International Energy Agency, "Energy Technology Perspectives 2020," *Energy Technology Perspectives*, 2020.

[41] International Energy Agency, "Transport sector CO2 emissions by mode in the Sustainable Development Scenario, 2000-2030 – Charts – Data & Statistics," IEA. Accessed: May 10, 2023. [Online]. Available: https://www.iea.org/data-and-statistics/charts/transport-sector-co2-emissions-by-mode-in-the-sustainable-development-scenario-2000-2030

[42] "CO2 emissions from cars: facts and figures (infographics)," European Parliament. Accessed: May 10, 2023. [Online]. Available: https://www.europarl.europa.eu/news/en/headlines/society/20190313STO31218/co2-emissions-from-cars-facts-and-figures-infographics

[43] European Energy Agency (EEA), "Analysis and data." Accessed: May 10, 2023. [Online]. Available: https://www.eea.europa.eu

[44] C. Buysse, J. Miller, J. Díaz, S. Sen, and C. Braun, "The role of the European Union's vehicle CO2 standards in achieving the European Green Deal," *International Council on Clean Transportation*, p. 22, 2021.

[45] J. Dornoff, "Policy update: CO2 emission standards for new passenger cars and vans in the European Union," *International Council on Clean Transportation*, 2023.

[46] European Commission, "Proposal for amending Regulation (EU) 2019/1242 as regards strengthening the CO₂ emission performance standards for new heavy-duty vehicles and integrating reporting obligations, and repealing Regulation (EU) 2018/956(COM(2023) 88 final)." 2023.

[47] J. Kerry and G. Mccarthy, "The Long-Term Strategy of the United States, Pathways to Net-Zero Greenhouse Gas Emissions by 2050," *United States Department of State and the United States Executive Office of the President, Washington DC*, 2021.

[48] Environmental Protection Agency (EPA) and National Highway Traffic Safety Administration (NHTSA), "Federal Register / Vol. 88, No. 87: Multi-Pollutant Emissions Standards for Model Years 2027 and Later Light- Duty and Medium-Duty Vehicles." 2023.

[49] Z. Yang, "Improving the conversions between the various passenger vehicle fuel economy/CO2 emission standards around the world," International Council on Clean Transportation. Accessed: Aug. 01, 2023. [Online]. Available: https://theicct.org/improving-the-conversions-between-the-various-passenger-vehicle-fuel-economy-co2-emission-standards-around-the-world/

[50] Environmental Protection Agency (EPA) and National Highway Traffic Safety Administration (NHTSA), "Federal Register / Vol. 88, No. 81: Federal Register / Vol. 88: Greenhouse Gas Emissions Standards for Heavy-Duty Vehicles — Phase 3." 2023.

[51] International Energy Agency, "Fuel economy in China – Analysis," IEA. Accessed: May 13, 2023. [Online]. Available: https://www.iea.org/articles/fuel-economy-in-china

[52] S. Mao, L. Yang, and Y. Zhang, "The Stage 4 proposed amendment to China's heavy-duty vehicle fuel consumption standard: ICCT reflections," *International Council on Clean Transportation*, 2023.

[53] J. Dornoff *et al.*, "Fit for 55: A review and evaluation of the European Commission proposal for amending the CO2 targets for new cars and vans," *International Council on Clean Transportation*, 2021.

[54] P. Slowik and Miller, "Aligning the U.S. greenhouse gas standard for cars and light trucks with the Paris Climate Agreement," International Council on Clean Transportation. Accessed: May 15, 2023. [Online]. Available: https://theicct.org/us-ghg-standard-paris-agreement-dec22/

[55] J. Callahan, "China's efforts to decarbonize road transport: Decent, but not sufficient," International Council on Clean Transportation. Accessed: May 08, 2023. [Online]. Available: https://theicct.org/china-ev-efforts-mar22/

[56] P. Mock and S. Díaz, "Pathways to decarbonization: The European passenger car market, 2021–2035," *International Council on Clean Transportation*, p. 48, 2021.

[57] "European Vehicle Market Statistics - Pocketbook 2022/23," *International Council on Clean Transportation*, 2023.

[58] Z. Yang and H. Cui, "Technology roadmap and costs for fuel efficiency increase and CO2 reduction from Chinese new passenger cars in 2030," *International Council on Clean Transportation*, 2030.

[59] "Global Memorandum of Understanding on Zero-emission Medium- and Heavy-duty Vehicles," Global Drive To Zero. Accessed: May 16, 2023. [Online]. Available: https://globaldrivetozero.org/mou-nations/

[60] J. Yang, "Beyond Europe: Are there ambitious electrification targets across major markets?," International Council on Clean Transportation. Accessed: May 16, 2023. [Online]. Available: https://theicct.org/global-oem-targets-cars-ldvs-nov22/

[61] A. Bouscayrol, G. Mihai Sirbu, A. Lepoutre, and E. Castex, "Impact Analysis report of the PANDA project," *H2020 European Project - grant agreement ID: 824256, Deliverable No. PANDA D6.6*, 2022.

[62] D. D. Walden, G. J. Roedler, K. Forsberg, R. D. Hamelin, and T. M. Shortell, *Systems engineering handbook: A guide for system life cycle processes and activities*. John Wiley & Sons, ISBN: 978-1-118-99940-0, 2015.

[63] H. Hick, M. Bajzek, and C. Faustmann, "Definition of a system model for model-based development," *SN Appl. Sci.*, vol. 1, no. 9, p. 1074, Sep. 2019, doi: 10.1007/s42452-019-1069-0.

[64] A. Bouscayrol *et al.*, "Power Advanced N-level Digital Architecture for models of electrified vehicles and their components," in *8th Transport Research Arena TRA 2020*, Helsinki, Finland, 2020.

[65] Electric Transportation Applications, "1999 EV America technical Specifications." 1999.

[66] D.-D. Tran, M. Vafaeipour, M. El Baghdadi, R. Barrero, J. Van Mierlo, and O. Hegazy, "Thorough state-of-the-art analysis of electric and hybrid vehicle powertrains: Topologies and integrated energy management strategies," *Renewable and Sustainable Energy Reviews*, vol. 119, p. 109596, Mar. 2020, doi: 10.1016/j.rser.2019.109596.

[67] W. Lhomme, "Structuration of real-time control using Energetic Macroscopic Representation for Hybrid Electric Vehicles," Dissertation of the accreditation to supervise research (Manuscrit d'Habilitation à diriger des Recherches HdR), University of Lille, France, 2020.

[68] Z. Wang, J. Zhou, and G. Rizzoni, "A review of architectures and control strategies of dual-motor coupling powertrain systems for battery electric vehicles," *Renewable and Sustainable Energy Reviews*, vol. 162, p. 112455, Jul. 2022, doi: 10.1016/j.rser.2022.112455.

[69] G. Wu, X. Zhang, and Z. Dong, "Powertrain architectures of electrified vehicles: Review, classification and comparison," *Journal of the Franklin Institute*, vol. 352, no. 2, pp. 425–448, Feb. 2015, doi: 10.1016/j.jfranklin.2014.04.018.

[70] K. Li, A. Bouscayrol, S. Han, and S. Cui, "Comparisons of Electric Vehicles Using Modular Cascade Machines System and Classical Single Drive Electric Machine," *IEEE Trans. Veh. Technol.*, vol. 67, no. 1, pp. 354–361, Jan. 2018, doi: 10.1109/TVT.2017.2743216.

[71] I. López, E. Ibarra, A. Matallana, J. Andreu, and I. Kortabarria, "Next generation electric drives for HEV/EV propulsion systems: Technology, trends and challenges," *Renewable and Sustainable Energy Reviews*, vol. 114, p. 109336, Oct. 2019, doi: 10.1016/j.rser.2019.109336.

[72] C. Liu, K. T. Chau, C. H. T. Lee, and Z. Song, "A Critical Review of Advanced Electric Machines and Control Strategies for Electric Vehicles," *Proc. IEEE*, vol. 109, no. 6, pp. 1004–1028, Jun. 2021, doi: 10.1109/JPROC.2020.3041417.

[73] E. Agamloh, A. Von Jouanne, and A. Yokochi, "An Overview of Electric Machine Trends in Modern Electric Vehicles," *Machines*, vol. 8, no. 2, p. 20, Apr. 2020, doi: 10.3390/machines8020020.

[74] L. Shao, A. E. H. Karci, D. Tavernini, A. Sorniotti, and M. Cheng, "Design Approaches and Control Strategies for Energy-Efficient Electric Machines for Electric Vehicles—A Review," *IEEE Access*, vol. 8, pp. 116900–116913, 2020, doi: 10.1109/ACCESS.2020.2993235.

[75] X. She, A. Q. Huang, O. Lucia, and B. Ozpineci, "Review of Silicon Carbide Power Devices and Their Applications," *IEEE Trans. Ind. Electron.*, vol. 64, no. 10, pp. 8193–8205, Oct. 2017, doi: 10.1109/TIE.2017.2652401.

[76] X. Ding, M. Du, T. Zhou, H. Guo, and C. Zhang, "Comprehensive comparison between silicon carbide MOSFETs and silicon IGBTs based traction systems for electric vehicles," *Applied Energy*, vol. 194, pp. 626–634, May 2017, doi: 10.1016/j.apenergy.2016.05.059.

[77] J. Reimers, L. Dorn-Gomba, C. Mak, and A. Emadi, "Automotive Traction Inverters: Current Status and Future Trends," *IEEE Trans. Veh. Technol.*, vol. 68, no. 4, pp. 3337–3350, Apr. 2019, doi: 10.1109/TVT.2019.2897899.

[78] R. Fischer, F. Küçükay, G. Jürgens, R. Najork, and B. Pollak, *The Automotive Transmission Book*. in Powertrain. Cham: Springer International Publishing, ISBN: 978-3-319-05262-5 978-3-319-05263-2, 2015. doi: 10.1007/978-3-319-05263-2.

[79] B. Gao *et al.*, "Topology optimization and the evolution trends of two-speed transmission of EVs," *Renewable and Sustainable Energy Reviews*, vol. 161, p. 112390, Jun. 2022, doi: 10.1016/j.rser.2022.112390.

[80] J. Doerr, N. Ardey, G. Mendl, G. Fröhlich, R. Straßer, and T. Laudenbach, "The new full electric drivetrain of the Audi e-tron," in *Der Antrieb von morgen 2019: Diversifizierung konsequent vorantreiben 13. Internationale MTZ-Fachtagung Zukunftsantriebe (pp. 13-37)*, Springer Fachmedien Wiesbaden GmbH, ISBN: 978-3-658-26055-2., 2019, p. 25.

[81] M. De Carlo and G. Mantriota, "Electric vehicles with two motors combined via planetary gear train," *Mechanism and Machine Theory*, vol. 148, p. 103789, Jun. 2020, doi: 10.1016/j.mechmachtheory.2020.103789.

[82] F. Machado, P. Kollmeyer, D. Barroso, and A. Emadi, "Multi-Speed Gearboxes for Battery Electric Vehicles: Current Status and Future Trends," *IEEE Open J. Veh. Technol.*, vol. 2, pp. 419–435, 2021, doi: 10.1109/OJVT.2021.3124411.

[83] B. Krüger, G. Keinprecht, G. Filomeno, D. Dennin, and P. Tenberge, "Design and optimisation of single motor electric powertrains considering different transmission topologies," *Mechanism and Machine Theory*, vol. 168, p. 104578, Feb. 2022, doi: 10.1016/j.mechmachtheory.2021.104578.

[84] D. Schweigert *et al.*, "On the Impact of Maximum Speed on the Power Density of Electromechanical Powertrains," *Vehicles*, vol. 2, no. 2, pp. 365–397, Jun. 2020, doi: 10.3390/vehicles2020020.

[85] M. Mileti, P. Strobl, H. Pflaum, and K. Stahl, "Design of a Hyper-High-Speed Powertrain for EV to Achieve Maximum Ranges," in *CTI SYMPOSIUM 2018*, EUROFORUM Deutschland GmbH, Ed., in Proceedings. , Berlin, Heidelberg: Springer Berlin Heidelberg, 2020, pp. 265–273. doi: 10.1007/978-3-662-58866-6_21.

[86] L. Shao, R. Navaratne, M. Popescu, and G. Liu, "Design and Construction of Axial-Flux Permanent Magnet Motors for Electric Propulsion Applications—A Review," *IEEE Access*, vol. 9, pp. 158998–159017, 2021, doi: 10.1109/ACCESS.2021.3131000.

[87] A. Selema, M. N. Ibrahim, and P. Sergeant, "Metal Additive Manufacturing for Electrical Machines: Technology Review and Latest Advancements," *Energies*, vol. 15, no. 3, p. 1076, Jan. 2022, doi: 10.3390/en15031076.

[88] S. Cai, J. L. Kirtley, and C. H. T. Lee, "Critical Review of Direct-Drive Electrical Machine Systems for Electric and Hybrid Electric Vehicles," *IEEE Trans. Energy Convers.*, vol. 37, no. 4, pp. 2657–2668, Dec. 2022, doi: 10.1109/TEC.2022.3197351.

[89] I. Aghabali, J. Bauman, P. J. Kollmeyer, Y. Wang, B. Bilgin, and A. Emadi, "800-V Electric Vehicle Powertrains: Review and Analysis of Benefits, Challenges, and Future Trends," *IEEE Trans. Transp. Electrific.*, vol. 7, no. 3, pp. 927–948, Sep. 2021, doi: 10.1109/TTE.2020.3044938.

[90] X. Hu, Y. Li, C. Lv, and Y. Liu, "Optimal Energy Management and Sizing of a Dual Motor-Driven Electric Powertrain," *IEEE Trans. Power Electron.*, vol. 34, no. 8, pp. 7489–7501, Aug. 2019, doi: 10.1109/TPEL.2018.2879225.

[91] Q. Jiang, F. Ossart, and C. Marchand, "Comparative Study of Real-Time HEV Energy Management Strategies," *IEEE Trans. Veh. Technol.*, vol. 66, no. 12, pp. 10875–10888, Dec. 2017, doi: 10.1109/TVT.2017.2727069.

[92] F. Roy, F. Ossart, and C. Marchand, "An Optimal Energetic Approach for Systemic Design of Hybrid Powertrain," in *2014 IEEE Vehicle Power and Propulsion Conference (VPPC)*, Coimbra, Portugal: IEEE, Oct. 2014, pp. 1–6. doi: 10.1109/VPPC.2014.7007014.

[93] L. Decker, D. Förster, F. Gauterin, and M. Doppelbauer, "Physics-Based and Data-Enhanced Model for Electric Drive Sizing during System Design of Electrified Powertrains," *Vehicles*, vol. 3, no. 3, pp. 512–532, Aug. 2021, doi: 10.3390/vehicles3030031.

[94] S. Ciceo, C. T. Faria, J. Gyselinck, and C. Martis, "Multi-Attribute, System-Level Design Process for Automotive Powertrain Electric Drives: An Integrated Approach," *SAE Int. J. Alt. Power.*, vol. 7, no. 2, pp. 117–128, Jun. 2018, doi: 10.4271/08-07-02-0007.

[95] A. Dianov, F. Tinazzi, S. Calligaro, and S. Bolognani, "Review and Classification of MTPA Control Algorithms for Synchronous Motors," *IEEE Trans. Power Electron.*, vol. 37, no. 4, pp. 3990–4007, Apr. 2022, doi: 10.1109/TPEL.2021.3123062.

[96] E. Roshandel, A. Mahmoudi, S. Kahourzade, and W. L. Soong, "Efficiency Maps of Electrical Machines: A Tutorial Review," *IEEE Trans. on Ind. Applicat.*, vol. 59, no. 2, pp. 1263–1272, Mar. 2023, doi: 10.1109/TIA.2022.3210077.

[97] G. Domingues-Olavarria, P. Fyhr, A. Reinap, M. Andersson, and M. Alakula, "From Chip to Converter: A Complete Cost Model for Power Electronics Converters," *IEEE Trans. Power Electron.*, vol. 32, no. 11, pp. 8681–8692, Nov. 2017, doi: 10.1109/TPEL.2017.2651407.

[98] A. Wintrich, U. Nicolai, W. Tursky, and T. Reimann, *Application manual power semiconductors*. in SEMIKRON International, ISBN: 978-3-938843-83-3. 2015.

[99] J. Urkizu *et al.*, "Electric Vehicle Inverter Electro-Thermal Models Oriented to Simulation Speed and Accuracy Multi-Objective Targets," *Energies*, vol. 12, no. 19, p. 3608, Sep. 2019, doi: 10.3390/en12193608.

[100] G. Mademlis, R. Orbay, Y. Liu, N. Sharma, R. Arvidsson, and T. Thiringer, "Multidisciplinary cooling design tool for electric vehicle SiC inverters utilizing transient 3D-CFD computations," *eTransportation*, vol. 7, p. 100092, Feb. 2021, doi: 10.1016/j.etran.2020.100092.

[101] J. W. Kolar and S. D. Round, "Analytical calculation of the RMS current stress on the DC-link capacitor of voltage-PWM converter systems," *IEE Proc., Electr. Power Appl.*, vol. 153, no. 4, p. 535, 2006, doi: 10.1049/ip-epa:20050458.

[102] J. Pyrhonen, T. Jokinen, and V. Hrabovcová, *Design of rotating electrical machines*. Wiley, ISBN: 978-0-470-69516-6, 2008.

[103] T. A. Lipo, *Introduction to AC machine design*. in IEEE Press series on power engineering. IEEE Press/Wiley, ISBN: 978-1-119-35216-7, 2017.

[104] C. Candelo-Zuluaga, A. Garcia Espinosa, J.-R. Riba, and P. Tubert, "PMSM Design For Achieving a Target Torque-Speed-Efficiency Map," *IEEE Trans. Veh. Technol.*, pp. 1–1, 2020, doi: 10.1109/TVT.2020.3040313.

[105] G. Lei, T. Wang, J. Zhu, Y. Guo, and S. Wang, "System-Level Design Optimization Method for Electrical Drive Systems—Robust Approach," *IEEE Trans. Ind. Electron.*, vol. 62, no. 8, pp. 4702–4713, Aug. 2015, doi: 10.1109/TIE.2015.2404305.

[106] V. Ruuskanen, J. Nerg, J. Pyrhonen, S. Ruotsalainen, and R. Kennel, "Drive Cycle Analysis of a Permanent-Magnet Traction Motor Based on Magnetostatic Finite-Element Analysis," *IEEE Trans. Veh. Technol.*, vol. 64, no. 3, pp. 1249–1254, Mar. 2015, doi: 10.1109/TVT.2014.2329014.

[107] P. Lazari, J. Wang, and L. Chen, "A Computationally Efficient Design Technique for Electric-Vehicle Traction Machines," *IEEE Trans. on Ind. Applicat.*, vol. 50, no. 5, pp. 3203–3213, Sep. 2014, doi: 10.1109/TIA.2014.2304619.

[108] A. G. Sarigiannidis, M. E. Beniakar, and A. G. Kladas, "Fast Adaptive Evolutionary PM Traction Motor Optimization Based on Electric Vehicle Drive Cycle," *IEEE Trans. Veh. Technol.*, vol. 66, no. 7, pp. 5762–5774, Jul. 2017, doi: 10.1109/TVT.2016.2631161.

[109] M. Yilmaz, "Limitations/capabilities of electric machine technologies and modeling approaches for electric motor design and analysis in plug-in electric vehicle applications," *Renewable and Sustainable Energy Reviews*, vol. 52, pp. 80–99, Dec. 2015, doi: 10.1016/j.rser.2015.07.033.

[110] V. Reinbold, E. Vinot, L. Garbuio, and L. Gerbaud, "Optimal sizing of an electrical machine using a magnetic circuit model: application to a hybrid electrical vehicle," *IET Electrical Systems in Transportation*, vol. 6, no. 1, pp. 27–33, Mar. 2016, doi: 10.1049/iet-est.2015.0008.

[111] M. L. Guyadec, L. Gerbaud, E. Vinot, V. Reinbold, and C. Dumont, "Use of reluctance network modelling and software component to study the influence of electrical machine pole number on hybrid electric vehicle global optimization," *Mathematics and Computers in Simulation*, vol. 158, pp. 79–90, Apr. 2019, doi: 10.1016/j.matcom.2018.06.001.

[112] F. Le Berr, A. Abdelli, and R. Benlamine, "Sensitivity Study on the Design Methodology of an Electric Vehicle," presented at the SAE 2012 World Congress & Exhibition, Apr. 2012, pp. 2012-01–0820. doi: 10.4271/2012-01-0820.

[113] A. Abdelli and F. Le Berr, "Analytical Approach to Model a Saturated Interior Permanent Magnet Synchronous Motor for a Hybrid Electric Vehicle," *SAE Int. J. Engines*, vol. 4, no. 1, pp. 301–313, Apr. 2011, doi: 10.4271/2011-01-0347.

[114] S. Kalt, J. Erhard, and M. Lienkamp, "Electric Machine Design Tool for Permanent Magnet Synchronous Machines and Induction Machines," *Machines*, vol. 8, no. 1, p. 15, Mar. 2020, doi: 10.3390/machines8010015.

[115] K. Li, S. Han, S. Cui, and A. Bouscayrol, "Sizing of Modular Cascade Machines System for Electric Vehicles," *IEEE Trans. Veh. Technol.*, vol. 68, no. 2, pp. 1278–1287, Feb. 2019, doi: 10.1109/TVT.2018.2886402.

[116] A. Mahmoudi, W. L. Soong, G. Pellegrino, and E. Armando, "Loss Function Modeling of Efficiency Maps of Electrical Machines," *IEEE Trans. on Ind. Applicat.*, vol. 53, no. 5, pp. 4221–4231, Sep. 2017, doi: 10.1109/TIA.2017.2695443.

[117] C. Lopez-Torres, A. Garcia Espinosa, J.-R. Riba, and L. Romeral, "Design and Optimization for Vehicle Driving Cycle of Rare-Earth-Free SynRM Based on Coupled Lumped Thermal and Magnetic Networks," *IEEE Trans. Veh. Technol.*, vol. 67, no. 1, pp. 196–205, Jan. 2018, doi: 10.1109/TVT.2017.2739020.

[118] D. Miler and M. Hoić, "Optimisation of cylindrical gear pairs: A review," *Mechanism and Machine Theory*, vol. 156, p. 104156, Feb. 2021, doi: 10.1016/j.mechmachtheory.2020.104156.

[119] American National Standards, "Fundamental Rating Factors and Calculation Methods for Involute Spur and Helical Gear Teeth." 2001.

[120] International Organization for Standardization, "ISO/TR 15144-2: Calculation of micropitting load capacity of cylindrical spur and helical gears." 2014.

[121] X. Liang, M. J. Zuo, and Z. Feng, "Dynamic modeling of gearbox faults: A review," *Mechanical Systems and Signal Processing*, vol. 98, pp. 852–876, Jan. 2018, doi: 10.1016/j.ymssp.2017.05.024.

[122] C. M. C. G. Fernandes, P. M. T. Marques, R. C. Martins, and J. H. O. Seabra, "Gearbox power loss. Part II: Friction losses in gears," *Tribology International*, vol. 88, pp. 309–316, Aug. 2015, doi: 10.1016/j.triboint.2014.12.004.

[123] F. Concli and C. Gorla, "Windage, churning and pocketing power losses of gears: different modeling approaches for different goals," *Forsch Ingenieurwes*, vol. 80, no. 3–4, pp. 85–99, Dec. 2016, doi: 10.1007/s10010-016-0206-9.

[124] Y. Shen and S. Rinderknecht, "A method on modelling and analyzing the power losses in vehicle transmission," *Forsch Ingenieurwes*, vol. 82, no. 3, pp. 261–270, Sep. 2018, doi: 10.1007/s10010-018-0276-y.

[125] F. Concli and C. Gorla, "Numerical modeling of the power losses in geared transmissions: Windage, churning and cavitation simulations with a new integrated approach that drastically reduces the computational effort," *Tribology International*, vol. 103, pp. 58–68, Nov. 2016, doi: 10.1016/j.triboint.2016.06.046.

[126] B. Morhard, D. Schweigert, M. Mileti, M. Sedlmair, T. Lohner, and K. Stahl, "Efficient lubrication of a high-speed electromechanical powertrain with holistic thermal management," *Forsch Ingenieurwes*, vol. 85, no. 2, pp. 443–456, Jun. 2021, doi: 10.1007/s10010-020-00423-0.

[127] E. Dlala *et al.*, "Efficiency map simulations for an interior PM motor with experimental comparison and investigation of magnet size reduction," in *2013 International Electric Machines & Drives Conference*, Chicago, IL, USA: IEEE, May 2013, pp. 23–29. doi: 10.1109/IEMDC.2013.6556124.

[128] C. Gorla *et al.*, "Hydraulic losses of a gearbox: CFD analysis and experiments," *Tribology International*, vol. 66, pp. 337–344, Oct. 2013, doi: 10.1016/j.triboint.2013.06.005.

[129] A. Desreveaux, E. Hittinger, A. Bouscayrol, E. Castex, and G. M. Sirbu, "Techno-Economic Comparison of Total Cost of Ownership of Electric and Diesel Vehicles," *IEEE Access*, vol. 8, pp. 195752–195762, 2020, doi: 10.1109/ACCESS.2020.3033500.

[130] C. Mayet *et al.*, "Comparison of Different Models and Simulation Approaches for the Energetic Study of a Subway," *IEEE Trans. Veh. Technol.*, vol. 63, no. 2, pp. 556–565, Feb. 2014, doi: 10.1109/TVT.2013.2280727.

[131] P. Gaudino, L. Strazzullo, and A. Accongiagioco, "Pseudo-Empirical Efficiency Model of a Gearbox for Passenger Cars, to Optimise Vehicle Performance and Fuel Consumption Simulation," presented at the SAE 2004 World Congress & Exhibition, Mar. 2004, pp. 2004-01–1617. doi: 10.4271/2004-01-1617.

[132] V. Ngo, T. Hofman, M. Steinbuch, and A. Serrarens, "Optimal Control of the Gearshift Command for Hybrid Electric Vehicles," *IEEE Trans. Veh. Technol.*, vol. 61, no. 8, pp. 3531–3543, Oct. 2012, doi: 10.1109/TVT.2012.2207922.

[133] K. Li, A. Bouscayrol, S. Cui, and Y. Cheng, "A Hybrid Modular Cascade Machines System for Electric Vehicles Using Induction Machine and Permanent Magnet Synchronous Machine," *IEEE Trans. Veh. Technol.*, vol. 70, no. 1, pp. 273–281, Jan. 2021, doi: 10.1109/TVT.2020.3047219.

[134] "Mechatronics – Backbone and Scalable Systems Platform." Accessed: Jun. 02, 2023. [Online]. Available: https://www.volkswagenag.com/en/strategy/mechatronics.html#

[135] Stellantis, "EV 2021 Stellantis Day, presentation slides." 2021.

[136] "Electric Drive Module: Efficient and Scalable Powertrain System for Electric and Hybrid Vehicles," Bosch. Accessed: Jun. 02, 2023. [Online]. Available: https://www.bosch-mobility-solutions.com/en/solutions/power-electronics/electric-drive-module/

[137] G. Rösel, N. Daun, P. Mönius, G. Mühlberg, and A. Reich, "Scalable Platform For An Efficient 400-Volt Axle Drive," in *42nd International Vienna Motor Symposium*, Vienna, Austria (virtual live event), 2021, p. 20.

[138] K. Ramakrishnan, S. Stipetic, M. Gobbi, and G. Mastinu, "Optimal Sizing of Traction Motors Using Scalable Electric Machine Model," *IEEE Trans. Transp. Electrific.*, vol. 4, no. 1, pp. 314–321, Mar. 2018, doi: 10.1109/TTE.2017.2750488.

[139] "Description – Vision xEV." Accessed: Aug. 19, 2021. [Online]. Available: https://vision-xev.eu/?page_id=36

[140] 1000KmPLUS, "Scalable and highly efficient powertrain technology platform." Accessed: Aug. 20, 2021. [Online]. Available: https://1000kmplus.automotive.oth-aw.de/index.php/project/supply-chain-1

[141] M. Budinger, J. Liscouët, F. Hospital, and J.-C. Maré, "Estimation models for the preliminary design of electromechanical actuators," *Proceedings of the Institution of Mechanical Engineers, Part G: Journal of Aerospace Engineering*, vol. 226, no. 3, pp. 243–259, Mar. 2012, doi: 10.1177/0954410011408941.

[142] F. Verbelen *et al.*, "Comparison of an optimized electrical variable transmission with the Toyota Hybrid System," *Applied Energy*, vol. 278, p. 115616, Nov. 2020, doi: 10.1016/j.apenergy.2020.115616.

[143] A. Aroua, W. Lhomme, E. Redondo-Iglesias, and F. Verbelen, "Fuel saving potential of a long haul heavy duty vehicle equipped with an electrical variable transmission," *Applied Energy*, vol. 307, p. 118264, Feb. 2022, doi: 10.1016/j.apenergy.2021.118264.

[144] A. Bouscayrol *et al.*, "Campus of University with Mobility Based on Innovation and Carbon Neutral," in *2017 IEEE Vehicle Power and Propulsion Conference (VPPC)*, Belfort: IEEE, Dec. 2017, pp. 1–5. doi: 10.1109/VPPC.2017.8331039.

[145] University of Lille, "CUMIN - International Research Program." Accessed: Jul. 31, 2023. [Online]. Available: https://cumin.univ-lille.fr/

[146] A. Bouscayrol, "Formalismes de representation et de Commande Appliques aux Systemes Electromecaniques Multimachines Multiconvertisseurs," Dissertation of the accreditation to supervise research (Manuscrit d'Habilitation à diriger des Recherches HdR), University of Lille, France, 2004.

[147] K. Li, "Modular Connected Machines System for Electrified Vehicles," Ph.D. dissertation, Joint Ph.D. thesis between University of Lille and Harbin Institute of Technology, France and China, 2020.

[148] T. Letrouvé, "Structuration de la commande de la simulation au prototype d'un vehicule hybride double parallele au travers de la Representation Energetique Macroscopique," Ph.D. dissertation, text in French, University of Lille, France, 2013.

[149] A. Pam, "Méthodologie d'émulation pour le test de chaîne de puissance de véhicules électrifiés," Ph.D. dissertation, text in French, University of Lille, France, 2020.

[150] J. Druant, "Modeling and Control of an Electrical Variable Transmission with Hybrid Excitation," Ph.D. dissertation, Ghent University, Belgium, 2018.

[151] F. Verbelen, "A Comparative Study of Mechanical and Electrical Variable Transmissions," Ph.D. dissertation, Ghent University, Belgium, 2019.

[152] Ghent University, "Test Facilities Campus Kortrijk," Universiteit Gent. Accessed: Jun. 04, 2023. [Online]. Available: https://www.ugent.be/ea/emsme/en/research/eelab/dynamicdrivetrains/facilitiescampuskortrijk

[153] S. Dereyne, P. Defreyne, E. Algoet, S. Derammelaere, and K. Stockman, "Efficiency measurement campaign on gearboxes," in *Energy Efficiency in Motor Driven Systems (EEMODS)*, Helsinki, Finland, 2015, p. 11.

[154] Ghent University, "Research Explorer - (DT4V) DT4V – Digital Twins for validation of dynamic performance & reliability of motion systems." Accessed: Sep. 06, 2021. [Online]. Available: https://research.ugent.be/web/result/project/ae42d6c4-0b43-4e3b-b77b-22c8d998aed7/details/en

[155] F. Verbelen, W. Lhomme, A. Aroua, A. Bouscayrol, and P. Sergeant, "Scalable Electrical Variable Transmission model for HEV simulations using Energetic Macroscopic Representation," in *2020 IEEE Vehicle Power and Propulsion Conference (VPPC)*, Gijon, Spain: IEEE, Nov. 2020, pp. 1–6. doi: 10.1109/VPPC49601.2020.9330957.

[156] W. Lhomme, F. Verbelen, M. N. Ibrahim, and K. Stockman, "Energetic Macroscopic Representation of Scalable PMSM for Electric Vehicles," in *2020 IEEE Vehicle Power and Propulsion Conference (VPPC)*, Gijon, Spain: IEEE, Nov. 2020, pp. 1–6. doi: 10.1109/VPPC49601.2020.9330981.

[157] A.-L. Allegre, A. Bouscayrol, J.-N. Verhille, P. Delarue, E. Chattot, and S. El-Fassi, "Reduced-Scale-Power Hardware-in-the-Loop Simulation of an Innovative Subway," *IEEE Trans. Ind. Electron.*, vol. 57, no. 4, pp. 1175–1185, Apr. 2010, doi: 10.1109/TIE.2009.2029519.

[158] E. Buckingham, "On Physically Similar Systems; Illustrations of the Use of Dimensional Equations," *Phys. Rev.*, vol. 4, no. 4, pp. 345–376, Oct. 1914, doi: 10.1103/PhysRev.4.345.

[159] M. D. Petersheim and S. N. Brennan, "Scaling of hybrid-electric vehicle powertrain components for Hardware-in-the-loop simulation," *Mechatronics*, vol. 19, no. 7, pp. 1078–1090, Oct. 2009, doi: 10.1016/j.mechatronics.2009.08.001.

[160] A. Varais *et al.*, "Scaling of wind energy conversion system for time-accelerated and size-scaled experiments," *Mathematics and Computers in Simulation*, vol. 158, pp. 65–78, Apr. 2019, doi: 10.1016/j.matcom.2018.05.015.

[161] G. Rizzoni, L. Guzzella, and B. M. Baumann, "Unified modeling of hybrid electric vehicle drivetrains," *IEEE/ASME Trans. Mechatron.*, vol. 4, no. 3, pp. 246–257, Sep. 1999, doi: 10.1109/3516.789683.

[162] O. Sundstrom, L. Guzzella, and P. Soltic, "Torque-Assist Hybrid Electric Powertrain Sizing: From Optimal Control Towards a Sizing Law," *IEEE Trans. Contr. Syst. Technol.*, vol. 18, no. 4, pp. 837–849, Jul. 2010, doi: 10.1109/TCST.2009.2030173.

[163] C. Wei, T. Hofman, and E. Ilhan Caarls, "Co-Design of CVT-Based Electric Vehicles," *Energies*, vol. 14, no. 7, p. 1825, Mar. 2021, doi: 10.3390/en14071825.

[164] F. J. R. Verbruggen, E. Silvas, and T. Hofman, "Electric Powertrain Topology Analysis and Design for Heavy-Duty Trucks," *Energies*, vol. 13, no. 10, p. 2434, May 2020, doi: 10.3390/en13102434.

[165] M. Pourabdollah, B. Egardt, N. Murgovski, and A. Grauers, "Convex Optimization Methods for Powertrain Sizing of Electrified Vehicles by Using Different Levels of Modeling Details," *IEEE Trans. Veh. Technol.*, vol. 67, no. 3, pp. 1881–1893, Mar. 2018, doi: 10.1109/TVT.2017.2767201.

[166] Q. Xun, N. Murgovski, and Y. Liu, "Joint Component Sizing and Energy Management for Fuel Cell Hybrid Electric Trucks," *IEEE Trans. Veh. Technol.*, pp. 1–1, 2022, doi: 10.1109/TVT.2022.3154146.

[167] K. B. Wipke, M. R. Cuddy, and S. D. Burch, "ADVISOR 2.1: a user-friendly advanced powertrain simulation using a combined backward/forward approach," *IEEE Trans. Veh. Technol.*, vol. 48, no. 6, pp. 1751–1761, Nov. 1999, doi: 10.1109/25.806767.

[168] L. Guzzella and A. Amstutz, "The QSS toolbox manual," *Institut für Mess-und Regeltechnik, Eidgenössische Technische Hochschule Zürich. Zürich*, 2005.

[169] S. Stipetic, J. Goss, D. Zarko, and M. Popescu, "Calculation of Efficiency Maps Using a Scalable Saturated Model of Synchronous Permanent Magnet Machines," *IEEE Trans. on Ind. Applicat.*, vol. 54, no. 5, pp. 4257–4267, Sep. 2018, doi: 10.1109/TIA.2018.2837672.

[170] D. Zarko, S. Frljic, and S. Stipetic, "Design of Premium Efficiency (IE3) Induction Motors Using Evolutionary Optimization and Scaling Laws," *PRZEGLĄD ELEKTROTECHNICZNY*, vol. 1, no. 12, pp. 183–186, Dec. 2016, doi: 10.15199/48.2016.12.46.

[171] E. S. Hamdi, *Design of small electrical machines*. John Wiley & Sons, Inc., 1994.

[172] M. D. Gennaro, P. Scheuermann, T. Wellerdieck, V. Ravello, G. Pellegrino, and E. Trancho, "The H2020 project FITGEN: preliminary results and design guidelines of an integrated e-axle for the third-generation electric vehicles," *Proc. of the 8th Transport Research Arena (TRA)*, p. 10, 2020.

[173] A. Borisavljevic, "Limits, Modeling and Design of High-Speed Permanent Magnet Machines," Ph.D. dissertation, Delft University of Technology, The Netherlands, 2013.

[174] M. Jufer, "Design and Losses - Scaling Law Approach," in *Nordic Research Symposium Energy Efficient Electric Motors and Drives*, Skagen, Denmark, 1996, p. 5.

[175] B. Multon, H. Ben Ahmed, M. Ruellan, and G. Robin, "Comparaison du couple massique de diverses architectures de machines tournantes synchrones à aimants," in *Electrotechnique du Futur*, Grenoble, France, 2005, p. 85. doi: 10.3845/ree.2006.064, text in French.

[176] B. Ge, M. Liu, J. Dong, and W. Liu, "Torque Production Limit of Surface Permanent Magnet Synchronous Machines and Their Electromagnetic Scalability," *IEEE Trans. on Ind. Applicat.*, vol. 57, no. 5, pp. 4353–4362, Sep. 2021, doi: 10.1109/TIA.2021.3084552.

[177] E. Grunditz and T. Thiringer, "Electric Vehicle IGBT Power Module Sizing and Drive Cycle Energy Efficiency for Various Switching Frequencies-Based on a Scalable Module Model," in *20th European Conference on Power Electronics and Applications (EPE'18 ECCE Europe)*, Riga, Latvia, 2018, p. 10.

[178] A. Merkert, T. Krone, and A. Mertens, "Characterization and Scalable Modeling of Power Semiconductors for Optimized Design of Traction Inverters with Si- and SiC-Devices," *IEEE Trans. Power Electron.*, vol. 29, no. 5, pp. 2238–2245, May 2014, doi: 10.1109/TPEL.2013.2294682.

[179] M. Schweizer, T. Friedli, and J. W. Kolar, "Comparative Evaluation of Advanced Three-Phase Three-Level Inverter/Converter Topologies Against Two-Level Systems," *IEEE Trans. Ind. Electron.*, vol. 60, no. 12, pp. 5515–5527, Dec. 2013, doi: 10.1109/TIE.2012.2233698.

[180] M. Kasper, D. Bortis, and J. W. Kolar, "Scaling and balancing of multi-cell converters," in *2014 International Power Electronics Conference (IPEC-Hiroshima 2014 - ECCE ASIA)*, Hiroshima, Japan: IEEE, May 2014, pp. 2079–2086. doi: 10.1109/IPEC.2014.6869875.

[181] J. Azurza Anderson, G. Zulauf, P. Papamanolis, S. Hobi, S. M. Miric, and J. W. Kolar, "Three Levels Are Not Enough: Scaling Laws for Multi-Level Converters in AC/DC Applications," *IEEE Trans. Power Electron.*, pp. 1–1, 2020, doi: 10.1109/TPEL.2020.3018857.

[182] R. Trigui, "Approche systémique pour la modélisation, la gestion de l'énergie et l'aide au dimensionnement des véhicules hybrides thermiques-électriques," Dissertation of the accreditation to supervise research (Manuscrit d'Habilitation à diriger des Recherches HdR), text in French, University of Lille & IFSTTAR, France, 2011.

[183] K. Zhou, A. Ivanco, Z. Filipi, and H. Hofmann, "Finite-Element-Based Computationally Efficient Scalable Electric Machine Model Suitable for Electrified Powertrain Simulation and Optimization," *IEEE Trans. on Ind. Applicat.*, vol. 51, no. 6, pp. 4435–4445, Nov. 2015, doi: 10.1109/TIA.2015.2451094.

[184] H. Ben Ahmed, N. Bernard, G. Feld, and B. Multon, "Machines synchrones - Principes généraux et structures," *Conversion de l'énergie électrique*, Aug. 2005, doi: 10.51257/a-v1-d3520, text in French.

[185] A. Krings, A. Boglietti, A. Cavagnino, and S. Sprague, "Soft Magnetic Material Status and Trends in Electric Machines," *IEEE Trans. Ind. Electron.*, vol. 64, no. 3, pp. 2405–2414, Mar. 2017, doi: 10.1109/TIE.2016.2613844.

[186] J. Regnier, "Conception de systèmes hétérogènes en Génie Électrique par optimisation évolutionnaire multicritère," Ph.D. dissertation, text in French, National Polytechnic Institute of Toulouse, France, 2003.

[187] M. Kuenzler, R. Pflueger, R. Lehmann, Q. Werner, and U. Schaefer, "Scalable Thermal Model of an Electric Machine for the Thermal Assessment in Different Electric Vehicle Use Cases," in *2020 International Symposium on Power Electronics, Electrical Drives,*

Automation and Motion (SPEEDAM), Sorrento, Italy: IEEE, Jun. 2020, pp. 281–286. doi: 10.1109/SPEEDAM48782.2020.9161850.

[188] N. Makowski and B. Helenbrook, "Scaling of Permanent Magnet Machines with Thermal Effects," in *2019 IEEE International Electric Machines & Drives Conference (IEMDC)*, San Diego, CA, USA: IEEE, May 2019, pp. 2035–2041. doi: 10.1109/IEMDC.2019.8785250.

[189] F. Pauli, A. Ruf, and K. Hameyer, "Thermal Overload Capability of Permanent Magnet Synchronous Motors Employing Scaling Laws," in *2018 XIII International Conference on Electrical Machines (ICEM)*, Alexandroupoli: IEEE, Sep. 2018, pp. 433–439. doi: 10.1109/ICELMACH.2018.8506826.

[190] B. Chen, C. Monissen, M. Ayyildiz, G. Birmes, J. Andert, and S. Pischinger, "A Study on Scaling Laws for Thermal Parameters of Permanent Magnet Synchronous Machines," in *2021 24th International Conference on Electrical Machines and Systems (ICEMS)*, Gyeongju, Korea, Republic of: IEEE, Oct. 2021, pp. 35–41. doi: 10.23919/ICEMS52562.2021.9634485.

[191] G. Dilevrano, P. Ragazzo, S. Ferrari, G. Pellegrino, and T. Burress, "Magnetic, Thermal and Structural Scaling of Synchronous Machines," in *2022 IEEE Energy Conversion Congress and Exposition (ECCE)*, Detroit, MI, USA: IEEE, Oct. 2022, pp. 1–8. doi: 10.1109/ECCE50734.2022.9947472.

[192] M. L. Guyadec, "Dimensionnement multi-physique des véhicules hybrides, de leurs composants et de la commande du système," Ph.D. dissertation, text in French, Université Grenoble Alpes, France, 2018.

[193] T. Burress and S. Campbell, "Benchmarking EV and HEV power electronics and electric machines," in *2013 IEEE Transportation Electrification Conference and Expo (ITEC)*, Metro Detroit, MI, USA: IEEE, Jun. 2013, pp. 1–6. doi: 10.1109/ITEC.2013.6574498.

[194] T. Burress, "Benchmarking State-of-the-Art Technologies," *2013 U.S. DOE Hydrogen and Fuel Cells Program and Vehicle Technologies Program Annual Merit Review and Peer Evaluation Meeting*, p. 21, 2013.

[195] V. Reinbold, "Méthodologie de dimensionnement d'un moteur électrique pour véhicules hybrides: optimisation conjointe des composants et de la gestion d'énergie," Ph.D. dissertation, text in French, University of Grenoble, France, 2014.

[196] Infineon Technologies, "Product Brief - HybridPACK™2", [Online]. Available: https://www.infineon.com/dgdl/Infineon-HybridPACK2_Power_Modules-PB-v01_00-EN.pdf?fileId=db3a3043353fdc16013557f17ce67b60

[197] Infineon Technologies, "Automotive IGBT & CoolSiC™ MOSFET Modules - Infineon Technologies." Accessed: Jan. 12, 2023. [Online]. Available: https://www.infineon.com/cms/en/product/power/igbt/automotive-qualified-igbts/automotive-igbt-coolsic-mosfet-modules/

[198] P. Delarue, A. Bouscayrol, and E. Semail, "Generic control method of multileg voltage-source-converters for fast practical implementation," *IEEE Trans. Power Electron.*, vol. 18, no. 2, pp. 517–526, Mar. 2003, doi: 10.1109/TPEL.2003.809349.

[199] N. Ulrich and A. Wintrich, "Determining switching losses of SEMIKRON IGBT modules, Application Note AN 1403." 2014.

[200] P. P. Pott, "Entwurfskriterien feinwerktechnischer integrierter Sensor-Aktor-Systeme," Habilitation dissertation for professorship (Habilitationsschrift), text in German, Technische Universität Darmstadt, Germany, 2015.

[201] U. Weinberger, F. Siglmüller, J. Götz, M. Otto, and K. Stahl, "Scaling of planetary gear stages according to gear excitation similarity," *Proceedings of the Institution of Mechanical Engineers, Part C: Journal of Mechanical Engineering Science*, vol. 233, no. 21–22, pp. 7246–7256, Nov. 2019, doi: 10.1177/0954406219851828.

[202] S. P. Radzevich, *Dudley's handbook of practical gear design and manufacture*, Third edition. Boca Raton: CRC Press, Taylor & Francis Group, ISBN:978-1-4987-5310-4, 2016.

[203] J. B. Boni, C. Changenet, and F. Ville, "Analysis of Flow Regimes and Associated Sources of Dissipation in Splash Lubricated Planetary Gear Sets," *Journal of Tribology*, vol. 143, no. 11, p. 111805, Nov. 2021, doi: 10.1115/1.4051389.

[204] A. Kahraman, D. R. Hilty, and A. Singh, "An experimental investigation of spin power losses of a planetary gear set," *Mechanism and Machine Theory*, vol. 86, pp. 48–61, Apr. 2015, doi: 10.1016/j.mechmachtheory.2014.12.003.

[205] D. C. Talbot, A. Kahraman, and A. Singh, "An Experimental Investigation of the Efficiency of Planetary Gear Sets," *Journal of Mechanical Design*, vol. 134, no. 2, p. 021003, Feb. 2012, doi: 10.1115/1.4005599.

[206] B.-R. Höhn, K. Michaelis, and T. Vollmer, "Thermal rating of gear drives: balance between power loss and heat dissipation," *American Gear Manufacturers Association Technical paper*, 1996.

[207] K. Michaelis, B. Höhn, and M. Hinterstoißer, "Influence factors on gearbox power loss," *Industrial Lubrication and Tribology*, vol. 63, no. 1, pp. 46–55, Feb. 2011, doi: 10.1108/00368791111101830.

[208] Y. Diab, F. Ville, and P. Velex, "Investigations on power losses in high-speed gears," *Proceedings of the Institution of Mechanical Engineers, Part J: Journal of Engineering Tribology*, vol. 220, no. 3, pp. 191–198, Mar. 2006, doi: 10.1243/13506501JET136.

[209] H. Xu, A. Kahraman, N. E. Anderson, and D. G. Maddock, "Prediction of Mechanical Efficiency of Parallel-Axis Gear Pairs," *Journal of Mechanical Design*, vol. 129, no. 1, pp. 58–68, Jan. 2007, doi: 10.1115/1.2359478.

[210] S. K. F. Bearings, "The SKF Model for Calculating the Frictional Moment," *SKF Technical paper*, Accessed: Aug. 04, 2023. [Online]. Available: https://cdn.skfmediahub.skf.com/api/public/0901d1968065e9e7/pdf_preview_medium/0901d1968065e9e7_pdf_preview_medium.pdf

[211] F. Concli, E. Conrado, and C. Gorla, "Analysis of power losses in an industrial planetary speed reducer: Measurements and computational fluid dynamics calculations," *Proceedings of the Institution of Mechanical Engineers, Part J: Journal of Engineering Tribology*, vol. 228, no. 1, pp. 11–21, Jan. 2014, doi: 10.1177/1350650113496980.

[212] C. Changenet, G. Leprince, F. Ville, and P. Velex, "A Note on Flow Regimes and Churning Loss Modeling," *Journal of Mechanical Design*, vol. 133, no. 12, p. 121009, Dec. 2011, doi: 10.1115/1.4005330.

[213] British Standards Institution, "ISO/TR 14179-1:2001: Gears — Thermal capacity — Part 1: Rating gear drives with thermal equilibrium at 95 °C sump temperature," *ISO*, 2001.

[214] J. J. Greenbaum, M. A. Kluger, and B. E. Westmoreland, "Manual Transmission Efficiency Trends and Characteristics," presented at the SAE Technical Paper Series, International Truck & Bus Meeting & Exposition, Nov. 1994.

[215] C. H. Wink, L. Marson, and S. Goyal, "Hybrid analytical-experimental method to map power losses of automotive transmissions over their operating range," *Tribology International*, vol. 143, p. 106070, Mar. 2020, doi: 10.1016/j.triboint.2019.106070.

[216] F. Verbelen, P. Defreyne, P. Sergeant, and K. Stockman, "Efficiency measurement strategy for a planetary gearbox with 2 degrees of freedom," in *Energy Efficiency in Motor Driven Systems (EEMODS)*, Tokyo, Japan, 2019, p. 13.

[217] Neugart, "Gearbox catalog - PSBN: The high-performance precision planetary gearbox with helical teeth for a particularly quiet drive."

[218] S. Derammelaere, S. Dereyne, P. Defreyne, E. Algoet, F. Verbelen, and K. Stockman, "Energy efficiency measurement procedure for gearboxes in their entire operating range," in *2014 IEEE Industry Application Society Annual Meeting*, Vancouver, BC, Canada: IEEE, Oct. 2014, pp. 1–9. doi: 10.1109/IAS.2014.6978376.

[219] The MathWorks, Inc, "Curve Fitting Toolbox User's Guide For Use with MATLAB®." 2002.

[220] C. Changenet and P. Velex, "A Model for the Prediction of Churning Losses in Geared Transmissions—Preliminary Results," *Journal of Mechanical Design*, vol. 129, no. 1, pp. 128–133, Jan. 2007, doi: 10.1115/1.2403727.

[221] T. T. Petry-Johnson, A. Kahraman, N. E. Anderson, and D. R. Chase, "An Experimental Investigation of Spur Gear Efficiency," *Journal of Mechanical Design*, vol. 130, no. 6, p. 062601, Jun. 2008, doi: 10.1115/1.2898876.

[222] Renault Group, "The New Twingo Z.E.: Twingo is more than ever the queen of the city." Press kit, 2020.

[223] "2019 Nissan Leaf S - Specifications and price," EVSpecifications. Accessed: Jan. 13, 2023. [Online]. Available: https://www.evspecifications.com/en/model/2bc417

[224] "BYD TRUCK ETM6." Accessed: Feb. 23, 2022. [Online]. Available: https://bydeurope.com/pdp-etm-6

[225] T. J. Barlow, S. Latham, I. S. McCrae, and P. G. Boulter, *A reference book of driving cycles for use in the measurement of road vehicle emissions*, TRL published project report PPR354., vol. Version 3. 2009.

[226] F. Rodríguez and O. Delgado, "The future of VECTO: CO2 certification of advanced heavy-duty vehicles in the European Union," *White paper of ICCT (Internatioanl Council on Clean Transportation)*, p. 37, 2019.

[227] J. Hemsen *et al.*, "Innovative and Highly Integrated Modular Electric Drivetrain," *WEVJ*, vol. 10, no. 4, p. 89, Dec. 2019, doi: 10.3390/wevj10040089.

[228] H. He, C. Wang, H. Jia, and X. Cui, "An intelligent braking system composed single-pedal and multi-objective optimization neural network braking control strategies for electric vehicle," *Applied Energy*, vol. 259, p. 114172, Feb. 2020, doi: 10.1016/j.apenergy.2019.114172.

[229] P. Saiteja, B. Ashok, A. S. Wagh, and M. E. Farrag, "Critical review on optimal regenerative braking control system architecture, calibration parameters and development challenges for EVs," *Intl J of Energy Research*, vol. 46, no. 14, pp. 20146–20179, Nov. 2022, doi: 10.1002/er.8306.

[230] P.-É. Vidal, B. Trajin, and F. Rotella, "Stratégie et technique pour le pilotage en modulation des convertisseurs statiques," *Technique de l'ingénieur*, Dec. 2019, doi: 10.51257/a-v1-e3969, text in French.

[231] A. Emadi, *Advanced Electric Drive Vehicles*. in CRC Press. 2015.

[232] A. Aroua, W. Lhomme, F. Verbelen, A. Bouscayrol, and K. Stockman, "Inversion-based Control of Scaled PMSM for Battery Electric Vehicles," in *2021 IEEE Vehicle Power and Propulsion Conference (VPPC)*, Gijon, Spain: IEEE, Oct. 2021, pp. 1–6. doi: 10.1109/VPPC53923.2021.9699198.

[233] T. Hofman and M. Salazar, "Transmission Ratio Design for Electric Vehicles via Analytical Modeling and optimization," in *2020 IEEE Vehicle Power and Propulsion Conference (VPPC)*, Gijon, Spain: IEEE, Nov. 2020, pp. 1–6. doi: 10.1109/VPPC49601.2020.9330997.

[234] T. Letrouve, A. Bouscayrol, W. Lhomme, N. Dollinger, and F. M. Calvairac, "Different models of a traction drive for an electric vehicle simulation," in *2010 IEEE Vehicle Power and Propulsion Conference*, Lille, France: IEEE, Sep. 2010, pp. 1–6. doi: 10.1109/VPPC.2010.5729209.

[235] European Environment Agency., *Decarbonising road transport: the role of vehicles, fuels and transport demand.* LU: Publications Office, 2022. Accessed: May 11, 2023. [Online]. Available: https://data.europa.eu/doi/10.2800/68902

[236] European Parliament, "Regulation of the European parliament and of the council amending regulation (EU) 2019/631 as regards strengthening the CO2 emission performance standards for new passenger cars and new light commercial vehicles in line with the union's increased climate ambition." 2023.

[237] National Highway Traffic Safety Administration (NHTSA) and Environmental Protection Agency (EPA), "Federal Register, 40, 25323-25728: Light-duty vehicle greenhouse gas emission standards and corporate average fuel economy standards; final rule." 2010.

[238] Environmental Protection Agency (EPA), "EPA and NHTSA Set Standards to Reduce Greenhouse Gases and Improve Fuel Economy for Model Years 2017-2025 Cars and Light Trucks." 2012.

[239] Environmental Protection Agency (EPA) and National Highway Traffic Safety Administration (NHTSA), "Federal Register / Vol. 85, No. 84:The Safer Affordable Fuel-Efficient (SAFE) Vehicles Rule for Model Years 2021–2026 Passenger Cars and Light Trucks." 2020. Accessed: May 12, 2023. [Online]. Available: https://www.govinfo.gov/content/pkg/FR-2020-04-30/pdf/2020-06967.pdf

[240] Environmental Protection Agency (EPA) and National Highway Traffic Safety Administration (NHTSA), "Federal Register / Vol. 86, No. 248: Revised 2023 and later model year light-duty vehicle greenhouse gas emissions standards." 2021.

[241] Environmental Protection Agency (EPA) and National Highway Traffic Safety Administration (NHTSA), "Federal Register / Vol. 76, No. 179: Greenhouse Gas Emissions Standards and Fuel Efficiency Standards for Medium- and Heavy-Duty Engines and Vehicles."

[242] Environmental Protection Agency (EPA), "Federal Register / Vol. 81, No. 206: Greenhouse Gas Emissions and Fuel Efficiency Standards for Medium- and Heavy-Duty Engines and Vehicles— Phase 2." 2011.

[243] "EV Database," EV Database. Accessed: Jun. 07, 2023. [Online]. Available: https://ev-database.org/

[244] "EV Tech Specs | myEVreview." Accessed: Jun. 07, 2023. [Online]. Available: https://www.myevreview.com/tech-specs

[245] "EVSpecifications - Electric vehicle specifications, electric car news, EV comparisons," EVSpecifications. Accessed: Jun. 07, 2023. [Online]. Available: https://www.evspecifications.com

[246] B.-H. Nguyễn, "Energy Management Strategies Of Electric And Hybrid Vehicles Supplied By Hybrid Energy Storage Systems," Ph.D. dissertation, Joint Ph.D between the University of Lille and the University of Sherbrooke, France and Canada, 2019.

[247] A.-L. Allegre, "Methodologies De Modelisation Et De Gestion De L'energie De Systemes De Stockage Mixtes Pour Vehicules Electriques Et Hybrides," Ph.D. dissertation, text in French, University of Lille, France, 2010.

[248] H. Polinder and M. . J. Hoeijmakers, "Eddy-current losses in the segmented surface-mounted magnets of a PM machine," *IEE Proceedings-Electric Power Applications*, vol. 146, no. 3, pp. 261–266, 1999.

[249] J. F. Gieras, *Permanent magnet motor technology: design and applications*, 3rd ed. Boca Raton: CRC Press, 2010.

[250] N. Marc, "Méthodologie de dimensionnement d'un véhicule hybride électrique sous contrainte de minimisation des émissions de CO2," Ph.D. dissertation, text in French, Orléans University, France, 2013.

[251] R. G. Budynas and J. K. Nisbett, *Shigley's mechanical engineering design*, 9th ed. in McGraw-Hill series in mechanical engineering, ISBN: 978-0-07-352928-8. New York: McGraw-Hill, 2011.

[252] HBK, "Datasheet GEN series GN310B (GN311B)."

[253] A. Bouscayrol, M. Pietrzak-David, P. Delarue, R. Pena-Eguiluz, P.-E. Vidal, and X. Kestelyn, "Weighted Control of Traction Drives With Parallel-Connected AC Machines," *IEEE Trans. Ind. Electron.*, vol. 53, no. 6, pp. 1799–1806, Dec. 2006, doi: 10.1109/TIE.2006.885106.

[254] S. Pfragner and C. Juwan, "AVL company presentation slides - Vehicle Benchmark of the BMW iX: How functions & features contribute to high level of driving excitement and efficiency," 2022.